

© 2015 Pervin Gizem Gezer

MANUFACTURE AND UTILIZATION OF A BIODEGRADABLE SENSOR
PLATFORM FROM GOLD COATED ZEIN NANOPHOTONIC FILMS TO
DETECT ACRYLAMIDE AND ARA-H1 USING SERS

BY

PERVIN GIZEM GEZER

DISSERTATION

Submitted in partial fulfillment of the requirements
for the degree of Doctor of Philosophy in Food Science and Human Nutrition
with a concentration in Food Science
in the Graduate College of the
University of Illinois at Urbana-Champaign, 2015

Urbana, Illinois

Doctoral Committee:

Professor Shelly J. Schmidt, Chair
Professor Jozef L. Kokini, Director of Research
Professor Gang Logan Liu
Professor Yong-Su Jin
Associate Professor Yuan Yao

ABSTRACT

With the current developments in biosensor and nanotechnology, detection of analyses that are important to food industry are becoming more commonplace. One of the strong tools that nanotechnology enabled is Surface Enhanced Raman Spectroscopy (SERS). SERS is a highly sensitive and specific technique which provides molecular fingerprinting, with the enhancement effect as a result of roughened noble metal surfaces. The platform for these surfaces are generally made out of non-biodegradable, plastic materials. As the one-time use, large-scale applications are needed for many fields such as medical, forensic and food industry, disposability of these sensors will pose a problem in the future.

In the scope of this dissertation, we investigated the feasibility of a biodegradable sensor platform that is made of zein, a corn protein, utilized in SERS measurements of food analytes. First, the effect of parent substrate (the surface, which zein was cast on) and plasticizer, oleic acid content, on the surface hydrophilicity of resulting zein films was analyzed. It was found that the surface chemistry of the parent substrate was more important than the topography of the parent substrate. Oxygen plasma was used to make the polydimethylsilohexane (PDMS) surfaces more hydrophilic and it was found that zein film surfaces that were in contact with PDMS also had more hydrophilic surfaces, compared to regular PDMS, which is a hydrophobic material. Water contact angle (WCA) method was used to quantify the hydrophilicity of zein films. WCA reached values as low as 20 degrees with a high oleic acid content. Increase in oleic acid content in the formulation of zein films as well as the parent substrate chemistry was found to influence the water affinity of zein films.

In the development of the fabrication method of nanopatterned and gold coated zein surfaces, a simultaneous three-dimensional transfer was used. Four different nanopatterns, namely positive pyramids, inverted pyramids, nano pillars and nano pores were transferred onto zein films along with either 80 or 200 nm gold coating by using solvent casting technique. Scanning microscopy images showed that the patterns were transferred onto zein films with high fidelity and success. The enhancement effect of these SERS substrates were tested by using a model molecule, Rhodamine 6G. It was found that the best enhancement effect was provided by inverse-pyramid structures coated with 200 nm gold. For the rest of the study, these structures were used.

Zein-SERS substrates were utilized in two different food analyte detection purpose, acrylamide and peanut allergen protein Ara h1. Acrylamide is a potential carcinogenic compound that is formed during high temperature food processing. French fries, potato chips, bread and coffee are some of the food products that may contain high amounts of acrylamide. Since Food and Drug Administration released a draft advisory for mitigation strategies for acrylamide content in foods, there is a need for routine testing technique of acrylamide in food products. In this research, acrylamide was detected by using zein-SERS substrates as a proof-of-concept. Limit of detection was found to be 10 micrograms/milliliter. Calibration curve was obtained with an R^2 value of 0.93 and 0.97 for log-log version.

Peanut allergies are among the most common food allergies, and they can result in life-threatening reactions in allergic patients. For this reason, it is extremely important to monitor the presence or cross-contamination of peanuts into food products. There are 8 identified peanut allergen proteins and Ara h1, consists of the largest percentage of protein content, in addition to causing reactions in almost 100 % of the patients. zein-SERS substrates were utilized in detection of Ara h1. With the use of statistical clustering technique called principal component analysis (PCA), it was possible detect and quantify Ara h1 protein. Limit of detection was found to be 0.14 mg/ml. The surface of the zein-SERS substrates were functionalized with monoclonal antibody and tested for capturing Ara h1 as

a proof-of-concept.

With this research, utilizing zein as a biodegradable sensor platform for SERS measurements were investigated for the first time. It was shown that detection of both acrylamide and Ara h1, peanut protein, was possible. The methods developed in this study for controlling the surface hydrophilicity of zein films and direct transfer of both micro and nano-scale patterns onto zein along with noble metals can be employed in other biosensor and biopolymer applications as well in the future. This kind of biodegradable platforms might be an alternative solution for environmentally friendly and large scale sensor applications.

To my family, for their love and support.

ACKNOWLEDGMENTS

This dissertation would not be possible without the support of many individuals whom I would like to thank in the following paragraphs.

First, I would like to express my gratitude to my advisor, Dr. Jozef Kokini, for originating the idea of biodegradable sensors and building a collaboration with Dr. Liu that enabled me to access the know-how in his laboratory and for helping me select the appropriate engineering courses that improved my background in this area. Despite the fact that he moved to another university during the second half of my graduate program, he was consistently available to discuss research with me. I feel grateful for his guidance and support throughout these years.

I would like to extend my gratitude to Dr. Logan Liu for allowing me to use the technology developed in his lab, helping me through the challenges of the project, and giving many useful suggestions during personal and committee meetings. I would like to thank his student, Dr. Austin Hsiao, for showing me the hands-on techniques and for the numerous discussions that we had on generating ideas and finding solutions to the research problems addressed in this dissertation.

Many thanks to my committee chair Dr. Shelly Schmidt, who made me feel welcome and gave me a lab group environment with her students at a time when all other members of my lab moved to another university. I am very grateful for her guidance throughout the last years of my journey and I feel lucky to be able to work as her TA during my last semester. I would also like to thank my committee members Dr. Yong-Su Jin and Dr. Yuan Yao for asking mind-provoking questions and giving suggestions during my exams. I would also like to extend my gratitude

to Dr. Kris Lambert for his guidance and support during the beginning of my PhD program.

I would like to express my gratitude to the Food Science and Human Nutrition department, particularly to Dr. Sharon Nickols-Richardson and Dr. Nicki Engeseth for facilitating the last two years of my PhD when my advisor was no longer at the university. Many thanks to the very helpful FSHN staff in this process as well.

I would like to thank Dr. Jarupat Luecha for teaching me the laboratory techniques and sharing the know-how that she developed, which enabled me to start my project with great speed. Many thanks to Serena Brodsky, for giving me the opportunity to be her mentor during her undergraduate research experience, for many useful discussions, and for help with the data collection required for the first objective of my dissertation.

I would like to thank the Imaging Technology Group Superusers at the Beckman Institute: Scott Robinson for scanning electron microscopy images and Dianwen Zhang for Raman spectroscopy measurements, and to both for training me and helping me troubleshoot my experiments. In addition, my thanks goes to Dr. Julio Soares for laser facility and to Dr. Kathy Walsh and Dr. Scott MacLaren for Atomic Force Microscopy as they were very helpful for certain aspects of data collection that I conducted in Materials Research Library.

I would also like to express my gratitude for my labmates during my first two years including Dr. Francesca de Vito, Shadi Ansari, Suzan Uzun, and Fatih Bozkurt for making the lab and office a happy and supportive environment. I also would like to thank Gamze, Hazal, Ozlem, Luis, and Jose for welcoming me to the lab and office during the two weeks I spent at Purdue University, which was a very crucial time for finishing my dissertation.

The four years that took me to finish this dissertation in Champaign-Urbana introduced me to many people that I hold dear to me. A big thank you for the amazing friendship and continuous support of Nadine Aubourg, Linda Moran and Gulcin Yildiz in this journey. Thank you Dr. Figen Oktem for being a great friend,

roommate, and eye-opener during the many discussions about academia that we had. Thank you Sam, Bilge and Mohit for being great and supportive friends. Thank you Mujde and Levent Gezer for the many homey gatherings that made being away from Turkey easier. Thank you to the amazing Turkish community that we have in Champaign-Urbana for making it fun. Thank you to the salsa community for taking my mind away from research at times and giving me many friends.

Last but not least, I would like to thank my mom, Oznur, my dad, Turgay, and my brother, Berk who supported and loved me unconditionally all my life. I would like to thank my mother-in-law, father-in-law, brother-in-law and sister-in-law for making me feel like a member of the family and helping me while walking on the road of this PhD. I would like to thank my friends Burcu, Destan, Deniz, Busra, Tulay, and Ozge for continuing to cheer me up thousands of miles away.

I don't have enough words to express my gratitude to my husband, Mikael, for his love and support through this challenging period of my life, for bearing countless ups and downs of this process with me, and for showing me what being there for each other means.

Finally, thank you, reader, for taking the time to read or look through my dissertation. I hope you will find something that will help you!

TABLE OF CONTENTS

LIST OF TABLES	xi
LIST OF FIGURES	xii
CHAPTER 1 INTRODUCTION	1
CHAPTER 2 LITERATURE REVIEW	4
2.1 Zein	4
2.2 Zein films	10
2.3 Biosensors	25
2.4 Surface Enhanced Raman Spectroscopy	26
2.5 Food contaminant and allergen detection	51
CHAPTER 3 MODIFICATION OF THE HYDROPHILIC / HYDROPHO- BIC CHARACTERISTIC OF ZEIN FILM SURFACES BY CON- TACT WITH OXYGEN PLASMA TREATED PDMS AND OLEIC ACID CONTENT ¹	62
3.1 Abstract	62
3.2 Introduction	63
3.3 Materials and methods	64
3.4 Results and discussion	69
3.5 Conclusion	80
CHAPTER 4 FABRICATION OF A NANOPHOTONIC PLATFORM ON ZEIN FOR SURFACE ENHANCED RAMAN SPECTROSCOPY ¹	84
4.1 Abstract	84
4.2 Introduction	85
4.3 Materials and Methods	87
4.4 Results and Discussion	93
4.5 Conclusion	111
CHAPTER 5 DETECTION OF ACRYLAMIDE USING ZEIN-SERS PLATFORM ¹	114
5.1 Abstract	114
5.2 Introduction	115

5.3	Materials and Methods	117
5.4	Results and Discussion	120
5.5	Conclusion	130
CHAPTER 6 DETECTION OF PEANUT ALLERGEN, ARA H1, USING ZEIN - SERS PLATFORM ¹		
6.1	Abstract	132
6.2	Introduction	133
6.3	Materials and Methods	133
6.4	Results and Discussion	137
6.5	Conclusion	149
CHAPTER 7 CONCLUSION		151
CHAPTER 8 REFERENCES		153
APPENDIX A		169
A.1	Example code for Principal component analysis	169
A.2	Specifications of Atomic Force Microscopy	185

LIST OF TABLES

2.1	Amino acid composition of 19 kDa and 22 kDa α -zein. Adapted from (Shewry and Tatham, 1990)	6
2.2	WAXS and SAXS measurement results (d-spacing) of different zein films (Lai et al., 1999)	12
2.3	Wavenumbers for some molecular groups (Vandenabeele, 2013) . .	30
2.4	Some examples of food analyte detection using SERS (analyte detected, SERS-substrate used, LOD: limit of detection	46
3.1	Peak assignments for Raman signature of PDMS films	70
4.1	ASTM D3359 Adhesion test classification	91
4.2	List of different fabrication strategies for zein films with nanophotonic structures	93
4.3	Surface properties of materials that were used to transfer metal onto zein (UVcP: Ultraviolet-cured polymer, PET: polyethylene terephthalate, PDMS: polydimethylsiloxane, Au: gold, Ag: Silver) References a: Dann (1970), b: Sowell et al. (1972), c: Vitos et al. (1998)	96
5.1	Amount of acrylamide in various food products (Krishnakumar et al., 2014)	116
5.2	Some characteristic peaks and vibration assignments of acrylamide and glass slide	121

LIST OF FIGURES

2.1	Different fractions of zein separated by SDS-PAGE (Shewry and Tatham, 1990)	5
2.2	The amino acid sequences of Z19 and Z22 (Shewry and Tatham, 1990)	7
2.3	Conformational model of α -zein (Matsushima et al., 1997)	8
2.4	Left: Proposed model for zein-oleic acid complex for resin films. Right: proposed alternative stacking options These models were proposed based on the WAXS and SAXS data, in addition to Matsushima’s model of zein structure: L (13 nm) x W (3 nm) x D (1.2 nm). (Lai et al., 1999)	13
2.5	Top: FTIR spectra of zein films without and with plasticizers or combination of plasticizers. Bottom: Calculated secondary structures based on FTIR measurements (Xu et al., 2012)	14
2.6	Differential Scanning Calorimetry measurements of cast zein films (dotted line) and resin zein films (solid line) Melting peak at 7 °C and crystallization peaks at - 0.9 °C and -4.3 °C of oleic acid were only observed for cast films (Lai and Padua, 1997).	15
2.7	Schematic of Surface Plasmon Resonance sensor. When the molecules bind to the gold side of the sensor chip, resonance angle shifts and the change in this angle can be observed kinetically as shown in the plots(Cooper, 2002).	16
2.8	Water contact angle and wettability θ_e . Adapted from (Lee and Owens, 2011)	18
2.9	Water contact angles of zein films cast on PE sheets with different conditions. White bars: air side, black bars: basal side. A/E: Acetone or Ethanol solution, First number: initial concentration of zein, Second number: drying temperature, Last number: drying relative humidity (Yoshino et al., 2000)	19
2.10	AFM Contact mode mechanism. Cantilever is in contact with the surface throughout the measurement while the height of the cantilever is adjusted based on the feedback loop (Asylum AFM-MRP-3D Manual)	21

2.11	AFM Tapping mode (AC) mechanism. Top: Cantilever oscillates with a certain amplitude while going over the surface. Bottom: height of the cantilever is adjusted based on the feedback to avoid cantilever damage (Asylum AFM-MRP-3D Manual) . . .	22
2.12	Atomic Force microscopy images of zein films a) on hydrophobic surface and b) on hydrophilic surface. The surface roughness for a is 1.35 nm whereas for b is 4.7 nm (Subramanian and Sampath, 2007a)	23
2.13	Proposed model of zein's film forming mechanism on top of hydrophilic (carboxylic-ended SAMs) and hydrophobic (methyl-ended SAMs) based on Matsushima's model (Subramanian and Sampath, 2007a)	24
2.14	Atomic force microscopy images of zein adsorbed onto 1-octanethiol surface (left) and 11-mercaptoundecanoic acid surface (right) (Wang et al., 2003a)	24
2.15	Interaction of light with a medium in different forms. Adapted from Zhang 2012	27
2.16	a) Energy level diagram of light scattering where E: energy of the photon, h: Planck constant, ν : frequency of the photon (Barron, 2013). b) Example Raman spectrum of potassium permanganate showing both Stokes and Anti-Stokes regions (Johnson et al., 2012)	27
2.17	Different modes of molecular vibrations for a three-atom molecule. Twisting, wagging, rocking and scissoring are types of bending vibrations (Nawrocka and Lamorska, 2013)	29
2.18	Baseline correction on a Raman spectrum. The solid line on top represents the original spectrum, the dotted line represents the fitted baseline curve, and the solid line at the bottom shows the subtracted spectrum. a) First iteration b) seventh iteration (Vandenabeele, 2013)	33
2.19	Diagram of dispersive Raman (a) and FT-Raman instruments (b) (Vandenabeele, 2013)	34
2.20	Schematic diagram of plasmon resonance on a flat surface (a) vs localized surface plasmon on a spherical nanoparticle (b). The free electrons oscillate with the electromagnetic wave as shown in this figure (Willetts and Van Duyne, 2007)	35
2.21	Nanoparticle resonance range of plasmon resonances for a variety of particle morphologies (Middle). Electron micrographs of gold spheres (a), silver spheres (b), silicon oxide/silver (core/shell) nanoshells (c), nanorods (d), triangular plates (e), nanocubes (f) and nanorices (g). (Retrieved from Liu et al. (2013b), Lal et al 2011, Grabar et al 1995, Wiley et al 2004, Nikoobakht and El-Sayed 2003, Washio et al 2006, Wiley et al 2006, Wang et al 2006)	37

2.22	Scanning electron microscope images of gold nanoparticles synthesized through chemical reduction process. Top: seeded growth, Bottom: particles made without pre-made seeds (Grzelczak et al., 2008)	38
2.23	Schematic of e-beam evaporator (Xu and Huq, 2005)	39
2.24	Fabrication process of positive and inverted pyramids replica SERS substrates. (a) Inverted pyramids silicon template. (b) Polymer molding on silicon master and cured by UV illumination. (c) Positive pyramids replica after being peeled off. (d) Positive pyramids template made by e-beam evaporation of 20 nm SiO ₂ onto positive pyramids replica. (e) Polymer molding on the positive pyramids template and cured by UV illumination. (f) Inverted pyramids replica after being peeled off. (g) Inverted pyramids SERS substrate completed by deposition of 10 nm of titanium followed by 200 nm of gold onto inverted pyramids replica. (h) Positive pyramids SERS substrate completed by deposition of 10 nm of titanium followed by 200 nm of gold onto positive pyramids replica. Retrieved from Xu et al. (2011).	41
2.25	Scanning electron micrographs of pyramids replica. (a) Positive pyramids replica. The inset is a zoomed-in image. (b) Positive pyramids replica with 200-nm thick gold deposited. (c) Inverted pyramids replica. The inset is a zoomed-in image. (d) Inverted pyramids replica with 200-nm thick gold deposited. Retrieved from Xu et al. (2011)	42
2.26	(A) Schematic of average number of pillars per unit area, (B) assumed structure for the nanopillar, (C) SEM of LLNL nanopillar substrate with 80 nm silver deposited pillar shown in the inset. Retrieved from Gartia et al. (2010)	42
2.27	Reflectance spectrum for silver film over nanospheres with different thickness (Lin 2010)	44
2.28	Principal component plots for adulterated and non-adulterated samples with Sudan I dye. Principle components were for Raman spectra of a) raw data b) Baseline corrected and smoothed data (Di Anibal et al., 2012)	51
2.29	Principal component plot for PC 1 and PC 2 for ferbam, a pesticide, at different concentrations (Zheng et al. 2013)	52
2.30	PCA plot showing discrimination between five Bacillus spore samples and Pantoea agglomerans (Guicheteau et al. 2008)	52
2.31	Crystal structure of the Ara h1 monomer (Left) and Trimer formed by Ara h1 (Right) with a 0 and 90 rotation (Chruszcz et. al. 2011).	53

2.32	Different types of ELISA, Left-top: Direct sandwich assay, Left-bottom: Indirect sandwich assay, Right-top: Direct competitive assay, Right-bottom: Indirect competitive assay (Schubert-Ullrich et al., 2009).	55
2.33	Top: the electrode used in the impedance-based electrochemical sensor, Rs: solution-phase resistance, Cd: differential capacitance, Rct: charge transfer resistance, and Zw: impedance. Bottom: correlation of Ara h1 concentration with charge transfer resistance (Huang et al., 2008)	56
2.34	Left: Primary antibody functionalized gold substrate for surface plasmon resonance system with three different test methods: label-free, secondary antibody and nanoparticle with secondary antibodies. Right: Corresponding wavelength shift plot for these three cases (Pollet et al., 2011)	57
2.35	Gold immunochromatography assay (GICA) strips for detection of peanut allergen Ara h1, 1: Extract buffer; 2:PBS; 3:1000; 4:500; 5:250; 6:100; 7:50; 8:25; 9:10; 10:5; 11:2.5 ng/ml. The concentrations indicated are the quantity of total protein per ml of crude peanut extract. +: positive; -: negative; +/-: not definitive (Ji et al., 2011)	58
2.36	Molecular structure of acrylamide (Jonathan, 1961)	60
2.37	Raman spectrum of 1 M solution of acrylamide in water (solid line) (Jonathan, 1961)	61
3.1	Schematic overview of the process of generating sandpaper textured PDMS and zein films	66
3.2	Raman spectra of PDMS O+ (blue) and PDMS O- (red) (A.u.: Arbitrary units)	70
3.3	Left: Comparison of water contact angle of the surface of PDMS, zein (contact side) and zein (air side). Light grey is O- (O min) and dark grey is O+ (1 min exposure to oxygen plasma). The inset shows the surfaces on which the water contact angle was measured. Right: Water contact angle measurement on the surface of zein film that was in contact with PDMS O+ vs direct exposure on zein films after film formation. Error bars represent standard deviation (n=3).	72

3.4	(a) A polydimethylsiloxane (PDMS) film exposed to O ₂ -plasma for 1 min; there is a mask placed to selectively treat the surface of the PDMS film. (b) Immediately after O ₂ -plasma treatment, the mask was removed and zein solution was cast over the PDMS film and (c) zein film cured in a vacuum desiccator, (d) Once it is cured, the zein film is separated from the PDMS film, (e) Visual comparison of PDMS film with mask and (f) Cured zein film shows replication of corresponding hydrophobic and hydrophilic regions on the zein film.	74
3.5	Optical absorbance measurement of hydrophilic and hydrophobic regions on zein film that was cast on treated PDMS film.	75
3.6	Microscopy images of zein surface cast on wax, sandpaper textured PDMS and smooth PDMS.	76
3.7	Graphical comparison of zein contact angles compared to the surface it was cast on. Error bars represent standard deviation (n=4).	77
3.8	Water contact angle of zein films (contact side) vs different oleic acid ratios for O+ vs O- (Left). The difference between water contact angles of O- vs O+ plotted against zein:OA ratio (Right).Error bars represent standard deviation for different sets of experiments (n=3), within each experiment WCA was calculated by averaging data points on the same sample (n=4)	78
3.9	AFM images of zein films. O+: zein was cast on PDMS exposed to oxygen plasma, whereas O-: zein was cast on PDMS. Numbers represent the zein: oleic acid ratio.Scale bars range from 5 nm (yellow) and -5 nm (blue).	82
3.10	Atomic Force microscopy images. (Left) macro image showing the location of edge between masked and unmasked area in zein films (Middle) height profile of this region (Right) Adhesion profile obtained by mapping of force curves.	83
4.1	Scanning electron microscopy images of nanophotonic master molds: Positive pyramids (Left), Negative pyramids (Middle) and Nanopillars (Right)(Xu et al., 2011; Gartia et al., 2010)	89
4.2	Schematic diagram of the direct transfer of three-dimensional metallic nanophotonic structures onto zein, a corn plant-based biopolymer. A template made of either PET or with nanophotonic structures (a) is deposited with 200 nanometers of noble metal using E-Beam Evaporation (b). Zein solution is solvent-casted over the metal-coated template (c), and after fully solidifying; the zein film with three-dimensional metallic nanophotonic structures is separated from the template (d)	90

4.3	The transfer of noble metal onto zein film. Unsuccessful transfer evident by the squared area having the patterns did not transfer onto zein film (on the right) (a), successful transfer of silver (b) and gold (c)	94
4.4	Representation of gold - sulfur bonding (Häkkinen, 2012)	97
4.5	Top-down view of the inverted pyramid nanophotonic structures and (b) positive pyramid nanophotonic structures transferred on zein (Scale bars: 2 μ m)	98
4.6	Different magnification scaled SEM images for zein with 200 nm gold coated inverted pyramids, master mold with nanopillars	99
4.7	Cross-sectional SEM images of gold coated inverted pyramid structures on zein films Scale bars: 2 μ m (a) and 0.5 μ m (b)	100
4.8	Scanning electron microscopy images of nanopillars on PET (a), gold coated nanopores on PDMS (b), gold-coated nanopores on zein (c) and gold-coated nanopillars on zein (d)	102
4.9	Different magnification scaled SEM images for master mold with nanopillars	103
4.10	Different magnification scaled SEM images for PDMS with 80 nm gold coated nanopores	104
4.11	Different magnification scaled SEM images for zein with 80 nm gold coated nanopores	105
4.12	Different magnification scaled SEM images for zein with 80 nm gold coated nanopillars/domes	106
4.13	Cross-sectional Scanning electron microscopy images of gold-coated nanopillars on zein (a) and gold coated nanopores on zein (b)	107
4.14	Reflectance spectra of 200 nm gold-coated inverted pyramids on zein (a) and 80 nm gold-coated nanopillars on zein (b) Lower reflectance is as a result of absorption of the light and thus, lowest possible reflection is preferred for laser selection for SERS	108
4.15	Raman spectra of Rhodamine 6G on gold-coated nanopillar zein sensors excited with 532 nm, 633 nm and 785 nm lasers. In these figures, raw data is presented and it was found that all lasers induced fluorescence (evident by the broad peak features of the baseline). 633 nm laser (middle) had the sharp Raman peaks with the best signal: noise ratio. In these figures, raw data is presented and it was found that all lasers induced fluorescence (evident by the broad peak features of the baseline). 633 nm laser (middle) had the sharp Raman peaks with the best signal: noise ratio.	109
4.16	Raw data of Raman spectrum of Rhodamine 6G at 9 different mapping locations.	110

4.17	Different concentrations of Rhodamine 6G on (a) 200 nm gold coated inverted pyramid sensor on zein, (b) 80 nm gold coated nanopores sensor on zein, (c) 80 nm gold coated nanopillars sensor on zein and (d) comparison of 100 μM concentration of these sensors. It was found that inverted pyramid structures yielded the highest enhancement as evident by the intensity of the characteristic peaks, such as 1370 and 1515 cm^{-1}	111
4.18	Comparison of SERS and normal Raman spectra of Rhodamine 6G	112
4.19	Macro images of zein sensors with 200 nm gold-coated inverted pyramids. Gold side of sensors, squared area has the nanophotonic patterns (a), zein side of sensors (b), thickness of the sensor (c) and size of the sensor (d)	113
5.1	Molecular structure of acrylamide (Jonathan, 1961)	115
5.2	Proposed formation of acrylamide through Maillard reaction (Mottram et al., 2002)	117
5.3	Zein-SERS sensor with a droplet of acrylamide solution, immobilized on a glass slide. The squared area in the middle has the nanophotonic structures	119
5.4	Coffee-ring effect for acrylamide solution	121
5.5	Microscopy image of dried acrylamide solution on glass slide. Big rectangular area shows the region in which Raman measurements were done. Small green rectangle represents inside of the droplet (low concentration), blue rectangle represents the edge of the droplet (high concentration) and grey rectangle represents the glass slide (no acrylamide). Color code represents the intensity of Raman signals over the region. Yellow color signifies higher concentration. Scale bar: 100 μm	122
5.6	Overlay of the Raman spectrum of glass slide (grey), edge of the droplet (blue) and inside the droplet (green)	123
5.7	Raman measurements of acrylamide on glass slide with concentrations of 100 mM (a) and 10 mM (b)	123
5.8	Microscopy image of zein-SERS substrates with acrylamide deposited on it. White line represents the edge of the ‘coffee ring’ shape. Red point shows the laser location on which the measurements were taken.	124
5.9	Comparison of the background signature of zein-SERS sensor (green) with acrylamide on top of the sensor (blue). Red dotted square indicates the peak at the wavenumber of 1447 cm^{-1} , which does not exist in the background, but exists in acrylamide signature. (A.u.: arbitrary units)	125
5.10	Surface enhanced Raman signatures of acrylamide with different concentrations on zein-SERS substrate	126

5.11	Subtracted Raman spectra of acrylamide on zein-SERS sensor from the background signature of the zein-SERS sensor.	127
5.12	Calibration curve for different concentrations of acrylamide	128
5.13	Log-log calibration curve for different concentrations of acrylamide	130
6.1	Schematic illustration of the functionalization of the gold surface .	135
6.2	Raman spectra of a) background of the zein-SERS sensor (average of 30 measurements 1 second each) b) Ara h1 on zein-SERS sensor (average of 30 measurements 1 second each)) c) background of the zein-SERS sensor (average of 5 measurements 1 second each) d) Ara h1 on zein-SERS sensor (average of 5 measurements 1 second each) Different colors represent individual Raman spectra at mapping points.	138
6.3	Principal component analysis of Raman spectra for the background and different concentrations of Ara h1. Top-left: PC1 vs PC2, Top-middle: PC1 vs PC3, Top-right: PC2 vs PC3, Bottom-left: PC1 vs PC2, Bottom -middle: PC1 vs PC3, Bottom-right: PC2 vs PC3. PC1 is usually the component that explains the variability best and PC2 is second best with the condition that it is orthogonal to PC1 and PC3 is the third best with the condition that it is orthogonal to both PC1 and PC2	139
6.4	Baseline corrected Raman spectra of a) background of the zein-SERS sensor (1s*30 acquisition time) b) Ara h1 on zein-SERS sensor (1s*30 acquisition time) c) background of the zein-SERS sensor (1s*5 acquisition time) d) Ara h1 on zein-SERS sensor (1s*5 acquisition time)	141
6.5	Principal component analysis of baseline-corrected Raman spectra for the background and different concentrations of Ara h1 average of 30 measurements at 1second (1s*30 acquisition time) I added the explanation before this the way you like OK. Left: normalized Raman spectral data plotted vs PC1 and PC2, Middle: normalized Raman spectral data plotted vs PC1 and PC3, Right: normalized Raman spectral data plotted vs PC2 and PC3.	142
6.6	Principal component analysis of baseline-corrected normalized Raman spectra for the background and different concentrations of Ara h1 (1s*5 acquisition time). Left: normalized Raman spectral data plotted vs PC1 and PC2, Middle: normalized Raman spectral data plotted vs PC1 and PC3, Right: normalized Raman spectral data plotted vs PC2 and PC3.	142

6.7	Principal component analysis of baseline-corrected Raman spectra for the background and different concentrations of Ara h1 (1s*5 acquisition time). Left: Normalized Raman spectral intensity data plotted vs the first two principal components PC1 and PC2, Right: Normalized Raman spectral intensity data plotted with respect to principal components PC2 and PC3, Black: background spectral intensity data of zein-SERS platform, Red: Normalized Spectral intensity data for 1.4 mg/ml Ara h1, Green: Normalized Spectral intensity data for 1 mg/ml, Blue: 0.25 Normalized Spectral intensity data for mg/ml Ara h1 .	143
6.8	Principal component analysis for 0.14 mg/ml Ara h1 protein on zein-SERS sensor. From left to right: PC1 vs PC2, PC1 vs PC3 and PC2 and PC3.	144
6.9	Left: Zein-SERS platform, after being immersed in 2M of 11-MUA solution inside a petri dish. Right: Close-up image of the zein-SERS sensor.	145
6.10	Raman spectra generated by Ara h1 protein captured with 2F7 antibody on different platforms. Red: zein-SERS, green: PET-SERS, blue: smooth gold	146
6.11	Principal component analysis PC1 vs PC2 (Left) and PC1 vs PC3 (Right) of baseline-corrected Raman spectra for background zein-SERS sensor (black), antibody-functionalized zein-SERS sensor (pink), Ara h1 protein captured by antibody-functionalized zein-SERS sensor (red), Ara h1 protein on functionalized zein-SERS sensor-not rinsed(cyan), Ara h1 protein captured by antibody-functionalized smooth gold surface (blue), and Ara h1 protein captured by antibody-functionalized PET-SERS substrate (green).	147
6.12	Principal component analysis (PC2 vs PC3) of baseline-corrected Raman spectra for background zein-SERS sensor (black), antibody-functionalized zein-SERS sensor (blue) and Ara h1 protein captured by antibody-functionalized zein-SERS sensor (red).	148
6.13	Principal component analysis (PC2 vs PC3) of baseline-corrected Raman spectra for background zein-SERS sensor (black), antibody-functionalized zein-SERS sensor (blue) and Ara h1 protein captured by antibody-functionalized zein-SERS sensor (red), Ara h1 protein captured by antibody-functionalized smooth gold surface (cyan), Ara h1 protein captured by antibody-functionalized PET-SERS substrate (green).	149
6.14	Principal component analysis (PC2 vs PC3) of baseline-corrected Raman spectra for background zein-SERS sensor (black), antibody-functionalized zein-SERS sensor (blue) and Ara h1 protein captured by antibody-functionalized zein-SERS sensor (red), Ara h1 protein on functionalized zein-SERS sensor- not rinsed(cyan). .	150

A.1 Specifications of Atomic Force Microscopy used in this study . . . 186

CHAPTER 1

INTRODUCTION

There is a need for useful, portable and inexpensive detection tools in the food industry. Biosensors have emerged to fulfill this need and are under extensive research to accomplish the actualization process. Biosensors are detection tools, which couple a biological recognition element with a transducer for either qualitative or quantitative detection of a certain analyte. For the utilization of a biosensor, there is a need for a sensor platform, a detection unit and a means to analyze the data. Biosensor platforms are generally made of plastic materials that are not biodegradable. For applications that are mass-scale, every-day-use, efficient disposal and waste management of these non-biodegradable sensors may become an issue. Biodegradable materials could be the solution for the disposability problem and provide an environmentally friendly alternative. Several materials such as silk and paper platforms have been proposed and used as sensor platforms.

In this dissertation, zein was investigated as a potential platform for biodegradable biosensor development. Zein is a prolamin, which is extracted from corn gluten meal. It has been utilized as a biopolymer since it was proven to fabricate free-standing films. Since zein is brittle in nature, plasticizers are used to give flexibility and moldability to zein films. One of the methods to manufacture free-standing films is casting. Casting includes the steps of preparation of a zein solution either with or without plasticizer and pouring on an ultimately non-stick mold, then after solvent evaporation films are peeled off from the mold. The first objective of this study was to investigate the effect of plasticizer content and the surface properties of the mold on the hydrophilicity of zein surfaces. To characterize the surface water contact angle measurements, optical absorbance atomic

force microscopy was used.

Biosensors utilize different physical phenomenon. They are generally classified in regards to the physical property they use as part of a transducer. There are optical, acoustic, piezoelectric, electrochemical, mechanical and electronic biosensors. In this research, an optical method namely surface enhanced Raman spectroscopy (SERS) was used. Raman spectroscopy is a strong molecular detection tool that gives fingerprints of the present molecules as a result of different vibrational modes. Even though Raman spectroscopy is a strong molecular fingerprinting technique, the intensity of inelastic scattering, which defines Raman scattering phenomenon, is intrinsically weak. It is possible to enhance the signal by means of photonic nano patterns that are used for surface enhancement. It was discovered that the presence of metallic particles or structures at nano or sub-micron scale in the vicinity of Raman measurement of an analyte results in high enhancement of Raman signal. Either nanoparticles or nanopatterned platforms are used for this purpose. The former gives more enhancement, but the latter is preferred for accuracy and reproducibility purposes.

The second objective of this dissertation was to manufacture a platform with noble metal coated nanopatterns on the biodegradable zein platform. Sub-micron scale pyramid structures, nanopillars and nanopores were fabricated and compared for the Raman enhancement effect of a model molecule, Rhodamine 6G. A novel imprinting technique was developed in order to manufacture these platforms. The technique included direct transfer of 3-dimensional metallic structures onto zein.

The third objective was to utilize the selected platform from the second objective, which was inverted pyramid structures with 200 nm gold coating, in detection of acrylamide. Acrylamide is a food contaminant that is formed during high-temperature processing of certain foods, such as bread, French fries, potato chips and coffee. Since acrylamide is considered to be a potential carcinogenic and neurotoxic compound for humans, there is a need for routine monitoring of the levels in the product lines of food industry. Zein-SERS platform was utilized for direct detection of acrylamide solutions at different concentrations and

a calibration curve was obtained.

The fourth objective of this study was to detect a peanut allergen protein, Ara-h1 by using the developed zein-SERS platform. Ara h1 is one of the 8 known allergen proteins of peanut. Peanuts cause severe allergic reactions in certain populations and it is among the most common food allergies. In order to provide safety in food production lines, cross-contamination should be tested frequently for the presence of peanut proteins in the system. In this research, as a proof-of-concept, both direct detection and antibody-capturing of Ara-h1 protein was tested. Principal component analysis technique was used to differentiate the presence and different concentrations of Ara h1 on zein-SERS platform.

This was the first time when zein, a biodegradable food polymer, was utilized as a platform to develop SERS application. The feasibility of the sensor was investigated by using a model molecule, Rhodamine 6G and two different analytes that are important to food industry, acrylamide and peanut allergen Ara h1.

CHAPTER 2

LITERATURE REVIEW

2.1 Zein

Zein comprises 50-70 % of the protein content of corn and it was first identified by Gorham in 1821 (Holding and Larkins, 2009). Due to its low nutritional quality, it has since found value and use as an industrial polymer, especially after its commercial production began in 1939 (Shukla and Cheryan, 2001). The protein-rich by-products of corn processing include corn gluten meal (CGM) and corn gluten feed (CGF) from wet-milling, and distillers dried grains (DDG) and distillers dried grains solubles (DDGS) from dry-milling (Shukla and Cheryan, 2001). Zein can be extracted from any of these by-products; however the commercialized zein is extracted from CGM (Anderson and Lamsal, 2011).

2.1.1 Amino acid composition and structure

Zein is a prolamin rich in proline and glutamine. Prolamins are not soluble in water or ethanol, but soluble in water-ethanol mixtures. Zein was first classified into different fractions by its solubility in aqueous alcohol solutions (Anderson and Lamsal, 2011). Today, the nomenclature in use relies not only on solubility, but also on molecular weight and amino acid structure. There are four fractions of zein: alpha, beta, gamma and sigma. Each fraction constitutes approximately 71-85%, 10-20%, 1-5% and 1-5% of total zein protein, respectively (Wilson, 1991; Anderson and Lamsal, 2011). α -zein is the most widely used because it is commer-

cially available (Lawton, 2002). Zein fractions can be separated and observed by sodium dodecyl sulfate polyacrylamide gel electrophoresis (SDS-PAGE) method. α -zein is found as two different polypeptide forms having either 19000 Da or 22 000 Da molecular weight (Figure 2.1) (Shewry and Tatham, 1990). These fractions are also referred to as 19 kDa and 22 kDa α -zeins, respectively.

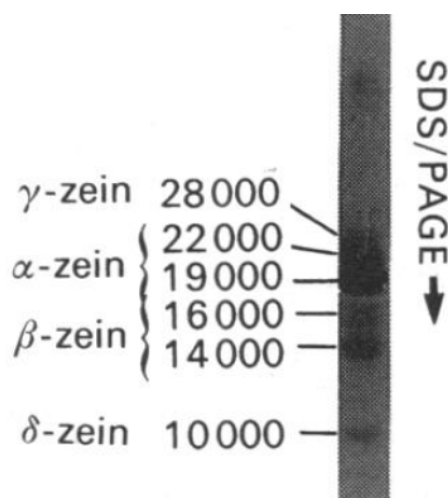


Figure 2.1: Different fractions of zein separated by SDS-PAGE (Shewry and Tatham, 1990)

Amino acid compositions of 19 kDa and 22 kDa α -zein are shown in Table 2.1. Both α -zeins with different molecular weights have amphiphilic polypeptides, as approximately %59 and %57 of the amino acids, respectively, are non-polar, such as alanine, leucine and proline. There are three segments in α -zein structure (Figure 2.2): 1) N-terminus consisting of 35-36 unique residues, 2) Repeat units of 20 residues and 3) C-terminus of 10 residues. Shewry and Tatham (1990) proposed that the difference between Z19 and Z22 is having either 9 or 10 repeat units in the second segment. On the other hand, Argos et. al. 1982 argued that the difference comes from extra 10-residue unit onto C-terminus in Z22.

The first model proposed for conformational structure of α -zein was by Argos and colleagues in 1982. Based on the known amino acid sequence and Circular Dichroism (CD) experiments, in which zein was found to have 50-60 % alpha-helix

Table 2.1: Amino acid composition of 19 kDa and 22 kDa α -zein. Adapted from (Shewry and Tatham, 1990)

Class	Amino acid	19 kDa α-zein	22 kDa α-zein
Nonpolar	Glycine	5	4
	Alanine	29	34
	Valine	5	15
	Leucine	43	44
	Isoleucine	9	8
	Phenylalanine	13	9
	Tryptophane	0	0
	Proline	23	22
-OH	Serine	15	16
	Threonine	5	8
	Tyrosine	8	8
-SH	Methionine	0	5
	Cysteine	2	1
Basic	Lysine	0	0
	Arginine	2	2
	Histidine	2	3
Acidic	Aspartic acid	0	0
	(as asparagine)	10	12
	Glutamic acid	1	1
	(as glutamine)	41	50
Total		213	242

structure, they suggested that the protein forms 9 adjacent helical units forming a distorted cylinder structure. Since CD experiments showed a high alpha-helical content, the 9 repeating units of amino acids in the primary structure were proposed to form these 9 alpha-helical units, combined with glutamine rich turns, based on the primary structure. They also suggested that these alpha-helical units show hydrophobic properties as most of the amino acids in the primary structures were non-polar, as opposed to polar glutamine residues on the turns.

The helical units showed non-polar characteristics, self assembling through

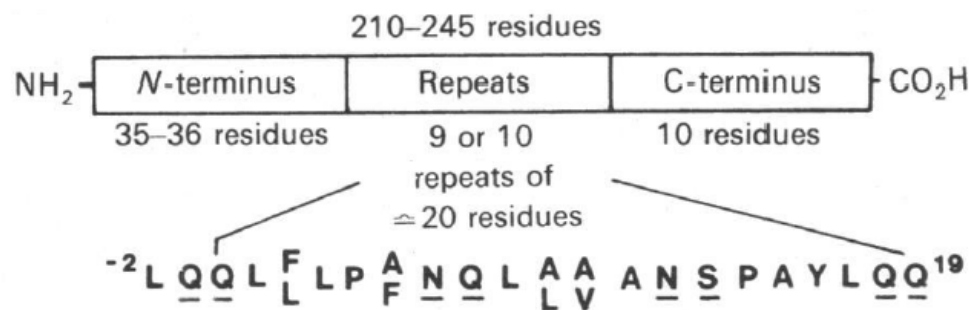


Figure 2.2: The amino acid sequences of Z19 and Z22 (Shewry and Tatham, 1990)

hydrophobic interactions, while the cap of the cylinders had polar glutamine-rich turns, allowing for interaction during stacking and solvation processes (Argos et al., 1982). The conformational model of Argos proposed that zein had symmetrical units with a 2:1 axial ratio. Tatham and co-authors (1993), with further investigation of α -zein's conformation in solution conducted by Small Angle X-Ray Scattering (SAXS) and viscometric measurements modified the conformational proposal to form an asymmetrical rod-like structure. This structure was suggested to give a better explanation of the film forming abilities of zein by considering the orientation of the rods into two- and three-dimensional stacking arrays (Tatham et al., 1993). They found different axial ratios from SAXS and viscometric measurements due to the differences between these methods. The dimensions they reported for rod-like structure were 15.3 nm in length and 0.69 nm in diameter (Tatham et al., 1993).

The most commonly used conformational model was developed by Matsushima and colleagues in 1997 with the help of another set of SAXS measurements, in which they calculated radius of gyration (R_g) and the corresponding radius of gyration of the cross-section (R_c) and used these values to estimate the dimensions of zein protein. They based their model on the findings of Argos' model: zein had alpha-helix tandem units joined by glutamine-rich turns or loops with N and

C termini. However, they disagreed with the proposed axial ratio. Instead, they proposed a model, in accordance with Tatham's study, wherein the shape was asymmetrical rather than a symmetrical cylinder. The model proposed had an axial ratio of 6:1 and formed a ribbon-like structure whose geometry could be approximated by a helical capsule shapes (R1, R2, ..., R9 shown in Figure 2.3) having the following dimensions: L (13 nm) x W (3 nm) x D (1.2 nm) (Matsushima et al., 1997). The proposed model can be seen in Figure 2.3. It is important to emphasize that the repeating neighboring units have hydrophobic surfaces, whereas the caps have hydrophilic loops and turns, giving the amphiphilic property to zein protein.

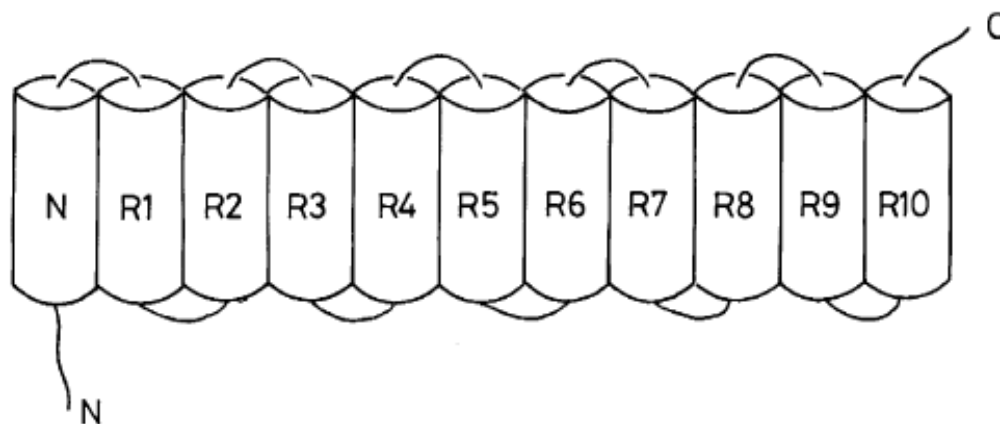


Figure 2.3: Conformational model of α -zein (Matsushima et al., 1997)

There have been other studies proposing conformational models based on data collected by Nuclear Magnetic Resonance (NMR) experiments (Bugs et al., 2004) and Fourier Transform Infra-Red (FTIR) Spectroscopy experiments (Forato et al., 2004b). However, their findings were not found to be credible by Momany and coworkers, since these models used water as a solvent during modeling, and zein is not soluble in water (Momany et al., 2006). The researchers using computational algorithms and published experimental data suggested that Z19 had three segments of helical coiled-coils, which have 4 residues/turns compared to 3.6 residues/turn as in alpha-helix (Momany et al., 2006). This model also allowed

the lutein (one of the carotenoids which is known to give zein its yellow color) to fit in the three-helical structure. It was argued that this could explain the difficulty in obtaining white zein (Momany et al., 2006). They reported an axial ratio of 6 - 7:1, which is in accordance with Matsushima's model (Matsushima et al., 1997). However, they noted that no concrete experimental data have confirmed any of the models proposed to date. They declared "No conclusive experimental data exist that positively confirm any particular 3D model of α -zein. However, the conformation described here is consistent with most physical measurements and awaits a definitive experiment to prove or disprove its correctness (Momany et al., 2006).

2.1.2 Solubility

Zein is soluble in a large number of solvents (around 70) and these solvents are classified as primary (Evans and Manley, 1941), secondary/binary (Evans, 1944) and ternary (Evans and Manley, 1944). Primary solvents alone can dissolve zein in a concentration of more than 10%, secondary solvents need to be combined with either water or an aliphatic alcohol to solve zein, and ternary solvents are mixtures of solvents, water and an aliphatic alcohol (Evans and Manley, 1941; Evans, 1944; Manley and Evans, 1943; Evans and Manley, 1944). A good solvent for an amphiphilic protein, needs to have both polar groups and non-polar carbon/methyl groups (Lawton, 2002). Even though zein is soluble in various organic solvents, such as ketones, amide solvents, glycols and chlorinated hydrocarbons, aqueous alcohols are most commonly used to dissolve zein (Lawton, 2002; Shukla and Cheryan, 2001). Aqueous alcohol used as a solvent is generally either ethanol or 2-propanol (Anderson and Lamsal, 2011). Zein is soluble in between 40 and 95% ethanol solutions, optimum solubility being around 70 - 75%. Aqueous solvents such as acetone, acetonylacetone, dioxane, and dioxolane were also found to be comparable to aqueous alcohol solvents, however they resulted in very low viscosity solutions (Manley and Evans, 1943). It was found that zein solutions

in aqueous ethanol showed Newtonian behavior, with a decrease in viscosity as ethanol content in water decreased (Fu and Weller, 1999).

2.2 Zein films

Zein has found a significant place in the field of biodegradable, natural material alternatives to synthetic polymers owing to its film forming abilities (Lawton, 2002). It has been used as coating, adhesive and packaging material (Shukla and Cheryan, 2001). Zein films are made in mainly two forms: resin films and cast films. Resin films are obtained by first solubilizing zein and additional reagents (e.g. plasticizers) in a solvent. This is followed by either kneading and rolling (Lai et al., 1997), precipitating in cold water (5°C) and kneading (Lai and Padua, 1997) or extruding (Wang et al., 2003b). Films of high quality are obtained by casting zein solution onto a non-stick surface and peeling off after solvent evaporation to form free-standing films (Lawton, 2002).

Zein films are brittle and plasticizers are needed to make them more flexible (Hansen, 1938). There have been numerous plasticizers identified and categorized as either primary or secondary plasticizers (Lawton, 2002). Primary plasticizers are grouped as follows: glycols, sulfonamides, fatty acids, amides, amines, esters glycol esters and glyceryl esters (Hansen, 1938). Secondary plasticizers are found to be effective only when they are used in combination with primary plasticizers, the most commonly used, being glycerol (Lawton, 2002). A good plasticizer, just as a good solvent, should have both polar and non-polar groups in order to effectively interact with zein (Lawton, 2002). Most widely used plasticizers are liquid organic molecules such as polyols, glycerol, mono- di- and oligosaccharides, lipids, lipid derivatives and fatty acids (e.g. palmitic, stearic and oleic acid) (Zhang and Mittal, 2010). The most effective of these plasticizers are amphiphilic, such as triethylene glycol, dibutyl tartrate and oleic acid (Corradini et al., 2014).

Zein films plasticized with oleic acid have been extensively studied due to their desired flexibility and hydrophobicity. The effect of different concentrations

and different casting conditions of oleic acid on thermal (Santosa and Padua, 2000), mechanical (Santosa and Padua, 1999) and barrier properties (Lai and Padua, 1998) of the films were investigated. Oleic acid was found to be one of the most effective plasticizers as it provided more flexibility to zein films suggested by its liquid crystalline state at room temperature (Yoshimoto and Sato, 1994). Films plasticized with oleic acid have lower water permeability since oleic acid is an unsaturated fatty acid, which is a desired quality in packaging applications (Lawton, 2004; Lai and Padua, 1998).

Role of oleic acid in plasticized zein film formation

Several researchers looked into the mechanism behind plasticization of zein films with oleic acid. Lai and colleagues proposed structural models for oleic acid - zein complex, after conducting solid state Wide-angle (WAXS) and small-angle X-Ray scattering (SAXS). They observed that the preparation method (either resin or cast films) made a difference in the periodicity of the films, where resin films had more periodicity compared to cast films (Lai et al., 1999). Because of the fact that zein powder and zein films without oleic acid did not show any periodicity in WAXS and SAXS experiments as opposed to zein films with oleic acid, they suggested that oleic acid plays an important role in plasticized film formation. For the resin films, the proposed models are shown in Figure 2.4. Table 2.2 summarizes the periodicity observed in zein films prepared in different ways, as well as granular zein and zein fiber. The 4.9 and 10 Å spacings observed in WAXS experiments were correlated with the inside packing of alpha-helices and the packing with neighboring alpha-helices, respectively. The fact that granular zein and zein fiber did not show any periodicity in SAXS patterns as opposed to zein films containing oleic acid suggested that oleic acid plays an important role in the film formation and periodicity.

Oleic acid can be seen in the form of bilayers having a 46 Å (for solid state) and zein as forming stacks of two helical models, with dimensions in accordance with

Table 2.2: WAXS and SAXS measurement results (d-spacing) of different zein films (Lai et al., 1999)

Samples	d-Spacing (Å)	
	WAXS	SAXS
Resin film, beam normal (biaxially deformed)	10.4, 10.9; 4.6, 4.8	165, ~ 45
Resin film, beam parallel	10.6; 4.9	135 (0°); 170 (90°)
Dried zein-oleic acid resin	10.5; 4.9	165; ~ 45 (?) ^a
Resin film (uniaxially deformed with a roller)	10.7; 4.9	170
Cast film, normal beam	10.6; 4.9	80; ~ 45 (?)
Cast film, beam parallel	10.2; 4.9	65 (0°); 80 (90°)
Granular zein	10.1; 4.7	— ^b
Zein fiber	9.9; 4.7	— ^b

^a (?), presence of peak is questionable due to breadth and low intensity.

^b No apparent peak.

Matsushima’s model (Lai et al., 1999; Matsushima et al., 1997). However, they noted that the same periodicity did not apply to cast zein films. Additionally, they did not have physical or chemical proof for how many oleic acid or zein layers stacked together in these proposed models. The models were based on the finding that zein’s secondary structure was not affected by the plasticization with oleic acid. The authors noted that even though the side-chain spacing may change, the alpha-helical structure (which accounts for 50% in zein) did not change as a result of heating, dissolution and mechanical processes (Lai et al., 1999). They explained this phenomenon as follows: “In the present study, the inter-chain spacing between the alpha-helices is about 10.5 Å. Assuming the zein molecule subunits in neighboring molecules are packed in a hexagonal array (considered to be a reasonable packing because zein is a storage protein), this corresponds to a diameter of the zein helix of 12.1 Å. This value is in good agreement with the 12 Å zein α -helix diameter assumed by (Matsushima et al., 1997) for construction of their model, with values of 10-14 Å being considered reasonable depending on the side-chain lengths.” This claim was supported by follow-up studies by the same group (Wang et al., 2005).

They did another set of SAXS and WAXS experiments and based on the d-spacings (they did not change), and they concluded that zein’s alpha helical structure was not affected by film forming process with plasticizer. In addition,

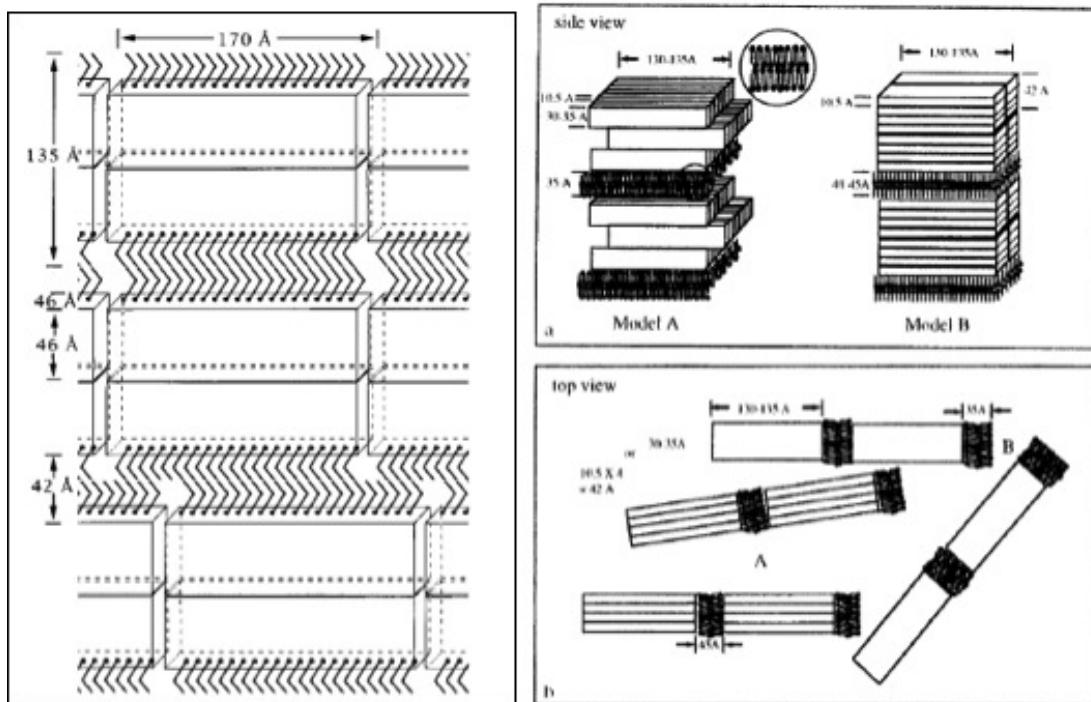


Figure 2.4: Left: Proposed model for zein-oleic acid complex for resin films. Right: proposed alternative stacking options. These models were proposed based on the WAXS and SAXS data, in addition to Matsushima's model of zein structure: L (13 nm) x W (3 nm) x D (1.2 nm). (Lai et al., 1999)

Xu and associates found through FTIR studies that secondary structure of zein plasticized with oleic acid did not differ from that of unplasticized zein films (Figure 2.5) (Xu et al., 2012). Rather, they suggested that oleic acid contributes to the supramolecular orientation of zein films through non-covalent bonding such as hydrophobic interactions, electrostatic interactions and/or van der Waals forces (Xu et al., 2012).

For cast films, several differential scanning calorimetry (DSC) experiments showed that not all oleic acid was interacting with zein within films. DSC peaks observed at 7.1 °C (melting of oleic acid) and at -0.9 °C and -4.3 °C (crystallization of oleic acid) suggested that oleic acid separated from cast zein films, as opposed to resin films in which these peaks were non-existent, where these peaks were non-existent as shown in Figure 2.6 (Lai and Padua, 1997). This was interpreted as higher interaction of zein with oleic acid in resin films, resulting

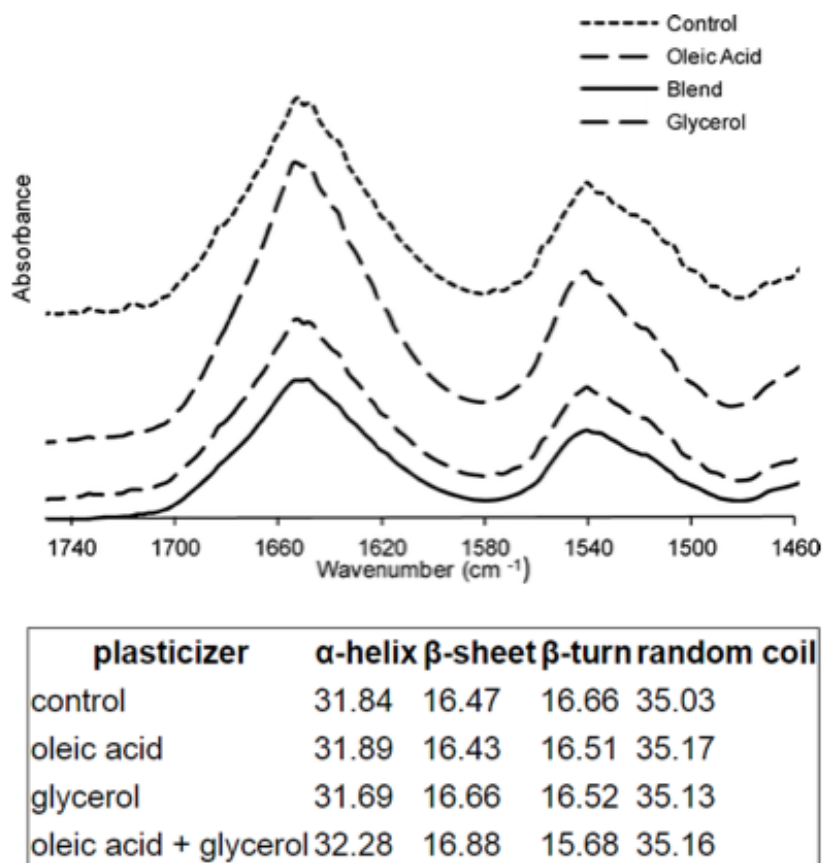


Figure 2.5: Top: FTIR spectra of zein films without and with plasticizers or combination of plasticizers. Bottom: Calculated secondary structures based on FTIR measurements (Xu et al., 2012)

in a stronger structural organization (Lai and Padua, 1997). The unbound oleic acid phenomenon was observed again by the same group when they were studying re-plasticization effects (Santosa and Padua, 2000).

DSC experiments conducted for plasticized zein films showed melting peaks of oleic acid at 5-7 °C, which suggested the presence of free oleic acid, which could be explained by incomplete miscibility of oleic acid with zein matrix. Based on these findings, it was proposed that cast zein films have oleic acid that is both free and bound and it is rather randomly stacked in between zein layers (Lai et al., 1999).

Oleic acid is an amphiphilic molecule, with a carboxylic (-COOH) head and a

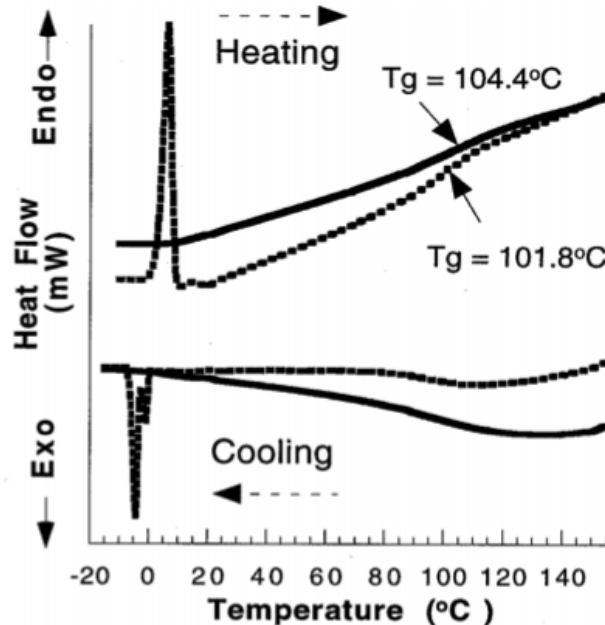


Figure 2.6: Differential Scanning Calorimetry measurements of cast zein films (dotted line) and resin zein films (solid line) Melting peak at 7 °C and crystallization peaks at - 0.9 °C and -4.3 °C of oleic acid were only observed for cast films (Lai and Padua, 1997).

carbon tail (18 C) with a methyl (-CH₃) end. The question whether oleic acid uses carboxylic or methyl end to interact with zein prompted a number of investigations using surface plasmon resonance (SPR) and NMR techniques (Wang et al., 2004b,a; Forato et al., 2004a). SPR is an optical sensing technique, which consists of a reflective surface (such as gold), and a detection system to observe the change in refractive index as a result of molecules adsorbing/binding to the gold surface. SPR system is shown in Figure 2.7. The mechanism behind SPR is that when polarized light (through prism) is incident on a metal-dielectric (air/water) interface, it creates an oscillation of electrons on the metal surface which propagates parallel to this interface. Thus it is very sensitive to any disturbance that may occur on this interface, e.g. a molecule binding to the surface. The change in the properties of reflected light is correlated with the presence and quantity of the binding molecules and this is detected by the optical detection unit (Figure 2.7). Specificity of these sensors is provided by immobilizing capture molecules on the

gold surface that binds to specific target analytes (orange dots in Figure) in the flow channel.

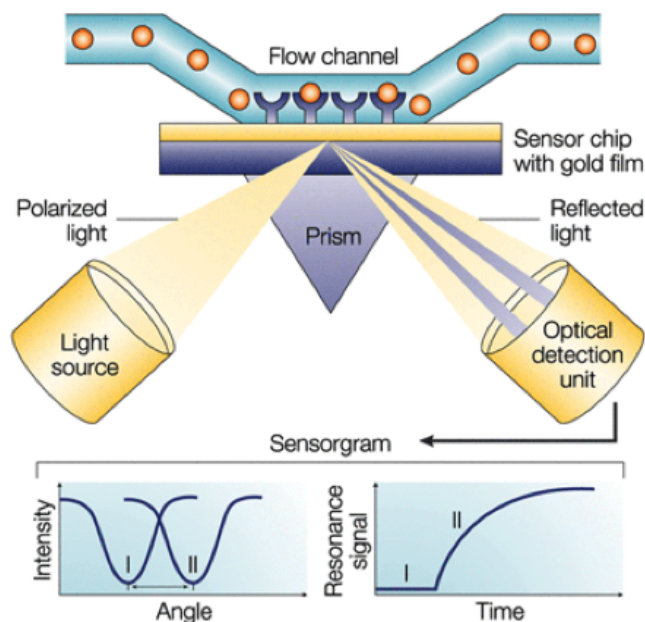


Figure 2.7: Schematic of Surface Plasmon Resonance sensor. When the molecules bind to the gold side of the sensor chip, resonance angle shifts and the change in this angle can be observed kinetically as shown in the plots (Cooper, 2002).

Wang and coworkers used this system to study zein's affinity towards carboxylic and methyl molecular groups, which would be an indication of zein-oleic acid inter-action. After functionalizing the gold surface with 11-mercaptoundecanoic acid (-COOH end) and 1-octanethiol (-CH₃ end), the surface was flushed with zein and washed with buffer in order to get rid of the excess (Wang et al., 2004a). These dynamic adsorption experiments showed that both the adsorption rate and maximum adsorption value were higher for zein on carboxylic end compared to methyl end. The results indicated that zein had higher affinity towards hydrophilic surfaces compared to hydrophobic ones. Furthermore, it was suggested that zein must be interacting with oleic acid through its carboxylic end (Wang et al., 2004a). Atomic force microscopy (AFM) images showed that zein formed high rising, rougher monolayers on hydrophilic surface (with 11-mercaptoundecanoic acid) as

opposed to smooth, short monolayers on hydrophobic one (1-octanethiol). This finding was interpreted as zein having a different footprint on these surfaces, and using different sides of the ribbon-like structure (Figure 2.3) to interact with and adsorb onto different molecular moieties (Wang et al., 2004b).

The hypothesis that oleic acid might be interacting with zein through carboxylic end was further confirmed through ^{13}C NMR studies ^{13}C . Interaction of ^{13}C labeled oleic acid with Z19 zein was studied and the results were interpreted as oleic acid interacting with zein through electrostatic interactions, rather than hydrophobic or ionic bonds. It was proposed that the carboxyl proton was dissociated as a result of this electrostatic interaction. The sites on zein to attract the oleic acid was suggested to be the arginine amino acids which provide a positive charge that attract the negatively charged carboxylic acid groups on oleic acid. Since the number of arginine amino acids are limited, authors have commented that when larger quantities of oleic acid was used it was found in both bound and free form (Forato et al., 2004a).

2.2.1 Surface properties of zein films

Water contact angle method

One of the important characteristics of zein films are the surface properties, such as wettability/water affinity and micro/nano structures formed on the surface. These properties have been shown to affect certain physical properties, such as water vapor permeability, oxygen permeability, cell attachment, absorption and adsorption of solvents/molecules that zein films come into contact with (Dong et al., 2013).

Surface wettability can be characterized by measuring the water contact angle (WCA). WCA is widely used to classify the surfaces based on hydrophilicity and hydrophobicity. It is measured by dropping a certain volume of water onto the surface of interest and measuring the angle between the droplet and surface. Figure 2.8 shows the range of WCA from 0 to 180 degrees. Increase in water

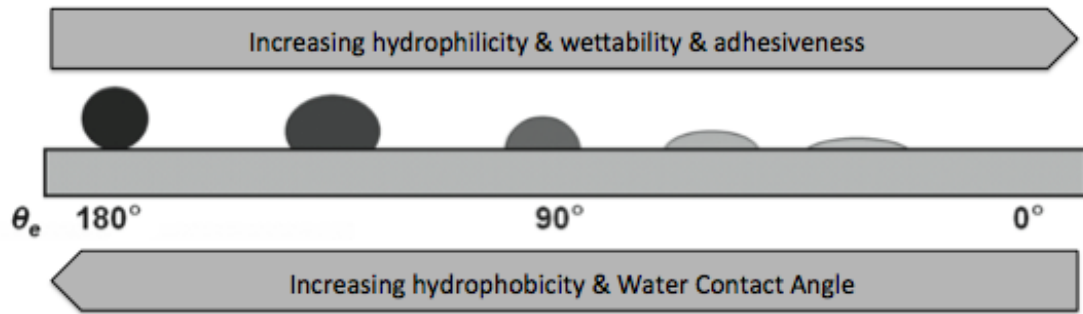


Figure 2.8: Water contact angle and wettability θ_e . Adapted from (Lee and Owens, 2011)

contact angle above 90 degrees is the result of hydrophobicity and above 150 degrees surfaces are super-hydrophobic. In contrast, decreasing water contact angle is associated with hydrophilicity, wettability, adhesiveness and increase in surface energy. Water contact angle measurements are done by dropping a known volume of water on the surface of the material of interest and measuring the tangential angle between the surface and the edge of the droplet. The equipment used in this study was VCA Optima from AST products, inc. The equipment had a measuring range of 0-180 degree, with 0.5 degree accuracy. Highest magnification was 51:1 and the sample stage had the dimensions of W: 6.5 in, L: 9 in and H: 2.5 in. The equipment had a 100 ml syringe and it was possible to automate the droplets on the surface with a range of 150-500 droplets.

The effect of different processing and production methods for zein on WCA were examined by several researchers. Yoshino and coworkers studied the effect of solvent, zein concentration and drying conditions on water contact angles, and found that zein surface's water affinity can be tuned by changing these parameters. They used polyethylene (PE) sheets to cast zein on and observed that WCA ranged between around 40 and 78 for the surface that was in contact with PE sheets (basal side). On the other hand, air side of the zein films differed than that of basal side. Air side had lower WCA, ranging between 20 and 50 degrees (Yoshino et al., 2000). Water contact angle measurements were reported as in

Figure 2.9. It was observed that for majority of the cases, WCA on the basal side of the zein films were higher than that of air side. The difference between the air side and basal side was observed on a visual level as one surface being dull and the other glossy when cast on a non-stick surface (Lai and Padua, 1997).

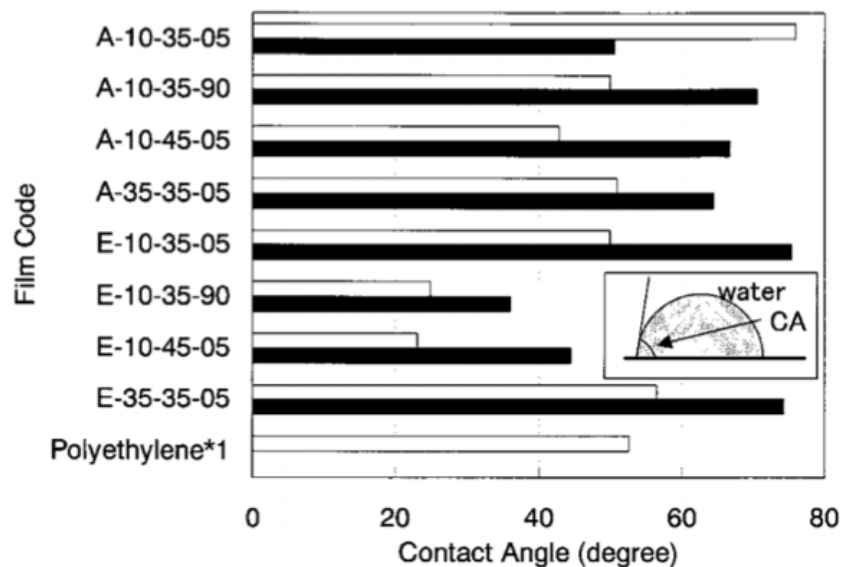


Figure 2.9: Water contact angles of zein films cast on PE sheets with different conditions. White bars: air side, black bars: basal side. A/E: Acetone or Ethanol solution, First number: initial concentration of zein, Second number: drying temperature, Last number: drying relative humidity (Yoshino et al., 2000)

In some cases, hydrophilicity is favored for zein film surfaces. For example 3-minutes of UV/Ozone treatment reduced WCA from 82 to 11 degrees (Shi et al., 2009). Furthermore, in the same study the difference between using acetic acid versus ethanol as a solvent for zein was studied. Films prepared with ethanol were more hydrophilic compared to films prepared with acetic acid. It was suggested that zein used different surfaces to form films, either stacking on top of hydrophobic surfaces, lateral sides of the helical structure as described in Matsushima's model (Figure 2.3), or stacking up in a vertical way which results in a hydrophilic surface (Shi et al., 2009).

In other cases, hydrophobicity is the desired property. In order to make the surface more hydrophobic, different approaches were tried. Biswas and associates

(2009) used derivatization with octenyl succinyl anhydride and alkyl and alkenyl ketene dimers and observed an increase in WCA, from 67 up to 96 degrees. Shi and coauthors used acylation in a later study and found an increase in WCA from 75 to 86 degrees when zein films formed after chemical modification with lauryl chloride acylation (Shi et al., 2010). A recent study showed that it was possible to obtain zein films with very hydrophobic characteristics (up to WCA 119) when cast on gold surfaces functionalized with methyl groups. The authors found that both solvent and zein concentration played a role in the water affinity of the surfaces. WCA decreased (from 115 to 73 degrees) with an increase in zein concentration (from 0.5 mg/ml to 5 mg/ml) when prepared with 80 % ethanol solution. On the other hand, when the zein concentration was kept constant at 0.5 mg/ml, WCA first increased (105 till 119 degrees and decreased 110 degrees) with an increase in ethanol content (40 % till 80 % and 95 %, respectively). They explained this process as evaporation induced self-assembly (EISA) owing to the amphiphilic characteristics of zein protein (Dong et al., 2013).

Atomic Force Microscopy

Atomic Force Microscopy (AFM) is also useful in studying changes in surface characteristics. In this method, a cantilever with a very sharp tip, with a nanometer scale radius of curvature, is used to scan a surface. The forces between the tip and the surface is measured by a laser and detector system and reconstructed into an image. AFM is different than other microscopy techniques as it is not the actual image, but an approximation of the surface properties and particularly the surface topography at the nanoscale. AFM operates mainly in either the contact mode or non-contact (tapping) mode. Contact mode is generally used for force measurements, whereas tapping mode is used for topography. Also as a general rule, it is suggested to use tapping mode for soft surfaces and contact mode for hard surfaces.

In contact mode (Figure 2.10), which is also referred to as static mode, tip is in contact with the surface and the force interaction of the tip with the surface can be used to measure surface properties. Cantilever, which holds the tip approaches

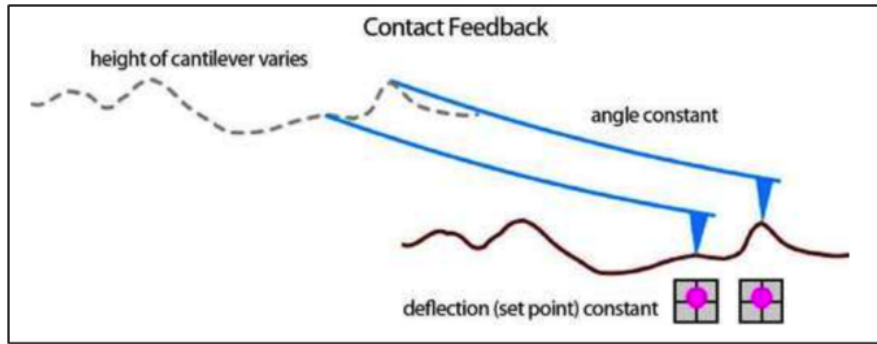


Figure 2.10: AFM Contact mode mechanism. Cantilever is in contact with the surface throughout the measurement while the height of the cantilever is adjusted based on the feedback loop (Asylum AFM-MRP-3D Manual)

the surface from a distance until it is in contact with it, any further movement would alter the deflection of the cantilever and/or damage the sample. Through the feedback system, the cantilever is pulled back to the original position. The force that the tip is exposed to while pulling back is related to the surface chemistry/physical properties in the form of adhesion or compliance. When working with soft samples, the contact mode tends to damage the sample and/or pick up debris from the surface. For this reason, tapping mode, also referred to as AC mode, was developed. In tapping mode (Figure 2.11), the cantilever is oscillating with a sinusoidal wave whose amplitude is kept constant through feedback mechanism. For instance, when there is a high feature on the surface, cantilever does not have the same space to oscillate and the amplitude decreases. On the other hand, when there is a dip on the surface cantilever has more space to oscillate and the amplitude increases. The detector measuring the change in amplitude thus is able to give out the topography of the surface.

The reconstructed image by AFM depends on several parameters such as tip geometry, tip material, surface chemistry and surface topography. Same sample might give different AFM images, when scanned with different tips, for this reason one should always keep in mind that an AFM image is not a photography of the sample surface, rather it is a convoluted image of the interaction between sample and the tip (West, 2007). In order to overcome this limitation, researchers need

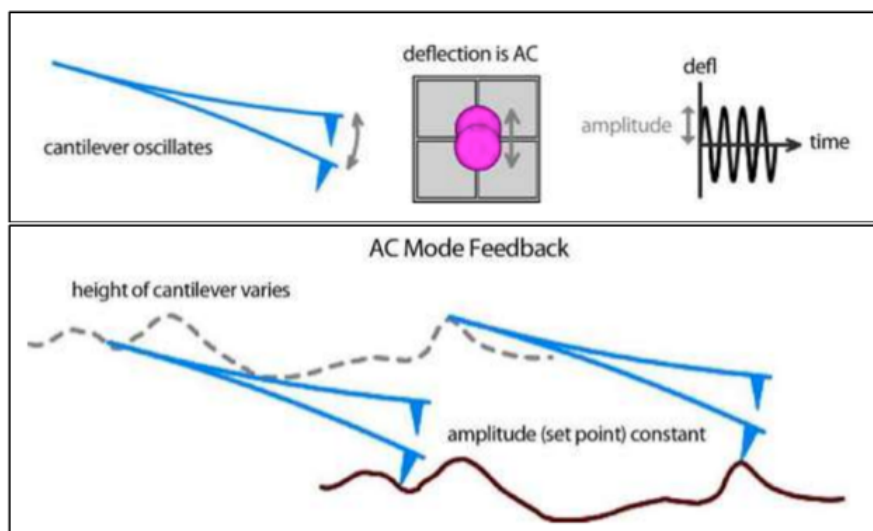


Figure 2.11: AFM Tapping mode (AC) mechanism. Top: Cantilever oscillates with a certain amplitude while going over the surface. Bottom: height of the cantilever is adjusted based on the feedback to avoid cantilever damage (Asylum AFM-MRP-3D Manual)

to select the tips with care. The material that the tip is composed of, its force constant and the geometry are all important parameters, need to be optimized depending on the application. In addition, working in a dust-free environment, such as clean rooms, would help eliminate the tip picking up contaminants and introducing error to the AFM images.

Zein films have been studied using AFM by several researchers (Subramanian and Sampath, 2007a; Wang et al., 2003a, 2008) in order to understand the surface topography and relate the topography to hydrophilicity or hydrophobicity. Zein's ability to self-assemble on both hydrophobic and hydrophilic surfaces was investigated and found that zein forms films with rough, vertical like surfaces when cast on hydrophilic surfaces and had smooth features when cast on hydrophobic surfaces. In order to form hydrophobic surface, researchers used self-assembled monolayers (SAM) with a methyl end, and to form hydrophilic surface, SAMs with a carboxylic acid end was used. These gold films with SAMs were immersed in zein solution (in 2-propanol) for 2 hours and rinsed with the solvent to remove loosely bound molecules. Figure 2.12 shows the AFM images of zein surface when

cast on hydrophobic (left) versus hydrophilic (right) SAMs. Surface roughness, reported as rms, was 1.35 nm for methyl-ended SAMs, whereas it was 4.7 nm for hydrophilic SAMs. The difference in the surface topography was interpreted as zein stacking on top of each hydrophobic helical group, resulting in a smooth surface when cast on methyl-ended SAMs. On the other hand, the packing during film formation occurred on top of the hydrophilic glutamine turns side of zein (as illustrated in Figure 2.13).

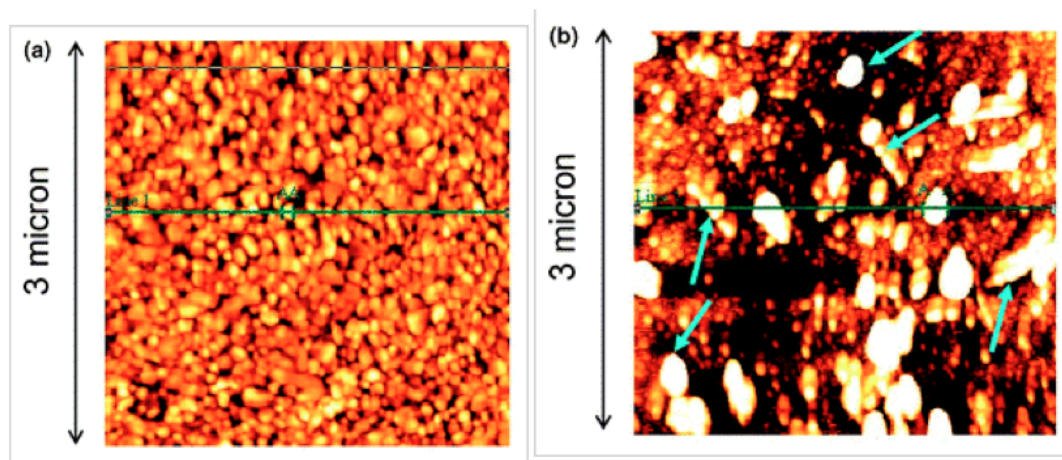


Figure 2.12: Atomic Force microscopy images of zein films a) on hydrophobic surface and b) on hydrophilic surface. The surface roughness for a is 1.35 nm whereas for b is 4.7 nm (Subramanian and Sampath, 2007a)

Another study which utilized Surface Plasmon Resonance system also showed similar results, i.e. hydrophilic surfaces having rougher features compared to hydrophobic ones. Zein solutions were run through gold surfaces that were functionalized with 1-octanethiol (hydrophobic) or 11-mercaptoundecanoic acid (11-MUA) (hydrophilic) (Wang et al., 2003a). Figure 2.14 shows the AFM images of zein film surfaces formed after SPR measurements. It was observed that zein formed uniform, smooth structures on hydrophobic surface and ring or cylinder like rough features on hydrophilic surface. Zein was thought to interact with methyl ends through hydrophobic interactions, whereas it adsorbed onto hydrophilic surface by using glutamine rich turn helical caps, which resulted in rough surface features. In this study, it was also noted that after zein solution (in 75% ethanol) run through

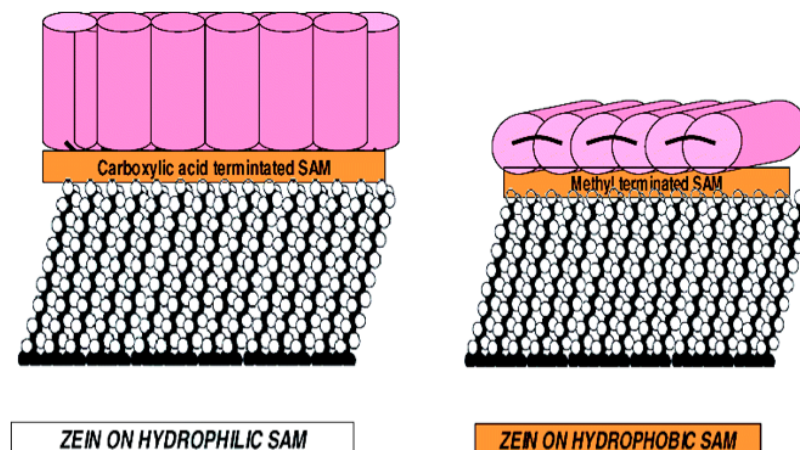


Figure 2.13: Proposed model of zein's film forming mechanism on top of hydrophilic (carboxylic-ended SAMs) and hydrophobic (methyl-ended SAMs) based on Matsushima's model (Subramanian and Sampath, 2007a)

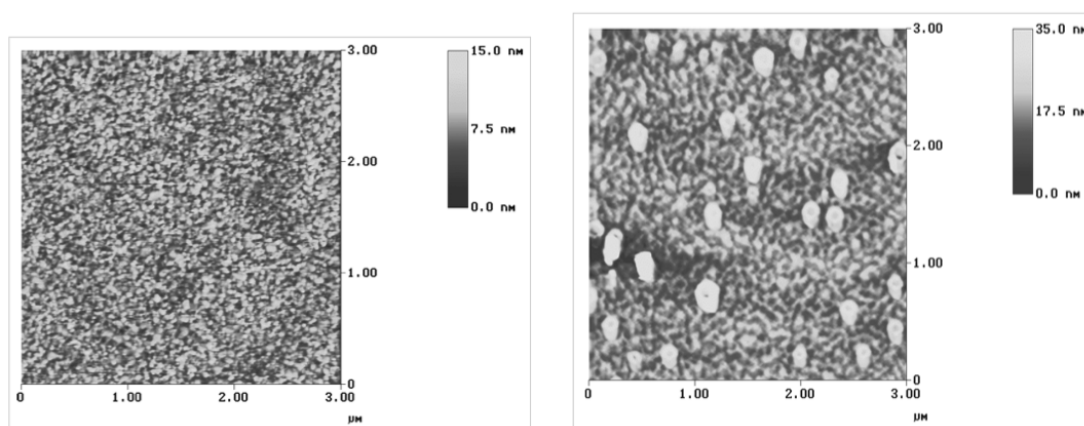


Figure 2.14: Atomic force microscopy images of zein adsorbed onto 1-octanethiol surface (left) and 11-mercaptoundecanoic acid surface (right) (Wang et al., 2003a)

SPR system, it was flushed with water, which introduced a change in polarity and caused zein to form cylinder-like structures on top of carboxylic-ended 11-MUA SAMs (Wang et al., 2003a).

2.3 Biosensors

In the food and agricultural industries, detection and monitoring of biological and chemical contaminants are crucial to ensure safety. For this reason, a variety of sophisticated analytical tools have been developed. Some examples are GCMS (Gas Chromatography - Mass Spectrometry), HPLC (High Performance Liquid Chromatography), ELISA (Enzyme linked immunosorbent assay) and PCR (Polymerase Chain Reaction). Most of these techniques require a laboratory with trained personnel and are generally time consuming. Thanks to developments in nanotechnology and molecular biology, biosensors that are sensitive, robust, fast, cost-effective and portable have become possible. Biosensors combine a biological recognition element with a physicochemical detector (Van Dorst et al., 2010).

The detection element of a biosensor can be electrochemical, optical, acoustic or colorimetric. The most common electrochemical biosensors are glucose sensors, which have been used for three decades to measure blood glucose levels. Even though glucose sensors for personalized home use are not as accurate as lab results, they have been widely accepted due to their low cost, ease of use and portability leading to point of care outcomes. Research has advanced since then on how to develop automated biosensors that are linked to insulin release (Oliver et al., 2009). The growth and success of biosensors is evident by this example and the biosensor industry today is worth billions of US dollars (Turner, 2013). Despite their success, biosensors have some challenges and limitations such as false positives, false negatives, lack of specificity, inadequate sensitivity and need for expensive equipment. False positives and false negatives can be equally harmful for certain areas, such as medical testing. False positives are observed when an unharmed analogue of a targeted analyte binds to the capturing element of the biosensor and gives positive result when in reality the analyte does not exist in the system. On the contrary, false negatives are observed the capturing element is unable to form a bond with the analyte due to problems such as diffusion, and this results in a negative reading even though the analyte is existent in a given

system. Lack of specificity can be caused by the high cost of producing highly specific capture elements, such as monoclonal antibodies. When the biosensor is produced with a marker that has affinity towards both harmful and unharmed analytes, the results may become hard to interpret. Inadequate sensitivity happens when signal to noise ratio is not at desired level or when there is interference from the medium to the measurement. Many of the highly specific, accurate and sensitive biosensors also require an expensive equipment set up.

Biosensors can make use of several different physical phenomenon, such as thermal, electrochemical, electrical, mass and optical properties. In the research of this dissertation, we utilized an optical technique: surface enhanced Raman spectroscopy, which is explained in detail in the next section.

2.4 Surface Enhanced Raman Spectroscopy

Light can interact with a medium in various ways, such as reflection, emission, transmission, absorption, diffraction and scattering (Figure 2.15). Each of these phenomena can be utilized in order to understand the nature of the medium by comparing the properties of the incident light source with what is collected back after interacting with the medium. For instance, when light scatters from a medium, its direction and energy might change as a result of the interaction with the molecules that constitutes the medium. Raman scattering is defined as the situation where the energy of the scattered light is different than that of incident light, which was first discovered by Sir C.V. Raman (Raman and Krishnan, 1928).

It is possible to measure the energy of the light that is sent to and scattered back from a sample. When the energy of light of the incident light is the same as the scattered light and there is no energy dissipation the phenomenon is called elastic scattering and has been named after its discoverer as Rayleigh scattering. Elastic scattering is the most commonly observed form of light scattering. When the energy is different between the incident and scattered light, it is called inelastic or Raman scattering. Raman scattering can be observed in two forms. In the first

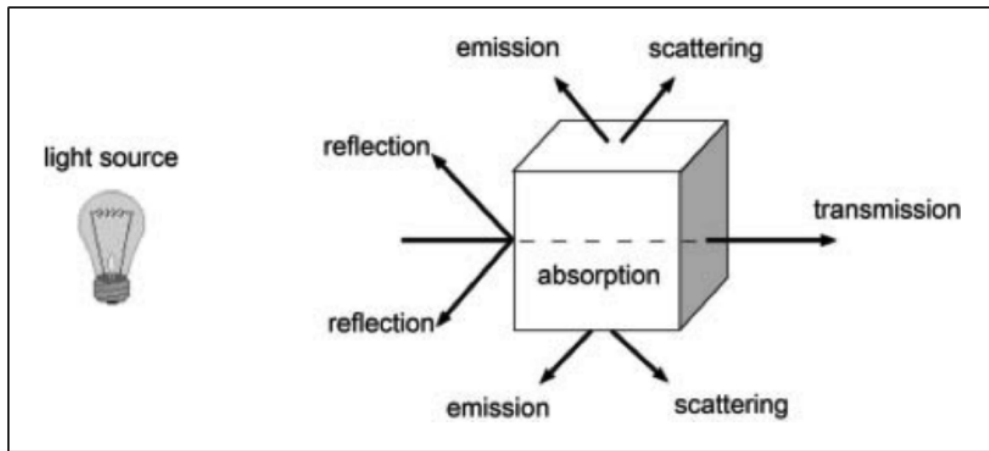


Figure 2.15: Interaction of light with a medium in different forms. Adapted from Zhang 2012

case the energy of the incident light is higher than the energy of scattered light (Stokes); in the second case the energy of the scattered light is higher than the incident light (Anti-Stokes). When light interacts with molecules, first the energy is absorbed and the molecules reach a temporary higher virtual energy state. Then, the light is emitted and the molecules go back to the ground energy states, as shown in Figure 2.16a. Most light scattering occurs as elastic Rayleigh scattering, whereas Raman scattering happens only 1 in every 10^7 incident photons.

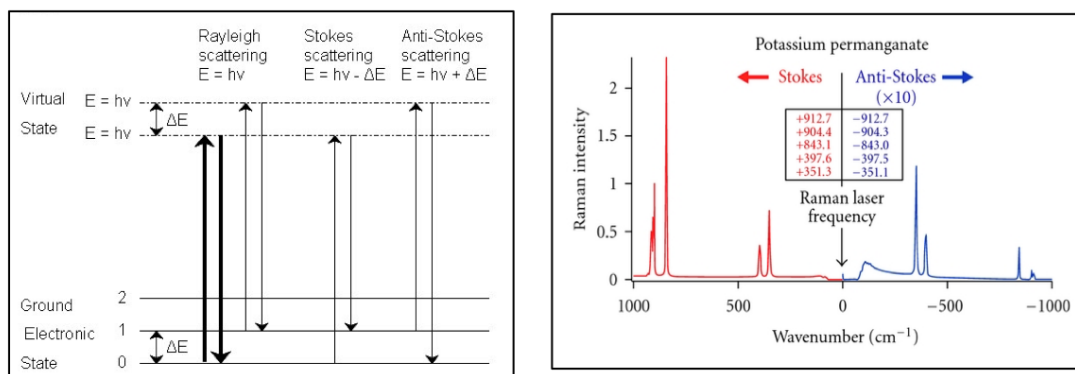


Figure 2.16: a) Energy level diagram of light scattering where E : energy of the photon, h : Planck constant, ν : frequency of the photon (Barron, 2013). b) Example Raman spectrum of potassium permanganate showing both Stokes and Anti-Stokes regions (Johnson et al., 2012)

A typical spectrum showing Stokes and Anti-stokes scattering is displayed in

Figure 2.16b. Raman spectrum is plotted as the intensity of the collected photons vs wavenumbers. Wavenumbers have the unit of cm^{-1} , which is the reciprocal of the wavelength. Wavenumbers (w) represent the difference between the frequency of laser wavelength (ν_0) and frequency of scattered light (ν_m) calculated by the following equation, where c is the speed of light.

$$w = \frac{\nu_0}{c} - \frac{\nu_m}{c} \quad (2.1)$$

For each molecule, absolute values of stokes and anti-stokes wavenumbers are identical. Stokes region has positive wavenumbers, whereas Anti-stokes region has negative wavenumbers. Anti-stokes intensity is much smaller compared to Stokes as it is less likely to have a molecule on a higher ground electronic state to begin with. For this reason, for most applications, only Stokes region is reported in the Raman spectrum. In the ensuing discussions in this dissertation, Stokes shifts will be referred to as Raman signals/shifts.

The reason for the Raman shifts is the vibrational modes of the molecules, and they are highly specific to the specific molecular bonds. Raman Effect only happens when the polarizability of the molecule changes, unlike Infra-Red spectroscopy, which requires a change in dipole moment of a molecule. The peak position of a bond is determined by two factors: the force constant and vibration mode (e.g. stretching, bending) of the bond, and the reduced mass of the molecules involved in the bond. Vibration modes are shown in Figure 2.17. The peak positions of stretching vibrations for the same molecule is observed at higher wavenumbers compared to bending ones.

Stronger bonds, e.g. C=C, compared to weaker bonds, e.g. C-C, also occurs at higher wavenumbers. Lastly, the molecules with low molecular weight, hence low reduced mass occurs at smaller wavenumbers. These rules apply to molecules in the absence of other molecules. When there are surrounding molecules, the band position might shift or overlap and width of a peak might change due to the influence of the surrounding molecules on a particular molecule. Some of the

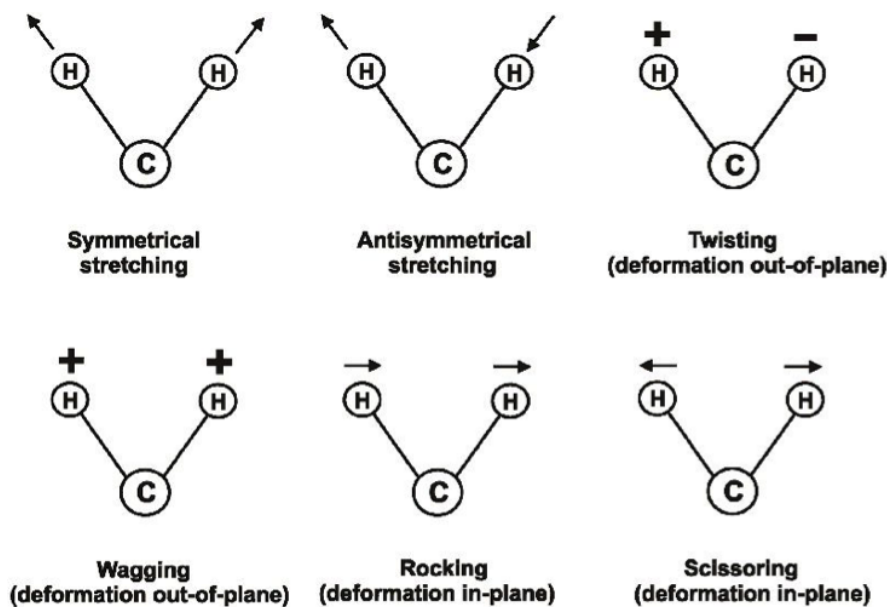


Figure 2.17: Different modes of molecular vibrations for a three-atom molecule. Twisting, wagging, rocking and scissoring are types of bending vibrations (Nawrocka and Lamorska, 2013)

Raman peak positions are given in Table 2.3.

Bandwidth can be influenced by a number of factors, the most important one being the molecular neighborhood in addition to the spectral resolution, which is influenced by the grating and laser type used in the Raman spectrometer (Nas-dala et al 2004). For instance, amorphous materials have broader Raman bands compared to crystalline ones. In addition, certain molecular interactions, such as Hydrogen bonding, may cause a shift and/or broadening of the bands, which is similar to the broadening phenomenon observed in Infra-red spectroscopy. Apart from the effects arising from the sample, the instrumental parameters, such as spectral resolution and laser wavelength stability, may also affect the bandwidth. For instance, if the spectral resolution is low, the bandwidth will be larger as the instrument will not be able to resolve fine details, on the other hand with high-resolution one would obtain sharper peaks with a smaller bandwidth.

The factors affecting the Raman peak intensity can be divided into two; parameters related to the instrument and parameters related to the sample. The instrument effect consists of three parameters: detector efficiency, analyzed vol-

Table 2.3: Wavenumbers for some molecular groups (Vandenabeele, 2013)

Vibration		Wavenumbers (cm^{-1})	Raman- intensity ¹
O–H stretch	$\nu(\text{O–H})$	3650–3000	w
N–H stretch	$\nu(\text{N–H})$	3500–3300	m
C–H stretch of alkynes	$\nu(\equiv\text{C–H})$	3350–3300	w
C–H stretch of alkenes	$\nu(=\text{C–H})$	3100–3000	s
C–H stretch of alkanes	$\nu(-\text{C–H})$	3000–2750	s
$\text{C}\equiv\text{C}$ stretch of alkynes	$\nu(\text{C}\equiv\text{C})$	2250–2100	vs
$\text{C}=\text{C}$ stretch of alkenes	$\nu(\text{C}=\text{C})$	1750–1450	vs–m
C–C stretch of aliphatic chains and cycloalkanes	$\nu(\text{C–C})$	1150–950	s–m
CC stretch of aromates [(substituted) benzene molecules]	$\nu(\text{CC})$	1600, 1580, 1500, 1450, 1000	s–m m–w s
C=O stretch	$\nu(\text{C=O})$	1870–1650	s–w
Antisymmetric C–O–C stretch	$\nu_{\text{asym}}(\text{COC})$	1150–1060	w
Symmetrical C–O–C stretch	$\nu_{\text{sym}}(\text{COC})$	970–800	s–m
CH_2 bending vibrations, antisymmetric CH_3 bend	$\delta(\text{CH}_2), \delta_{\text{asym}}(\text{CH}_3)$	1470–1400	m

ume and the laser intensity. The area of the collected signal is inversely related to the intensity, i.e. larger the area, smaller the intensity. The intensity of the laser is directly proportional to the intensity. Shorter wavelength of laser results in higher intensity. However, too strong lasers, such as UV range, may result in degradation of the sample. Raman intensity is directly correlated with the number of molecules under the measured area, i.e. concentration as well as the average polarizability of the molecule. Polarizability is defined as the ability of the

molecule to respond to an electric field with a distortion in its electron cloud. In general, molecules with higher molecular weights have higher polarizability since they held onto the electrons more loosely. Molecular orientation may also affect polarizability as a result of having electron dense sites within the molecule.

The bands are generally classified as weak, medium and strong based on their relative intensity compared to the most intense Raman band. The collection of Raman spectrum can be hindered by absorption effects of the medium. The incident or scattered light might be absorbed by the medium, which results in lower intensity of Raman peaks. Raman intensity is affected by both laser frequency and laser power. Higher the frequency and laser power, higher the Raman intensity. If some of the energy of the laser is absorbed by the medium and cannot be used to excite the target molecule, this results in a decrease of intensity of Raman peaks.

Ambient light, photodecomposition of the sample and fluorescence of the sample interfere with Raman spectroscopy. Since ambient light has the visible light spectrum of wavelengths and certain lasers such as 532 nm and 633 nm are also in the visible range, ambient light could potentially introduce noise and interference to the collected data. Ambient light effect is generally eliminated by working in a dark room. Photodecomposition can be controlled by choosing a laser with a suitable wavelength and exposure time. On the other hand, fluorescence, which is frequently observed with colored biological samples, is a severe interference as it gives a large broad peak. In order to eliminate fluorescence, longer wavelength of laser lines might be chosen. Unfortunately, since the Raman intensity drops with the 4th power of laser frequency, this would strongly affect and reduce the Raman intensity. Another technique would be to photobleach the sample or removing its color before taking Raman measurement, but it has the risk of damaging the sample if waited for long times. For this reason, post-processing techniques, such as baseline subtraction and smoothing might be used to eliminate the fluorescence effect on Raman signal.

Baseline corrections

In order to eliminate the noise in a Raman spectrum that arise from other phenomena than Raman, such as fluorescence or background radiation, baseline correction is usually applied. This can be done in two ways: first by selecting the points that are on the assumed baseline and subtracting it from the spectrum, second is to fit a curve, either exponential or polynomial, to the baseline and subtract this from the spectral data. The first method is very time consuming for large sets of data. The second method might not be fully accurate if an n-degree polynomial does not fully fit the baseline. In certain Raman software programs, it is possible to automatically fit a curve to the baseline and manually add several points to the baseline to obtain the best-fitted baseline curve. An example of polynomial curve fitting is given in Figure 2.18 where the impact of an iterative procedure on the quality of the spectrum is shown. The data clearly shows that a relatively precise fit of the baseline results in significant improvement in the Raman spectrum obtained.

2.4.1 Raman spectroscopy

Raman shifts are currently measured by Raman spectrometers. These can be custom-made in various forms, however there are mainly two commercial forms of Raman spectrometers; dispersive Raman and Fourier-transform (FT)-Raman instruments. The diagram for these are shown in Figure 2.19a and b, respectively.

Dispersive Raman systems utilizes a grating and multi-channel detector, such as charge-coupled device (CCD), whereas FT-Raman systems use a multiplexer and inverse Fourier-transformation to obtain the Raman spectrum. Laser wavelengths used in dispersive Raman are 514, 532, 633, 785 and 850 nm, on the other hand longer wavelength, 1064 nm, is preferred in FT-Raman systems.

Surface Enhanced Raman Spectroscopy

Raman spectroscopy is capable of giving molecular level information. It is non-destructive, if a suitable laser wavelength and exposure time are selected so that the sample is not damaged. It is also a label-free technique, i.e. it does not

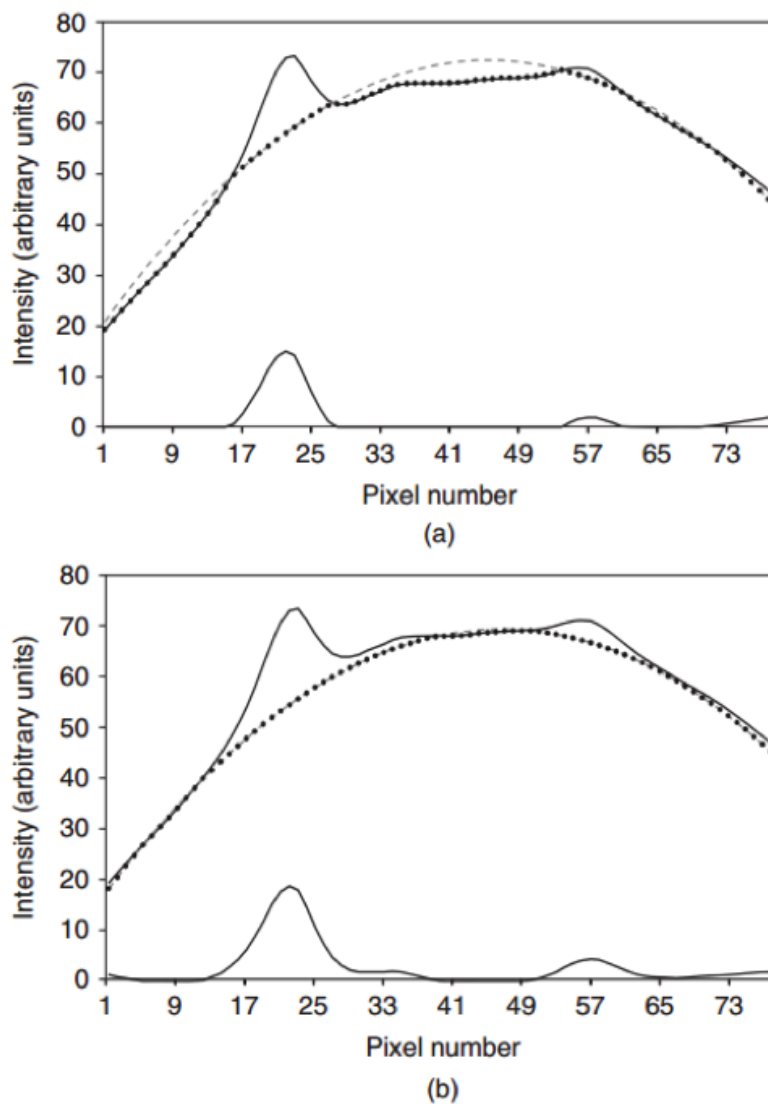


Figure 2.18: Baseline correction on a Raman spectrum. The solid line on top represents the original spectrum, the dotted line represents the fitted baseline curve, and the solid line at the bottom shows the subtracted spectrum. a) First iteration b) seventh iteration (Vandenabeele, 2013)

require any fluorescence dye/quantum dots/enzymatic tags for detection purposes. However, the Raman signal is inherently weak due to the low chance of occurrence of inelastic light scattering. There are certain approaches to enhance the signal, such as tip enhanced Raman scattering, resonance enhanced Raman Scattering, surface enhanced Raman scattering and sometimes a combination of these.

Surface Enhanced Raman Scattering (SERS) effect was discovered in 1977

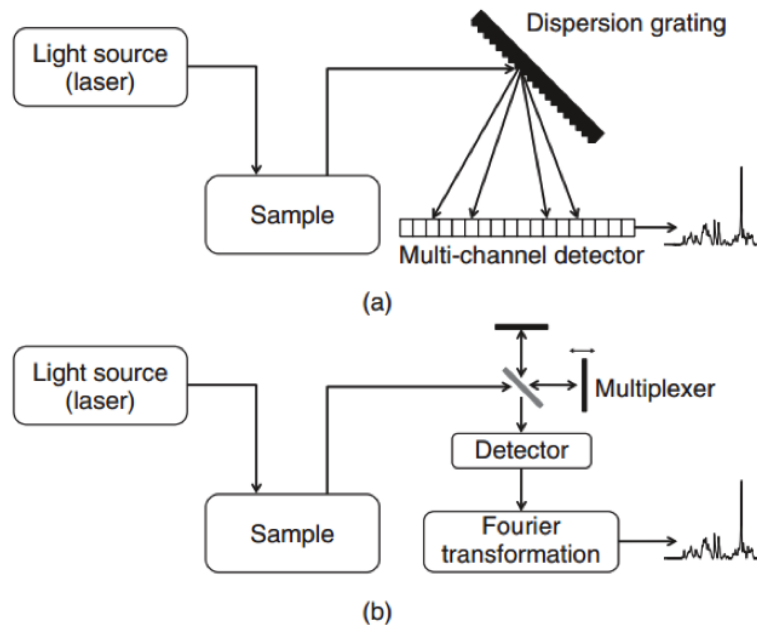


Figure 2.19: Diagram of dispersive Raman (a) and FT-Raman instruments (b) (Vandenabeele, 2013)

(Jeanmaire and Van Duyne, 1977; Albrecht and Creighton, 1977), after being observed for the first time in 1974 as an enhanced Raman signal of pyridine on rough silver surfaces (Fleischmann et al., 1974). It was hypothesized by Martin Moskovits that this enhancement was a result of excitation of surface plasmons when sub-micron or nano-sized noble metals were in contact with a laser source (Moskovits, 1985). Surface plasmons are defined as ‘collective and periodic free electron movement in the metallic structures under the electromagnetic excitation’ (Liu, 2010). A schematic for this periodic electron oscillation is shown in Figure 2.20. Metals with high density of electrons have some free electrons that are not bound to the nucleus and thus can be excited with an electromagnetic field within the physical boundary of the metal. When the excitation wavelength of the incident light, i.e. laser, matches the resonance mode of the nanophotonic structure, these oscillating electrons form a dipole and are capable of reemitting light. This reemitted light, may excite the surrounding molecules and the metal itself, resulting in an enhanced electromagnetic (EM) field in addition to the

incident EM field.

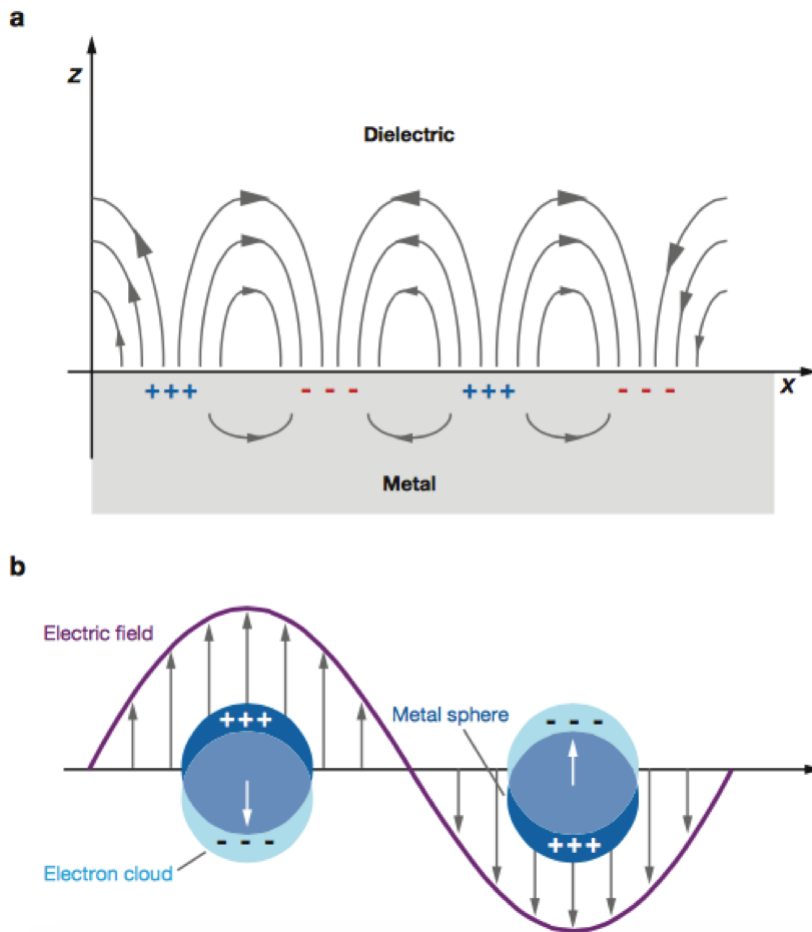


Figure 2.20: Schematic diagram of plasmon resonance on a flat surface (a) vs localized surface plasmon on a spherical nanoparticle (b). The free electrons oscillate with the electromagnetic wave as shown in this figure (Willets and Van Duyne, 2007)

Enhanced EM field is the most commonly accepted and studied phenomenon behind SERS technique. Enhancement of EM field is highly dependent on the shape, size, and aspect ratio of the surface roughness, the electron density of the metals and the wavelength of the laser used (Petryayeva and Krull, 2011). It was found that the electron density can be artificially engineered to be concentrated at very small surface areas, such as sharp tips, corners and contact points, which results in so-called “hot spots” in SERS. These are the regions where the localized surface plasmon resonance is observed. There are two important factors to

take into consideration about SERS. First, the enhanced EM field dissipates as the molecules move away from the hot spots. Second, the wavelength of the laser should be carefully picked to match the surface resonance modes. The wavelength of the laser can be determined with the help of transmittance/reflectance measurements on a nanophotonic surface. Since the metals mostly used, gold and silver, are highly reflective when their surface is smooth, choosing the wavelength at which the light is absorbed would be indicative of the case where the light couples with the rough surface (Liu, 2010).

Another reason to cause enhancement of the Raman signal in SERS is the chemical-enhancement effect. The chemical-enhancement has been suggested to arise from several different mechanisms, physisorption, chemisorption and charge-transfer. Chemical enhancement is not as effective as the EM enhancement effect. It can provide 100 folds of increase in the signal in contrast to potential 10^6 - 10^9 enhancement with noble metal coating. However it might cause new Raman bands to occur or the position of existing Raman bands to shift as a result of this chemical interaction of the analyte with the surface metal (Vandenabeele, 2013).

Fabrication of SERS-active substrates

There are mainly two ways to fabricate SERS-active substrates: bottom-up chemical synthesis and top-down nanofabrication. Bottom-up techniques involve wet chemistry where different shape and size of nanoparticles are synthesized. Some of the reported shapes of nanoparticles are rods, pyramids, plates, spheres, micelles etc. (Burda et al., 2005).

Plasmon resonance is influenced by shape and size of these nanoparticles. The simplest form and widely used nanostructures are nanospheres, such as silver or gold nanospheres as shown in Figure 2.21. Gold nanospheres show plasmon resonance around 520 nm wavelength and it can only be tuned within 50 nm range (Sun et al., 2003). On the other hand, silver nanoparticles show plasmon resonance at lower wavelengths. Nanoshells, nanorods, triangles, cubes and nanorices have more tunable characteristics depending on the fabrication as shown in Figure 2.21, they have a longer range which they can exhibit plasmon resonance (Lal

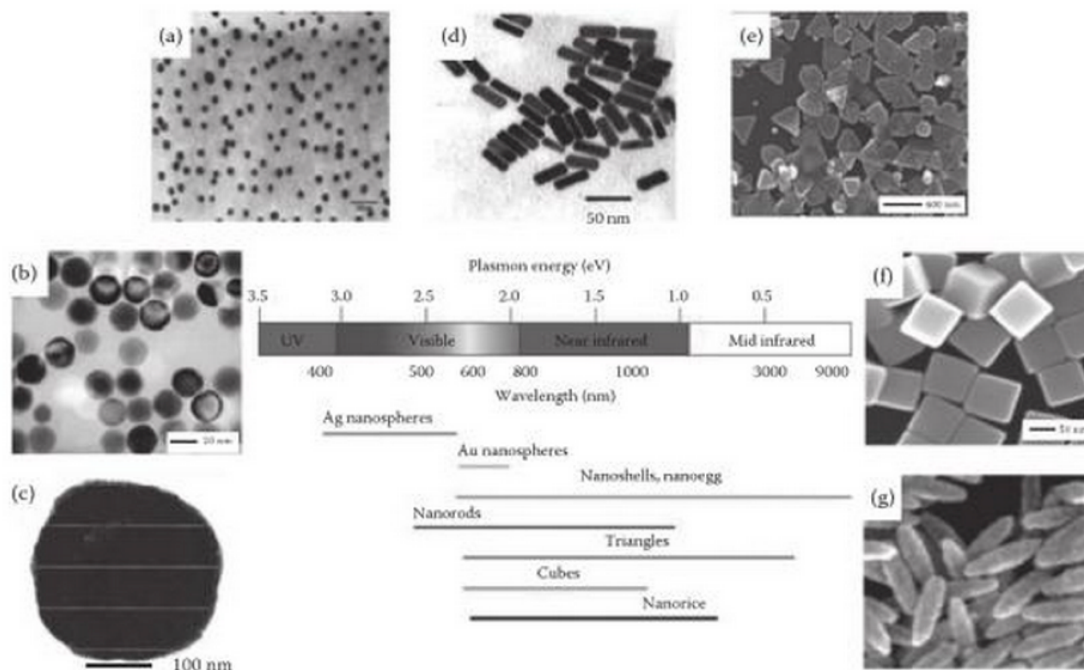


Figure 2.21: Nanoparticle resonance range of plasmon resonances for a variety of particle morphologies (Middle). Electron micrographs of gold spheres (a), silver spheres (b), silicon oxide/silver (core/shell) nanoshells (c), nanorods (d), triangular plates (e), nanocubes (f) and nanorices (g). (Retrieved from Liu et al. (2013b), Lal et al 2011, Grabar et al 1995, Wiley et al 2004, Nikoobakht and El-Sayed 2003, Washio et al 2006, Wiley et al 2006, Wang et al 2006)

et al., 2011). Branched nanostructures, such as stars can be advantageous due to their sharp edges in creating hot spots of enhanced electron magnetic field due to plasmon resonance (Barbosa et al., 2010).

These structures can be prepared by several methods, such as sol-gel, pyrolysis, chemical precipitation and chemical reduction (Burda et al., 2005). Inorganic polymerization reactions are used in the sol-gel method. Precursors of the metal or nonmetal alkoxides are the initial compounds and they are hydrolyzed with water or alcohols. Condensation of water or alcohol follows the hydrolysis process to obtain the gel. Then this gel is dried and decomposed at high temperature in order to remove the solvent. Control of the particle size is achieved by tuning solution composition, pH and temperature. Nanostructures such as TiO₂, ZnO, CuO, Al₂O₃ among others have been obtained using this method (Burda et al.,

2005; Li et al., 2003; Mondelaers et al., 2002; Viano et al., 2003). Prolysis is another technique to produce nanoparticles by decomposing chemical precursors into a solid compound by thermal treatment. This method is used to obtain metal nanoparticles such as Ag, Au and carbon nanotubes (Weiping and Lide, 1997; Maya et al., 1996; Jou and Hsu, 2004). Chemical reduction is the method that is most commonly used for metal nanoparticles. In this method, metal salts are reduced in the presence of a stabilizer. The role of the stabilizer is to govern the size and shape of nanoparticles and provide colloidal stability (Sepúlveda et al., 2009). For instance, seeded growth approach of this method has been shown to be successful in fabricating rods, plates, stars and other geometries as shown in Figure 2.22.

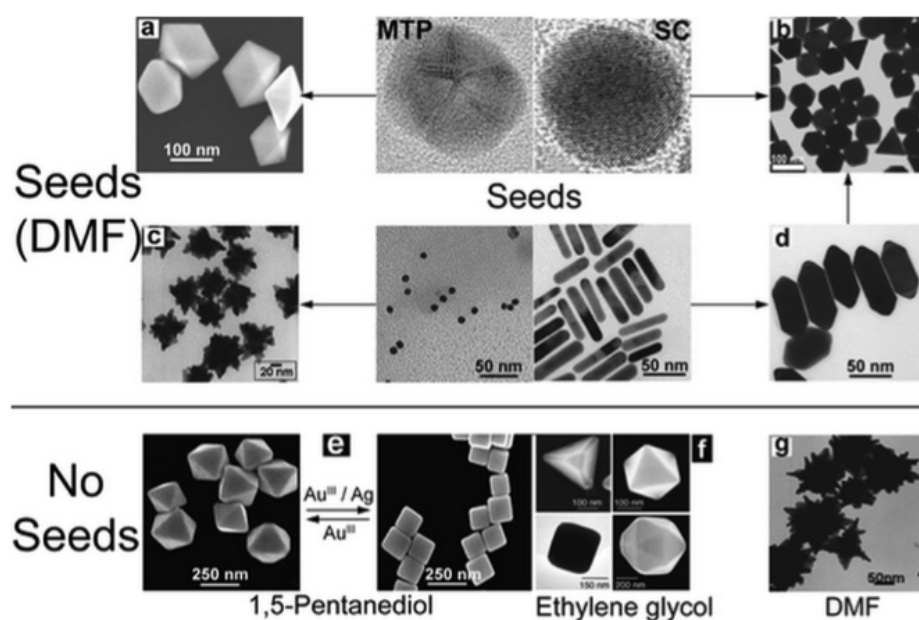


Figure 2.22: Scanning electron microscope images of gold nanoparticles synthesized through chemical reduction process. Top: seeded growth, Bottom: particles made without pre-made seeds (Grzelczak et al., 2008)

These nanoparticles are relatively easy to fabricate, however aggregation and lack of uniformity and regularity pose certain challenges for sensing purposes because there is a non uniform distribution of hot spots and a distribution of proximities between nanoparticles leading to a wide distribution of the intensity

of the signal. Top-down nanofabrication techniques consist of two steps. The first step is to create regular uniform nano-sized features by nanofabrication techniques such as nanolithography etching or template-based methods in order to reduce local variations. The second step is to deposit metal onto these features to obtain a noble-metal coated rough surface at the nanoscale.

Electron-beam metal evaporation

The metal deposition can be done by electron-beam evaporator system. A schematic of the e-beam metal evaporator is shown in Figure 2.23.

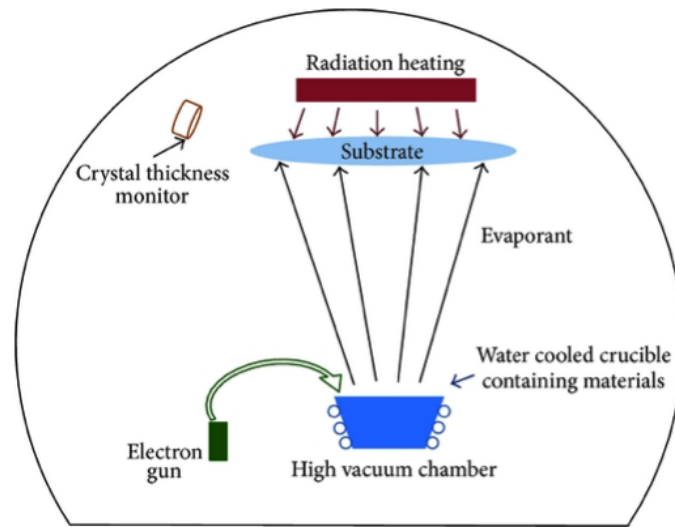


Figure 2.23: Schematic of e-beam evaporator (Xu and Huq, 2005)

E-beam evaporation is conducted under high vacuum at least around 7.5×10^{-5} Torr. The metal to be deposited is inserted in the crucible, which has a water cooling system. Then, this metal is bombarded with electrons with the help of an electron gun and magnets to direct the beam onto the crucible. The substrate is generally rotated in the chamber in order to obtain uniform coating. The rate of the metal deposition may range between 1 nm/min and 1 $\mu\text{m}/\text{min}$, allowing precise control of the thickness on the substrate. This deposition rate is measured by a crystal inserted in the chamber as shown in Figure 2.23. Due to the low vacuum and high temperatures reached inside the chamber, organic polymers are not suitable for coating in this system and alternative and intelligent methods

need to be developed.

Nanophotonic patterns used in this study

In this project, nanophotonic patterns previously developed in Prof. Logan Liu's lab were used. The patterns tested include pyramids and nanopillars. First, sub-micron scaled pyramid structures, were developed by using a high-cost commercial SERS substrate, Klarite. Klarite was the first commercialized SERS substrate by a company called Mesophotonics, now owned by Reinshaw Diagnostics. Klarite substrates have inverted pyramid structures produced on Silicon wafers, which were immobilized onto glass. In his paper, Xu et al. (2011), explains a way to reproduce these structures onto polyethylene terephthalate (PET) templates with replica-molding technique. The Si Klarite template was used only once at the beginning. They suggested that with their facile molding technique, it was possible to produce low-cost and high throughput samples. The schematic diagram of the production is shown in Figure 2.24 and explained in the legend of the figure.

The SERS-enhancement effectiveness was measured by using Rhodamin 6G, a model molecule frequently used in SERS enhancement studies (Michaels et al., 2000). It was found that the positive pyramids had an enhancement factor (EF) of 3.2×10^4 , whereas inverted pyramid structures had 1.6×10^6 . It was suggested that the difference was the result of laser wavelength not matching the resonance mode of the positive pyramids, evident by the lack of absorbance at that wavelength. The reason for 200 nm thickness of gold was to make sure the polymer underneath the gold would not give any peaks to interfere with the actual analyte Raman signal. The substrates were first coated with 10 nm thick Titanium to serve as an adhesion layer between the UV-cured polymer and gold. Gold was chosen as the noble metal due to its better durability compared to Silver or Copper. Scanning electron microscopy (SEM) images of the resulting substrates are shown in Figure 2.25.

The second SERS-active template used in this study was the nanopillars, which were also developed by Dr. Logan Liu's group in collaboration with the Lawrence

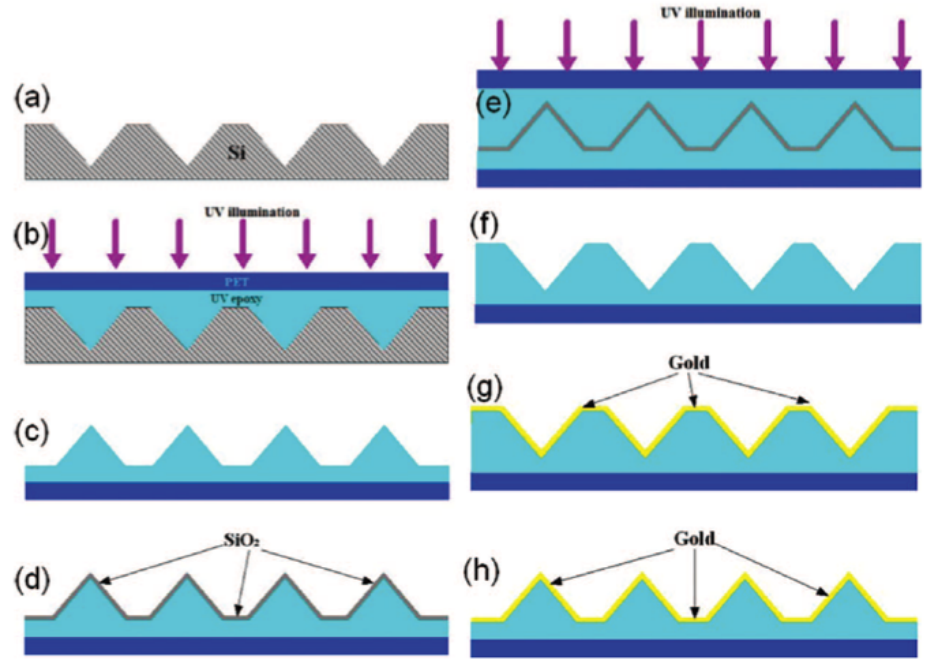


Figure 2.24: Fabrication process of positive and inverted pyramids replica SERS substrates. (a) Inverted pyramids silicon template. (b) Polymer molding on silicon master and cured by UV illumination. (c) Positive pyramids replica after being peeled off. (d) Positive pyramids template made by e-beam evaporation of 20 nm SiO_2 onto positive pyramids replica. (e) Polymer molding on the positive pyramids template and cured by UV illumination. (f) Inverted pyramids replica after being peeled off. (g) Inverted pyramids SERS substrate completed by deposition of 10 nm of titanium followed by 200 nm of gold onto inverted pyramids replica. (h) Positive pyramids SERS substrate completed by deposition of 10 nm of titanium followed by 200 nm of gold onto positive pyramids replica. Retrieved from Xu et al. (2011).

Livermore National Lab (LLNL) (Gartia et al., 2010). Figure 2.26.A shows the distribution of nanopillars over a $1 \mu\text{m}$ by $1 \mu\text{m}$ area. Figure 2.26.B shows that the pillars did not have a cylindrical shape, but rather they resembled a conical structure. Figure 2.26.C shows SEM images of nanopillars, which were coated with 80 nm coinage metal.

These structures were fabricated by the following technique. A silicon dioxide wafer was coated with photoresist and exposed to 413 nm wavelength laser interference illumination (40 mJ cm^{-2} dose). After the photoresist development, the wafer was covered by a photoresist mask. This mask had a uniform array of

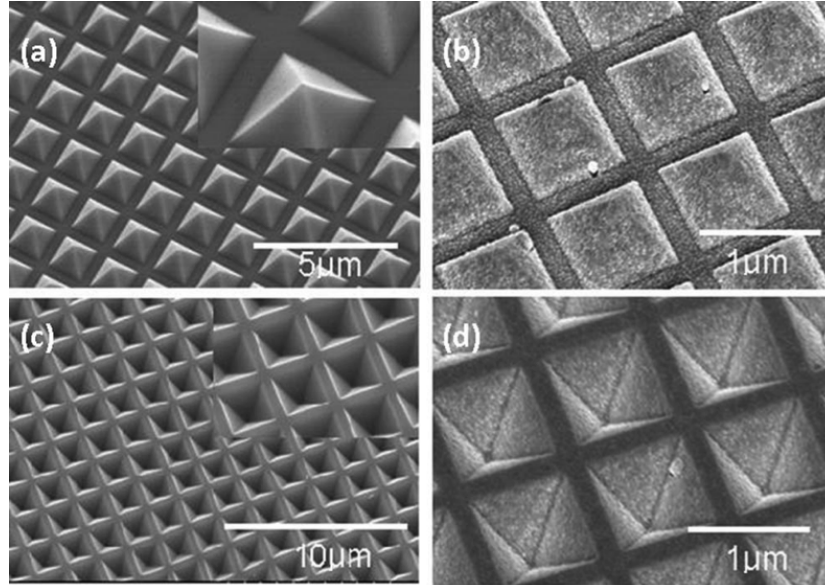


Figure 2.25: Scanning electron micrographs of pyramids replica. (a) Positive pyramids replica. The inset is a zoomed-in image. (b) Positive pyramids replica with 200-nm thick gold deposited. (c) Inverted pyramids replica. The inset is a zoomed-in image. (d) Inverted pyramids replica with 200-nm thick gold deposited. Retrieved from Xu et al. (2011)

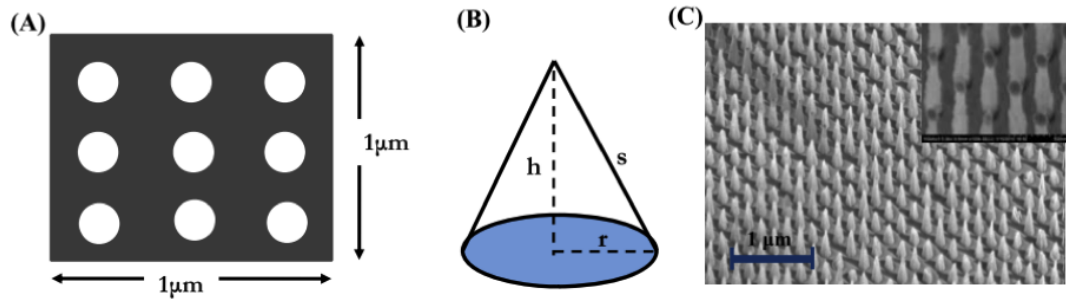


Figure 2.26: (A) Schematic of average number of pillars per unit area, (B) assumed structure for the nanopillar, (C) SEM of LLNL nanopillar substrate with 80 nm silver deposited pillar shown in the inset. Retrieved from Gartia et al. (2010)

nanoscale circles with 150 nm diameter and 350 nm spacing distance. Then, the wafer was subjected to ion milling deep reactive ion etching. The deep-reactive ion etching was conducted in Bosch process. This process consists of two steps that are alternating. First step is an isotropic plasma etch, in which the ion containing plasma attacks silicon from a vertical angle. Second step is the deposition of

protective layer, such as Octafluorocyclobutane, to cover the surface and protect the top and side surfaces of the substrate. Then the cycle goes back to step one and keep etching towards the bottom, since side and top surfaces are protected. This way deep holes can be created. The unprotected silicon dioxide area was etched down 500 nm leaving behind the array of silicon dioxide nanopillars. Since there was also lateral etching to the photoresist-protected area, the silicon dioxide nanopillars are tapered and have sharp tips at the top. Finally, after complete removal of photoresist, the wafer covered with nanopillar array structures was subjected to 80 nm-thick metal deposition by e-beam evaporation (Gartia et al., 2010).

Selecting the laser wavelength for high quality Raman measurements

It is very important to select the wavelength of the laser to use when working with Raman spectroscopy. There are several factors to consider in this decision making process. It is known that higher laser energy corresponds to higher intensity for Raman signal. So working with shorter wavelength of lasers would give higher intensity, thus better sensitivity in the detection. It is also important to take interferences into consideration, such as photodecomposition and background fluorescence. Working with high-energy lasers may cause photodecomposition of the sample. In addition, if the laser is in the range of excitation of the matrix molecules it will cause fluorescence. Clearly there is an optimization process in this selection and while high intensity lasers desirable it might be advantageous to avoid the wavelength ranges where photobleaching and fluorescence would cloud the quality of the data.

SERS effect is only observed if the light couples with the surface, i.e. when that specific wavelength of a photon is in resonance with the roughened metal surface. Reflectance measurements are conducted in order to understand the range in which the SERS-active substrate exhibits enhanced EM field effect. Figure 2.27 shows an example reflectance spectrum for a nanophotonic pattern. This example illustrates the dependence of reflectance spectrum on the thickness of silver film. Three different colors show different thicknesses as indicated by the legend. It is

important to select the laser wavelength that the spectrum shows minima in the reflectance. Minima in the reflectance indicate that the surface, rather than being reflected back absorbs the light. Only at these wavelengths that show minima, it is possible to observe the enhanced EM field. It is important to note that, there might not be a commercially available laser at the exact wavelength that the structures exhibit minima.

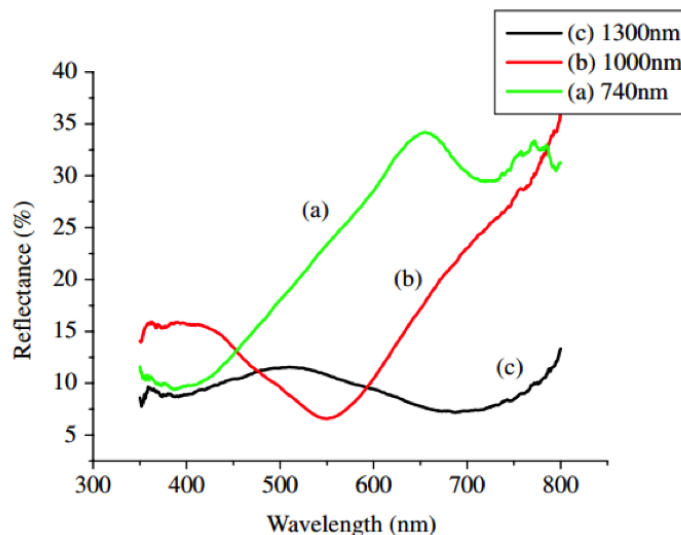


Figure 2.27: Reflectance spectrum for silver film over nanospheres with different thickness (Lin 2010)

Another aspect to consider in selecting laser wavelength is the Resonance Raman phenomenon. Resonance Raman is observed when the laser excites the electrons of the molecule of interest to an electronic excited state (Figure 2.16.a). This results in much higher Raman intensity compared to non-resonant Raman. If there is a specific molecular bond to be studied, it is preferable to work with that specific wavelength of laser that gives Resonance Raman enhancement on top of SERS.

It is apparent that it would not be possible to satisfy all of these criteria simultaneously. Thus an optimization step in deciding which laser to use for specific SERS-active substrates as well as specific analytes is needed.

2.4.2 SERS applications in food science

There is a need for reliable, fast, non-destructive technique for food analysis for traceability purposes in food and agricultural industry. Researchers have studied SERS as a potential technique for detection of food additives, chemical contaminants, antibiotics and illegal drugs, melamine, illegal food colorants, mycotoxins and small-molecular toxins, and food allergens and protein toxins (Zheng and He, 2014). Some examples of food additives studied were aspartame (Peica, 2009), monosodium glutamate (Peica et al., 2007), flavones (Teslova et al., 2007; Corredor et al., 2009) and benzoic acid (Gao et al., 2013). These studies mainly focused on the adsorption behavior and the difference in the spectrum between Raman and SERS (Zheng and He, 2014). For pesticides, there have been several studies with a commercial Q-SERS system (Liu et al., 2013b), silver dendrites (He et al., 2014), and silver or gold nanoparticles (Li et al., 2010; Liu et al., 2011). In these studies, the detection was fast even though the detection limits were not at the desired level (Zheng and He, 2014). Antibiotics and illegal drugs, such as antifungals in fish industry were studied in solvents using SERS. Some examples are furaltadone (Xie et al., 2012), tetracycline (Li et al., 2011), ciprofloxacin (He et al., 2010), enrofloxacin (Zhang et al., 2012), and chloramphenicol (Lai et al., 2011), brilliant green (Stropp et al., 2003), and crystal violet He et al. (2008a); Hu et al. (2011). Detection limits for some of the sensors are reported in Table 2.4.

These antifungal agents are mostly dye molecules, and they are generally Raman-active. For this reason, it makes it easier to study them with Raman spectroscopy (Zheng and He, 2014). Some of the challenges the researchers face regarding food analyte detection is the interference of food matrix and complexity of the molecules. Separation of target molecules from food matrix has high importance and effect in the final result of SERS detection. Even though SERS is a fingerprinting technique, it does not automatically separate the target analyte from the signals coming from the matrix (Zheng and He, 2014). For this rea-

son, statistical clustering technique was applied if it was not possible to eliminate interference during measurement (Zheng et al., 2013).

Table 2.4: Some examples of food analyte detection using SERS (analyte detected, SERS-substrate used, LOD: limit of detection)

Analyte	Substrate	LOD	References
Aspartame	Silver films	Not reported	(Peica, 2009)
Monosodium glutamate	Silver colloids	10-5 M	(Peica et al., 2007)
Flavones	Ag colloids and Ag electrode	Not reported	(Teslova et al., 2007)
Flavones	Citrate reduced Ag colloids.	Not reported	(Corredor et al., 2009)
Benzoic acid	Au colloids	Not reported	(Gao et al., 2013)
Pesticides	Q-SERS Au substrate	3-7 ppm	(Liu et al., 2013a)
Pesticides	silver dendrites	0.01 ?g/mL	(He et al., 2014)
Pesticides	Ag-coated Au-nanoparticles	25?100 ng/cm ²	(Liu et al., 2011)
Pesticides	Au/SiO ₂ nanoparticles	Not reported	(Li et al., 2010)
Furaltadone	Au colloids	5 ppm	(Xie et al., 2012)
Tetracycline	Ni/Au core-shell microparticles	100 ppm	(Li et al., 2011)
ciprofloxacin	Ag dendrites	20 ppb	(He et al., 2010)
enrofloxacin	Klarite TM Au substrate	Not reported	(Zhang et al., 2012)
chloramphenicol	Klarite TM Au substrate	50 ppb	(Lai et al., 2011)
brilliant green	Ag films over nanospheres	10-6 M	(Stropp et al., 2003)
crystal violet	Au colloids	200 ppt	(He et al., 2008a)
crystal violet	Q-SERS Au substrate	20 ppb	(Hu et al., 2011)

Melamine attracted attention due to the intentional adulteration of infant formula events in 2007 and 2008. Some of the efforts to detect its presence were with SERS. Some of the substrates utilized to detect melamine were KlariteTM substrate (He et al., 2008b; Lin et al., 2008b; Cheng and Dong, 2011). Klarite substrates were able to provide an enhancement factor of 5×10^4 for melamine detection, based on the intensity of the peak at 690 cm^{-1} location (Cheng and Dong, 2011). Lin et al. (2008b) worked with food samples and found that with Klarite it was possible to detect melamine in wheat gluten with an LOD of 0.1% concentration, chicken with 0.05 % LOD, cakes with 0.05 % LOD and noodles

with 0.07 %. Gold nanoparticle agglomerates (Mecker et al., 2012), Silver colloids and composites (Zhang et al., 2010; Zhao et al., 2013), and gold nanorods (Peng et al., 2013). Gold nanoparticle agglomerates used as SERS material was able to detect melamine in the range of 100-200 ppb in various food matrices (Mecker et al., 2012), on the other hand silver colloids were only able to detect concentration above 500 ppb, in which milk was used as food matrix (Zhang et al., 2010). Another silver nanoparticle approach was amino-modified polystyrene microspheres coated with silver nanoparticles. This system had the LOD of $2 * 10^{-8}$ M. Gold nanorods showed a very good sensitivity in detecting melamine at the concentration level of 10^{-15} M. There have been studies for mycotoxins such as aflatoxins (Wu et al., 2012) and ochratoxin-A (Galarreta et al., 2013). Researchers were able to detect ochratoxin-A using an aptamer-based SERS system embedded onto a microfluidic platform. The aptamer functionalization onto gold surface with triangular patterns provided specificity. The only used $2.5 \mu\text{M}$ concentration in this proof-of-concept study. They exploited the aptamer-ochratoxin binding phenomenon, which alters the Raman signature of the sensor.

The attempts to detect allergen proteins with SERS are very limited. Since most proteins show similar Raman footprints, it is harder to differentiate them from the matrix by their characteristic peaks. For this reason, one method used was to label the proteins with dyes and essentially detect the presence of the dye molecule through SERS (Lin et al., 2008a; Song et al., 2009). Another study showed that detecting egg allergen ovalbumin and ricin was possible through capturing them with antibody on SERS substrate. However, the distinction, and thus detection was achieved through a statistical technique called Principal component analysis (He et al., 2011a,b).

Principal Component Analysis

Principal component analysis (PCA) is a widely used statistical technique, which reduces the number of variables in a set of data into substantially smaller number of variables, which better represents the differences between data sets. It was first conceived and developed by Pearson in 1901 and later independently

developed by Hotelling in 1933 (Dunteman, 1989). PCA analysis takes a Raman spectrum and gives different scores and loadings (principal components) to characteristic clusters of the data. First principal component is the best approximation of the original data and offers the strongest ability to explain the data. Second principal component is the next best approximation and so on and so forth. In PCA analysis, a plot of different principal components (PCs), i.e. PC1 vs PC 2, is obtained to visually differentiate different samples (Viereck et al., 2009) and to create clusters of the data with common characteristics. This technique has been applied in numerous different fields, such as medicine, biochemistry, social sciences, chemistry and geology (Dunteman, 1989) especially where discrimination and prediction of the data from raw data is very difficult.

Mathematical basis of PCA can be explained as follows. Let's assume that we have a matrix X ($m \times n$) where m is the number of different samples/situations and n is the number of repetitions in each situation. PCA is an orthogonal linear transformation of original data into a new coordinate system that helps identify the differences in the data set. This transformation can be mathematically expressed as follows:

$$t_{k(i)} = X_{(i)} * w_k \quad (2.2)$$

W_K are called loadings that map each row of $X_{(i)}$ into principal component scores of $t_{k(i)}$. Each W are unit vectors and individual variables of t is supposed to provide maximum possible variance from X . To satisfy this condition, for the first principal component (with highest degree of variance) can be written as follows:

$$W_{(1)} = \arg \max_{\|W\|=1} \sum_i (t_i)_{\{i\}}^2 = \arg \max_{\|W\|=1} \sum_i (X_i * w)^2 \quad (2.3)$$

$$W_{(1)} = \arg \max_{\|W\|=1} \{ \|Xw\|^2 \} = \arg \max_{\|W\|=1} \{ w^T X^T X w \} \quad (2.4)$$

$$W_{(1)} = \arg \max \frac{w^T X^T X w}{w^T w} \quad (2.5)$$

The result to satisfy this maximization function occurs when w is the eigenvector, when the max value is the corresponding eigenvalue. When the first component is calculated to have the highest variance, the rest of the components (say n^{th} component) can be calculated as follows:

$$\hat{X}_n = X - \sum_{s=1}^{n-1} X W_{(s)} W_{(s)}^T \quad (2.6)$$

$$W_{(n)} = \arg \max_{\|W\|=1} \{ \|\hat{X}_n w\|^2 \} = \arg \max \frac{w^T \hat{X}_n^T \hat{X}_n w}{w^T w} \quad (2.7)$$

This would maximize the variance in the data when the previous components are already extracted. The final transformation can be summarized as follows:

$$T = X * W \quad (2.8)$$

Where W is a matrix whose columns are the eigenvectors of $X^T X$. Once all the loadings are calculated, we can obtain the principal component scores (T), and use it to visualize data in two or three-dimensional plots on this new coordinate system. If certain sample groups have similar level of variance from the mean/original data set, with this transformation it becomes possible to cluster them by plotting different principal components against each other. If there is no difference, or the variance is random, PCA analysis would not be able to show any clustering of the transformed data.

PCA has been also utilized for SERS applications. Di Anibal and colleagues investigated differentiation between adulterated and non-adulterated spices with Sudan I dye, which is not allowed in food stuffs, through SERS (Di Anibal et al., 2012). They demonstrated the importance of post-processing in the form of baseline correction and smoothing of the Raman data in order to obtain best results. Figure 2.28.a represents the PCA plot for adulterated (blue squares) and non-

adulterated (red triangles) samples, when the analysis was done on raw data. Figure 2.28.b, on the other hand, represents the same groups, after Raman spectra were baseline corrected and smoothed. It was observed that raw data was not suitable enough for differentiation, however successful results were obtained after post-processing of the data. Since PCA analysis is a method to understand and plot the factors that cause largest variance within the data, raw data PCA analysis did not work as the biggest variance was different level of intensities due to autofluorescence. However, when the correction was done in the form of post-processing, this variance was eliminated from the system and PCA was able to distinguish adulterated and unadulterated samples. It was possible to obtain separate clusters in PCA plots for both PC1 vs PC2 and PC2 vs PC3 (Di Anibal et al., 2012).

Zheng and others demonstrated that PCA could be utilized to quantify the amount of a pesticide, Ferbam with SERS (Zheng et al., 2013). In this study, a hand-held Raman spectrometer was investigated for its efficiency in quantification and found that with the help of PCA different concentrations can be differentiated from each other. Figure 2.29 shows the PC 1 vs PC 2 plot. Concentrations of 0, 4, 7 and 14 ppm were found as separate clusters in this study.

As in the previous examples, PCA plots are generally constructed with 2 components, however sometimes there is a need for third PC in order to be able to differentiate between samples. Guicheteau and colleagues studied SERS to observe gram-positive *Bacillus* spores (*Bacillus atrophaeus*, *Bacillus anthracis*, and *Bacillus thuringiensis*) and Gram-negative bacterium *Pantoea agglomerans* (Guicheteau et al., 2008). The PCA plot for these species is shown in Figure 2.18. Three PCs were used in this analysis and the plot had three axis as follows: PC 1, PC 2 and PC 3. Each cluster is shown in a different color to represent *Bacillus* spore samples and *Pantoea agglomerans*.

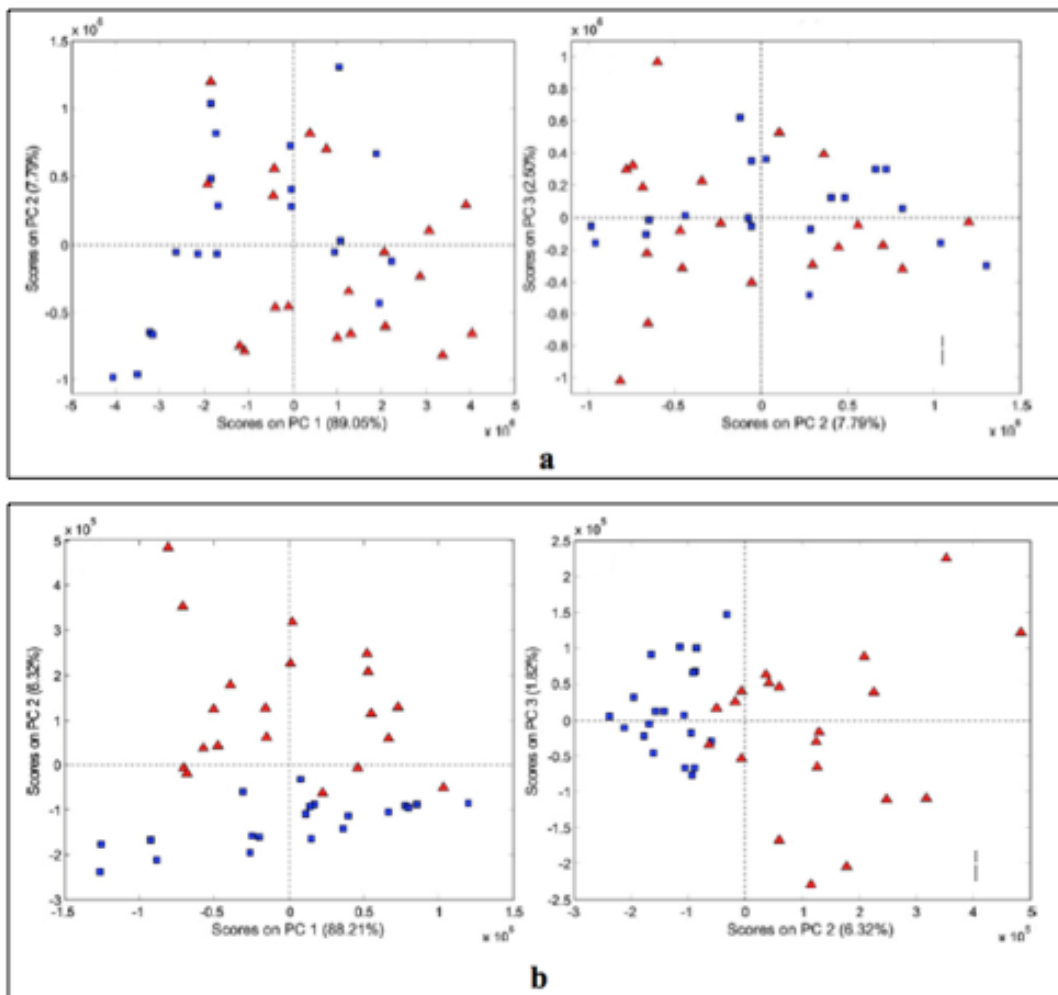


Figure 2.28: Principal component plots for adulterated and non-adulterated samples with Sudan I dye. Principle components were for Raman spectra of a) raw data b) Baseline corrected and smoothed data (Di Anibal et al., 2012)

2.5 Food contaminant and allergen detection

2.5.1 Peanut allergen

Food allergy is one of the major health issues concerning the food industry since the consequences can be lethal for susceptible populations. Most of the food allergies are associated with cow's milk, eggs, soy, wheat, peanuts, tree nuts, fish and shellfish. Food allergies can cause a potentially fatal reaction called anaphylaxis. Peanuts and tree nuts are the reason for the majority of cases (Al-

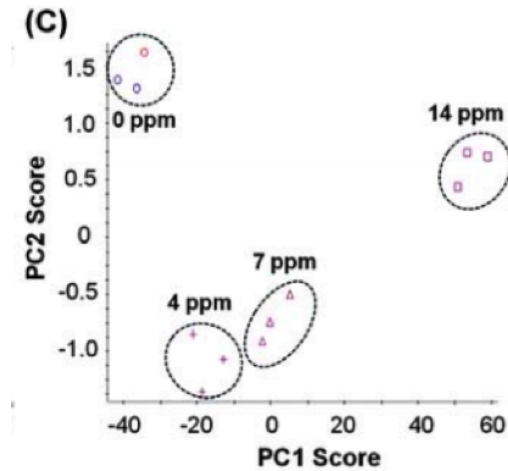


Figure 2.29: Principal component plot for PC 1 and PC 2 for ferbam, a pesticide, at different concentrations (Zheng et al. 2013)

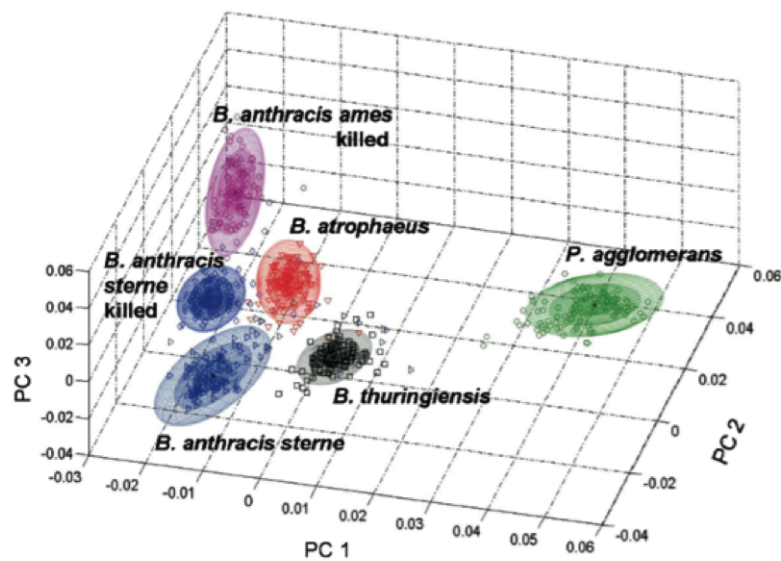


Figure 2.30: PCA plot showing discrimination between five *Bacillus* spore samples and *Pantoea agglomerans* (Guicheteau et al. 2008)

Muhsen et al., 2003). Peanuts (*Arachis hypogea*) belong to the legume family, which includes peas, lentils and soybeans. There has been eight identified peanut allergens so far: Ara h1 to h8. Ara h1 and Ara h2 are two major allergens (Wen et al., 2007) and Ara h1 constitutes the main protein component of peanuts (12-16 %). This protein affects up to 100 % of the allergic patients (Koppelman et al., 2001; Burks et al., 1992).

Ara h1 is a glycoprotein consisting of 586 amino acids with a molecular weight of 63.5 kDa. This protein can form a stable trimer through hydrophobic interactions as shown by Chruszcz et al. (2011), with a short recombinant Ara h1 purified protein. As shown in Figure 2.31 (Left), Ara h1 has Alpha-helices (red), beta-strands (yellow), and loop regions (green) in its structure. The trimers shown in Figure 2.31 (Right) are formed by hydrophobic interactions through alpha-helices as well as overall interaction of monomers with each other. I added the information about the antibody here. The biochemical mechanism of the allergic reaction is an IgE-mediated type I hypersensitivity reaction (Al-Muhsen et al., 2003). It has been found that some of the IgE-binding sites on Ara h1 are very stable and are not affected by heating or digestion with pepsin, trypsin or chymotrypsin (Wen et al., 2007).

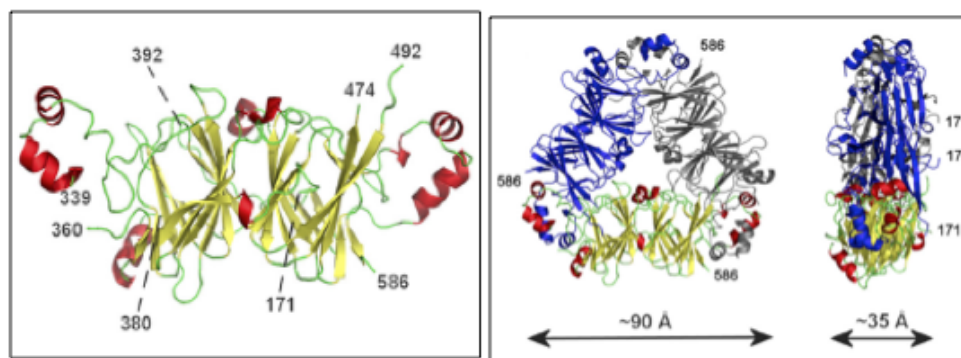


Figure 2.31: Crystal structure of the Ara h1 monomer (Left) and Trimer formed by Ara h1 (Right) with a 0 and 90 rotation (Chruszcz et. al. 2011).

According to Food Allergen Labeling and Consumer Protection Act, manufacturers have to label their products if it contains peanuts in any amount. For this reason, cross-contamination on the production lines becomes a very significant issue. The end products and lines have to be monitored for the presence of the allergens. It has been shown that an amount as low as 2 mg can cause allergic reaction in kids (Flinterman et al., 2006), thus the limit of detection should be in the low ppm range (van Hengel, 2007) in order to ensure safety.

Testing methods for this allergenic protein have been a major priority for the

food industry. The fact that the traditional analytical techniques, e.g. liquid chromatography and gas spectroscopy, are time consuming, expensive, complicated and laborious made the development of the rapid, on-site diagnostic tools very important for the food industry (McGrath et al., 2012).

As reported by Pomés et al. (2003), four different antibodies were developed by using mice for Ara h1 and labelled as: 2C11, 2F7, 2C12, and 2F8. We used 2F7 in this study, which did not show any cross-reactivity with 13 selected and tested legumes (Pomés et al., 2003). Among these four antibodies, 2F7 showed optimal binding to Ara h1 along with 2C12. 2F7 was also the antibody used in order to purify Ara h1 protein, which was commercially supplied for this research.

The most widely used rapid analytical technique is enzyme-linked immunosorbent assays, ELISA and there are commercially available kits employing qualitative or semi-quantitative results within 30 - 60 minutes (Schubert-Ullrich et al., 2009). Other major immunoassay-based methods are lateral-flow assays and dipstick test (Picó, 2012). These are commercialized methods, which were also validated by institutions such as, Association of Analytical Chemist-Research Institute, validation according to the Performance Tested Method Program. These immunoanalytical techniques are based on the interaction of the allergen protein with an antibody-linked compound, which results in color formation. A common enzyme used is alkaline phosphatase, which gives yellow color with the addition of the substrate, p-Nitrophenyl Phosphate. ELISA can be employed in a number of different methods as described in Figure 2.32. As it detects the allergy causing protein, it is a direct method compared to the alternative DNA-based detection. After the target genes are identified and sequenced, polymerase chain reaction (PCR) enables the detection with the help of appropriate primers. DNA-based techniques also offer semi-quantitative measurements of the allergens and some commercialized PCR kits can be obtained from several suppliers. These kits are reported to give results in 5-10 minutes, however only one method has been validated by Association of Analytical Communities (Picó, 2012). The draw-back of DNA-based techniques is their false negatives if the food is low in DNA content

but high in protein content if DNA is degraded by food processing (van Hengel, 2007).

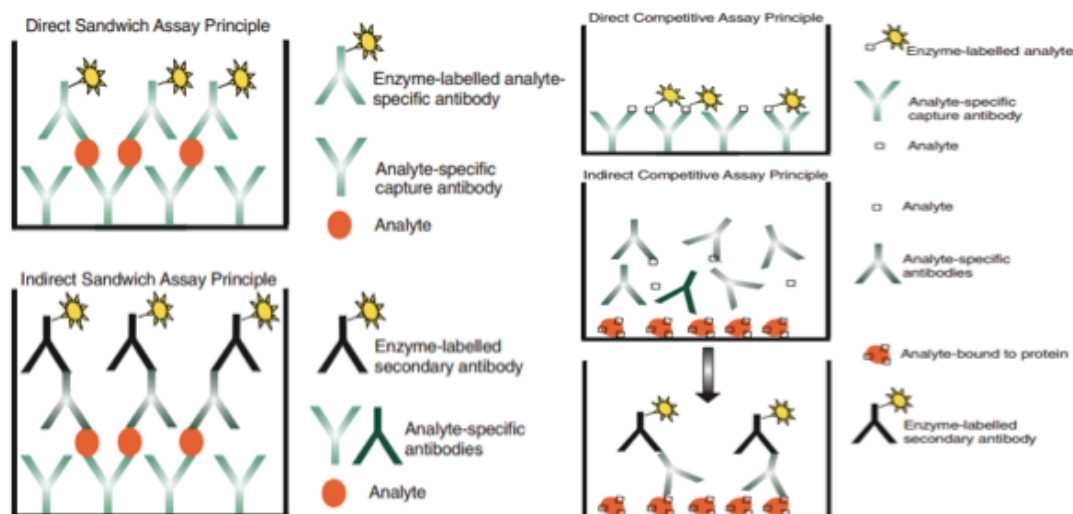


Figure 2.32: Different types of ELISA, Left-top: Direct sandwich assay, Left-bottom: Indirect sandwich assay, Right-top: Direct competitive assay, Right-bottom: Indirect competitive assay (Schubert-Ullrich et al., 2009).

Due to their high speed, ease of use and high degree of automation, biosensors present an alternative solution to the allergen detection problem. In recent years, there has been an increase in the publications of this innovative field (Pilolli et al., 2013). So far, some optical, electrochemical and electromechanical techniques were attempted. A reagentless electrochemical impedance sensor was employed to detect the protein Ara h 1 with a limit of detection (LOD) of 0.3 nm (Huang et al., 2008). An impedance circuit system as shown in Figure 2.33 was used in this study with an antibody functionalized gold electrode. When Ara h1 protein binds to the antibody functionalized on the surface, charge-transfer resistance (R_{ct}) changed in correlation with the concentration of the antibody (Figure 2.33 bottom). The measurement required several stabilization steps after addition of each molecule such as 11-MUA as a linker between Antibody and gold surface (30 minutes), and monoclonal antibody 2F7. However, they reported that the measurement of the binding of Ara h1 at different concentrations took only 2 minutes.

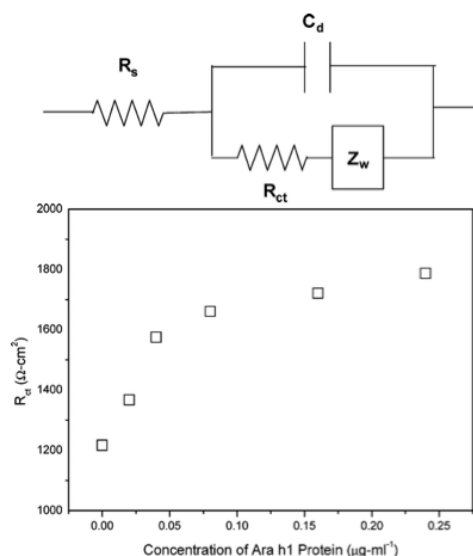


Figure 2.33: Top: the electrode used in the impedance-based electrochemical sensor, R_s : solution-phase resistance, C_d : differential capacitance, R_{ct} : charge transfer resistance, and Z_w : impedance. Bottom: correlation of Ara h1 concentration with charge transfer resistance (Huang et al., 2008)

Among the optical techniques, Surface plasmon resonance (SPR) seems to be the most popular one. SPR sensors use the refractive-index change close to a surface that happens when the antigen binds to antibody. It is a real-time, label-free technique and an LOD around 0.1- 12.5 $\mu\text{g}/\text{ml}$ food samples are achieved (Pollet et al., 2011; Mohammed et al., 2001). One of the studies that detected Ara h1 with SPR used nanobead enhancement technique as shown in Figure 2.34. First, gold surface was functionalized with polyclonal antibodies and then both the presence of secondary antibody and secondary antibody immobilized onto nanobeads were tested. It was found that nanobeads provided good enhancement in the shift of reflected light wavelength (Figure 2.34). Limit of detection was found to be 9 $\mu\text{g}/\text{ml}$ for label-free Ara h1 test, 0.21 $\mu\text{g}/\text{ml}$ for secondary antibody enhancement and 0.09 $\mu\text{g}/\text{ml}$ for nanobead enhancement. The calibration curve for quantification was obtained for Ara h1 concentration vs wavelength shift and it showed non-linear characteristics.

Some other examples of biosensors developed for allergen detection can be given as gold immunochromatography assay (GICA) and optical biosensor immu-

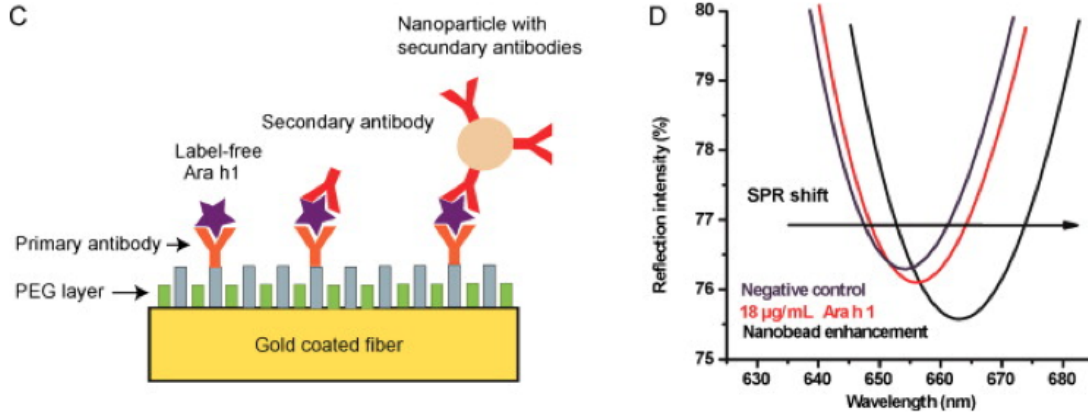


Figure 2.34: Left: Primary antibody functionalized gold substrate for surface plasmon resonance system with three different test methods: label-free, secondary antibody and nanoparticle with secondary antibodies. Right: Corresponding wavelength shift plot for these three cases (Pollet et al., 2011)

noessay (Ji et al., 2011; Yman et al., 2006). Gold immunochromatography assay (GICA) utilized a two-monoclonal antibody system, in which one of them stationary and the other was mobile, which resulted in a color change in the presence of Ara h1 (Figure 2.35). The LOD was reported was 10 ng/ml. However, this was not a quantitative test, rather it gave results as positive/negative with the suggestion that it can be used in the customs as pre-screening (Ji et al., 2011).

For the protein-based techniques, there are two types of antibodies; monoclonal and polyclonal. Whereas monoclonal ones are highly specific to the target allergen, they are more expensive to produce compared to polyclonal ones. They might sometimes give false negatives because they have a very specific amino acid sequence they recognize. If this sequence is denatured in the protein they are not able to recognize it. Polyclonal antibodies are typically used due to the lower production costs (Picó, 2012). They respond to several amino acid sequences within the proteins. This introduces the problem of cross-reactivity of other proteins with the antibody, leading to false positives in the test results. It is therefore important that the specificity of the antibody towards that specific fraction be demonstrated doing Western Blot Experiments. It has been shown that Ara h 1 has around 30 to 45 % amino acid identity with other vicilin proteins, of which

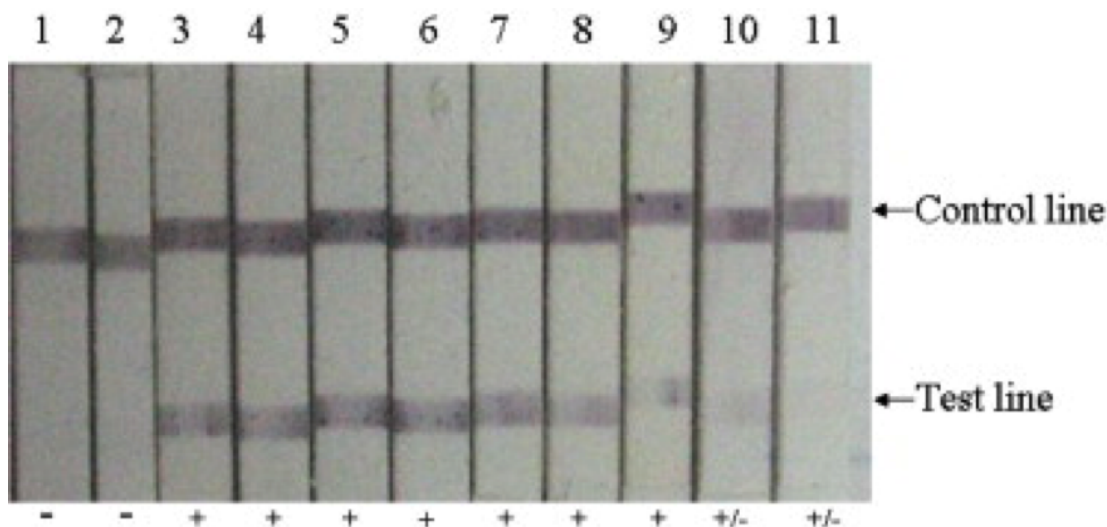


Figure 2.35: Gold immunochromatography assay (GICA) strips for detection of peanut allergen Ara h1, 1: Extract buffer; 2:PBS; 3:1000; 4:500; 5:250; 6:100; 7:50; 8:25; 9:10; 10:5; 11:2.5 ng/ml. The concentrations indicated are the quantity of total protein per ml of crude peanut extract. +: positive; -: negative; +/-: not definitive (Ji et al., 2011)

it is a member of, such as soybean and other beans (Ji et al., 2011). Surface enhanced Raman spectroscopy based nanophotonic biosensor potentially offers a solution to the reliance on the interaction of antibody-antigen reaction without any proof-checks. False positives might be eliminated as the technique involves the requirement for the right signature in the scattered signals. For instance, it could be possible to tell the difference between the actual analyte vs an interfering molecule binding to the antibody by looking at their Raman signature. Most antibody-based biosensor tools do not have other specificity measures as opposed to SERS.

2.5.2 Acrylamide detection

Since the discovery of acrylamide in food in 2002 (Tareke et al., 2002), it has drawn lots of attention due to its potential neurotoxicity, reproductive toxicity and carcinogenicity (Friedman, 2003). Acrylamide is formed as a result of the Maillard reaction, between asparagine and a reducing sugar or alpha-dicarbonyls (Blank,

2005). It is found in plant-based foodstuffs that are heated over 120°C mostly during processes such as baking and frying. Some food products that are mostly associated with high-acrylamide content are potato chips, French fries, bread and coffee. The USDA released draft guidance for industry on reduction of acrylamide in November 2013. Acrylamide is considered as a health concern and there is a continuous effort to develop strategies to reduce its consumption. Reduction can be done either by prevention or removal intervention such as vacuum treatment (Anese et al., 2013). Several researchers have developed models that correlate the acrylamide content in the product with the composition of the raw material and certain attributes of the product such as color (Pedreschi et al., 2005). One of the highest concerns of acrylamide exists for potato products, such as chips or crisps as the content ranges between 117 - 4215 $\mu\text{g}/\text{kg}$ (Lineback et al., 2012). The temperature of the process, moisture content, levels of asparagine and sugar were all found to be factors affecting the acrylamide content of the end product. As the content varies a lot, companies need a fast point of care, on location assessment technique as a quality control tool. Common techniques are sophisticated, labor intensive and expensive such as gas chromatography combined with one or tandem mass spectroscopy (GC-MS or GC-MS-MS), liquid chromatography (LC) combined with these or high-pressure liquid chromatography (HPLC) (Bethke and Bussan, 2013). Near Infra Red (NIR) was studied as a promising technique and showed a relatively large, prediction error of 266 $\mu\text{g}/\text{kg}$ (Segtnan et al., 2006) so there is still need for improvement for this near-real time technique to be used.

In order for acrylamide to be regulated properly, there is a requirement for a rapid, affordable detection technique. Experts keep suggesting new methods such as adsorption stripping voltammetry, capillary zone electrophoresis and non-aqueous capillary electrophoresis (Vesela et al., 2013; Bermudo et al., 2006; Başkan and Erim, 2007). To this date, any reliable detection technique with Raman spectroscopy has not been reported. However, the Raman signature of acrylamide in water was studied (Jonathan, 1961). The structure of acrylamide can be seen in Figure 2.36 and the Raman signature of 1 M solution acrylamide in water can be

seen in Figure 2.37. The peaks observed at specific wavelengths were assigned to specific vibration modes. O=C-N bending peak was observed at 498 cm^{-1} , whereas C-C stretching peak was seen at 978 cm^{-1} . Three peaks at locations 1057 , 1128 and 1289 cm^{-1} were assigned to CH_2 rotation, NH_2 rotation and C-N stretching. One of the most prominent peaks was observed at 1439 cm^{-1} which is associated with bending deformation of CH_2 and CH bonds. The peak at 1606 cm^{-1} was observed due to NH_2 bending. Peaks around 1636 and 1673 cm^{-1} were associated with C=C and C=O stretching respectively. Peak at 2789 was observed due to stretching of C-H bond.

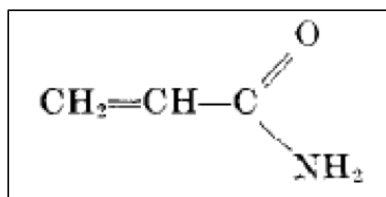


Figure 2.36: Molecular structure of acrylamide (Jonathan, 1961)

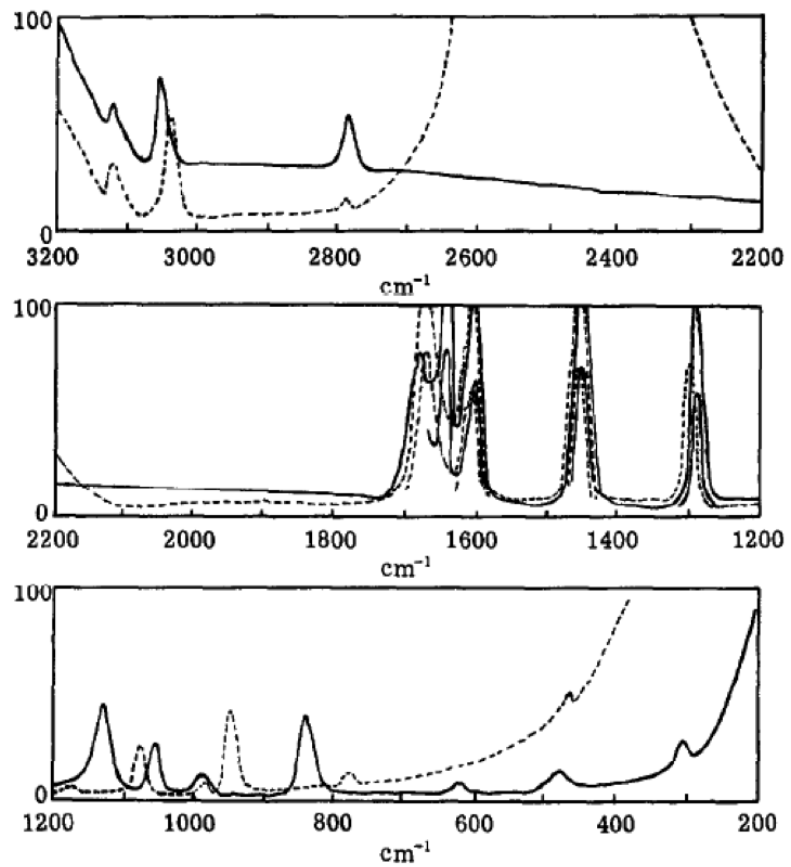


Figure 2.37: Raman spectrum of 1 M solution of acrylamide in water (solid line) (Jonathan, 1961)

CHAPTER 3

MODIFICATION OF THE HYDROPHILIC / HYDROPHOBIC CHARACTERISTIC OF ZEIN FILM SURFACES BY CONTACT WITH OXYGEN PLASMA TREATED PDMS AND OLEIC ACID CONTENT¹

3.1 Abstract

Zein has been widely studied as a biopolymer due to its unique film-forming abilities. Surface properties are of high importance for certain applications which include microfluidics and tissue engineering, as they drastically affect the end result. It is important to develop techniques to modify zein surface properties without compromising bulk material properties. In this study, we developed a facile technique to change the water affinity of zein film surfaces, compatible with patterning techniques via soft lithography. This is achieved by a simple solvent casting technique onto a polydimethylsilohexane (PDMS) substrate that was exposed to oxygen plasma. Water contact angle measurements (WCA) were used to assess the hydrophilicity of zein surfaces and they reached as low as 20 degrees. Atomic Force Microscopy, optical absorbance and light microscopy were used to study the characteristics of the film and its surface topography. Hydrophilic zein surfaces had higher roughness values compared to hydrophobic ones. Surface roughness, introduced by sandpaper and gratings does not have the same effect as surface chemistry. The amphiphilic nature of plasticizer oleic acid also contributed to the change in the water contact angle of the films. In

¹Reprinted with permission, from P. G. Gezer, S. Brodsky, A. Hsiao, G. L. Liu, J. L. Kokini “Modification of the hydrophilic/hydrophobic characteristic of zein film surfaces by contact with oxygen plasma treated PDMS and oleic acid content” *Journal of Colloids and Surfaces B: Biointerfaces*, 135, 433-440 (2015).

conclusion, we demonstrated that zein film's surface properties can be controlled by its ability to self-assemble depending on the substrate that it is being cast on.

3.2 Introduction

Zein is an amphiphilic corn protein, with an almost equal distribution of hydrophilic and hydrophobic amino acids (Gianazza et al., 1977). It is soluble in a variety of solvents including 70% ethanol, 70% acetone, glacial acetic acid, propylene glycol and others (Evans and Manley, 1941; Manley and Evans, 1943) with 70% ethanol as the most widely used solvent. It is renewable, biodegradable and environmentally friendly. It is able to form free-standing, flexible films by the addition of plasticizers (Kanig and Goodman, 1962) and it has been demonstrated to successfully replicate micro and nano scale features, such as microfluidic channels and reservoirs (Altunakar et al., 2010; Luecha et al., 2011). Zein microfluidic based platforms engineered using soft lithography yield a hydrophobic surface, which may pose a challenge for water flow in the channels due to a high surface energy barrier.

Zein can be used for cell and tissue engineering due its biocompatibility (Dong et al., 2004; Sun et al., 2005). It has been reported that certain cells have a higher affinity towards hydrophilic surfaces on which they better adsorb and grow (Wang et al., 2008). Thus there is a need for a hydrophilic surface on zein films for the aforementioned applications.

Zein film's surface can be modified to be either more hydrophobic or hydrophilic depending on the treatment and manufacturing conditions (Wang et al., 2008; Biswas et al., 2009; Shi et al., 2009). It is possible to derivatize the zein surface through treatment with certain chemical solvents, to have different wetting properties (Biswas et al., 2009). Huang and Kokini (2009) reported a drastic drop in the Water Contact Angle of zein after UV-Ozone exposure. The UV-Ozone exposure forms additional carboxylic groups (Shi et al., 2009). Zein is also able to align itself with the material that it is in contact with during film forma-

tion (Wang et al., 2004b,a). resulting in both hydrophilic and hydrophobic areas, induced by methyl and carboxylic chemical groups. In addition, fibroblasts were used to engineer a hydrophilic surface for tissue development (Wang et al., 2008).

Oxygen plasma treatment has been used in microfluidics to increase the wettability of the surface to the flow of aqueous solutions and to permanently bond polydimethylsiloxane (PDMS) films to glass slides (Plecis and Chen, 2007). Oxygen plasma is known to introduce hydroxyl groups on the surface of PDMS (Bodas and Khan-Malek, 2007).

In this study, we aim to show that it is possible to change the surface properties of zein films through contact with PDMS exposed to oxygen plasma to fabricate zein films with different hydrophilic/hydrophobic surfaces. The effect of the parent substrate (PDMS, oxygen plasma exposed PDMS, sandpaper textured PDMS and wax) on zein surface properties has been investigated using water contact angle (WCA) measurements. We also investigated the effect of oleic acid content as a plasticizer on the hydrophilic/hydrophobic properties of the surface and we offer a mechanism of action. Atomic Force Microscopy (AFM), and optical absorbance were used to offer nanoscale insights on the organization of the supramolecular structure of zein leading to changes in surface properties.

3.3 Materials and methods

3.3.1 Zein formulation

Zein (Sigma Aldrich) was dissolved in 75% ethanol at 65 C at a ratio of 1:5 (g/ml). The mixture was stirred over heat for 5 minutes to ensure a homogenous solution. Oleic acid and emulsifier (monoglyceride) were then added at ratios of 1 gram zein: 1 gram oleic acid: 0.15 g emulsifier. The mixture was then heated and continuously stirred for an additional five minutes. For different oleic acid content experiments, the oleic acid amount added to 1 gram of zein was changed as follows: 0 grams, 0.25 g, 0.50 g, and 1 g. Emulsifier content was kept constant as 0.15 g

regardless of the oleic acid content, with the exception of 0 g oleic acid content (no emulsifier was added to this solution). Zein films which are not referred with a ratio such as 1:0, 1:0.25, 1:0.5 or 1:1, were prepared as 1 g zein: 1 g oleic acid ratio.

3.3.2 Different parent substrate preparation methods and oxygen plasma exposure

Parent substrate is the substrate zein was cast on, in solution form and then allowed to dry in a vacuum desiccator for 2-3 days at room temperature (21°C) in full contact with the parent substrate. In this study paraffin wax, polydimethylsiloxane (PDMS), sandpapers textured PDMS, grating textured PDMS, and oxygen plasma exposed PDMS, were used as parent substrates. The preparation methods are explained below

Paraffin wax

bulk paraffin wax (Gulfwax, melting point: 128°F) was melted onto a plastic petri dish (60 mm x 15 mm) at an approximate volume of 4 ml. After cooling, the wax was removed and flipped to expose the smooth side facing the plate. Zein was cast on top of the smooth side of the wax.

PDMS

Five-millimeter thick PDMS films were cured by mixing elastomer base and curing agent with the ratio of 10:1 (w/w) (Sylgard 184 Silicone elastomer kit, Dow Corning). The PDMS mixture was poured in a petri dish (60 mm diameter x 15 mm height). It was then degassed for 30 minutes under vacuum and cured at 50 °C on a hot plate for 2 hours.

Sandpaper textured PDMS

PDMS was cast on top of Grade 220 Sandpaper and cured. The PDMS and sandpaper were then separated and the PDMS was cleaned with a series of water-ethanol-water washings. Zein was cast on the sandpaper textured PDMS side (Figure 3.1).

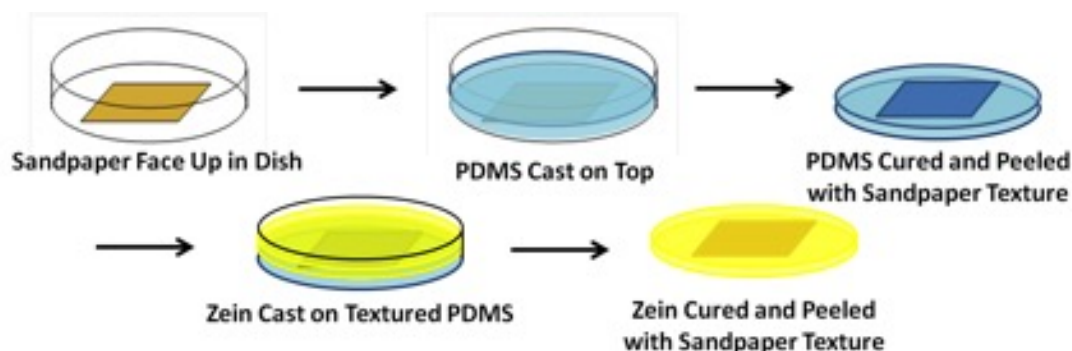


Figure 3.1: Schematic overview of the process of generating sandpaper textured PDMS and zein films

Grating textured PDMS

PDMS was cast on top of 1-dimensional diffraction gratings (1000 lines/mm and 500 lines/mm) (Rainbow Symphony, Reseda, CA, USA). PDMS was then removed and flipped to expose the grating textured side facing the plate. Zein solutions were immediately poured on the grated PDMS films in order to avoid contamination of the surface and allowed to dry.

Oxygen plasma exposed PDMS

The cured PDMS films were exposed to oxygen plasma (O₂ purity: 99.9994%) at 50% of 200-W maximum power (Pico, Diener Electronic, Reading, PA). The duration of the oxygen plasma exposure was 1 minute except where we studied the effect of oxygen plasma treatment duration on water contact angle. In these experiments exposure time was changed between 0.1 to 3 minutes (0.1, 0.2, 0.3,

0.5, 1 and 3). In a second series of experiments, portions of the PDMS film was masked with a comb shaped mask (5-mm spacing and 5-mm gaps) during the oxygen plasma treatment to develop intermittent hydrophilic and hydrophobic regions. The regions masked were not exposed to Oxygen plasma and the rest were exposed to Oxygen plasma. The zein solution was poured onto the PDMS film immediately after the oxygen plasma treatment and dried to form a film in a vacuum desiccator. In this paper the notation O- (O minus) was used when PDMS was not exposed to Oxygen plasma and O+ (O plus) was used when PDMS was exposed to oxygen plasma. In a third set of experiments zein films were also directly exposed to oxygen plasma at different times, after being cured on unexposed PDMS between 0.1 to 3 minutes (0.1, 0.2, 0.3, 0.5, 1 and 3 minutes).

3.3.3 Water contact angle measurements

A volume of 2 μ L droplets of deionized water was dispensed onto the surface of the film that was studied. A photograph of each droplet was taken 30 seconds after contact with the surface using the VCA Optima contact angle analyzer (AST products, Billerica, MA) and its software was used to measure the stable contact angle at the water zein film interface. Water contact angle measurements were conducted in triplicate for both the parent substrates described above and the zein surface (both on air side and contact side).

3.3.4 Optical absorbance measurement

Squares of zein films (1 cm x 1 cm) with constant thickness from regions in contact with Oxygen plasma-treated PDMS film and from regions in contact with Oxygen plasma-untreated PDMS films were placed inside individual wells of a 96-well plate. The optical absorbance of the zein films was measured in triplicate for three different samples at 450 nm, 570 nm, and 630 nm using an absorbance micro-plate reader (BioTek Synergy HT, BioTek, USA).

3.3.5 Raman spectroscopy measurements

Raman spectra of PDMS films were recorded with a Thermo-Scientific DXR Dispersive Raman microscope with a 532 nm laser. A 10 mW laser with 1800 lines/mm grating was used and the exposure time was 1 second for 30 times. The average of the 30 Raman spectra on a given sample are being reported for each measurement. PDMS films were removed from dried zein films right before taking Raman spectroscopy measurements. PDMS (O-) and one minute oxygen plasma exposed PDMS (O+) were used for these experiments. Zein films that were cast and dried on these PDMS was prepared as explained in section 2.1 with a 1:1 zein: oleic ratio.

3.3.6 Atomic force microscopy

Tapping mode AFM (Asylum Research MFP-3D) measurements were performed for 2 μm x 2 μm area on the surface of (10 mm x 10 mm) zein films. The surface roughness (rms value) was calculated by averaging the point surface roughness over the entirety of the surface images. Force curves were obtained in contact mode and the adhesion map was obtained with the help of Igor software on the AFM equipment.

3.3.7 Statistical analysis

Statistical analysis was done by using the Minitab Release 17 software. Two-way regression analysis of variance (ANOVA) was applied to see the differences between both the substrate (pdms vs oxygen plasma exposed pdms) and oleic acid content for water contact angle measurements. One-way ANOVA was applied for analysis for one parameter. Difference between each sample was tested through the Tukey pairwise comparison method. A confidence interval of 95% was used for tests.

3.4 Results and discussion

3.4.1 Effect of oxygen plasma on surface properties of PDMS

PDMS has hydrophobic properties, with a contact angle around 110 degrees. Oxygen plasma exposure of PDMS is an effective treatment to obtain more hydrophilic PDMS surfaces (Owen and Smith, 1994); however this change is only temporary (Bodas and Khan-Malek, 2007; Owen and Smith, 1994; Hillborg and Gedde, 1999; Eddington et al., 2006). PDMS is capable of considerable self hydrophobic recovery in an hour and full recovery after 24 hours due to the low molecular weight chains' migration from bulk to the surface (Owen and Smith, 1994; Hillborg and Gedde, 1999; Eddington et al., 2006). For this reason, in all the experiments conducted zein solution was cast on PDMS as soon as possible (within 1-2 minutes). This showed that PDMS became more hydrophilic by having Si-OH and/or Si-O groups as a result of oxygen plasma treatment consistent with the literature (Bodas and Khan-Malek, 2007).

Raman spectroscopy was conducted on PDMS right after it was separated from the zein film. Raman spectroscopy measurements done on PDMS O- and O+ in order to observe the change in molecular groups are shown in Figure 3.2 and the assigned characteristic peaks are listed in Table 3.1. It was observed that the peaks associated with hydrophilic groups such as Si-OH bending at 557 cm^{-1} , Si-OH symmetric stretching at 955 cm^{-1} and Si-O stretching at 1090 cm^{-1} exist predominantly at PDMS O+, whereas they are non-existent or comparatively smaller for PDMS O- spectra. Furthermore, the intensity of the peaks for Si-CH₃ bond such as in 858 and 1415 cm^{-1} was higher for PDMS O- compared to PDMS O+.

Clearly the enhanced engineered hydrophilic surface characteristic of PDMS were conserved during the zein film formation as the Raman spectra were measured right after the zein films were peeled off. The decrease in water contact angle of PDMS surface from 80 to 50 degrees (Figure 3.3) confirmed this re-

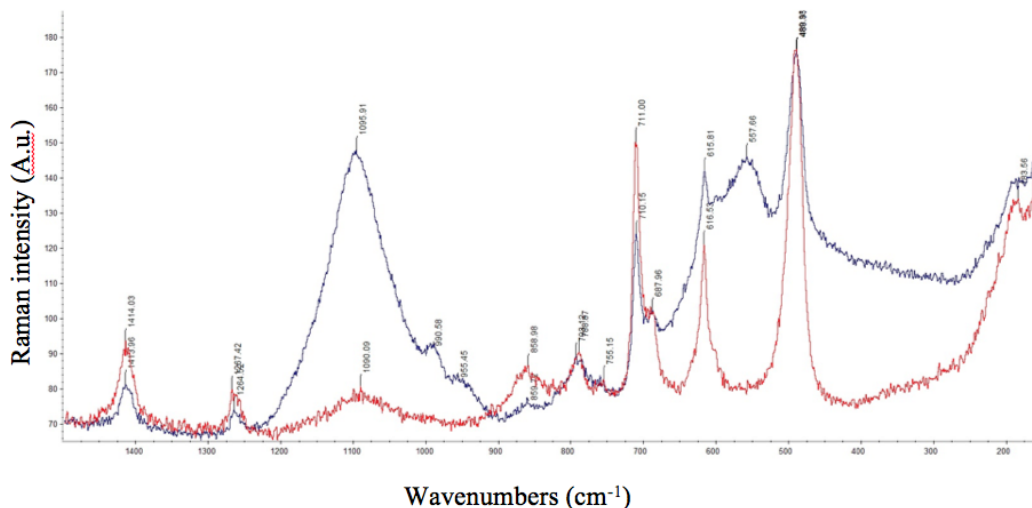


Figure 3.2: Raman spectra of PDMS O+ (blue) and PDMS O- (red) (A.u.: Arbitrary units)

Table 3.1: Peak assignments for Raman signature of PDMS films

Peak wavenumber (cm-1)	Assigned chemical group	Reference
488	Si-O-Si rock	(Aguiar et al., 2009)
557	Si-OH bending	(Oh et al., 2003)
858	Si-CH3 stretching	(Oh et al., 2003)
955	Si-OH sym. stretching	(Oh et al., 2003)
1090	Si-O stretching	(McKeown, 2005)
1269	Si-CH3 sym. bending	(Oh et al., 2003)
1415	Si-CH3 asym. stretching	(Oh et al., 2003)

sult. In contrast, when the Raman measurements were conducted a day after zein films were peeled off, all the engineered hydrophilicity disappeared and there was no difference between O+ vs O- spectra of PDMS due to the reversibility of its surface hydrophilicity (data not shown).

3.4.2 Effect of oxygen plasma exposed PDMS on the hydrophilicity of zein film surfaces

Zein is an amphiphilic protein with a hydrophathy value around 60. The hydrophilicity of the zein film surface changes depending on the way it self assembles. There are two different self-assembly processes on two different surfaces, first the self-assembly at the contact side surface with the parent substrate second, the self-assembly, on the side which is exposed to air. Figure 3.3 shows the difference between water contact angles (WCA) for 1) PDMS alone 2) zein on the contact side with PDMS and 3) zein on the air side for both PDMS O+ vs PDMS O-. Zein films that were in contact with PDMS showed hydrophilicity increase between PDMS O+ vs PDMS O-. WCA decreased from 55 degrees (O-) to 20 degrees (O+) when the zein surface was in contact with PDMS O+. This sharp drop in the WCA of the zein film happens very fast between 6 and 12 seconds of PDMS Oxygen Plasma treatment (Figure 3.3, Left) and was preserved for over a year. However, for the zein film on the air side, WCA remained unchanged (55 degrees (O-) and 50 degrees (O+)) (Figure 3.3, Right).

Zein is an amphiphilic protein with roughly an equal ratio of hydrophilic and hydrophobic amino acids. This gives it unique self-assembly properties depending on the surface that it is being cast on even though it has more hydrophobic characteristics, evident by its hydrophathy value around 60. The hydrophilicity of the zein film surface changes depending on the way it self assembles. There are two different self-assembly processes at two different surfaces as a result of the casting method. First the self-assembly at the contact side surface with the parent substrate. Second, the self-assembly, on the side which is exposed to air. Figure 3.3 shows the difference between water contact angles (WCA) for 1) PDMS alone 2) zein on the contact side with PDMS and 3) zein on the air side for both PDMS O+ vs O- cases. Zein films that were in contact with PDMS showed hydrophilicity increase between PDMS O+ vs O-. WCA decreased from 55 degrees (O-) to 20 degrees (O+) when the zein surface was in contact with the Oxygen plasma treated

PDMS. This sharp drop in the WCA of the zein film happens very fast between 0.1 and 0.2 minute of PDMS Oxygen Plasma treatment (Figure 3.3). However, for the surface of the zein film on the air side, WCA remained unchanged (55 degrees (O-) and 50 degrees (O+) (Figure 3.3).

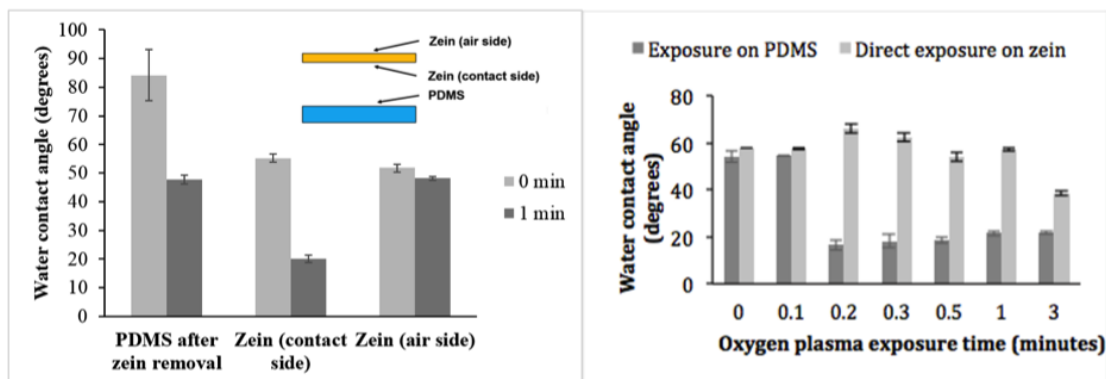


Figure 3.3: Left: Comparison of water contact angle of the surface of PDMS, zein (contact side) and zein (air side). Light grey is O- (O min) and dark grey is O+ (1 min exposure to oxygen plasma). The inset shows the surfaces on which the water contact angle was measured. Right: Water contact angle measurement on the surface of zein film that was in contact with PDMS O+ vs direct exposure on zein films after film formation. Error bars represent standard deviation (n=3).

As shown on the right side of Figure 3.3, direct exposure of zein films to oxygen plasma was only partially effective and not as effective as casting them onto PDMS O+. The water contact angle of zein films dropped from 57 degrees to only 38 degrees after oxygen plasma exposure of 3 minutes, whereas 12 seconds exposure on PDMS was sufficient to obtain a zein film with a considerably more hydrophilic surface (20 degrees WCA). Longer duration of oxygen plasma exposure on PDMS did not cause any significant difference in the contact angle based on the Tukey pairwise comparisons after ANOVA. For direct exposure, WCA was only significantly different for 3 min exposure (based on comparison with Tukey method.)

The schematic diagram in Figure 3.4 shows the procedure that was followed for direct comparison of hydrophilic and hydrophobic regions of zein films as well as their optical properties resulting from the use of the comb like mask.

Regions of zein film that were in contact with the PDMS O+ film showed lower water contact angle, and were more hydrophilic, (20 degrees), in contrast, to the masked regions of PDMS film showed higher water contact angle (55 degrees) consistent with the results of earlier experiments we conducted. Hydrophobic regions appeared visually more transparent than the hydrophilic regions and were confirmed through optical absorbance measurement of the two regions on zein film at 450 nm, 570 nm, and 630 nm (Figure 3.5). The difference in the optical absorbance of the two regions might be due to the vertical organization of zein bodies because of the increased affinity of the hydrophilic region for water and the surface swelling of zein making the film somewhat thicker and more opaque.

Matsushima and others proposed a well accepted model of zein molecule organization as closely packed helix coils with the polar (hydrophilic) amino acid residues oriented outward and non-polar (hydrophobic) amino acid residues located in the interior of the helix (Matsushima et al., 1997). The outcome of this helical conformation is that the surface of zein films can be engineered to exhibit either hydrophobic or hydrophilic property. In earlier studies the self-assembly property of zein was controlled by changing the pH of the solvent using acetic acid as the solvent (Shi et al., 2009) and concentration of solvent (Wang et al., 2004b). In this study, we observed that this self-assembly can be achieved by simply casting zein on PDMS, either exposed to Oxygen plasma or not. Oxygen plasma induced hydrophilicity to PDMS which was transferred to zein as a result of contact of zein with PDMS. This can be achieved in a patterned matter by using the mask method. In fact, this treatment is compatible with the previously reported method of three-dimensional feature replication where micro and nano features have been successfully transferred to zein from PDMS with great fidelity (Luecha et al., 2011). Both treatments can be simultaneously carried out using the same PDMS film with Oxygen plasma treatment to imprint three-dimensional features with the additional ability to modify the hydrophilicity/hydrophobicity of their surface.

Since the water contact angle change only happens significantly on the surface

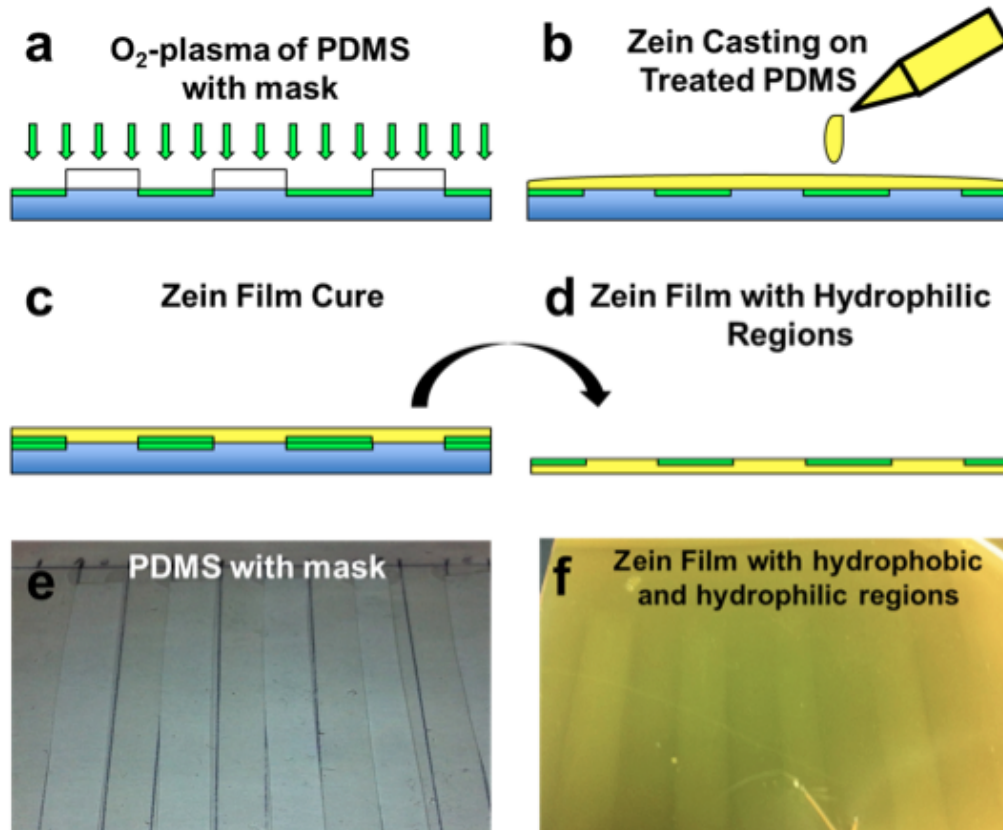


Figure 3.4: (a) A polydimethylsiloxane (PDMS) film exposed to O₂-plasma for 1 min; there is a mask placed to selectively treat the surface of the PDMS film. (b) Immediately after O₂-plasma treatment, the mask was removed and zein solution was cast over the PDMS film and (c) zein film cured in a vacuum desiccator, (d) Once it is cured, the zein film is separated from the PDMS film, (e) Visual comparison of PDMS film with mask and (f) Cured zein film shows replication of corresponding hydrophobic and hydrophilic regions on the zein film.

that is in contact with the PDMS, but not as much on the air side which is not in contact with PDMS, these findings suggest that zein film surface has the ability to organize itself to mimic the surface that it is in contact with. This is consistent with prior studies (Yoshino et al., 2002) where zein films with different water contact angles on the air-side and contact side of the films were also obtained when zein was brought into contact with a polyethylene (PE) sheet. The water contact angle of unplasticized zein films ranged between 20 and 60 degrees for the air side, whereas it was between 40 and 75 degrees on the PE contact side depending on

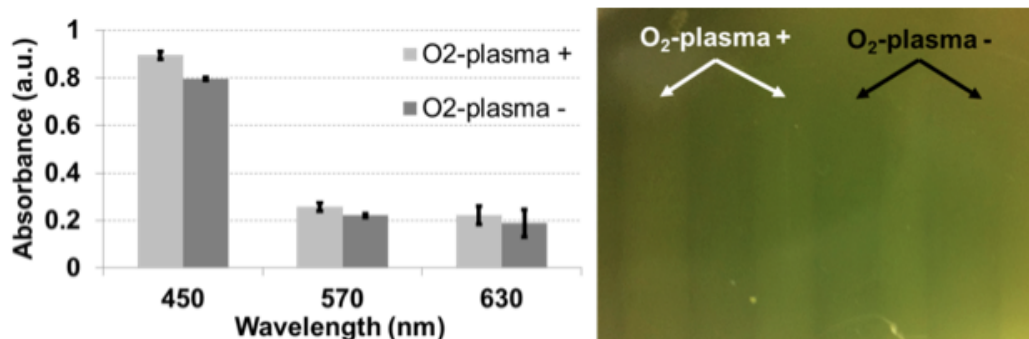


Figure 3.5: Optical absorbance measurement of hydrophilic and hydrophobic regions on zein film that was cast on treated PDMS film.

zein concentration, drying temperature and drying relative humidity. This application promoted hydrophobic surface properties on the contact side in contrast to our work with Oxygen plasma exposed PDMS which promoted hydrophilic surface properties. Furthermore, in our study it was possible to obtain intermittent hydrophilic/hydrophobic regions on the zein films.

3.4.3 Effect of surface roughness on hydrophilicity of zein film surfaces

Smooth PDMS, sandpaper textured PDMS, and paraffin wax were used to study the effect of macroscopic differences on the water affinity of zein films. As can be seen from microscopy images in Figure 3.6, the texture and topography of the films were different for these samples on a macroscopic scale. However, WCA angles of zein films were not different as a result of the roughness change at this scale. Figure 3.7 shows the comparison between the water contact angles of zein films and the materials that they were cast on. WCA angles of zein films were not different as a result of the roughness change at this scale. It was found that there was no significant difference between zein films that were cast on these three different surfaces ($p > 0.05$) even though there was a significant difference between the WCA of parent substrates, i.e. wax, sandpaper textured PDMS and PDMS

($p < 0.05$). This shows that the chemistry during self-assembly of zein on PDMS is more important than the texture of the surface in terms of affecting surface WCA for zein. The degree of hydrophilicity achieved by casting zein on PDMS is far superior compared to surface textures engineered for different degrees of capillary action.

The degree of hydrophilicity achieved by casting on PDMS is far superior compared to the microscopic surface textures engineered that might attract water because of capillary action and the water contact angles are approximately the same in all of the textured surfaces.

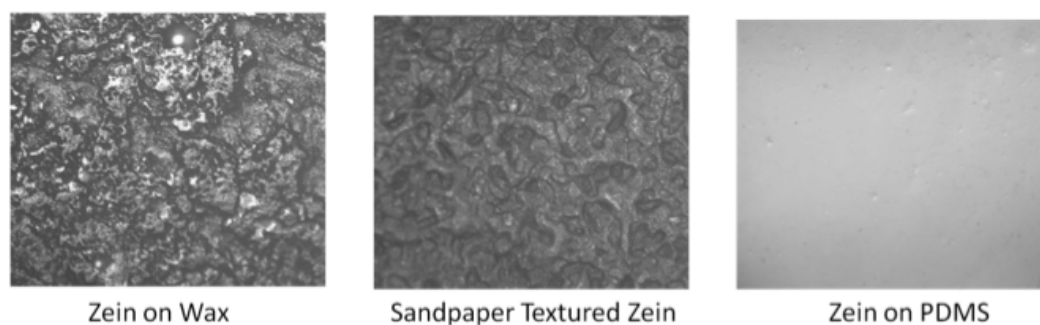


Figure 3.6: Microscopy images of zein surface cast on wax, sandpaper textured PDMS and smooth PDMS.

Zein films, were also cast on PDMS O+ and PDMS O- substrates, both with one-dimensional line patterns with periodicity of 1000 lines 1/mm and 500 lines 1/mm, 1 μm -wide and 2 μm -wide lines respectively. The line features were successfully transferred onto the zein film from the PDMS substrate due to the accurate replication ability of zein casting. The line features can be observed through diffraction patterns generated by optical illumination. The films that were cast on the PDMS O+ again retained increased hydrophilicity compared to the untreated zein films with corresponding water contact angles of 26 degrees versus 57 degrees respectively. These results indicate once more that a well-defined fine texture of the parent substrate has an insignificant effect on the hydrophobicity of zein, compared to the self-assembly promoted by the surface chemistry of the

material it is cast on.

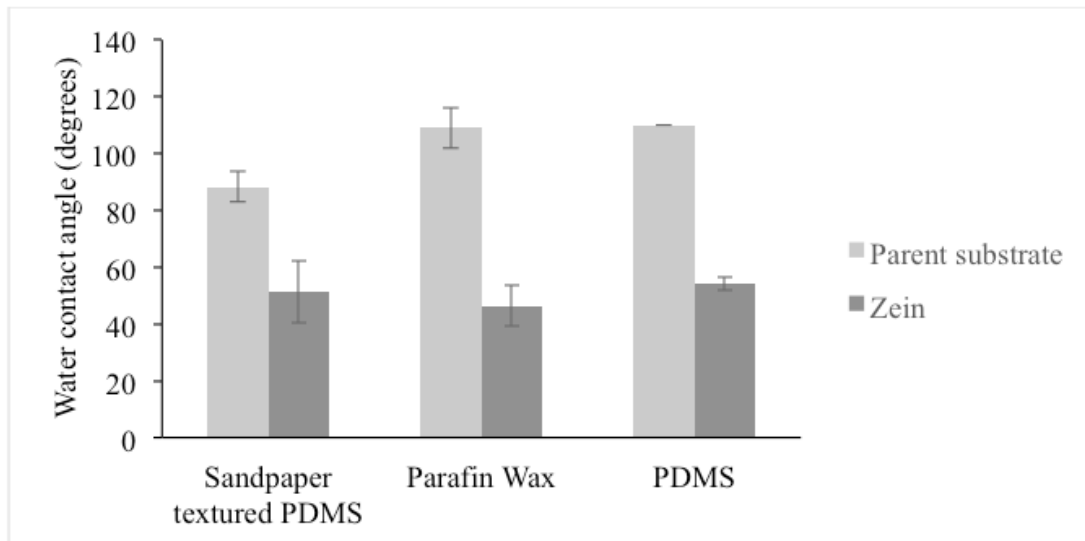


Figure 3.7: Graphical comparison of zein contact angles compared to the surface it was cast on. Error bars represent standard deviation (n=4).

3.4.4 Effect of oleic acid content on the self-assembly of zein films

The difference in water contact angles between O+ and O- increased as the oleic acid content increased as illustrated in Figure 3.8 Right. When there was no oleic acid, there is a difference between the surface cast on PDMS O+ vs O-; however this effect was more prominent with zein to oleic acid of 1:1 ratio (Figure 3.8 Left). ANOVA combined with Tukey tests showed that there was a significant difference among water contact angles between different oleic acid contents ($p < 0.05$). There was significant difference between O+ and O- surfaces as well ($p < 0.05$). Oleic acid is an amphiphilic molecule with a hydrophobic methyl end a hydrophilic carboxylic head. If the surface is hydrophilic then oleic acid migrated to the contact surface and exposed the carboxylic head; in contrast if the surface is hydrophobic then it exposed the methyl end. When there is more oleic acid there is an increase in the amount of hydrophilic head groups exposed at the interface and the difference between the hydrophilic WCA and the hydrophobic WCA increases as shown in Figure 3.8 Right. This further indicates that the

carboxylic groups of oleic acid are preferentially oriented towards the interface contributing to increasingly pronounced hydrophilic character of zein as a result of coming into contact with Oxygen plasma treated PDMS. We conclude that oleic acid plays a unique role in the self assembly of zein cast on PDMS O+ or O-.

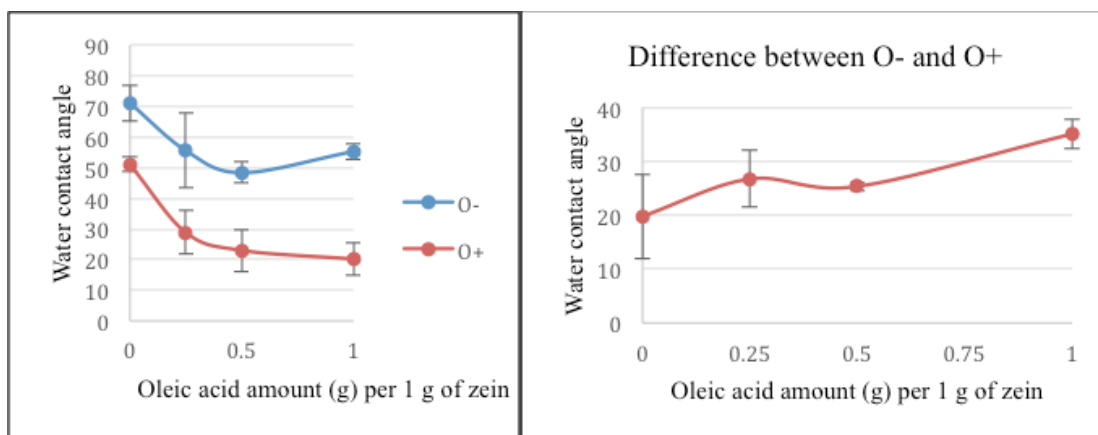


Figure 3.8: Water contact angle of zein films (contact side) vs different oleic acid ratios for O+ vs O- (Left). The difference between water contact angles of O- vs O+ plotted against zein:OA ratio (Right). Error bars represent standard deviation for different sets of experiments (n=3), within each experiment WCA was calculated by averaging data points on the same sample (n=4)

3.4.5 AFM analysis of zein films

In order to understand the effect of the self-assembly as a result of the PDMS treatment and the increase in oleic acid content on surface topography, AFM measurements were also conducted. AFM results showed that films that were cast on PDMS O+ were rougher than those that were cast on PDMS O-, for all oleic acid contents as can be seen in Figure 3.9. The roughness value measured as rms (root mean square) was 4.5 nm for zein films with 1:1 ratio cast on PDMS treated with oxygen plasma, whereas it was 0.6 nm for the zein films with same oleic acid ratio but cast on oxygen plasma untreated PDMS. Our findings are consistent with earlier studies where zein forms rougher surfaces when cast on hydrophilic surfaces and exhibits more hydrophilic properties compared to hydrophobic ones

(Shi et al., 2009; Wang et al., 2004a,b; Subramanian and Sampath, 2007b). It was proposed that the asymmetrical structure of zein having hydrophilic and hydrophobic ends contributes to this nanoscale roughness difference as zein uses different sides to either adsorb to the surface or expose itself to air. The packing of helix coils Matsushima et al. (1997) parallel to the surface of the substrate were shown to produce a higher nano-scale surface roughness.

Moreover, we observed that the difference between the rms values between O+ and O-decreased as the oleic acid content decreased. The difference was 3.7 nm for zein films with 1:1 ratio, 0.45 nm for 1:0.5 ratio and 0.19 nm for 1:0.25 oleic acid content films. This suggests that, oleic acid-zein orientation changes with the amount of oleic acid as well as the parent substrate.

Furthermore, a force curve analysis was conducted on the zein films that had an intermittent mask, in order to understand the differences between two regions. A relatively hydrophilic Silicon tip was used with a contact a water contact angle of 38 degrees (Arkles, 2006). Figure 3.10 shows the AFM cantilever positioned on top of the edge and able to scan on both sides (O+ and O-). In this figure, the right side was hydrophilic zein, which was zein film cast on oxygen plasma exposed PDMS. The left side was hydrophobic zein, which was cast on regular PDMS. The topography difference (hydrophilic part was rougher) was analyzed at the nano-scale in Figure 3.9 through AFM images. In Figure 3.10, the force mapping results show both height and adhesion profile. The adhesion profile gives new information, which was not apparent through the nanoscale topography images. In the patterns reported in Figure 3.10 the light grey regions correspond to larger forces and as the adhesion force becomes smaller the patterns become darker. There is a characteristic pattern between the hydrophilic and hydrophobic parts of this figure with the hydrophilic parts showing relatively light grey (higher adhesion) profiles while the hydrophobic part shows relatively darker patterns with an intersection region separating the two different adhesion profiles from each other. This intersection region is not observed in height profiles suggesting that the force profiles are more sensitive to small changes when compared to the

height (topography) profiles. This proves that different force values are obtained due to the surface hydrophilicity/hydrophobicity difference on the surfaces and offer additional information, which is largely complementary but more sensitive than the height profiles. The consistency between all different type measurements offer irrevocable proof of the impact of the Oxygen plasma treatment coupled with changing oleic acid content in zein films on conformational changes and organization of zein films.

When the values were compared for two different regions (hydrophilic) and (hydrophobic). It was found that the force values ranged between 5.8 nN and 11 nN for hydrophilic region, whereas they ranged between 5.8 nN and 7 nN for the hydrophobic region. There is more variation (apparent from topography as well) in the hydrophilic region, which is due to the way zein organizes itself in the presence of oleic acid. When there is more oleic acid the fact that the carboxylic groups bind to the hydrophilic amino acids could result in a network which favors protein and oleic acid layers partly alternating between each other where the matrix is held together with the ampiphilic emulsifier. On the other hand, hydrophobic region is formed by a singular layer, which is more uniform with either the methyl ends of oleic acid or the hydrophobic region of zein protein.

3.5 Conclusion

In conclusion, here we demonstrated a method to fabricate zein films with a preferred surface hydrophobicity/hydrophilicity. The effect of surface roughness, either on macro or micro scale was found not to be significant. The hydrophobicity/hydrophilicity of the surface is found to be more important and effective to induce self-assembly of the zein molecules. PDMS and Oxygen plasma treated PDMS enabled control of zein films' water contact angles. Oleic acid also has a key role in the self-assembly process. AFM analysis demonstrated that hydrophilic zein films were rougher than hydrophobic ones consistent with previous findings. The simultaneous replication of three-dimensional features and sur-

face property can be accomplished on a large surface area in one step offering nanomanufacturing opportunities. Simultaneous replication of three-dimensional patterns and surface property is possible due to the use of PDMS to replicate patterns through soft lithography and also to induce hydrophilicity via O₂-plasma treatment. Also when variable hydrophilic/hydrophobic properties are needed a shadow mask with desired patterns can be used to have PDMS with intermittent exposure to O₂-plasma treatment, thereby inducing a distribution of hydrophilicity/hydrophobicity. This processing technique offers a great deal of flexibility for the fabrication of biodegradable protective coatings or thin films, which can be used for microfluidic and/or tissue engineering applications.

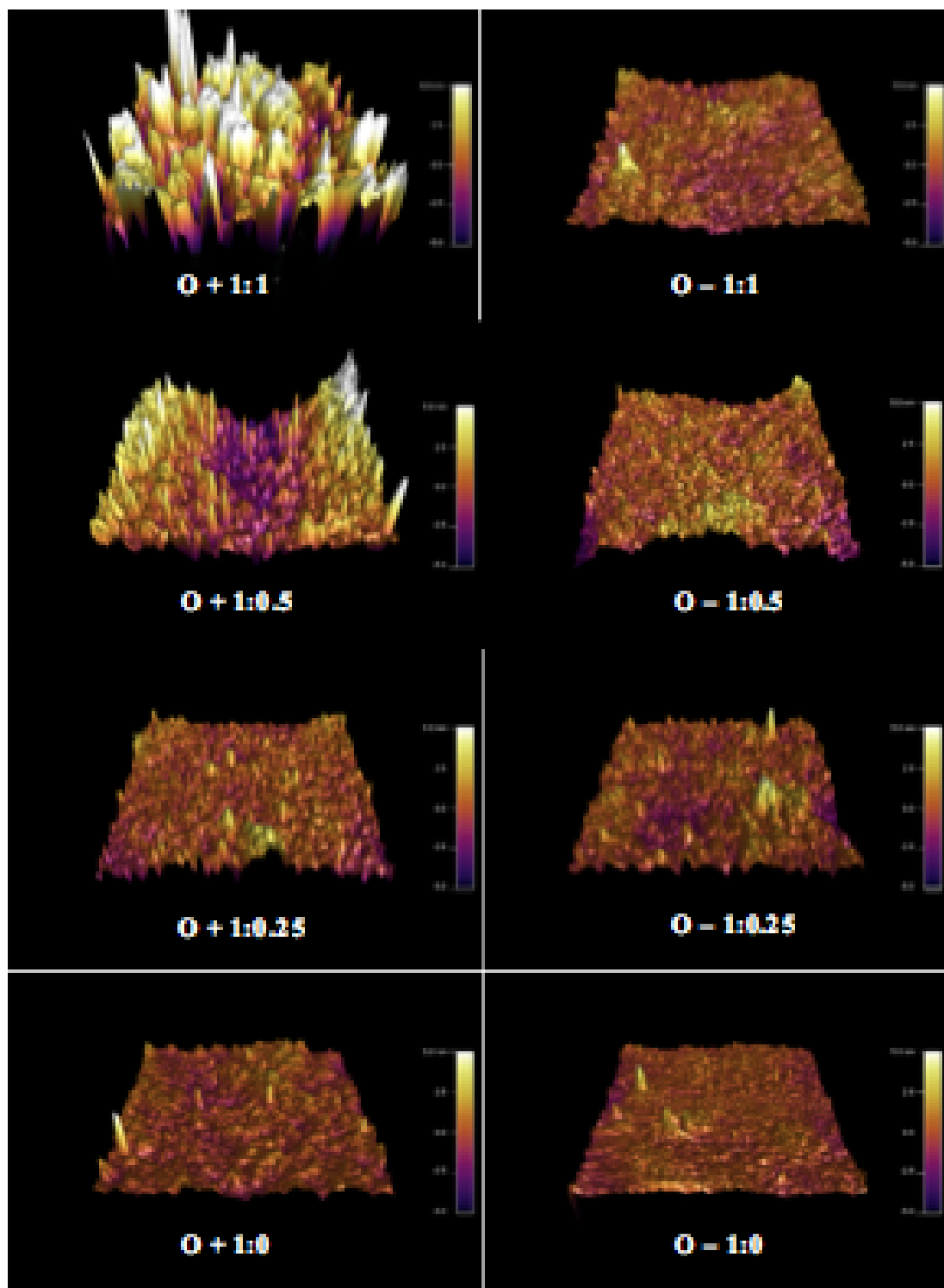


Figure 3.9: AFM images of zein films. O+: zein was cast on PDMS exposed to oxygen plasma, whereas O-: zein was cast on PDMS. Numbers represent the zein: oleic acid ratio. Scale bars range from 5 nm (yellow) and -5 nm (blue).

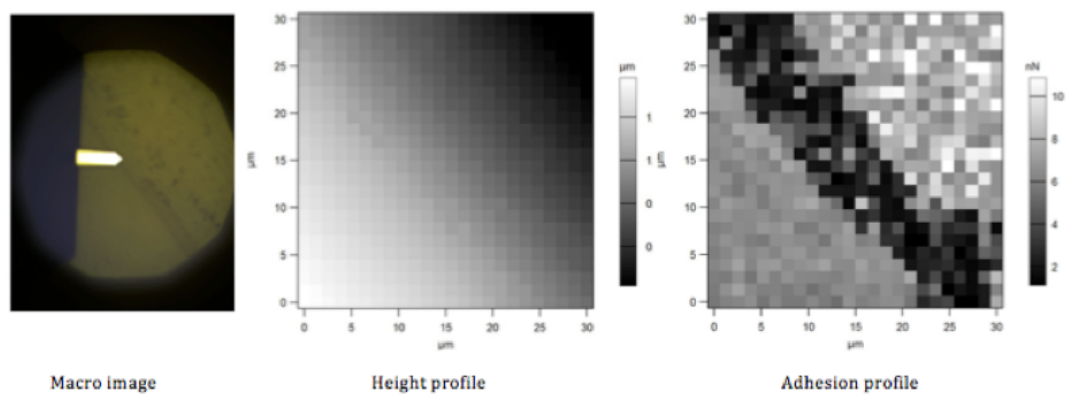


Figure 3.10: Atomic Force microscopy images. (Left) macro image showing the location of edge between masked and unmasked area in zein films (Middle) height profile of this region (Right) Adhesion profile obtained by mapping of force curves.

CHAPTER 4

FABRICATION OF A NANOPHOTONIC PLATFORM ON ZEIN FOR SURFACE ENHANCED RAMAN SPECTROSCOPY¹

4.1 Abstract

In this paper, we report a method to manufacture green nanophotonic sensors made out of corn protein zein. The method is direct transfer of three-dimensional metallic (gold and silver) nano structures onto biodegradable zein films. We have transferred both micro scale and nano-scale structures with several geometries. Inverted and positive pyramid structures, with 2 μm by 2 μm square base, nanopores and nanopillars with an approximately 250 nm diameter were successfully transferred onto zein along with 200 nm and 80 nm thick gold layer onto pyramids and nanopillars/pores respectively. Rhodamine 6G was used as a model molecule for surface enhanced Raman spectroscopy measurements and was found that the inverted pyramid gold zein sensors had the highest enhancement factor, compared to the other zein-sensors. The novel zein sensor platform we developed has the potential to serve as a biodegradable SERS platform for applications in agricultural, medical and food analysis purposes.

¹This work is currently under review as P. G. Gezer, A. Hsiao, G. L. Liu, J. L. Kokini “Simultaneous transfer of noble metals and three-dimensional micro and nano-patterns onto zein for fabrication of nanophotonic platforms” *Journal of Material Science*.

4.2 Introduction

The rapid development of biosensors and lab-on-a-chip technologies promises to make available routine, widespread analyses useful in healthcare, environmental monitoring, agricultural and food quality and toxicology assessment. This may be possible with cheap, miniature platforms combined with portable detection systems. One of the key concerns of these new miniature technologies is the disposability and generation of environmental pollutants, especially for agricultural and food applications. For these reasons interest in biodegradable and biocompatible materials has recently increased (Domachuk et al., 2010). Some examples of biodegradable materials include silk (Tao et al., 2012), polycaprolactone (Van der Schueren et al., 2013), amyloid fibrils (Li et al., 2012) and paper-based analytical devices (Martinez et al., 2009).

In this study the focus is imprinting nanophotonics structures on biodegradable materials by using the science and technological tools offered by nanophotonics. Nanophotonics deals with the behavior and interactions of light with matter and structures at the nano-scale. This research is advancing the state of the art by showing the feasibility of using biodegradable natural materials in biosensor lab-on-a-chip platforms.

One of the ways to make use of nanophotonics in sensors is by using regular and reproducible nano-scaled structures coated with noble metal surfaces, which may result in localized surface plasmon (LSP) effect. Localized surface plasmons are an oscillating electron cloud in the boundaries of a high-electron density metal, which arise from the interaction of the metal with an electromagnetic field at carefully controlled conditions. LSPs cause an enhancement of the electromagnetic field around these nano-scale metal coated nanostructures and are utilized in developments of biosensors, two major categories being Surface Plasmon Resonance (SPR) biosensors and Surface Enhanced Raman Spectroscopy (SERS) biosensors (Hutter and Fendler, 2004). Raman spectroscopy gives highly specific information at the molecular level, and enhancement of the Raman signal occurs by using

nanophotonic structures coated with noble metals. The signal is then enhanced up to several, sometimes up to ten orders of magnitude. Raman signal enhancement occurs with both nanoparticles as well as nano-arrayed structures. In many cases, the latter is preferred for the sake of signal uniformity and reproducibility. SERS have numerous potential applications in biomedical, pharmaceutical, forensic, environmental, art, archeological sciences and in food science and food analysis in detection of food pathogens, contaminants and adulterants (Craig et al., 2013).

The conventional support material for imprinting nano-shape metallic structures generally is based on silicon or other plastic materials, which are non-biodegradable. In this study, we propose to utilize corn zein a biodegradable protein polymer, to fabricate a biodegradable nanophotonic platform that can be used for SERS applications to engineer sensors to detect and measure important food analytes especially allergens. Zein has an amphiphilic nature, which makes it tunable into different properties, such as water vapor permeability, surface topography and surface water affinity. It was shown to possess self-assembly properties owing to its amphiphilic nature. Both hydrophilic and hydrophobic surface tuning can be obtained, while bulk properties are preserved, which makes it desirable and sometimes preferable in many applications such as packaging, encapsulation, and pharmaceutical coatings, adhesive and biodegradable films (Corradini et al., 2014). Recently, zein has attracted attention as a potential material for cell and tissue engineering (Dong et al., 2004). It has well-established film forming abilities whose mechanical, thermal and surface properties can be tuned depending on the desired end-goal. It is able to form free-standing films by both extrusion and casting techniques. It was combined with several plasticizers, cross-linkers and nanoclays to have different mechanical and surface properties. It has also been shown to replicate micro-structures such as wells, pores and microfluidic channels by solvent-casting technique (Altunakar et al., 2010). While replication of micro- and nano-scale features on biopolymers are possible, metallized three-dimensional nanostructures on protein-based films are not achievable using thermal or electron-beam evaporation due to low glass-transition temperature of

the polymers, at or above which surface features manufactured can be distorted or destroyed (Vroman and Tighzert, 2009).

In this research, we present a technique to fabricate a biodegradable zein nanophotonic platform, via direct transfer of three-dimensional (3D) metallic structures onto zein to be utilized in SERS applications. Four different types of metallic nano-structures; positive and inverted pyramids, nanopillars and nanopores were successfully transferred onto zein. Three of them were compared for their Raman signal enhancement capability of a model molecule, Rhodamine 6G.

4.3 Materials and Methods

Fabrication of the sensor included three steps; production of polymer molds with nanopatterns, noble metal deposition and 3-dimensional transfer of the patterns along with metal onto zein. Each of these steps is described below in detail, followed by the mechanical (ASTM D3359 adhesion test) and optical (Scanning electron microscopy and Raman spectroscopy) characterization techniques that were used in this study.

4.3.1 Fabrication of polymer molds with nanophotonic structures

Polyethylene tetrphthalate (PET) and polydimethylsiloxane (PDMS) were used as polymer mold materials for transfer of nanophotonic patterns, using two methods. The nanophotonic patterned substrates were developed previously (Xu et al., 2011; Gartia et al., 2010). The first method was replica-molding used with PET which was done in Dr. Liu's lab. A small volume that covers the surface with the nanophotonic patterns of UV-curable polymer (UVcP) (Norland Products Inc., Cranbury, NJ or Gelest Inc., Morrisville,PA) was dropped onto the surface of the master and a PET sheet was placed on top of the UV-curable polymer. After the placement of the PET sheet a Teflon roller was used to cause the polymer to flow and conform to the inverted pyramids on the surface of the master The UV-

curable polymer was then cured 60 seconds using an ultraviolet lamp (10^5 mW cm^{-2}) and adhered to the PET sheet. The PET sheet was then manually separated from the master mold. Soft lithography was the second replication method and was used for PDMS. A PDMS mixture was prepared using a 10:1 v/v ratio of base to curing agent at a volume to fill a petri dish to half thickness. This ratio allows for an organometallic crosslinking reaction to occur between siloxane base vinyl groups with the cross-linking curing agent with at least 3 silicon hydride bonds being formed (Dow Corning, Midland, MI) and cast on the PET molds with the nanophotonic patterns, and allowed to cure overnight. After curing, the PDMS polymer mold was separated from the PET. Detailed explanations of the development of these patterns can be found in Chapter 2. As a summary, molds with pyramid patterns were prepared by replica-molding method as also explained above and both negative and positive pyramids obtained. For the nanopillars, ion milling deep reactive ion etching technique was used to obtain pillar structures, which are much finer in size.

The nanophotonic patterns of the master were either pyramid or pillar structures. Pyramid patterns had a base of $2\ \mu\text{m}$ by $2\ \mu\text{m}$ with a periodicity of $2\ \mu\text{m}$ (from center to center), and height of $2.1\ \mu\text{m}$, whereas the pillar structures were $150\ \text{nm}$ in diameter, $500\ \text{nm}$ in height and $350\ \text{nm}$ apart (Xu et al., 2011; Gartia et al., 2010).

Electron beam evaporator (Temescal, Livermore, CA) which enabled deposition of gold or silver at the rate of $1/\text{s}$ was used to deposit noble metals onto polymer molds. Pyramid molds were covered with 200-nanometer thick noble metal (gold or silver), whereas nanopillars or pores were covered with 80-nanometer thick gold. The thickness of the metal coating ($200\ \text{nm}$ for pyramids and $80\ \text{nm}$ for nanopillars/pores) was based on the original SERS-active substrates, which were used as templates (without coating) in this study. The original molds utilized as master in this study are shown in Figure 4.1.

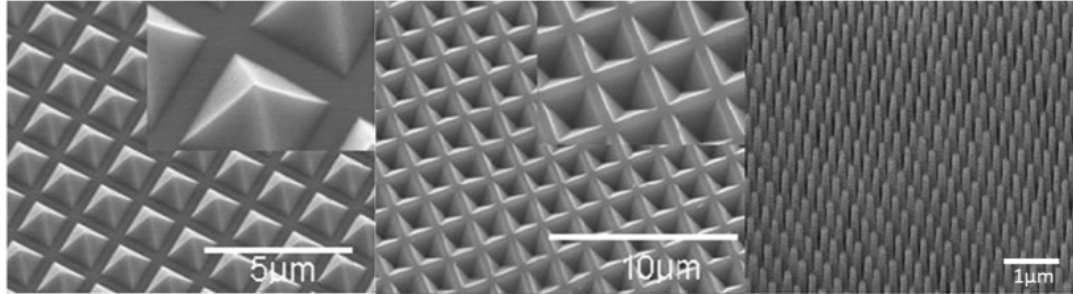


Figure 4.1: Scanning electron microscopy images of nanophotonic master molds: Positive pyramids (Left), Negative pyramids (Middle) and Nanopillars (Right)(Xu et al., 2011; Gartia et al., 2010)

4.3.2 Fabrication of protein films with nanophotonic structures

Zein (Sigma Aldrich, Milwaukee, WI) solution was prepared by dissolving zein powder in 75% Ethanol (1 g of zein in 5 mL of ethanol) together with oleic acid (Sigma Aldrich, Milwaukee, WI) and an emulsifier, monoglyceride (Caravan Ingredients, Lenexa, KS) at a ratio of 1 g zein: 1 g oleic acid: 0.05 g emulsifier and mixed at 65 °C for five minutes. The emulsifier was used to bind zein to the oleic acid phase and the mixture is essentially a solid emulsion. It was sonicated for 2 minutes at 245 mW power to remove air bubbles, which was established before for best results with zein film formation (Luecha et al., 2011). The solution was then poured over the polymer molds, at a volume depending on the volume of the petri dish being used, and dried at room temperature in a vacuum desiccator for 24-48 hours. Once solidified, the protein film was removed with a razor blade and lifted directly off the polymer mold. The direct transferability of the noble metal film was assessed by whether or not the cured protein film could be cleanly and easily separated from the polymer mold. The schematic diagram in Figure 4.2 illustrates the procedure.

4.3.3 Characterization of zein films with nanophotonic structures

Surface and cross-section views of the protein film with nanophotonic structures were obtained by scanning electron microscopy (Either Philips XL30 ESEM-FEG,

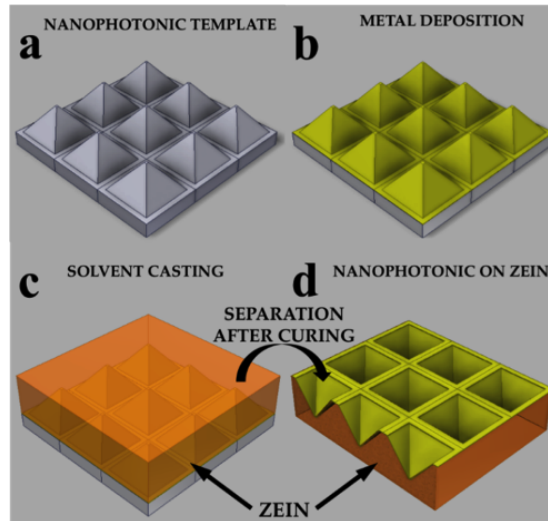
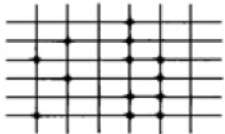
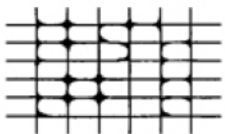
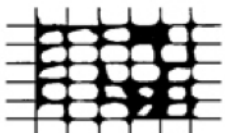
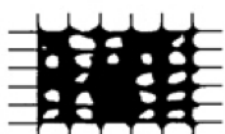


Figure 4.2: Schematic diagram of the direct transfer of three-dimensional metallic nanophotonic structures onto zein, a corn plant-based biopolymer. A template made of either PET or with nanophotonic structures (a) is deposited with 200 nanometers of noble metal using E-Beam Evaporation (b). Zein solution is solvent-casted over the metal-coated template (c), and after fully solidifying; the zein film with three-dimensional metallic nanophotonic structures is separated from the template (d)

or Hitachi S-4700). These experiments were conducted with the following settings: 10 μA and voltage ranging between 5 kV and 15 kV depending on the sample. Normal operation mode and long working distance (in general 12 mm) was used. These are also reported on the SEM images. The cross-section view was obtained by first cutting the film with a sharp razor blade and then smoothing the imaged area with a microtome diamond blade. The adhesion between the metallic layer and the zein films was assessed using the ASTM D3359 test described in detail in Materials and Methods section. For measuring adhesion, a tape (rated at 570 grams per centimeter of adhesion strength) was placed over the metallic layer and left for 90 seconds and then removed back on itself parallel to the surface of the film at constant speed. This was repeated for 3 samples. The experiment focuses on the extent of sticking of the metal onto the tape and the quantitative characterization is done by comparison with the template offered by ASTM D3359 also described in the Materials and Methods section. The decision criteria are

tabulated in Table 4.1.

Table 4.1: ASTM D3359 Adhesion test classification

Classification	Surface of cross-cut areas from which listing has occurred. (Example for six parallel cuts.)	Rate of adhesion
5B	None	The edges of the cuts are completely smooth; none of the squares or the lattice are detached.
4B		Small flakes of coating are detached at intersections; less than 5% of the area is affected.
3B		Small flakes of coating are detached along edges and at intersections of cuts. The area affected is 5 to 15% of the lattice.
2B		The coating has flaked along the edges and at parts of the squares. The affected area is 15 to 35% of the lattice.
1B		The coating has flaked along the edges of cuts in large ribbons and entire squares have detached. The area affected is 35 to 65% of the lattice.
0B	Flaking and detachment in excess of 65%.	

Contact angle measurements were performed with a VCA Optima Surface goniometer (AST products, Billerica, MA) and consisted of dispensing 5 μL of solution (either water or zein in 75% ethanol) on the surface of a film and measuring the angle using the VCA Optima's software of the system. Equipment has a

syringe that can dispense a measured amount of liquid by giving commands. After the droplet touched the surface, we waited for 30 seconds to take measurements for equilibration and standardization of the WCA measurements. The contact angle is calculated with the help of a camera and software of VCA Optima.

The reflectance spectrum of the nanophotonic structures on protein film was measured using an epi-illumination microscope (Carl Zeiss, Thornwood, NY) coupled to a 500-800 nm range spectrometer (Control Development, South Blend, IN). The samples were scanned in this range and their reflectance spectra were measured. The wavelength at which the reflectance spectra underwent a minimum was considered to decide which laser would perform best during Raman spectroscopy.

For Raman spectroscopy, 2 μL of a solution having the target molecule was placed onto the surface of the nanophotonic protein film and dried at room temperature. A model molecule, Rhodamine 6G (R6G) was used to evaluate the signal enhancement of each nanostructured platform compared to normal Raman spectroscopy. Serial dilutions of R6G were prepared ranging from 1 μM to 100 μM . The background signatures of the sensors resulting from the chemistry of the protein were obtained to differentiate the characteristic peaks coming from the R6G from those of the sensor. Dispersive Raman spectroscopy measurements were performed using a commercial Raman spectroscopy equipment (Horiba LabRAM HR) with a 50x objective and 300 lines/mm grating. The acquisition time was a few seconds for all measurements. 10 mM R6G solution was placed on a clean Silicon wafer to serve as a reference material and concentration and measured using the same settings. In order to eliminate the effects of auto fluorescence baseline correction was done by fitting a polynomial to the baseline and subtracting it from the spectra, by LabSpec 5 software, provided by HORIBA Raman microscopy system.

4.4 Results and Discussion

4.4.1 Direct transfer of 3D metallic structures onto zein and mechanical characterization

The first objective of this study was to determine if three-dimensional transfer of metallic nanostructures onto zein by soft lithography method is feasible and results in high fidelity nanostructures on zein surfaces. Three different patterns were chosen as master molds as shown in Figure 4.1, which resulted in 4 different templates (positive pyramids, inverted pyramids, nanopillars and nanopores). Two different noble metals were used, silver and gold, with two different thicknesses 200 nm and 80 nm. The templates used are summarized in Table 4.2.

Table 4.2: List of different fabrication strategies for zein films with nanophotonic structures

PET with UVcP	PDMS	Metal coating	Zein
Inverted pyramids		200 nm gold/silver	Positive pyramids
Positive pyramids		200 nm gold/silver	Inverted pyramids
Inverted pyramids	Positive pyramids	200 nm gold	Inverted pyramids
Positive pyramids	Inverted pyramids	200 nm gold	Positive pyramids
Nanopillars	Nanopores	80 nm gold	Nanopillars
Nanopillars		80 nm gold	Nanopores

First, PET templates with two different UV-curable polymers (UVcP) layers with confidential chemistry not disclosed by the company (Gelest and Norland) were tested. The bulk polymer was PET with the curable polymer used to duplicate the surface nanopatterns. It was found that gold transfer onto zein was successful with UVcP, an acrylate modified silicon polymer from Gelest source. However, it was not possible from the Norland source, which is a photopolymer. In both cases, the bare metal (no nanopatterns) on the PET sheet was perfectly transferred onto zein. Figure 4.3 shows the successful and partly-successful metal transfer from template onto zein films. Figure 4.3a shows that when Norland

UVcP was used, the area having the pyramid patterns did not transfer well onto zein, whereas the rest of the gold was transferred from the PET sheet onto the zein film. Figure 4.3b and c show that the transfer of silver and gold from the Gelest source for UVcP was successful. The area in the dotted square (5 mm x 5 mm) in the figure is where the pyramid patterns are. The reason for the color difference is the reflection of light at different wavelengths in the visible spectrum between 500 - 700 nm due to these patterns.

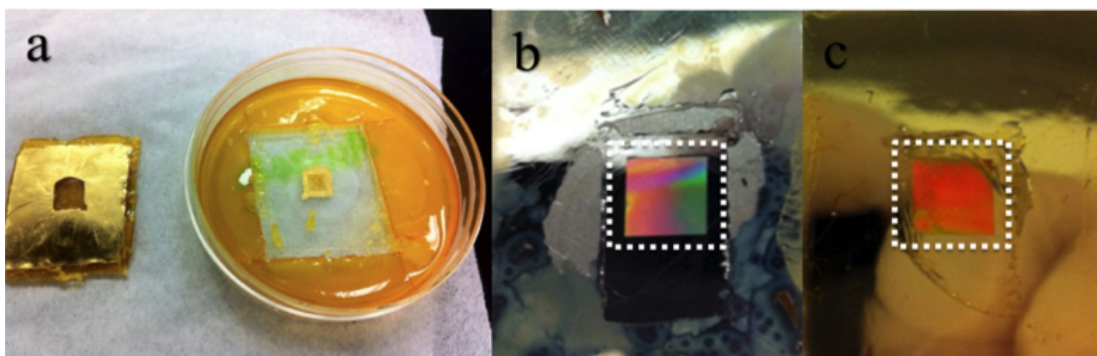


Figure 4.3: The transfer of noble metal onto zein film. Unsuccessful transfer evident by the squared area having the patterns did not transfer onto zein film (on the right) (a), successful transfer of silver (b) and gold (c)

For the ease of handling and use purposes, the patterns were transferred onto Polydimethylsiloxane (PDMS). PDMS is a commonly used elastomeric material in soft lithography. When the patterns were transferred onto PDMS, the opposite of the patterns were obtained. For instance, if PET mold had inverted pyramids, PDMS had positive pyramids. We conducted most of our studies with PDMS molds because PDMS production does not require any additional step other than mixing the base with curing agent as opposed to UV-curing of PET molds. One other advantage of PDMS is that it can be reused after the gold transfer is completed. It was found that PDMS was a suitable substrate for noble metal transfer onto zein films. It was found that PDMS was an efficient substrate for noble metal transfer onto zein films. This is a new discovery related to zein substrates and resulting films. We also tried to use 80 nm metal-coated glass substrates to transfer nanopatterns onto zein, however this was not successful. Metal did not

transfer onto zein films; it rather stayed on the glass surface.

The reason of the successful versus unsuccessful transfer is the affinity resulting from the surface energy or adhesiveness of gold onto a substrate. If the metal has higher affinity towards the substrate that it was coated on in the case of glass for example, it did not transfer. On the other hand, if the metal has higher adhesion towards zein, it did transfer. Adhesion is related to wettability of the surface with that material and consequently surface energies of the substrates. Surface energy directly relates to the adhesion, meaning if the surface energy is low, its ability to have strong adhesive bonds is also low. In order to analyze these, we conducted both Water Contact Angle (WCA) measurements and compared the surface energies.

Table 4.3 summarizes the surface energy values in mJ/m^2 , water and zein contact angles on several parent substrate materials as well as the metals. High surface energy is correlated with high adhesion (Kendall, 1971). Glass has a surface energy ranging between 2000 and $4000 \text{ mJ}/\text{m}^2$, as a result it is highly adhesive towards many solutions/substrates with surface energies lower than glass. In contrast, PDMS has a surface energy of $20.9 \text{ mJ}/\text{m}^2$ which makes it a non-adhesive surface to many materials. PET lies in between glass and PDMS, however its surface energy value ($43 \text{ mJ}/\text{m}^2$) is closer to that of PDMS, which makes the transfer possible. Since UVcP1 and UVcP2 are commercial polymers, it was not possible to obtain the chemical formulas and/or the surface energies of these polymers. The difference in the surface properties of these cured polymers might have resulted in the fact that it was possible to transfer from UVcP2, but not UVcP1 as these were provided by different companies. Water contact angles (WCA) are also representative of the adhesion of hydrophilic materials as they are correlated with the wettability of the surface with hydrophilic substrates. The WCA of glass is 9.9 degrees, whereas the WCA of PDMS is 110 degrees. It is easier to wet glass than PDMS with a hydrophilic solution. These results also helped explain the adhesion difference between different materials.

Zein in ethanol solution contact angles were also measured the same way as

Table 4.3: Surface properties of materials that were used to transfer metal onto zein (UVcP: Ultraviolet-cured polymer, PET: polyethylene terephthalate, PDMS: polydimethylsiloxane, Au: gold, Ag: Silver) References a: Dann (1970), b: Sowell et al. (1972), c: Vitos et al. (1998)

Contact angle (degrees)						
	Material	Surface Energy mJ/m ²	Water	Zein solution	Direct transfer	Reference
Parent substrates	Glass	>2000	9.9	9.8	No	n/a
	UVcP1 (Norland)	n/a	52.4	8.6	No	n/a
	UVcP2 (Gelest)	n/a	50.4	12.3	Yes	n/a
	PET	43	59.1	20.4	Yes	a
	PDMS	20.9	110	42.9	Yes	b
Coinage materials	Au	1500	96.5	29.1	Yes	c
	Ag	1250	74.7	24.1	Yes	c

WCAs, the only difference was that zein ethanol solution was dispensed on the surface rather than water. The values for zein solution in 75% ethanol contact angle were 29.1 and 24.1 degrees for gold and silver, respectively and showed that zein was able to successfully wet gold and silver, which explains the ease of gold and silver transfer onto zein when cast in solution form. Therefore in order for metal transfer to occur onto zein from a parent substrate including, glass, PET and PDMS, there are two conditions to be satisfied. First, zein should have a low contact angle, i.e. high wettability, towards the deposited metal; second, the parent substrate has to have a low surface energy to easily peel off the metal.

The strength of the adhesion between metal and zein was also experimentally assessed using ASTM D3359 for measuring adhesion by tape test where a standard adhesive tape provided by ASTM is being used to test if the gold coating on the surface of zein can be peeled off by the tape. The standard test quantifies the degree of adhesiveness through a standard chart that accompanies the test provided by ASTM described in the Materials and Methods section of this thesis.

Complete lack of separation of metallic layer from the gold-zein laminate proved that there was a strong adhesion between metal and zein. For nanophotonic applications, there is generally an adhesion layer deposition between the substrate and the target metal (Bowden et al., 1998). We found that zein did not need this adhesion layer, in order to strongly adhere to the metal-zein 3D structure and this was an advantage compared to other methods.

Adhesion is the ability of dissimilar molecules to cling to each other. There are several mechanisms of adhesion, such as mechanical, chemical, dispersive, diffusive and electrostatic adhesion. Zein solution, prepared with plasticizer and ethanol as solvent, was able flow and fill all the nano and micro scale voids of the metal-coated polymer molds. This is expected because of capillary forces at the Nanoscale and further the crosssectional SEM pictures in Figure 4.7 clearly show that there is complete contact between gold and zein. This causes a strong mechanical adhesion when zein films were cured and solidified in these structures. Zein had long been recognized as an adhesive material for certain applications, such as wood wiener and binder for cork (Lawton, 2002). We believe that chemical adhesion also played a role potentially by sulfide and hydrogen bonding. Zein has a number of cysteine and methionine amino acids, containing sulfur, and these may have formed gold-sulfide bonds (Figure 4.4) (Häkkinen, 2012).

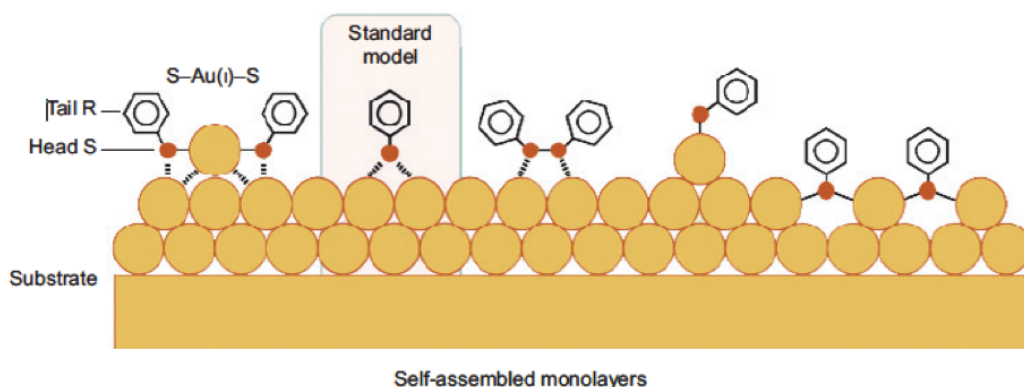


Figure 4.4: Representation of gold - sulfur bonding (Häkkinen, 2012)

4.4.2 Scanning electron microscopy imaging of pyramid structures

Scanning Electron Microscopy (SEM) was used to image the fidelity of the transferred 3-D metallic surfaces. Since, the surface of zein was already coated with a conductive metal (gold or silver) there was no need for additional metal deposition, for SEM imaging. Figure 4.5 shows the SEM images of submicron scale pyramid structures on zein inverted (a) and positive (b) pyramids. As can be seen from these images, it was possible to transfer this 3D structure onto zein along with the noble metal with high fidelity. Both positive and negative pyramids were transferable over a large area and the shape of the pyramids were conserved. This feature was maintained over the entire surface area (5 mm by 5 mm).

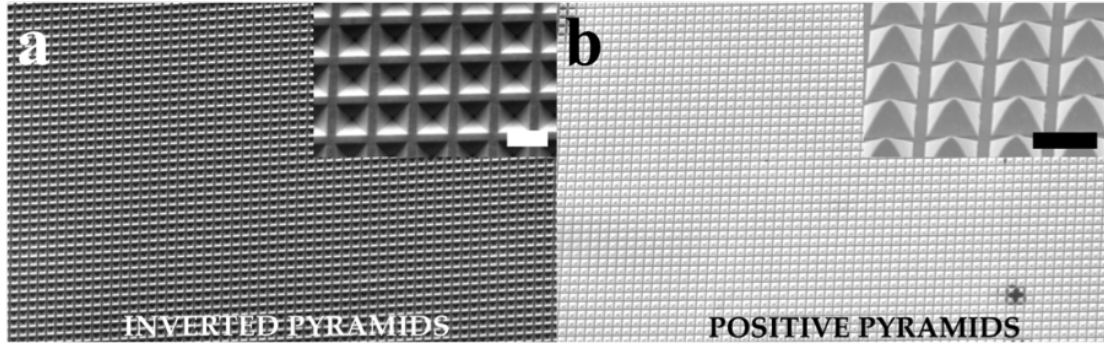


Figure 4.5: Top-down view of the inverted pyramid nanophotonic structures and (b) positive pyramid nanophotonic structures transferred on zein (Scale bars: 2 μm)

In Figure 4.5.a, the inset shows a smaller scale image over the large area. In Figure 4.5.b, the inset shows again the smaller scale of positive pyramids. The transferred nano/micro structures have lateral base dimensions of 2 μm by 2 μm , calculated by image analysis using Image J, which matches well with the original dimensions of the template (Xu et al., 2011). The figure clearly shows the excellent fidelity in a surface area (50 x 50 micron) of the film with the exception of a small defect in the case of upright pyramids. The defect shown in Figure 4.5.b resulted from the distortion/melting effect of the electron beam during the imaging process. Since zein is a biopolymer, SEM imaging has to be done fast of the order of 10-20 seconds in order not to damage the surface. Figure 4.6 shows

the high fidelity of the gold-coated zein- inverted pyramid sensors at different scales.

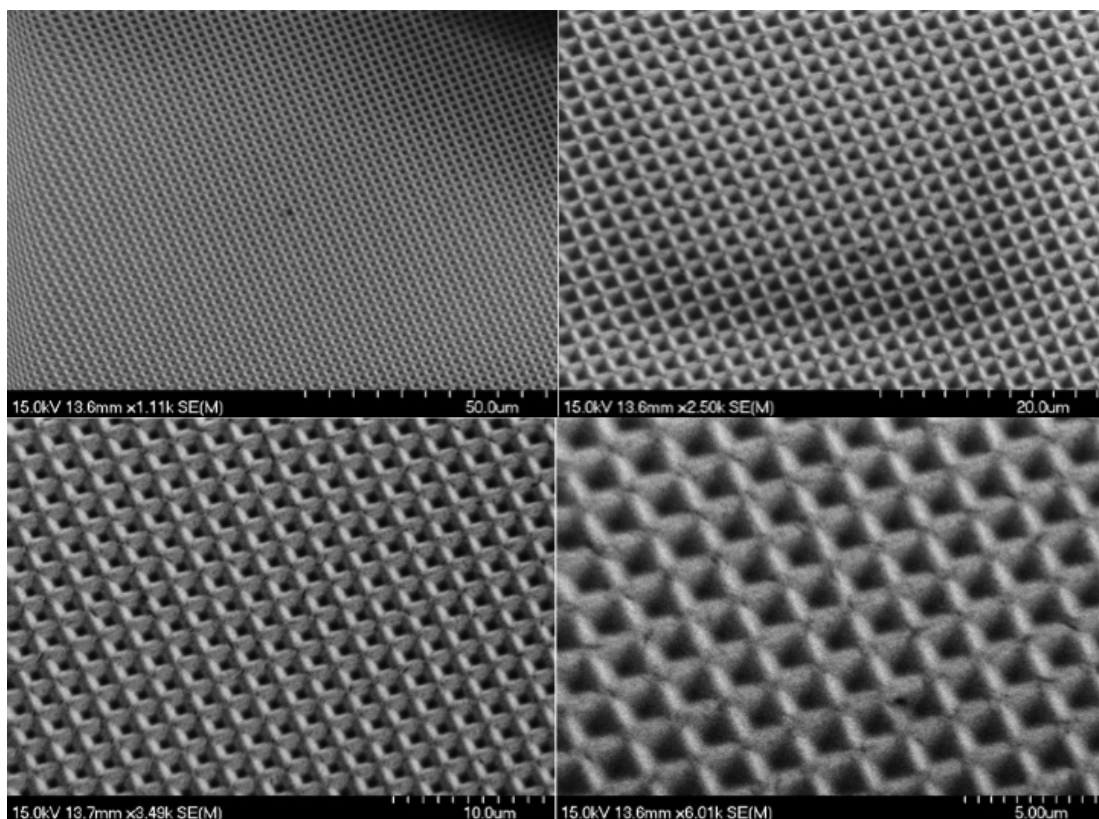


Figure 4.6: Different magnification scaled SEM images for zein with 200 nm gold coated inverted pyramids, master mold with nanopillars

In order to observe the metal to zein interface, cross-sectional images of inverted pyramids were obtained with SEM. Zein films with a gold coating were first cut with a razor blade and sharpened with a diamond blade, in order to obtain a cross-sectional image as opposed to a top-down image as shown in Figure 4.5 or 4.6. This image was important to be able to observe the state of zein-metal adhesion. Figure 4.7.a shows the different areas of the cross-section SEM images. Dashed lines were drawn for ease of identifying the inverted pyramid structures. We cut the pyramids in a diagonal way since during sectioning, it is not possible to target the pyramids and cut them half-way. This enabled us to observe pyramids in various cut images. The top image in Figure 4.7.a illustrates a pyramid cut nearly through its center, and the bottom image illustrates a cut towards the

edge. Figure 4.7.b focuses on the intersection between metal layer and zein. Due to the conductivity differences of metal and zein, it was possible to observe them as separate layers even though there was no topological difference at the interface. Metal is more conductive, thus it looks brighter and zein is more insulating, so it looks darker in this image. The metal layer thickness was about 200 nm, which shows complete transfer of the metal film. This was also evident from the fact that, parent substrate did not have any metal residues after the transfer.

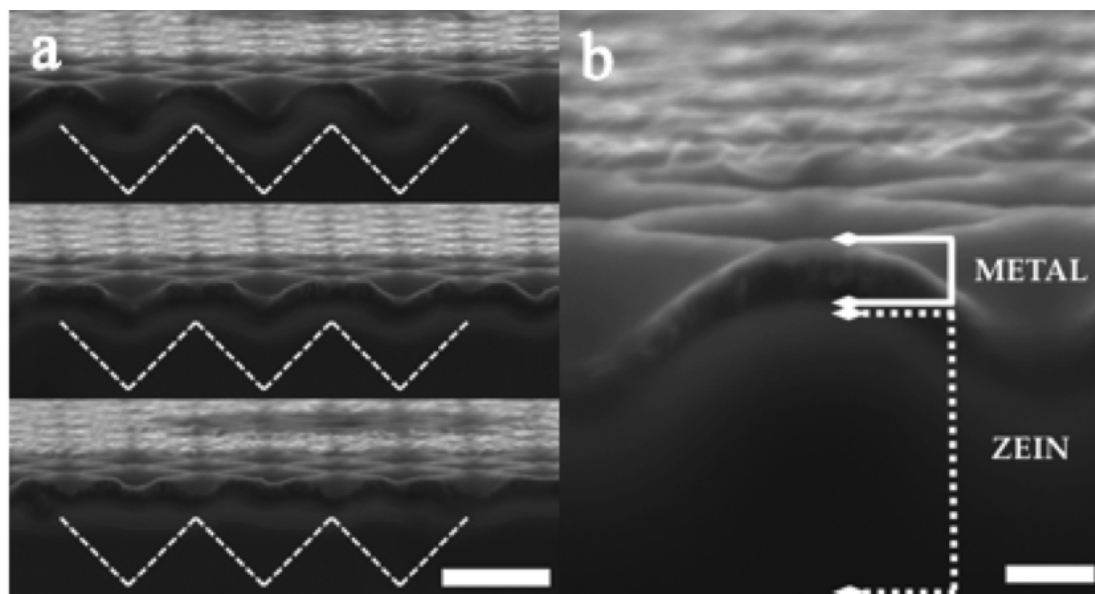


Figure 4.7: Cross-sectional SEM images of gold coated inverted pyramid structures on zein films Scale bars: 2 μ m (a) and 0.5 μ m (b)

4.4.3 Scanning electron microscopy imaging of pillar and pore structures

PET template with nanopillars was first used to transfer silver and gold onto zein films. We found that silver oxidizes and tarnishes quickly so we abandoned the silver coating process. We did the coating process in two different ways. First, PET templates with nanopillars were coated with 80 nm of gold and transferred onto zein films to have nanopores. Second, PET template with nanopillars was used to produce nanopores on PDMS and coated with gold, and then it was

transferred onto zein to obtain nanopillars. An SEM image of the original PET mold is shown in Figure 4.8.a. The pillars had the dimensions of 250 nm base diameter, approximately 150 nm tip diameter and approximately 300 nm height. After these pillars on PET were coated with gold with an e-beam evaporator, the nanopore structure on zein was obtained as shown in Figure 4.8.c. The diameter of these pores was accurately preserved as demonstrated through measurements using Image J and the transfer was successful as evident by these measurements and visually by observing the SEM image. The diameter of the pores was measured to be approximately 230 nm, whereas the spacing between two pores was 220 nm.

Figure 4.8.b shows the PDMS with nanopores coated with gold, after being transferred from the nanopillar template of PET. Due to the metal coating on top of the pores, the shape of the holes were somewhat distorted and did not have the same depth as the original pillars had. These pores were then transferred onto zein to form nanopillars on zein, which resembled a dome structure. The diameter of these domes was approximately 240 nm and the spacing in between was approximately 210 nm as measured using Image J. Based on these measurements, we concluded that the lateral dimensions were preserved. It is important to note that these structures were about 10 times smaller than the pyramid structures. The SEM images showed that it was possible to replicate nano-scale features along with the metal transfer on top of zein using this method. Figures 4.9-4.12 demonstrates the reproducibility and success of the 3D-metallic transfer at different scales of SEM imaging for the nanopillars on PET, gold coated nanopores on PDMS, gold-coated nanopores on zein and goldcoated nanopillars on zein, respectively.

Since it was not possible to observe the depth of the pores or pillars through top-down or tilted SEM imaging, cross-sectional SEM imaging was conducted. Due to the small scale of the structures and the biological nature of the zein, it was not possible to obtain as clear edges as it was for inverted pyramid structures. The cross-sectional images obtained are shown in Figure 4.13.

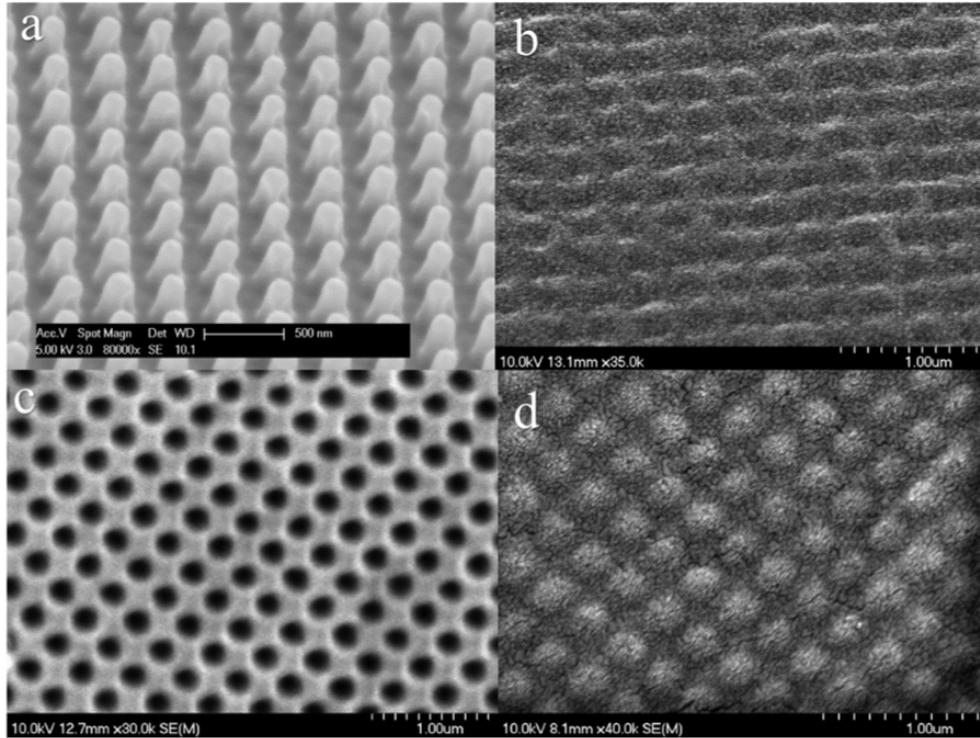


Figure 4.8: Scanning electron microscopy images of nanopillars on PET (a), gold coated nanopores on PDMS (b), gold-coated nanopores on zein (c) and gold-coated nanopillars on zein (d)

Figure 4.13.a illustrates the nanopillars on zein, which resemble nanodome structures. The height of these was calculated to be approximately 90 nm. The size of the nanopillars and the intermediate PDMS step affected the shape of these pillars, and it was not possible to preserve and transfer the exact dimensions from PET to zein. However, we obtained these smaller size (80 nm) dome structures coated with gold. Figure 4.13.b shows the cross-section images of nanopores, cut into half. The depth of these pores was approximately 200 nm. The original templates were approximately 280 nm in height and they were covered with 80 nm gold. Having 200 nm pores on zein showed that the transfer of the nanostructures were successful. Zein was in good contact with the gold as evident by the darker color zein layer below the bright gold regions. The reason why the bottom part of this SEM image looks brighter is because it was painted with silver in order to increase conductivity required to obtain SEM images.

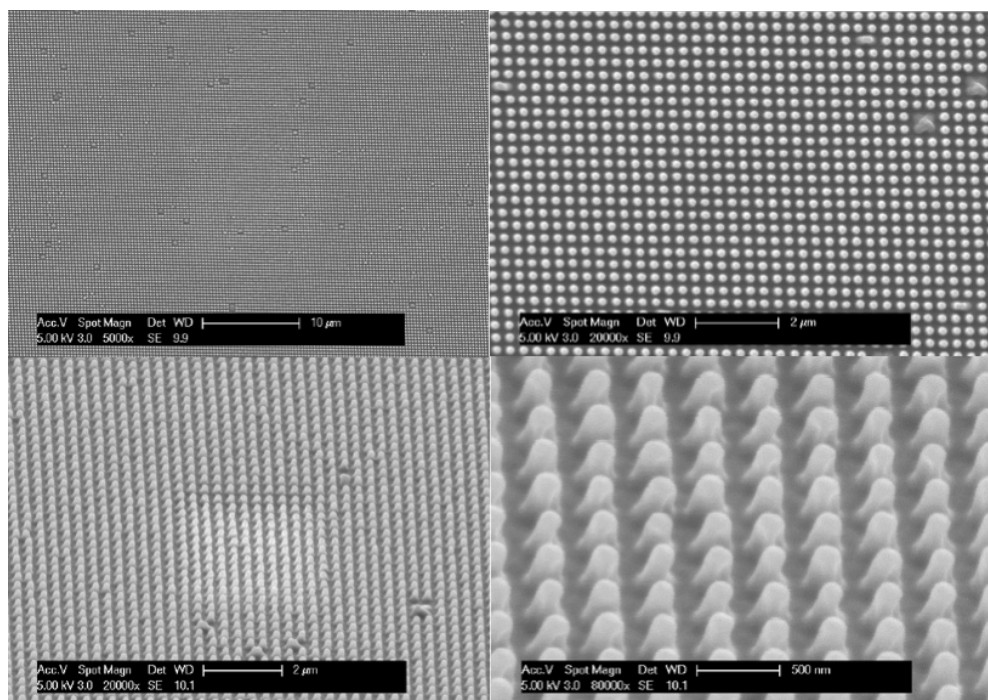


Figure 4.9: Different magnification scaled SEM images for master mold with nanopillars

4.4.4 Optical characterization of nanophotonic zein protein films

The purpose of development of these nanophotonic structure imprinted zein films coated with gold or silver was to use them in conjunction with Surface Enhanced Raman Spectroscopy (SERS) to detect various analytes. Localized surface plasmon resonance is the major cause giving the SERS effect, as discussed in detail in Chapter 2. The plasmon resonance occurs when the laser light used in Raman Spectroscopy couples with the surface at a specific wavelength. At this wavelength the light is not reflected (as gold/silver are highly reflective materials), instead it is absorbed by the surface. In order to find the specific wavelengths that where surface plasmon resonance occurs, reflectance analysis was conducted within the range of 500 and 800 nm wavelengths.

Percent reflectivity for the nanopatterns is shown in Figure 4.14. It was found that inverted pyramids displayed minima in the reflectivity curves around 530 and 630 nm regions. Reflectivity measurement is a way to find at which wavelength

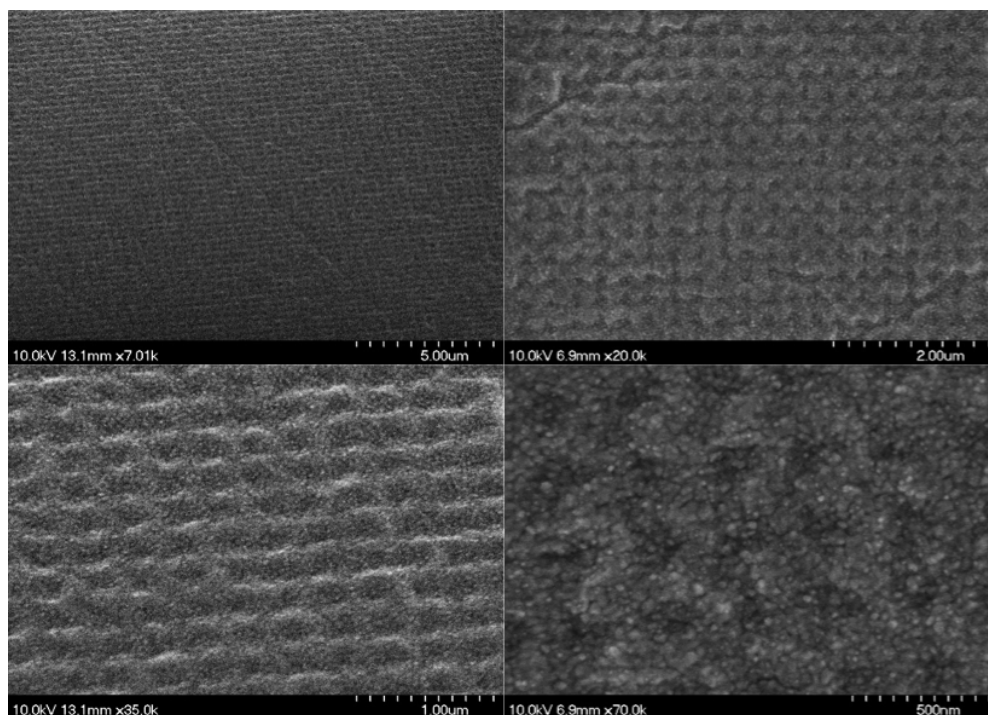


Figure 4.10: Different magnification scaled SEM images for PDMS with 80 nm gold coated nanopores

laser couples with the surface, thus gives better enhancement effect in SERS. It is preferred to work with the actual wavelength of laser, however practically we can only work with the commercially available lasers for a detection of analyte purpose. Gold-coated nanopillars reflectivity curves did not have any specific minima, but had overall lower reflection in the same regions. There are only a number of lasers available in the commercial setting that we used, namely 405 nm, 532 nm, 633 nm and 785 nm used for Raman spectroscopy.

In order to have the best SERS enhancement effect, a model molecule, Rhodamine 6G was used to determine the surface enhancement effect of each zein-SERS sensors. As discussed in Chapter 2, choosing a laser wavelength is crucial, to obtain the optimum results. For this reason, Raman spectrum of Rhodamine 6G was recorded with 4 different most commonly used lasers with wavelengths 532 (green), 633 (red) and 785 nm (near IR).

There are many factors influencing the laser choice, but it can be mainly summarized into three. First, wavelength at which the SERS-substrates are most

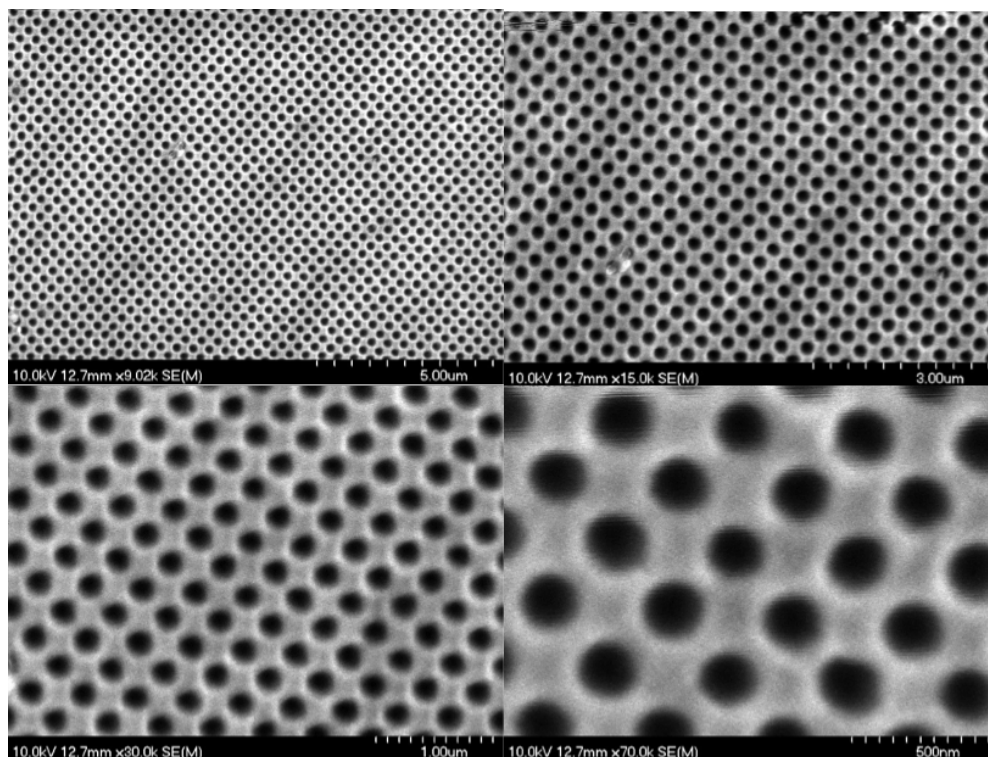


Figure 4.11: Different magnification scaled SEM images for zein with 80 nm gold coated nanopores

active, this was analyzed by the reflectivity measurement. Second, fluorescence interference coming from the sample. Third, the wavelength at which the molecule of interest shows resonance modes, resulting in higher intensity signal. For the sake of optimization, Raman spectrum of Rhodamine 6G was recorded with three lasers and Figure 4.15 shows the raw Raman spectra of nanopillar sensors when excited with these lasers. It was evident from the raw spectra that all of the lasers induced a certain amount of fluorescence in these gold-coated zein sensors. However, 633 nm laser found to enhance the characteristic peaks of Rhodamine 6G, such as 615, 775, 1370 and 1515 cm^{-1} , as these were observed as sharp Raman peaks despite the fluorescence broad band. For this reason, different concentration measurements and the comparisons between sensors were conducted with 633 nm laser.

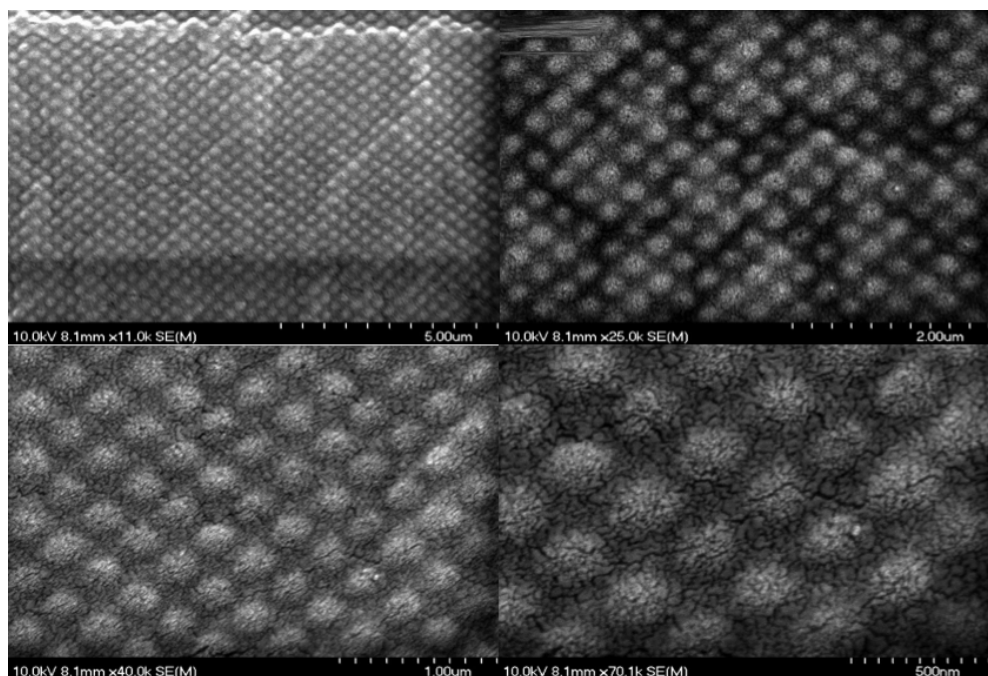


Figure 4.12: Different magnification scaled SEM images for zein with 80 nm gold coated nanopillars/domes

4.4.5 Raman spectra of Rhodamine 6G on different zein sensors

Raman spectra of Rhodamine 6G was collected with 633 nm laser and by mapping on a 3 by 3 square geometry, spacing between each mapping point was 30 μm . The raw data is represented in Figure 4.16. Since the base level of each Raman signal intensity was not the same and there was apparent fluorescence, baseline correction was applied before averaging over 9 points. For comparison, baseline corrected-averaged spectra were used.

Different concentrations of Rhodamine 6G (R6G) was dispensed onto the zein sensors with 200 nm gold-coated inverted pyramid patterns, 80 nm gold-coated nanopillar patterns and 80 nm gold-coated nanopore patterns. Figure 4.17 illustrates both the comparison of different concentrations for each sensor and the comparison between different sensors.

The peaks at locations 1370, 1515 and 1606 cm^{-1} are associated with C-C stretching and at 615 and 775 cm^{-1} are associated with C-C-C deformation and C-H deformation vibrations, respectively (Figure 4.17) (Hildebrandt and Stock-

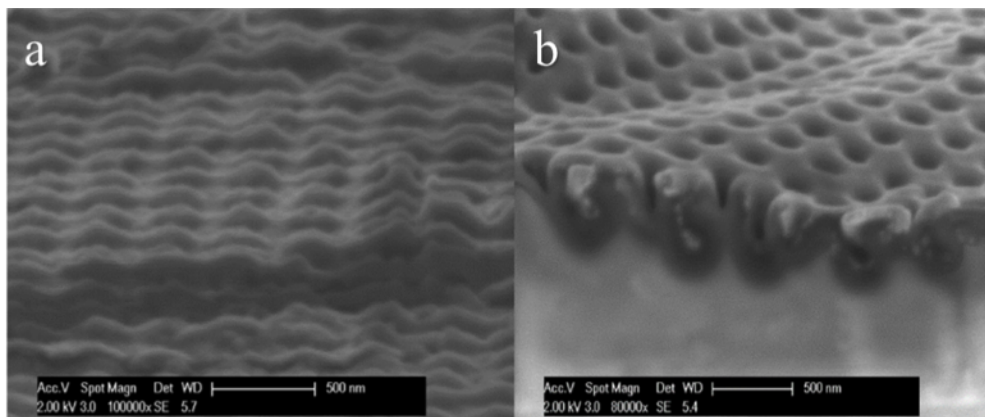


Figure 4.13: Cross-sectional Scanning electron microscopy images of gold-coated nanopillars on zein (a) and gold coated nanopores on zein (b)

burger, 1984). It was also observed that the zein-sensor itself contributed certain peaks into the spectra, such as 1330 and 750 cm^{-1} . In each of these cases there was a gold layer on top of zein and the gold layer was expected to eliminate any peaks that might arise from the zein layer underneath the gold layer. However, some of the zein peaks were observable on each of the sensors. Thinner gold coating, 80 nm compared to 200 nm gold coating resulted in higher intensity zein peaks as can be seen in Figure 4.17.b and c. Zein peaks might have resulted from either or both of the following facts: there could be nano-sized fractures during the metallic transfer, which lets the zein underneath the gold come into contact with the laser light and show Raman scattering along with Rhodamine 6G. It could also be due to the fact that the vertical penetration depth of the laser was larger than the gold layer thickness, which resulted in the observance of certain zein peaks, even though the electromagnetic effect simulations for the original sensor (Xu et al., 2011) found that laser would not penetrate into 200 nm of gold layer.

Figure 16 4.17d compares the Raman intensities of all the fabricated sensors. The inverted pyramids (blue) had the best enhancement of Raman signal. Nanopores (red) had better enhancement than nanopillars (green), but not nearly as good as the inverted pyramid structures. Since nanopillars were distorted during the production and formed nanodomes as opposed to pillars of the original master might have resulted in the reduction of the enhancement effect of these

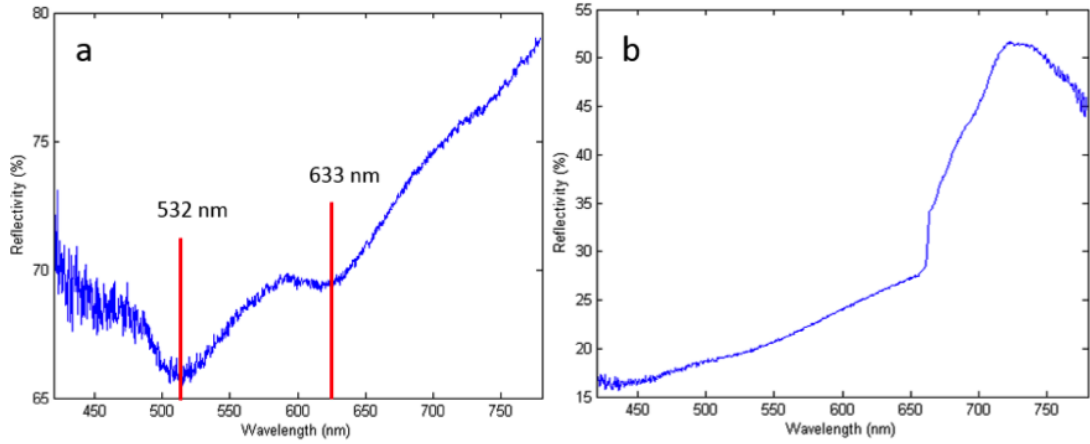


Figure 4.14: Reflectance spectra of 200 nm gold-coated inverted pyramids on zein (a) and 80 nm gold-coated nanopillars on zein (b) Lower reflectance is as a result of absorption of the light and thus, lowest possible reflection is preferred for laser selection for SERS

structures. Based on this comparison, we concluded that the best result came from zein sensors with 200 nm gold-coated inverted pyramids.

The enhancement factor of zein-inverted pyramid SERS sensors was calculated by comparing the intensity of the 1370 cm^{-1} peak with R6G Raman signature obtained on bare Si wafer. Si wafer does not show any auto fluorescence effect and it did not have any roughened noble metal structure on it. Therefore, the Raman signature of R6G obtained on it is weak. For this reason 10 mM of R6G was used in order to calculate the enhancement factor and the following formula was applied (Xu et al., 2011).

$$EF = \frac{I_{SERS} * N_{Normal}}{I_{Normal} * N_{SERS}} \quad (4.1)$$

Comparison of Raman spectra between 10 mM R6G on Si wafer (blue) and 100 μM R6G on zein-inverted pyramid sensors (red) are shown in Figure 4.18. Enhancement Factor (EF) was calculated as 1.3×10^4 . We found that the enhancement factor of zein-SERS sensors with inverted pyramid patterns and 200 nm gold coating was similar to the original SERS substrate, which we used as

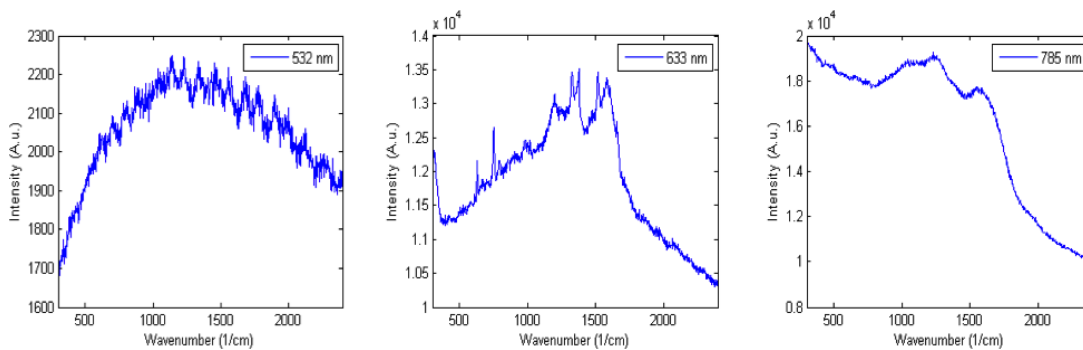


Figure 4.15: Raman spectra of Rhodamine 6G on gold-coated nanopillar zein sensors excited with 532 nm, 633 nm and 785 nm lasers. In these figures, raw data is presented and it was found that all lasers induced fluorescence (evident by the broad peak features of the baseline). 633 nm laser (middle) had the sharp Raman peaks with the best signal: noise ratio. In these figures, raw data is presented and it was found that all lasers induced fluorescence (evident by the broad peak features of the baseline). 633 nm laser (middle) had the sharp Raman peaks with the best signal: noise ratio.

a template for this study. The enhancement factor of these original SERS substrates which consisted of UV curable polymer on PET was found to be 1.6×10^6 (Xu et al., 2011).

One of the limitations of the original inverted pyramid sensors on PET was that the gold layer was not adhering strongly onto the UV curable polymer despite the adhesion layer of Titanium and was peeling off when a liquid sample was applied to the surface (Xu et al., 2011). By utilizing zein instead of a PET coated with UVcP, we eliminated this problem as zein had a very strong adhesion towards gold and silver.

4.4.6 Macro images of zein SERS sensors

It is important to note that the zein SERS sensors developed and fabricated in this study are free-standing films as shown in Figure 4.19. The thickness and size can be adjusted during fabrication by changing the zein solution volume and cutting the sensor with a razor before lifting it up from the parent substrate, respectively. Figure 4.19.a illustrates the zein sensor on the gold coated side,

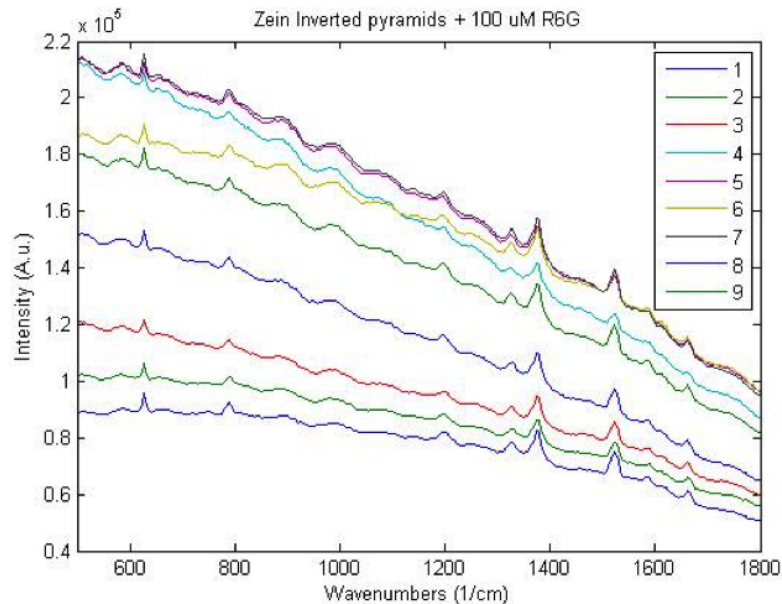


Figure 4.16: Raw data of Raman spectrum of Rhodamine 6G at 9 different mapping locations.

the squared area (5 mm x 5 mm) having the pyramid structures. Figure 4.19.b illustrates the sensor on the zein side. Zein has the color of yellow to orange due to the bound carotenoids (Huang et al., 1987). Figure 4.19.c shows the thickness of sensor as 0.35 mm and Figure 4.19.d shows the size of sensor of (10 mm x 10 mm). A penny was to serve as a visual scale. The advantage of this size of sensors is that these are light, portable and they require very little (as low as 2 μ L) of sample volume in order to get Raman spectra owing to the surface enhancement effect.

Free-standing zein sensors with the gold coating and nanopatterns were obtained in this study is the first time for a direct transfer of 3-dimensional metallic structures onto a food polymer. Plasticized zein films with oleic acid are highly flexible and shown to conform to various micro-scale molds previously (Altunakar et al., 2010; Luecha et al., 2011). The flexibility and the adhesiveness of zein played a crucial role in this 3-D metallic transfer process as explained previously.

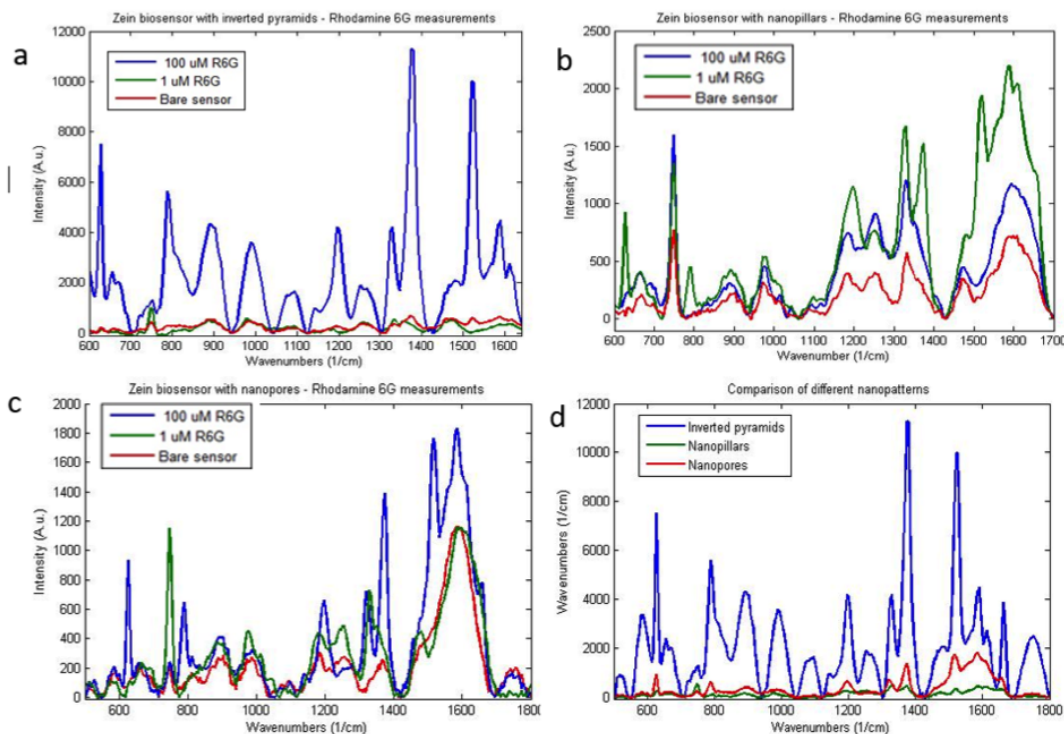


Figure 4.17: Different concentrations of Rhodamine 6G on (a) 200 nm gold coated inverted pyramid sensor on zein, (b) 80 nm gold coated nanopores sensor on zein, (c) 80 nm gold coated nanopillars sensor on zein and (d) comparison of 100 μM concentration of these sensors. It was found that inverted pyramid structures yielded the highest enhancement as evident by the intensity of the characteristic peaks, such as 1370 and 1515 cm^{-1} .

4.5 Conclusion

In this research, direct transfer of 3D metallic structures onto a food biopolymer, zein, was successfully demonstrated for the first time. Zein, a corn protein, was plasticized with oleic acid and as a result the resulting sensor films were flexible enough to conform and peel off from the parent substrate coated with gold or silver. Parent substrates used in this research were nanophotonic patterns already established to have surface enhanced raman spectroscopy (SERS) characteristics. SERS is a technique to enhance the signal of highly specific vibrational Raman scattering, which has the potential for lab-on-chip sensor technologies. Three different patterns were transferred onto zein films along with different thickness

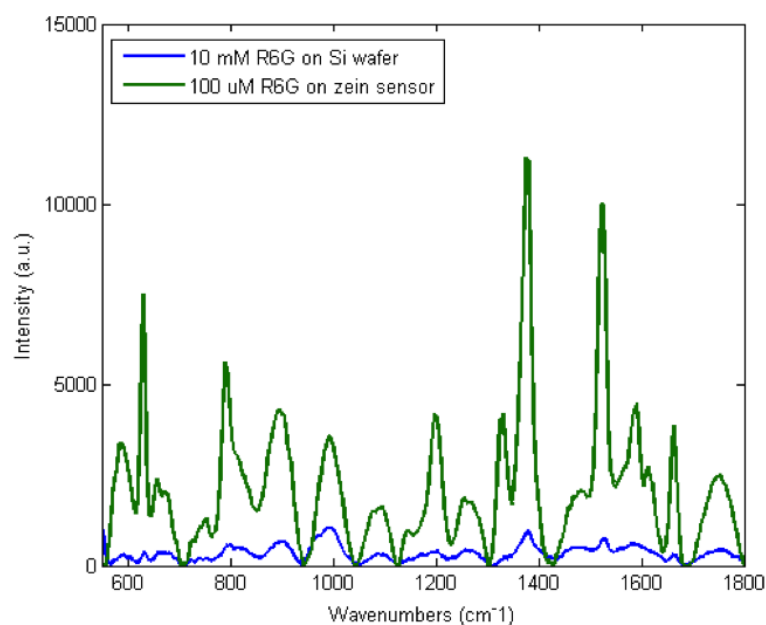


Figure 4.18: Comparison of SERS and normal Raman spectra of Rhodamine 6G

of metal: 200 nm gold coated inverted pyramids, 80 nm gold coated nanopillars and nanopores. The resulting zein SERS substrates were compared with each other via a model molecule Rhodamine 6G Raman spectra. It was found that the inverted pyramid gold zein sensors had the highest enhancement factor, 1.3×10^4 , compared to the other zein-sensors. The volume needed for these measurements were only 2 μL and the size of the zein sensors was 10 mm x 10 mm, with a thickness of 0.35 mm. This zein sensor can potentially serve as a biodegradable SERS substrate for numerous applications in agricultural, medical and food field.

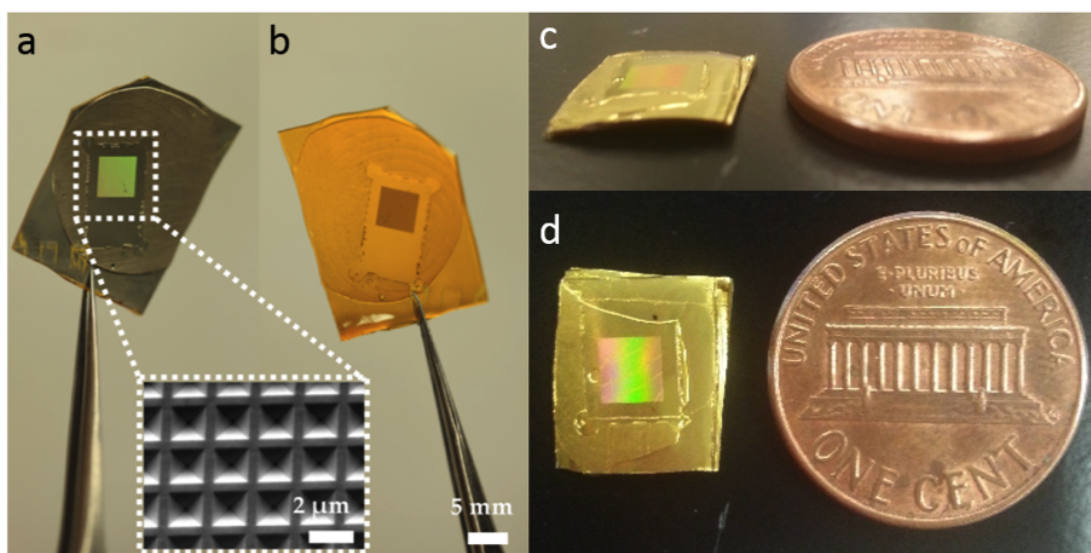


Figure 4.19: Macro images of zein sensors with 200 nm gold-coated inverted pyramids. Gold side of sensors, squared area has the nanophotonic patterns (a), zein side of sensors (b), thickness of the sensor (c) and size of the sensor (d)

CHAPTER 5

DETECTION OF ACRYLAMIDE USING ZEIN-SERS PLATFORM ¹

5.1 Abstract

In this study, a biodegradable zein/gold SERS platform was tested as a potential tool to detect acrylamide for the first time. It was found that the presence of acrylamide resulted in a characteristic marker SERS peak that did not exist in the background SERS spectrum of the sensor. This unique peak was at 1447 cm^{-1} . This peak was used to detect and quantify acrylamide in aqueous solutions and a calibration curve was obtained using acrylamide solutions within the range of 10 mg/ml and 10 $\mu\text{g/ml}$. After 10 $\mu\text{g/ml}$ of concentration, it was not possible to make reliable measurements. The error or variation for each concentration in the range of 0.4 mg/ml (for 1 mg/ml) and 1.8 mg/ml (for 10 mg/ml) was observed. SERS was found to be an accurate technique for quantification purposes, in the concentration range studied. The calibration curve had an R^2 value of 0.93 and 0.97 (for log-log calibration curve). This was a proof-of-concept study to investigate the potential of a SERS sensor designed on a biodegradable platform and it was shown that this method can be potentially used with a careful design of acrylamide extraction from food samples.

¹This work is currently under review as P. G. Gezer, G. L. Liu, J. L. Kokini “Detection of acrylamide using a biodegradable zein-based sensor with surface enhanced Raman spectroscopy” Food Control.

5.2 Introduction

Acrylamide (Figure 5.1) is a small organic molecule with the chemical formula of C_3H_5NO . It is an odorless, white compound, which is soluble in water and ethanol. It is generally used in its polymeric form, polyacrylamide, in the plastic industry (Tekkeli et al., 2012). It has carcinogenic and toxic properties in animals, and can possibly be harmful to humans. For this reason, the level of acrylamide in water is regulated by Environmental Protection Agency in the US. Swedish scientists discovered in 2002 that certain foods contain acrylamide. The most common examples are French fries, potato chips and toasted bread (Mottram et al., 2002). These foods along with their acrylamide ranges are reported in Table 1.

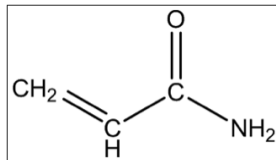


Figure 5.1: Molecular structure of acrylamide (Jonathan, 1961)

Acrylamide is a by-product of Maillard reaction that occurs during high-temperature processing of starchy foods. The mechanism proposed is that the arginine amino acid goes under reaction with reducing sugars, i.e. glucose or fructose, and then the reaction further proceeds to form acrylamide as shown in Figure 2 (Mottram et al., 2002). The cooking temperature, cooking method, initial content of arginine and reducing sugar in the product, time and moisture of the cooking affect the amount of acrylamide formed in a food system (Arvanitoyannis and Dionisopoulou, 2014).

In food products that are rich in proteins, the range of acrylamide found after high-temperature processing was moderate and between 5 - 50 $\mu\text{g}/\text{kg}$ of food, whereas for carbohydrate rich foods it ranged between 150 - 4000 $\mu\text{g}/\text{kg}$ (Tareke et al., 2002). Whereas the main focus and concern has been on potato chips/crisps

Table 5.1: Amount of acrylamide in various food products (Krishnakumar et al., 2014)

Product/ Product group	Acrylamide range ($\mu\text{g kg}^{-1}$)
Bakery products and biscuits	18-3324
Breads	<10-3200
Bread (toast)	25-1430
Breakfast cereals	<10-1649
Chocolate products	<2-826
Coffee substitute	80-5399
Dairy products	<10-130
French fries/chips	59-5200
Meats	<10-116
Potatoes (raw)	<10-<50
Potato chips/crisps	117-4215
Roasted coffee	45-9359

(with a content between 117 - 4215 $\mu\text{g}/\text{kg}$) and French fries/chips (59 - 5200 $\mu\text{g}/\text{kg}$), some other products, such as roasted coffee (45 - 9359 $\mu\text{g}/\text{kg}$) showed very high acrylamide content in certain cases. Bakery products (18 - 3324 $\mu\text{g}/\text{kg}$) and bread (10 - 3200 $\mu\text{g}/\text{kg}$) also are a source of concern, especially when the Maillard reaction progresses extensively and they are dark brown (Krishnakumar et al., 2014).

In November 2013, FDA released a draft for acrylamide control and mitigation strategies for industry. Since the industry is trying to control the levels of acrylamide formation, there is a need for fast and routine quality control methods for detection of acrylamide in the food industry. The current techniques used have the following steps: aqueous extraction of acrylamide from food, concentration of the sample and analysis by either gas/liquid chromatography-mass spectroscopy or high performance liquid chromatography (Bethke and Bussan, 2013). The whole process takes a considerable amount of time and requires both sophisticated equipment and trained personnel. For this reason, there is a need for a simple, robust

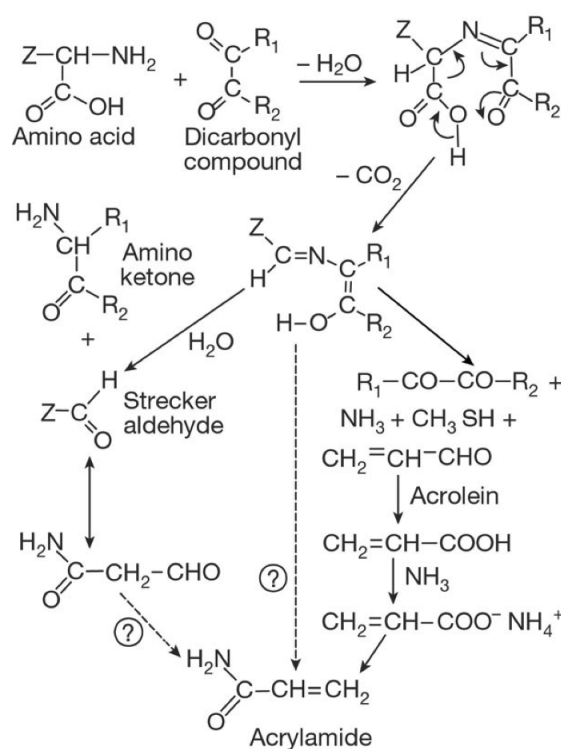


Figure 5.2: Proposed formation of acrylamide through Maillard reaction (Mottram et al., 2002)

and fast detection method for acrylamide. In this area, there has been some effort to develop alternative techniques such as the adsorption stripping voltammetry, capillary zone electrophoresis and none-aqueous capillary electrophoresis (Vesela et al., 2013; Bermudo et al., 2006; Bařkan and Erim, 2007). To this date, detection of acrylamide by utilizing Raman spectroscopy has not been reported. In this paper, we investigated the use of Surface Enhanced Raman spectroscopy on a biodegradable platform as a potential detection platform for acrylamide.

5.3 Materials and Methods

5.3.1 Preparation of acrylamide solution

Acrylamide, >99%, for biochemistry, electrophoresis grade (Acros Organics) used in this study. Acrylamide was stored at 4°C in a refrigerator. All solutions

were freshly prepared before use. Distilled water was used as the solvent. The concentrations of the acrylamide solutions used on SERS-active substrates were as follows: 10 mg/ml, 7.5 mg/ml, 5 mg/ml, 2.5 mg/ml, 1 mg/ml, 100 $\mu\text{g}/\text{ml}$, 10 $\mu\text{g}/\text{ml}$. Environmental Protection Agency (EPA) suggests not consuming more than 2 μg acrylamide per kg body weight of a person per day as a maximum reference threshold toxicity dose. The concentrations of the acrylamide solutions used on glass were as follows: 100 mM and 10 mM (approximately 7 mg/ml and 0.7 mg/ml).

5.3.2 Preparation of SERS-active substrates

In this study, SERS-active zein substrates were fabricated following the methods described in Chapter 4. Polydimethylsiloxane (PDMS) with positive pyramid structures was used as a template. The template had pyramids with the base squared dimensions of 2 μm by 2 μm and the height of 2.1 μm . PDMS template was coated with 200 nm gold using an e-beam evaporator. Zein solution was prepared by first dissolving zein in 75 % ethanol (1 g: 5 mL) and mixing with oleic acid and emulsifier (1 g zein: 1 g oleic acid: 0.05 g emulsifier). This solution was stirred on a hot plate for 5 minutes. After ultrasonification to remove air bubbles, zein solution was cast on PDMS template with gold coating. After drying in a vacuum dessicator at room temperature, dried zein films were cut and removed from the PDMS. 200 nm gold along with the pyramid structures were transferred onto zein, resulting in an inverted gold pyramid structure on zein. Macro and SEM images can be found in Chapter 4.

5.3.3 Raman spectroscopy measurements

Samples for Raman spectroscopy were prepared by dropping 5 μl of one of the acrylamide solutions at a given concentration on one of two platforms consisting either of a glass slide or zein-SERS sensor and letting it air dry at room temper-

ature. Figure 5.3 illustrates the droplet deposition on a zein-SERS sensor. The prototype simple laboratory sensor was immobilized onto a glass slide with tape in order to obtain a flat and stable surface. 5 μl of acrylamide solution was dropped into the region where the nanophotonic structures are. Background measurements were done on the nanophotonic structures that did not have any solution.

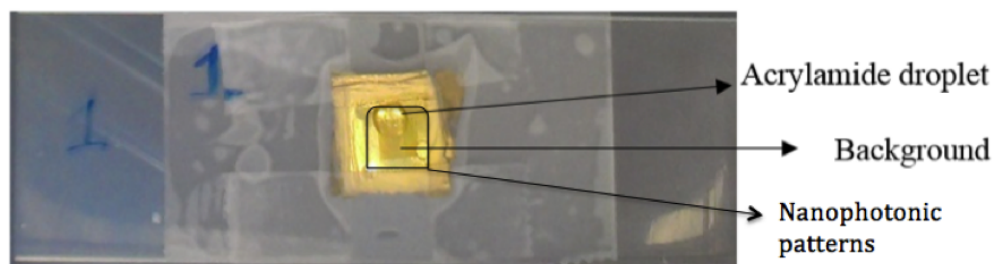


Figure 5.3: Zein-SERS sensor with a droplet of acrylamide solution, immobilized on a glass slide. The squared area in the middle has the nanophotonic structures

Two Raman systems were used in this study: Nanophoton Raman-11 and Horiba LabRAM HR. In both systems, 532 nm laser was used. In the Nanophoton system, the excitation power was 5.35 mW (no filter was used). The objective used was 10 X and the grating was 600 lines/mm. The slit was 60 μm and the wavenumber range covered was 400 to 3000 cm^{-1} . The measurement was done in “Fast x-y scan” mode with 1 second of exposure time. An area over the edge of the dried droplet was scanned with this system.

In Horiba LabRAM HR confocal-Raman microscopy system, the grating was 300 lines/mm the slit was 100 μm and the hole was 300 μm . 50 X objective and D 1 filter was used. The Raman spectra were collected in the wavenumber range of 500 to 1800 cm^{-1} . For quantification measurements, individual spectra over 5 different points were collected and the exposure time was kept constant at 1 second x 30 times.

Data analysis

Baseline correction was carried out to eliminate the fluorescence interference. A 5th order polynomial was fit to the baseline using the ‘baseline correction’ option of the LabSpec 5 (provided by Horiba). Additional points were added to the baseline to ensure a perfect fit, if needed. This baseline was subtracted from the Raman spectrum.

For quantification measurements, peak fitting function of the same software (LabSpec 5) was used. Gauss-Loren peak fitting function was used and peak intensities were calculated. For each concentration the average of 5 points was used to calculate the peak intensity as well as the standard deviation.

For measurements using the Nanophoton brand Raman spectrometer, the program allows for averaging the spectra over a selected area. For measurements on the edge of the droplet, three different areas were selected: 1) outside the droplet (glass slide); 2) inside the droplet (glass slide + low concentration of acrylamide); 3) edge of the droplet (concentrated acrylamide).

5.4 Results and Discussion

5.4.1 Raman measurements of acrylamide on glass slide

A glass slide was used as one of the platforms in order to obtain the Raman signature of acrylamide. When a volume of acrylamide solution is dropped on a surface and left to dry, it forms a coffee ring shaped residual. The term ‘coffee ring effect’ has been coined to describe this phenomenon in physics (Deegan et al., 1997). When a liquid with dispersed solids evaporates, the capillary forces bring most of the solids towards the edge of the droplet, causing a high concentration and leaving a low concentration inside the droplet (Figure 5.4). In the first part of this study, the effect of this phenomenon was studied for acrylamide deposited on a glass slide.

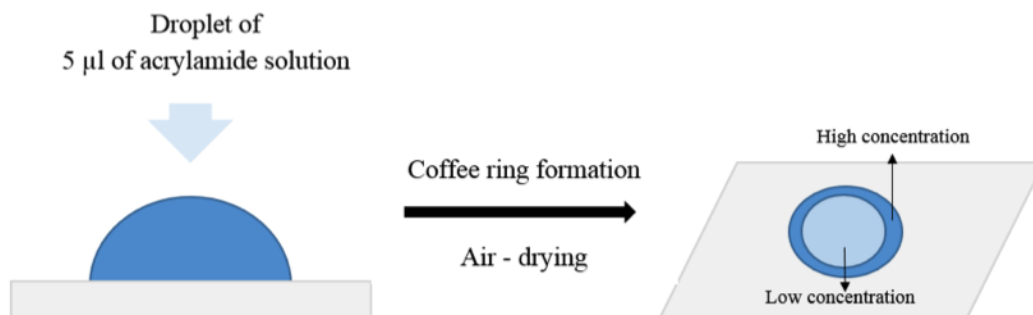


Figure 5.4: Coffee-ring effect for acrylamide solution

Figure 5.5 shows the microscopy images of the edge of the droplet (100 mM acrylamide solution) and makes a distinction between glass slide, inside of the droplet and the edge of the droplet. The Raman signatures of each of the regions are plotted in Figure 5.6. In this analysis, it was found that the glass slide had a background signal as shown in grey. Raman signals showed both glass and acrylamide peaks inside the droplet. The edge of the droplet showed high intensity, sharp Raman peaks as expected from the high concentration of acrylamide in this region. Some of the key characteristic peaks of acrylamide are reported in Table 5.2.

Table 5.2: Some characteristic peaks and vibration assignments of acrylamide and glass slide

Raman peaks (cm ⁻¹)	Bond	Type of vibration	Material
562	Si-O-Si	Bending	Glass slide
850	C-C side chain	Stretching	Acrylamide
966	CHHC	Wagging	Acrylamide
996	Si-ring	Breathing	Glass slide
1098	SiO	Stretching	Glass slide
1298	C-H bending	Bending	Acrylamide
1440	CH ₂	Bending	Acrylamide
1640	C-C stretching	Stretching	Acrylamide
1685	C-O stretching	Stretching (amide I)	Acrylamide

From the edge of the droplet experiment, it was concluded that for each con-

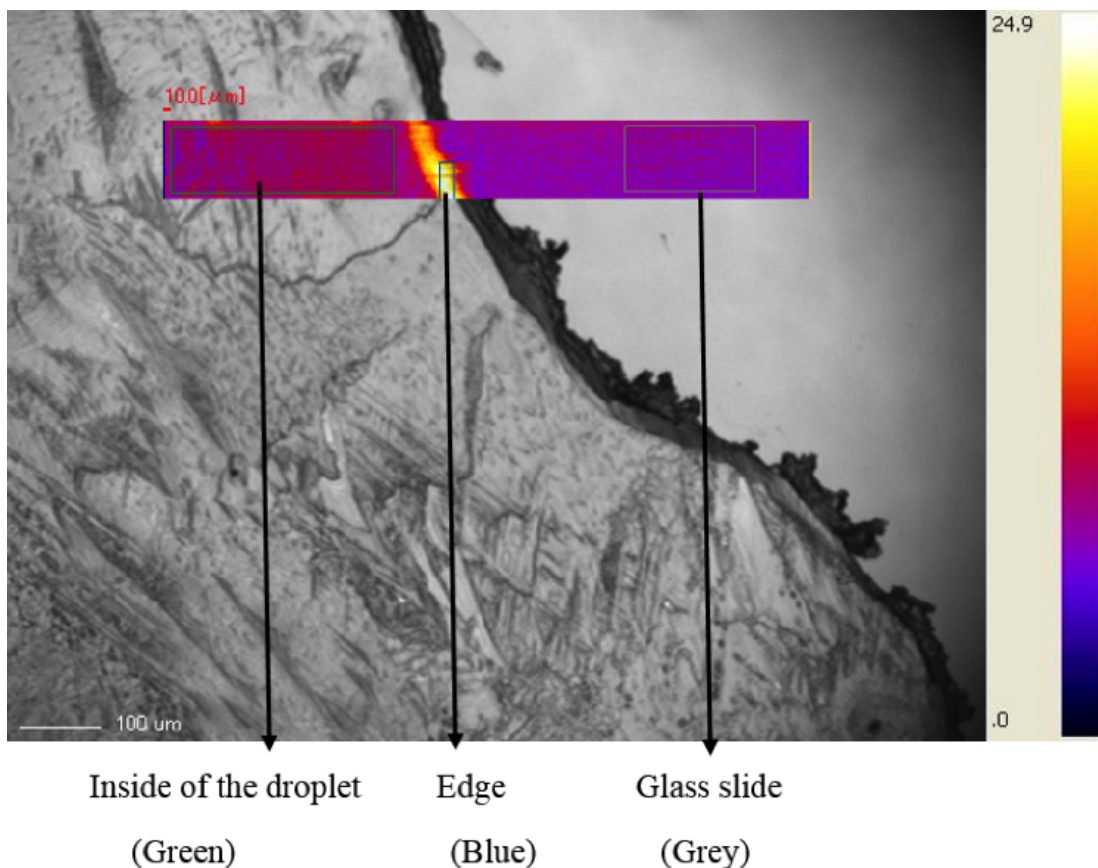


Figure 5.5: Microscopy image of dried acrylamide solution on glass slide. Big rectangular area shows the region in which Raman measurements were done. Small green rectangle represents inside of the droplet (low concentration), blue rectangle represents the edge of the droplet (high concentration) and grey rectangle represents the glass slide (no acrylamide). Color code represents the intensity of Raman signals over the region. Yellow color signifies higher concentration. Scale bar: 100 μm

centration of acrylamide obtaining Raman spectra measurements on the edge of the droplet would be the most beneficial as the acrylamide concentration was the highest in this region as indicated above, consistent with prior studies of Sun and Wiederrecht (2007) who also benefitted from this phenomenon. Therefore, in the rest of the acrylamide Raman measurements spectra were collected from the edge of the droplet. Figure 5.7 shows the Raman spectra of both 100 mM and 10 mM acrylamide on glass slides with the Horiba LabRAM Raman microscope. The 100 mM concentration in Figure 5.7a showed the expected characteristic peaks;

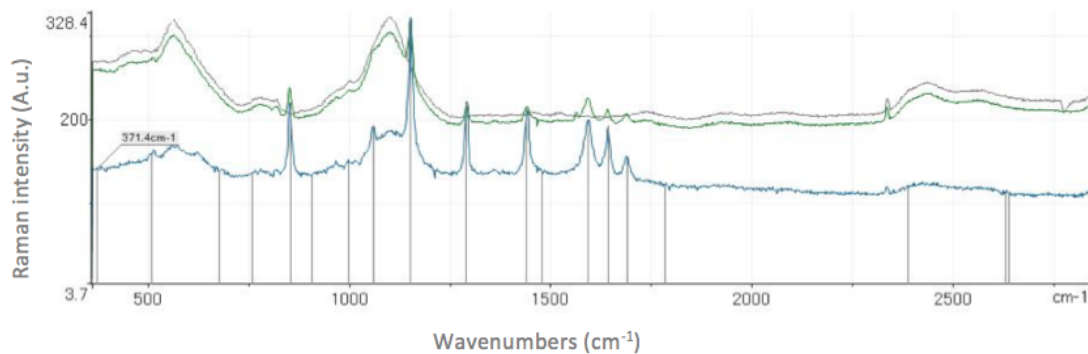


Figure 5.6: Overlay of the Raman spectrum of glass slide (grey), edge of the droplet (blue) and inside the droplet (green)

however the 10 mM concentration of acrylamide spectra shown in Figure 5.7b were overwhelmed by the glass slide spectra and it was not possible to collect or identify any Raman peaks of acrylamide. Glass slides are known to give background signature, as this was the case for our situation. Table 5.2 summarizes the peaks that are coming from glass vs acrylamide. Glass slide gave peaks such as Si-O-Si bending at 562 cm^{-1} , Si-ring breathing at 996 cm^{-1} and SiO stretching at 1098 cm^{-1} . Acrylamide gave peaks C-C side chain stretching at 850 cm^{-1} , CH-HC wagging) at 966 cm^{-1} , C-H bending at 1298 cm^{-1} , CH₂ bending at 1440 cm^{-1} , C-C stretching at 1640 cm^{-1} and C-O stretching at 1685 cm^{-1} .

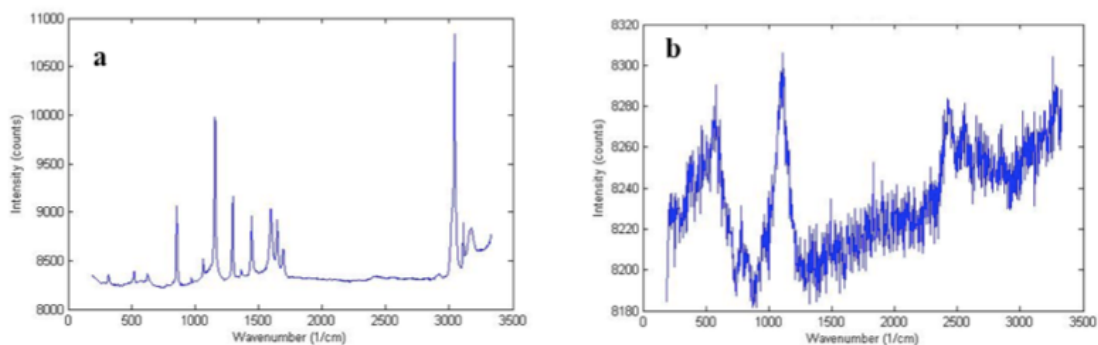


Figure 5.7: Raman measurements of acrylamide on glass slide with concentrations of 100 mM (a) and 10 mM (b)

5.4.2 SERS measurements of acrylamide on zein substrates

Since acrylamide is a small molecule and glass Raman spectra give overwhelming background signatures, it was not possible to measure low concentrations of acrylamide with normal Raman spectroscopy. In order to enhance the spectral intensities SERS-active substrates made out of zein were used.

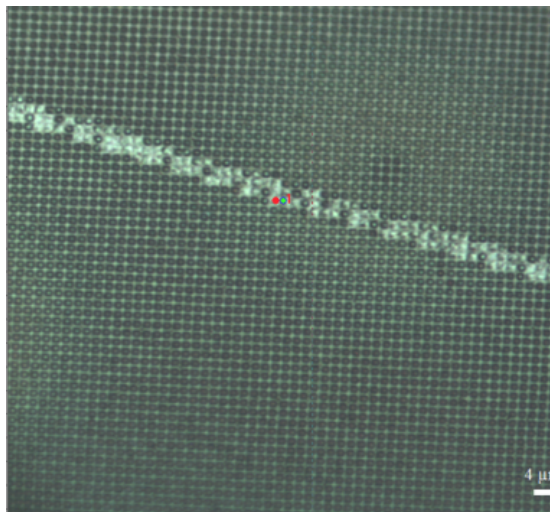


Figure 5.8: Microscopy image of zein-SERS substrates with acrylamide deposited on it. White line represents the edge of the ‘coffee ring’ shape. Red point shows the laser location on which the measurements were taken.

As discussed in Chapter 4, zein-SERS substrates also gives background signal and it was important to identify a characteristic peak of acrylamide that is different than the background. Figure 5.9 shows the comparison between background signature of the substrates and acrylamide with $10 \mu\text{g}/\text{mg}$ concentration on top of the substrate. From this comparison, it was concluded that many of the Raman peaks of acrylamide overlapped with the background signal, such as 966 cm^{-1} , 1298 cm^{-1} , 1640 cm^{-1} . However, the peak at 1447 cm^{-1} , which was CH_2 deformation peak did not exist in the background signature. For this reason, this peak was used for quantification purposes. Different concentrations of acrylamide on zein-SERS sensor can be found in Figure 5.10. As the concentration decreased, the intensity of the peaks decreased as well. When the parameters, such as laser power, laser area, conditions of the Raman instrument remained same, intensity

of the Raman peak is directly correlated with the concentration of the molecule of the interest. All the above mentioned parameters kept the same and the intensity of the peaks were plotted against the concentration of known acrylamide.

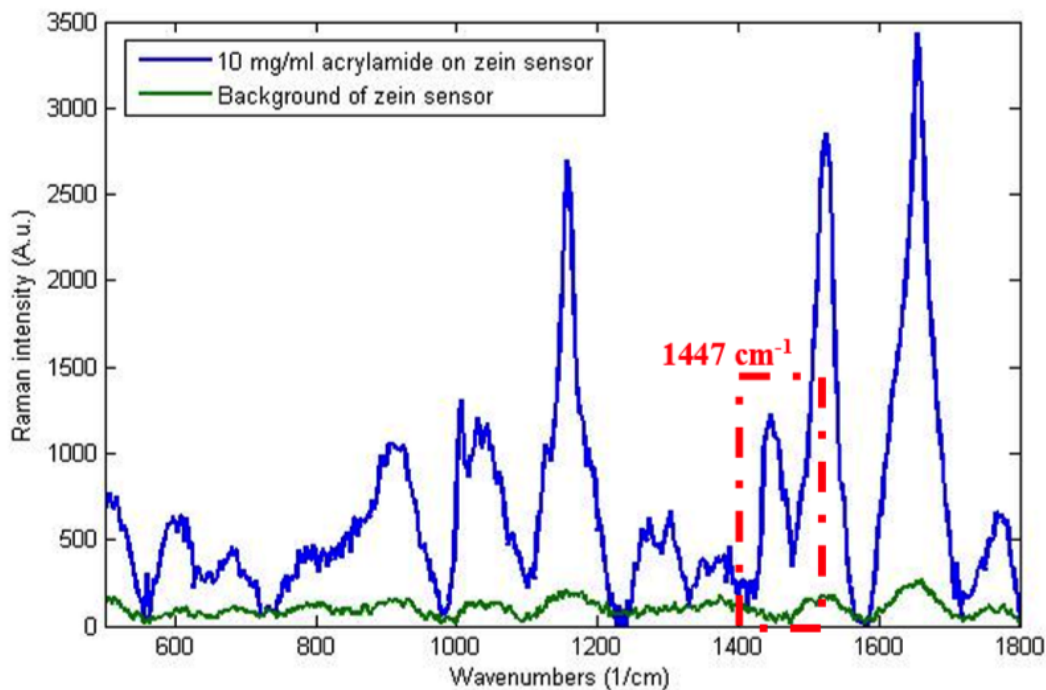


Figure 5.9: Comparison of the background signature of zein-SERS sensor (green) with acrylamide on top of the sensor (blue). Red dotted square indicates the peak at the wavenumber of 1447 cm^{-1} , which does not exist in the background, but exists in acrylamide signature. (A.u.: arbitrary units)

As discussed in Chapter 4, zein-SERS substrates also give background signal and it was important to identify a characteristic peak of acrylamide that is different than the background. Figure 5.9 shows the comparison between background SERS spectra of the gold coated zein substrates and acrylamide with 10 mg/ml concentration on top of the substrate. From this comparison, it was concluded that many of the Raman peaks of acrylamide overlapped with the background signal, such as 966 cm^{-1} (CH-HC wagging), 1298 cm^{-1} (CH bending), 1640 cm^{-1} (C-C stretching). However, the peak at 1447 cm^{-1} , which was CH_2 bending peak coming from acrylamide did not exist in the background signature. For this reason, this peak was used as the characteristic marker peak for quantification of the

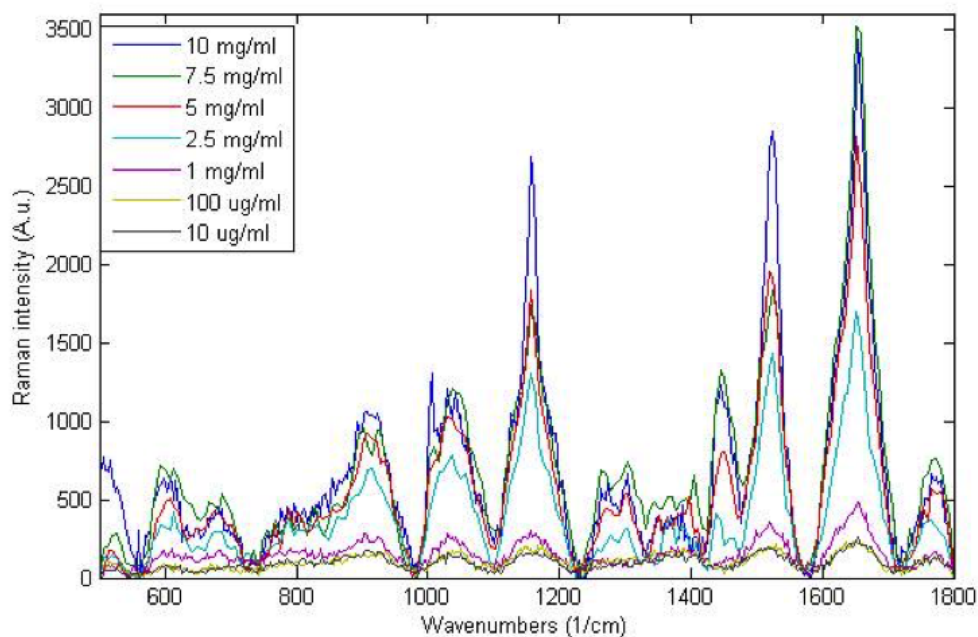


Figure 5.10: Surface enhanced Raman signatures of acrylamide with different concentrations on zein-SERS substrate

concentration of acrylamide. Different concentrations (10 mg/ml, 7.5 mg/ml, 5 mg/ml, 2.5 mg/ml, 1 mg/ml, 100 µg/ml, 10 µg/ml) of acrylamide on zein-SERS sensor are shown in Figure 5.10. As the concentration decreases, the intensity of the peaks decreased as well. When the parameters, such as laser power, laser area, conditions of the Raman instrument remained same (laser: 532 nm, grating: 300 lines/mm, slit: 100 µm, hole: 300 µm, objective: 50 X, filter: D1, wavenumber range: 500 - 1800 cm^{-1} and acquisition time: 1s 30 times) the intensity of the Raman peak is directly correlated with the concentration of the molecule of the interest. All the above-mentioned parameters kept the same and the intensity of the peaks were plotted against the concentration of known acrylamide.

Subtraction of the Raman spectra from the background Raman spectra of the sensor might sometimes give desirable results in identifying the different peaks. Figure 5.11 shows the result of Raman spectrum of background zein Sensor subtracted from the Raman spectrum of acrylamide on zein-SERS sensor. It was found that the subtraction resulted in a too noisy spectrum. Thus, we decided to

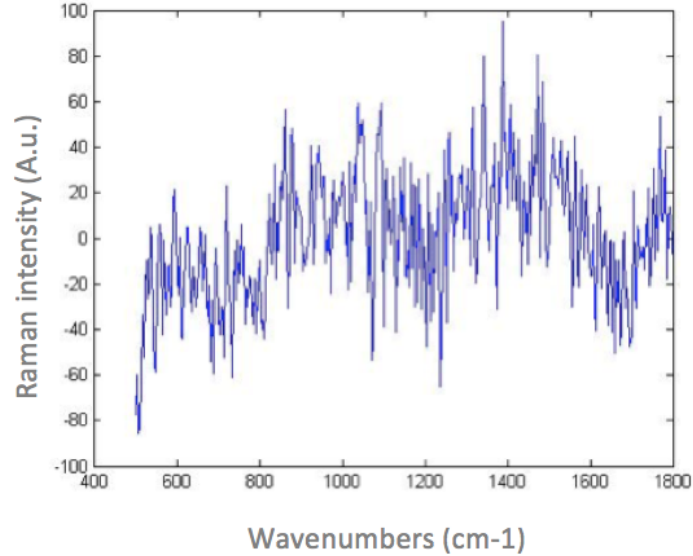


Figure 5.11: Subtracted Raman spectra of acrylamide on zein-SERS sensor from the background signature of the zein-SERS sensor.

use the original spectrum in the calibration curve calculations.

A calibration curve (Figure Figure 5.12) was obtained using different concentrations of acrylamide ranging from 10 mg/ml to 10 g/ml, specifically 10 mg/ml, 7.5 mg/ml, 2.5 mg/ml, 1 mg/l, 100 $\mu\text{g/ml}$, and 10 $\mu\text{g/ml}$. It was found that the intensity of the Raman peak at the location 1447 cm^{-1} increased with increasing concentration of acrylamide. Each value was obtained by averaging the intensity over at least 3 different locations on the edge of the formed “coffee ring” structure. It was found that there was a certain amount of variation between different spots. Standard deviation was 403, 216, 66, 18, 94, 6 and 0 for concentrations of 10 mg/ml to 10 $\mu\text{g/ml}$, specifically 10 mg/ml, 7.5 mg/ml, 2.5 mg/ml, 1 mg/l, 100 $\mu\text{g/ml}$, and 10 $\mu\text{g/ml}$, respectively. The slope of the calibration curve (Figure 5.12) was 0.12 and R^2 was 0.9325. On the other hand, when the intensity versus calibration was plotted on the log-log scale, the calibration curve obtained had a better R^2 value of 0.9687 (Figure 5.13). This calibration curve was used to determine the concentration of several samples by using the average intensity of 1447 cm^{-1} peak over at least 3 points. We estimated a sample’s concentration to be 5.2 mg/ml when it actually was 6 mg/ml by using concentration curve

linear equation. There was a 0.8 mg/ml error. For another sample of 1 mg/ml concentration, calculated concentration was 0.6 mg/ml, which caused 0.4 mg/ml error. When the intensity of a sample of 10 mg/ml concentration was used, the concentration was estimated to be 8.2 mg/ml. The variation was 1.8 mg/ml for 10 mg/ml sample. This variation may be the result of several factors. First, Surface Enhanced Raman measurements are known to exhibit a certain variability in the signal intensity due to the distribution of the so-called ‘hot spots’. Second, when working with a confocal microscope, the position, i.e. focus, of the objective affects the Raman intensity. When taking measurements at different spots, re-focusing was done. However, there might have been variation in the degree of focus that resulted in the intensity change observed in this study. Last, the local concentration of acrylamide molecules adsorbed to the surface while drying might differ at different locations and also in terms of orientation as well as thickness of the layers. Even though there was a certain variation at each point, which was unavoidable, there was a trend in which increasing concentration corresponded to increasing Raman peak intensity.

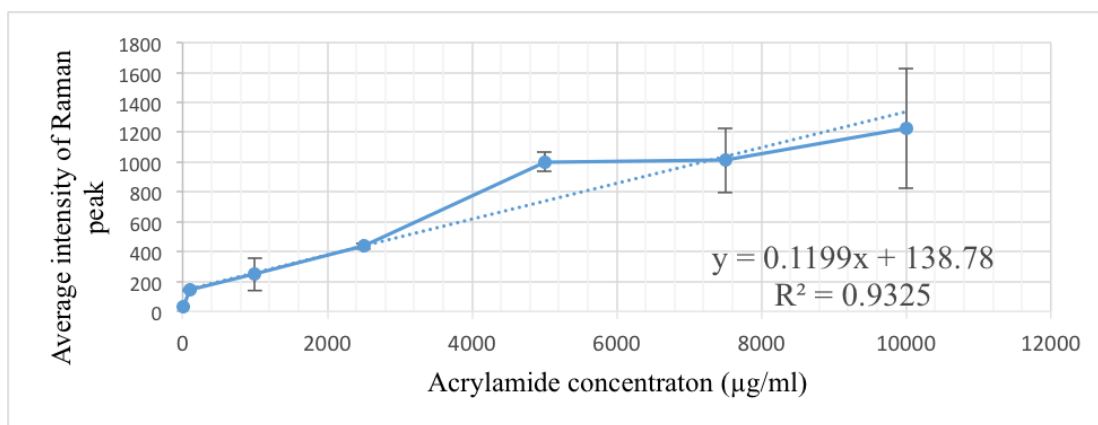


Figure 5.12: Calibration curve for different concentrations of acrylamide

At the concentration of 10 µg/ml, it was only possible to observe the characteristic Raman peak at one location among all the measurements taken on the sample. This means that the concentration was too low to form a clear coffee-ring structure and background signature became overwhelming, similar to the case of

glass slide. From this it was concluded that the limit of detection (LOD) for this set up was 10 $\mu\text{g}/\text{ml}$. This value was compared with the other LODs which were reported in the literature for the conventional systems. In the literature, LODs are generally reported as $\mu\text{g}/\text{kg}$ food. In the conventional systems, acrylamide is extracted from a given amount of food and then concentrated before being injected into chromatography systems, such as gas or liquid chromatography in tandem with mass spectroscopy. The extent of extraction and concentration processes determines the final composition of acrylamide (mass/volume solvent) in the sample to be analyzed. The amount of acrylamide in foodstuffs ranges from 150 - 4000 $\mu\text{g}/\text{kg}$ food (Keramat et al., 2011). The LODs reported in the literature varies between 30 $\mu\text{g}/\text{kg}$ and 0.1 $\mu\text{g}/\text{kg}$, depending on the technique used (Tekkeli et al., 2012). For example, LC-MS-MS systems reported gave a sensitivity of 25 $\mu\text{g}/\text{kg}$ for carbohydrate-based foods (Croft* et al., 2004), whereas the same system in another study was able to detect as low as 1 $\mu\text{g}/\text{kg}$ for baby food/infant formula samples (Jiao et al., 2005). On the other hand, GC-MS systems showed higher detection limits in general, such as 5 $\mu\text{g}/\text{kg}$ for coffee and coffee products (Soares et al., 2006), 5-50 $\mu\text{g}/\text{kg}$ for potato chips (Fernandes and Soares, 2007). However, in the cases of GC-MS-MS or GC was coupled with electron capture detector (ECD) it was possible to detect 0.1 $\mu\text{g}/\text{kg}$ acrylamide in potato crisps and French fries (Lee et al., 2007). When zein-SERS sensor is directly compared with the conventional techniques, it can be seen that it is not as sensitive as the other techniques. Even though SERS is considered to be a very sensitive technique in the examples of silver nanoparticles or metallic platforms on non-biodegradable surfaces, for our zein-SERS system there was a trade-off between sensitivity and biodegradability. However, depending on the extraction technique, the calibration curve obtained in this study could be applicable. For instance, Rosén and Hellenäs (2002) reported sample preparation starting with 4 g of crispbread, which had 35 $\mu\text{g}/\text{kg}$ acrylamide, and obtaining a 10 μl solution that is injected into a gas chromatograph. This protocol would result in having 14 $\mu\text{g}/\text{ml}$ in the final solution. A concentration of this level could be detected with the zein-SERS sensor reported

here. However, other extraction methods were such that the concentration in the final solution would be as low as 5 ng/ml, which would not be possible to detect with the zein-SERS sensor. Since these are extraction methods, they do not have sensitivity data and an optimization process is needed when the method is applied for food samples.

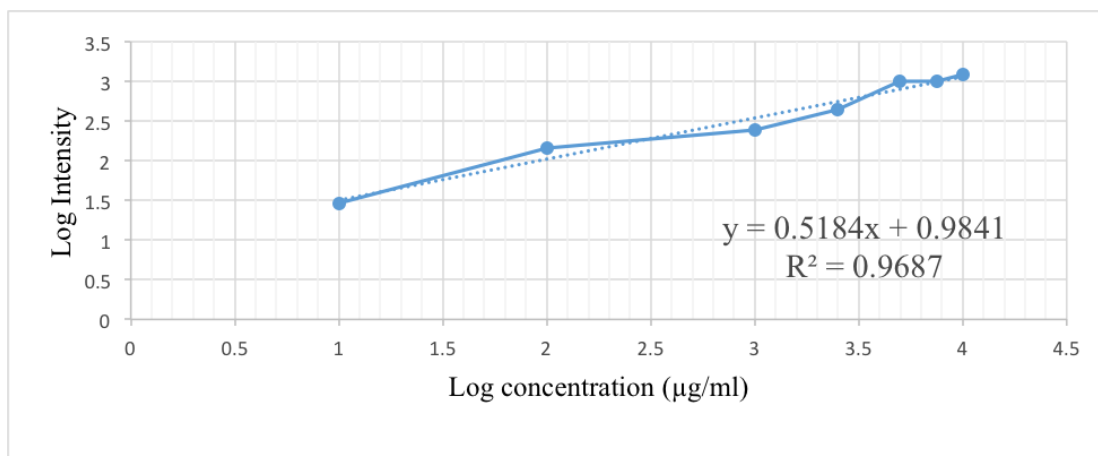


Figure 5.13: Log-log calibration curve for different concentrations of acrylamide

5.5 Conclusion

In this study, a zein/gold SERS platform was tested as a potential tool to detect acrylamide for the first time. Only 5 µl of acrylamide solution was used in detection. After the droplet was air-dried on the substrate, a ‘coffee ring’ structure was observed. The coffee ring method was utilized to detect acrylamide on the edge of the ring where the concentration is highest. It was found that the presence of acrylamide resulted in a SERS peak that did not exist in the background SERS spectrum of the sensor. This unique peak was at 1447 cm⁻¹. This peak was used to detect and quantify acrylamide in aqueous solutions and a calibration curve was obtained using acrylamide solutions within the range of 10 mg/ml and 10 µg/ml. After 10 µg/ml of concentration, it was not possible to observe the ring structure due to low concentration and for the 10 µg/ml concentration, it was only possible to observe 1447 cm⁻¹ peak at one location despite of the multiple

measurements taken on the ring structure. Further studies are needed to design a platform that has a better sensitivity. The error or variation for each concentration in the range of 0.4 mg/ml (for 1 mg/ml) and 1.8 mg/ml (for 10 mg/ml) was observed. Even though SERS was not found to be most accurate technique for quantification purposes, we still found that it gave reasonable approximation of the concentration in the given range with an R^2 value of 0.93 and 0.97 (for log-log calibration curve). This was a proof-of-concept study to investigate the potential of a SERS sensor designed on a biodegradable platform and it was shown that this method can be potentially used with a careful design of acrylamide extraction from food samples.

CHAPTER 6

DETECTION OF PEANUT ALLERGEN, ARA H1, USING ZEIN - SERS PLATFORM¹

6.1 Abstract

Peanuts are among the most common food allergies, which may result in life-threatening reactions in certain people. For this reason, it is very important to monitor the presence of peanuts in the food system. Biosensors are an emerging way of detecting allergen proteins. In this research, we present a surface enhanced Raman spectroscopy (SERS) technique to detect the main allergen protein, Ara h1. The sensors were biodegradable and made out of a corn protein, zein. Nanophotonic structures on zein films consisted of gold coated pyramid structures. It was found that both detection and quantification was possible by using a statistical clustering technique principal component analysis (PCA). An optimization in data processing yielded the result that baseline correction and shorter data collection times were needed in order to successfully cluster data. Furthermore, specificity of the sensor was provided by functionalizing the surface with monoclonal antibodies of Ara h1. Antibody functionalization, and Ara h1 capturing was tested and identified by also utilizing PCA analysis. As a proof-of-concept, this study showed that a biodegradable platform can be used in detection of a peanut allergen protein, Ara h1, by using surface enhanced Raman spectroscopy.

¹This work is currently under review as P. G. Gezer, G. L. Liu, J. L. Kokini “Development of a biodegradable sensor platform from gold coated zein nanophotonic films to detect peanut allergen, Ara h1, using surface enhanced raman spectroscopy” Food Control.

6.2 Introduction

Peanuts are one of the leading causes of food allergy, along with tree nuts, cow's milk, eggs, fish, seafood, soy, wheat and additives (Osterballe et al., 2005). The reaction to peanuts ranges from mild oral effects to potentially fatal ones such as anaphylaxis, which results in itchy rash, low blood pressure and throat swelling. Currently, there is no known antidote for this allergy. Prevention relies solely on avoiding peanuts and peanut containing food products (Xiaoyan et al., 2014). For this reason, it is very important for the food industry to monitor the presence and cross-contamination of peanut proteins in various food products. The most commonly used monitoring technique is based on enzyme-linked immunosorbent assays (ELISA), by either using monoclonal or polyclonal antibodies (Pomés et al., 2003). These methods target the detection of the allergenic proteins of peanuts, which are identified as Ara h1 - h8. Among these, Ara h1 constitutes the largest portion of proteins in peanuts. In addition, it causes allergic reactions in more than 95 % of the susceptible population (Koppelman et al., 2001; Burks et al., 1992). Detection systems as a result, target mostly the Ara h1 protein. Besides detecting the protein itself, there are several studies that detect the DNA responsible for the production of Ara h1 protein. Polymerase chain reaction (PCR) with gel electrophoresis, real-time PCR and PCR-ELISA are some of the techniques that have been utilized to detect DNA of Ara h1 (Wen et al., 2007).

6.3 Materials and Methods

6.3.1 Materials used

Peanut allergen, natural Ara h1 and its monoclonal antibody, 2F7 Anti Ara h1 were purchased from Indoor Biotechnologies (Charlottesville, VA). In order to avoid freeze-thaw cycles, both allergen protein and antibody was divided into 5 or 10 μ l aliquots and stored at Micro Nano Technology Lab Building, in Bionano

Lab facilities in a refrigerator of which the temperature was set at -20°C . Required number of aliquots were thawed at room temperature before direct use. The concentrations used for Ara h1 were 1.4 mg/ml, 0.5 mg/ml, 0.25 mg/ml and 0.14 mg/ml. 11-Mercaptoundecanoic acid (11-MUA), N-(3-Dimethylaminopropyl)-N-ethylcarbodiimide hydrochloride (EDC) and (N-Hydroxysuccinimide) NHS needed to crosslink the 2F7 Anti Ara h1 onto the zein/gold SERS platform were purchased from Sigma Aldrich. 11-MUA and NHS were stored in a refrigerator, whereas EDC was stored at -20°C . The solutions were freshly prepared before each use. 11-MUA solutions were prepared in 100% ethanol. For all the other solutions or dilutions, MilliQ purified water was used.

6.3.2 Preparation of SERS-active substrates

SERS-active zein substrates were fabricated as described in Chapter 4. Polydimethylsiloxane (PDMS) with positive pyramid structures were used as a template. The template had pyramids with the base squared dimensions of $2\ \mu\text{m}$ by $2\ \mu\text{m}$ and a height of $2.1\ \mu\text{m}$. The PDMS template was coated with 200 nm gold by using e-beam evaporator. The details of these procedures are given in Chapter 4. Zein solution was prepared by first dissolving zein in 75 % ethanol (1g: 5 mL) and mixing with oleic acid and emulsifier (1g zein: 1g oleic acid: 0.05 g emulsifier). This solution was stirred on a hot plate for 5 minutes. After ultrasonification to remove air bubbles, zein solution was cast on PDMS template with gold coating. The solution cast on PDMS was allowed to dry and form a film and after drying in a vacuum dessicator at room temperature, dried zein films were cut and peeled off from the PDMS base. 200 nm gold along with the pyramid structures were transferred onto zein, resulting in an inverted pyramid structure on zein. Macro and SEM images are shown in Chapter 4.

6.3.3 Functionalization of zein-SERS substrates

The gold surface of zein-SERS substrates were functionalized with the monoclonal antibody of Ara h1, 2F7. The functionalization scheme is illustrated in Figure 6.1. First, the surface was functionalized with 11-MUA ethanolic solution (2 M) by dropping 50 μl of solution on the gold surface of the SERS platform. The 11-MUA functionalized gold/zein platform was kept in a humidity-controlled incubator for 16 hours. Then, the surface was rinsed both with ethanol and water, followed by drying with a nitrogen stream. Second, carboxylic groups of 11-MUA were activated by the EDC: NHS solution. A 1:1 mixture of 0.4 M EDC and 0.1 M NHS was applied to the gold surface by dropping 50 μl of solution and incubating for 45 minutes. The same washing procedure was applied as before. Third, 30 μl of anti-Ara h1 with the concentration of 50 $\mu\text{g}/\text{ml}$ was dropped on top of the EDC-NHS activated surface. It was incubated for 30 minutes, before washing out the excess using the same procedure.

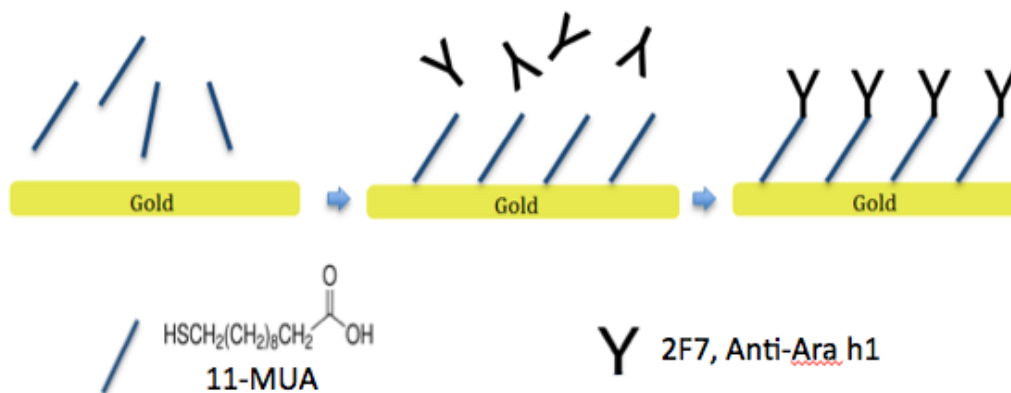


Figure 6.1: Schematic illustration of the functionalization of the gold surface

6.3.4 Raman spectroscopy measurements

Samples for Raman spectroscopy were prepared by placing 2 μl of Ara h1 solution at one of the concentrations used in this study on one of the two platforms (either smooth gold surface or zein-SERS sensor) tested in this study and letting

it air dry at room temperature. The zein/gold functionalized surface of the gold functionalized surface was immobilized onto a glass slide with tape in order to obtain a flat and stable surface. Background Raman spectra were obtained on the nanophotonic structures that did not have any Ara h1 protein solution for comparison with those that would have the protein solution. The HORIBA LabRAM HR Raman Spectroscope was used with a 532 nm laser. The hole diameter was 300 μm , the slit selected was 100 μm and the grating used was 300 lines/mm. The Raman spectrum was recorded in the wavenumber range between 500 and 1800 cm^{-1} . Spectra were collected for 30 times for a period of 1 second of 5 times for a period of 1 second. Each individual final spectrum used is an average of these acquisitions. X-Y Mapping was used to collect data on a 30 μm by 30 μm square. For the functionalized samples, after Ara h1 solution application with the concentration of 0.2 mg/ml, the surface was dried and the surface of the SERS film was washed with ethanol and water.

Data analysis

For each Raman spectrum, baseline correction was carried out in order to eliminate the effect of fluorescence interference. A polynomial was fit to the baseline with the “baseline correction” option of the LabSpec 5 (provided by Horiba). Additional points were added to the baseline to ensure a perfect fit, if needed. This baseline was subtracted from the Raman spectrum. Principal Component Analysis (PCA) was done using Matlab R2013a software. Different Principal Components (PCs) were plotted and color-coded by using the same software.

6.4 Results and Discussion

6.4.1 Detection of Ara h1 on zein-SERS substrates

As discussed in Chapter 5 with our studies related to detection of acrylamide using SERS, Raman spectra using zein-SERS substrate give a background signature. For this reason, the first step in this study was to identify the characteristic Raman peaks resulting from the allergen protein, Ara h1. However, since both Ara h1 and underlying zein are proteins, all of the peaks overlapped. This resulted in a challenge in detection and quantification of Ara h1 through our zein-gold platform. However, as reported in the literature, a statistical clustering technique, Principal Component Analysis (PCA) can be potentially utilized to discriminate various samples from each other. In this study, the PCA technique was investigated and was used to obtain characteristic clusters of the raw Raman spectra data, baseline corrected data at different acquisition times as well as different concentration of the allergen protein.

For each sensor, Raman spectra were collected by mapping measurements at 9 separate points. Example spectra are shown in Figure 6.2. Raman spectra in Figure 6.2.a and b were collected by using 30 separate measurements at each point for 1 second each, and Raman spectra in Figure 6.2.c and d were collected by using 5 separate measurements at each point for 1 second each. Figure 6.2a and c show the background signal coming from the zein-SERS sensor, whereas Figure 6.2.b and d represents the spectra when Ara h1 was deposited on the zein-SERS sensor. As evident from these figures, there was variable and significant amount of auto fluorescence in the Raman signal.

Furthermore, there was not a unique marker peak that resulted from the addition of Ara h1 on the zein-SERS platform. First, PCA analysis was applied to the raw data and the results are shown in Figure 6.3. In principal component analysis, generally biplots are used in which one axis is one of the principal component and the other axis is another principal component. For most of the cases,

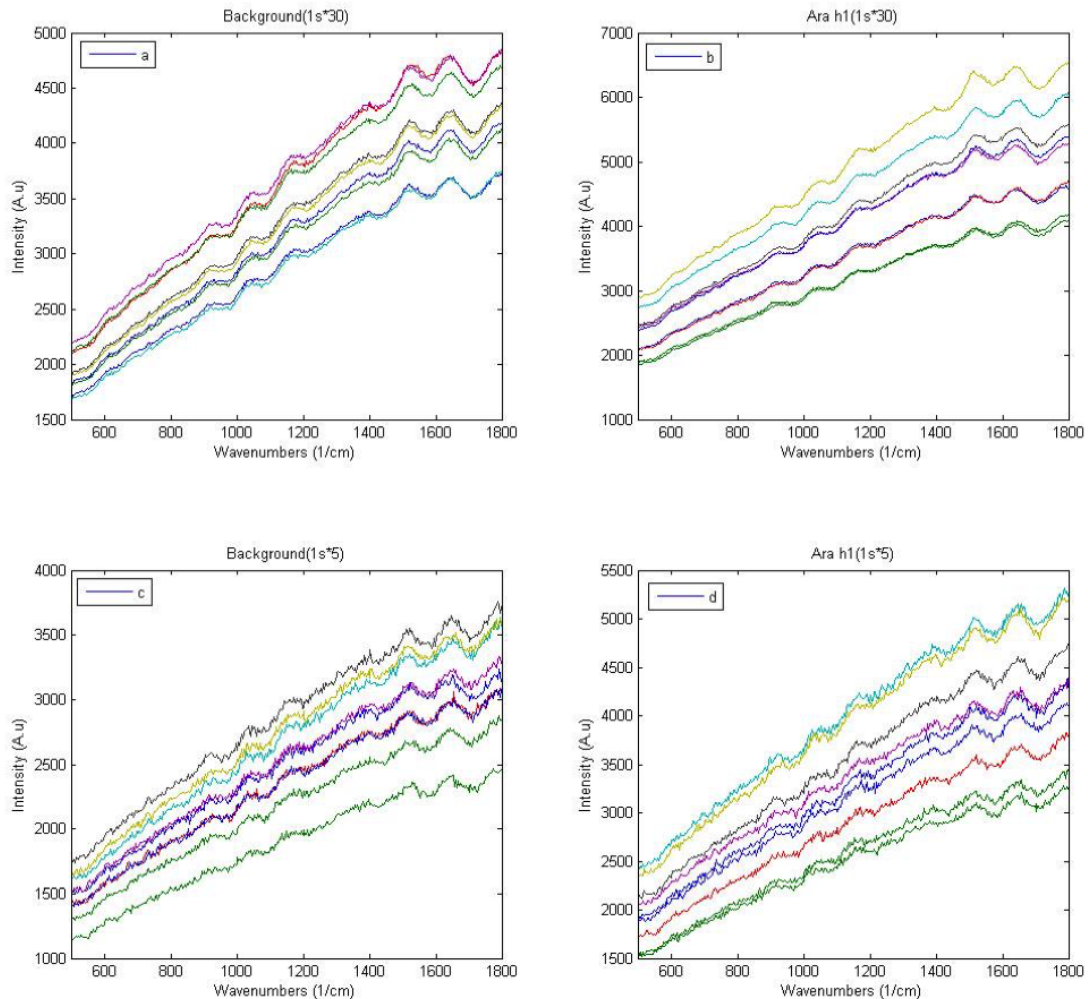


Figure 6.2: Raman spectra of a) background of the zein-SERS sensor (average of 30 measurements 1 second each) b) Ara h1 on zein-SERS sensor (average of 30 measurements 1 second each) c) background of the zein-SERS sensor (average of 5 measurements 1 second each) d) Ara h1 on zein-SERS sensor (average of 5 measurements 1 second each) Different colors represent individual Raman spectra at mapping points.

PC1 and PC2 is plotted versus each other since those are the two that represent the largest variance in data. However, in certain cases other principal component biplots might be used if the variance coming from, let's say 3rd component is more relevant to the analysis is being conducted than the 1st or 2nd principal component. These biplots help to visualize clusters of data, which has similar variance from the data set, as a result which show similar results to each other. This way one can understand trends and or similarities in data that is otherwise

too complex. In the context of Raman spectroscopy, PCA biplots might be able to differentiate between different samples and/or different concentrations of the sample.

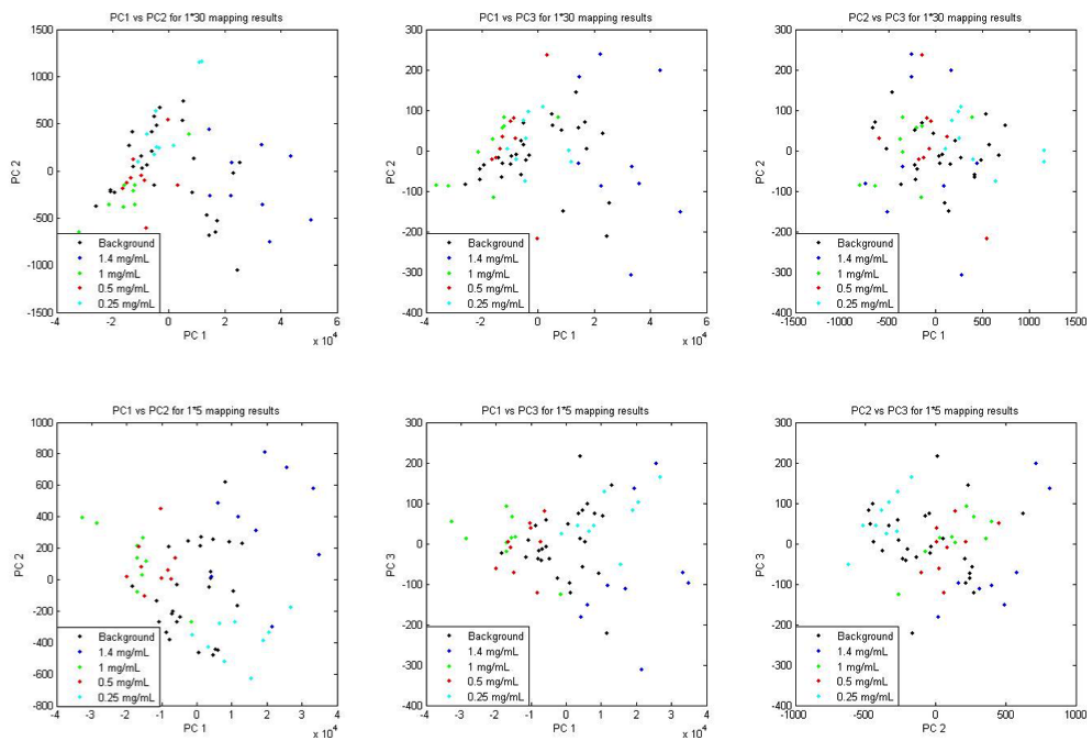


Figure 6.3: Principal component analysis of Raman spectra for the background and different concentrations of Ara h1. Top-left: PC1 vs PC2, Top-middle: PC1 vs PC3, Top-right: PC2 vs PC3, Bottom-left: PC1 vs PC2, Bottom -middle: PC1 vs PC3, Bottom-right: PC2 vs PC3. PC1 is usually the component that explains the variability best and PC2 is second best with the condition that it is orthogonal to PC1 and PC3 is the third best with the condition that it is orthogonal to both PC1 and PC2

Top three plots represent PCA analysis for the 30 measurements at 1 second acquisition time, whereas bottom three plots show the 5 measurements at 1 second acquisition time measurements for PC1 vs PC2, PC1 vs PC3 and PC2 vs PC3 from left to right. None of the Principal Component Analysis technique gave a clear clustering between the background or different concentrations. The reason for this is that varying levels of autofluorescence contributes the largest variation in the data, clouding useful correlations between Raman spectra, and thus the

PCA method does not enable differentiation.

Auto-fluorescence arising from proteins causes a broad band, which can be observed in Figure 6.4. In order to correct for the auto-fluorescence, baseline correction was done to make the baseline linear and eliminate the effect of the broad band and a couple of examples of the resulting spectra are shown in Figure 6.4. Raman spectra in Figure 6.4.a and b were baseline subtracted which is the average of 30 measurements at 1second acquisition time. Figure 6.4.c and d were collected by using the average of 5 measurements at 1 second acquisition time and baseline corrected through polynomial fitting and subtracting. Figure 6.4.a and c shows the background signal coming from the zein-SERS sensor, and Figure 6.4.b and c represents the spectra when Ara h1 was deposited on the zein-SERS sensor. It was found that baseline correction was successful in terms of eliminating the variation as a result of auto-fluorescence. As can be seen in Figure 6.4, spectra at different mapping points (different colors) appear to have the same baseline, intensities and characteristic peaks. It was also found that the Raman spectrum collection was uniform as the mapping points for each of the collection overlapped.

Principal component analysis was applied to the baseline corrected spectra collected both by the average of 30 measurements at 1second (1s*30 acquisition) time and the average of 5 measurements at 1second (1s*5 acquisition) time. The results for 1s*30 acquisition time are shown in Figure 6.5. It was found that none of the principal component comparisons were able to differentiate between Ara h1 concentrations and the background. On the other hand, 1s*5 acquisition time principal component analysis showed promising results (Figure 6.6). Both plots of the Raman signals plotted vs. for PC1 and PC2 as well as PC2 and PC3, showed clear differences between the background data and the data with the presence of Ara h1 allergen protein. Furthermore, it was possible to cluster different concentrations of Ara h1 together, which is illustrated in Figure 6.7.

As shown in Figure 7, it was found that when Raman spectral intensity data was plotted vs. PC1 and PC2 as well as PC2 and PC3 it was possible to separate the data into clusters of different concentrations of Ara h1 as well as the back-

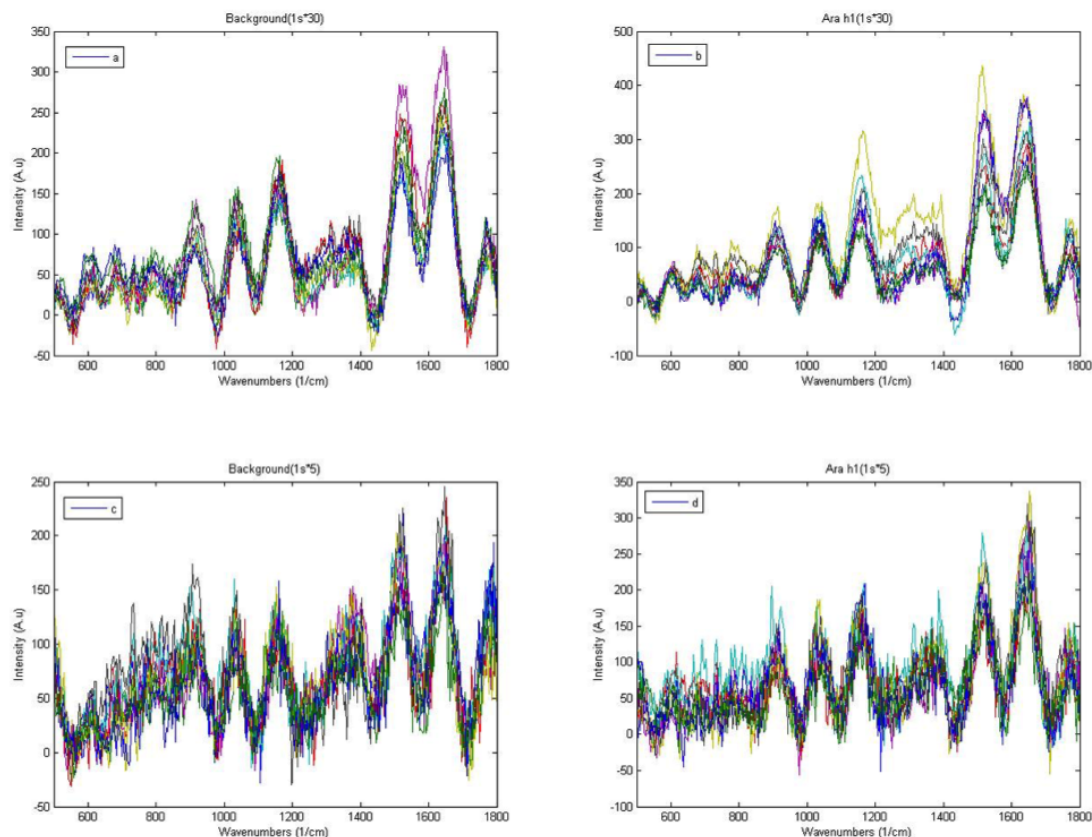


Figure 6.4: Baseline corrected Raman spectra of a) background of the zein-SERS sensor (1s*30 acquisition time) b) Ara h1 on zein-SERS sensor (1s*30 acquisition time) c) background of the zein-SERS sensor (1s*5 acquisition time) d) Ara h1 on zein-SERS sensor (1s*5 acquisition time)

ground enabling the separation of Raman spectral data of different concentrations. In both normalized Raman spectral data plots vs PC 1 and PC 2 as well as PC 2 and PC 3 plots, background of zein-SERS sensors (black stars) were clustered in a separate region than the Ara h1 protein. It was also observed that different concentrations, 1.4 mg/ml (red dots), 1 mg/ml (blue dots), and 0.25 mg/ml (green dots), were clustered together and formed the elliptic clusters expected from a plot of the data against two principal components.

Based on the PCA, it was concluded that it is not possible to differentiate different concentrations of Ara h1 by using raw Raman data of SERS data which has not been corrected for fluorescence through baseline correction. This results

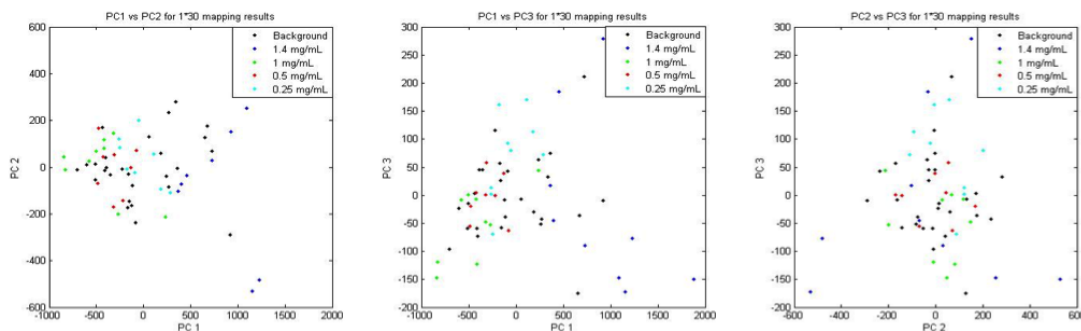


Figure 6.5: Principal component analysis of baseline-corrected Raman spectra for the background and different concentrations of Ara h1 average of 30 measurements at 1second (1s*30 acquisition time) I added the explanation before this the way you like OK. Left: normalized Raman spectral data plotted vs PC1 and PC2, Middle: normalized Raman spectral data plotted vs PC1 and PC3, Right: normalized Raman spectral data plotted vs PC2 and PC3.

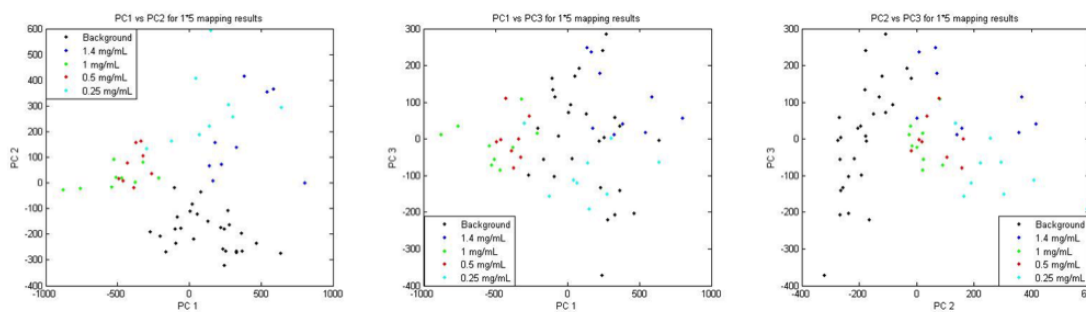


Figure 6.6: Principal component analysis of baseline-corrected normalized Raman spectra for the background and different concentrations of Ara h1 (1s*5 acquisition time). Left: normalized Raman spectral data plotted vs PC1 and PC2, Middle: normalized Raman spectral data plotted vs PC1 and PC3, Right: normalized Raman spectral data plotted vs PC2 and PC3.

from the fact that different levels of auto-fluorescence make the biggest contribution to the PCA, which does not leave room for differentiation between samples. Furthermore, when the acquisition time was kept longer (1s*30), differentiation was not achieved. However, we found that when the acquisition time is shorter, (1s*5) in this case, it was possible to identify the presence and quantify Ara h1 allergen protein on zein-SERS sensors.

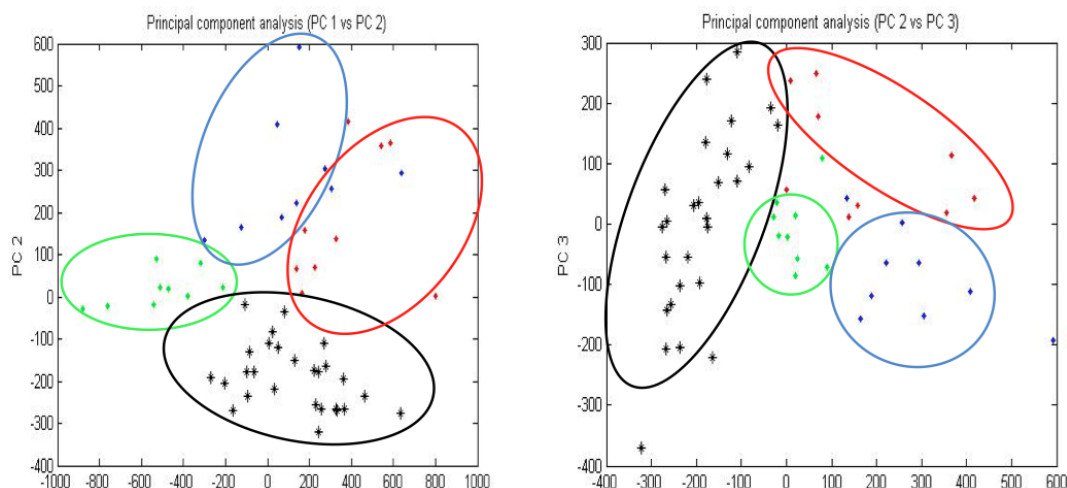


Figure 6.7: Principal component analysis of baseline-corrected Raman spectra for the background and different concentrations of Ara h1 (1s*5 acquisition time). Left: Normalized Raman spectral intensity data plotted vs the first two principal components PC1 and PC2, Right: Normalized Raman spectral intensity data plotted with respect to principal components PC2 and PC3, Black: background spectral intensity data of zein-SERS platform, Red: Normalized Spectral intensity data for 1.4 mg/ml Ara h1, Green: Normalized Spectral intensity data for 1 mg/ml, Blue: 0.25 Normalized Spectral intensity data for mg/ml Ara h1

6.4.2 Limit of detection for zein-SERS sensors

Limit of detection (LOD) is considered to be the concentration at or below which is not possible to detect the presence of the analyte using a sensor. In order to estimate the LOD, serial dilutions were made and found that the concentration of 0.14 mg/ml would be the LOD for this zein-SERS sensor. At this concentration, it was not possible to discriminate the background from the case in which Ara h1 added to the sensor. Figure 6.8 shows three different principal component analysis plots (PC 1 vs PC 2, PC 1 vs PC 3 and PC 2 vs PC 3). None of these plots were able to form distinguished clusters, unlike higher concentrations of Ara h1. From this we can conclude that it would not be possible to detect the presence of Ara h1 if it is less concentrated than 0.14 mg/ml in a given sample solution with our zein-SERS sensor. The original concentration of purified protein was 1.4 mg/ml, which was provided in a very minimal amount, after one-log reduction

in the concentration, it was not possible to differentiate its presence from the background. However it was possible to differentiate double amount of it. For this reason, we believe it is safe to say that the LOD is 0.14 mg/ml.

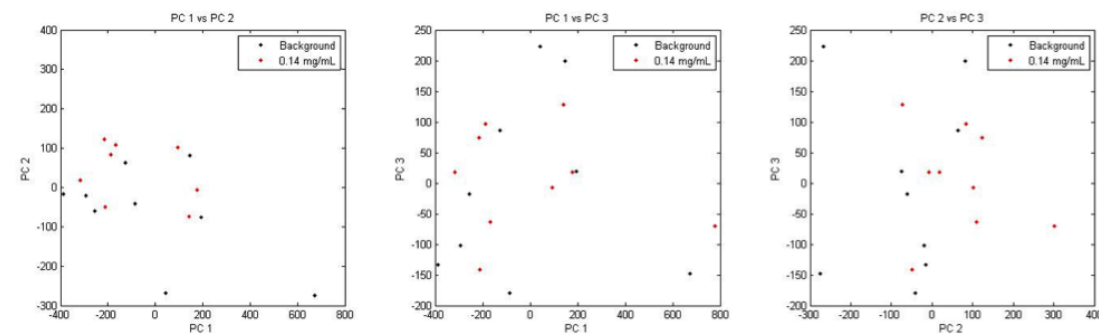


Figure 6.8: Principal component analysis for 0.14 mg/ml Ara h1 protein on zein-SERS sensor. From left to right: PC1 vs PC2, PC1 vs PC3 and PC2 and PC3.

6.4.3 Antibody capturing of Ara h1 on zein-SERS substrates

In order to functionalize the surface with antibodies, there is a need for a linker molecule. We used 11-MUA as it has both SH and CH₃ ends. SH molecular group is capable of forming bonds with gold surfaces. Many functionalization protocols require the surface to be immersed in the solution containing the target molecule, however for the zein-SERS platform, this posed a problem of disintegration because zein is soluble in 70% ethanol. Figure 6.9 shows the disintegration of the zein-SERS sensor after being immersed in ethanol solution of 11-MUA.

In order to avoid disintegration, a droplet of 2 M 11-MUA was dropped on the area covering only the pyramid-patterned area was used to functionalize the surface. This also created some deformation on the sensor, due to the absorbance of the solvents. In order to account for the effect of the solvents being absorbed by the sensor, a control consisting of the original gold zein film was used. All functionalization steps were applied to the control, except for the active materials (11-MUA, EDC-NHS solution, 2F7 antibody and Ara h1). For instance, the same volume of ethanol was used instead of the 11-MUA in ethanol solution or same

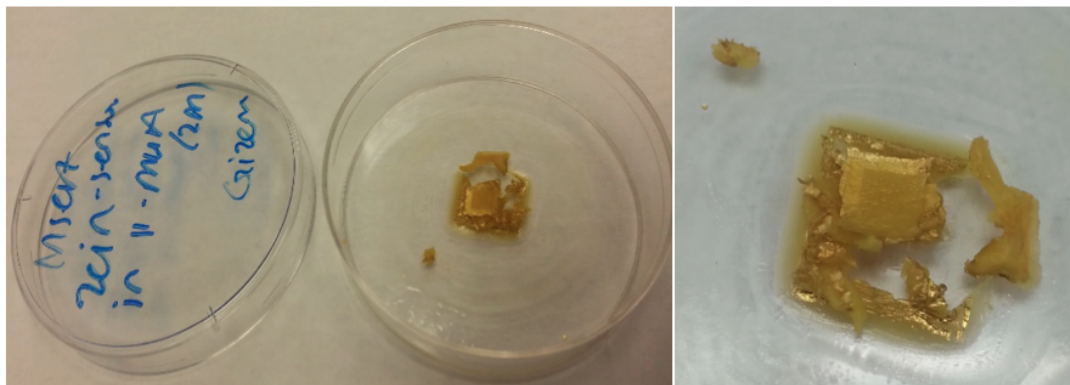


Figure 6.9: Left: Zein-SERS platform, after being immersed in 2M of 11-MUA solution inside a petri dish. Right: Close-up image of the zein-SERS sensor.

volume of water was used instead of the aqueous solution of antibody. The control sensor was also exposed to all the washing and drying steps that occurred during the process of functionalization. For simplicity, in this section, this control sensor will be referred to as background zein-SERS sensor, as it represents the potential Raman signals coming from the sensor + side effects of the functionalization process.

Furthermore, a gold surface (coated on PET) and gold coated pyramid patterns on PET were also used as a control to ensure the functionalization and Ara h1 capturing was successful. Figure 6.10 shows the baseline subtracted and averaged Raman signatures of Ara h1 on functionalized surfaces after rinsing process: smooth gold surface, PET-SERS substrate, and zein-SERS substrate. As expected, smooth gold surface gave the lowest intensity signal, since there is no SERS effect in the absence of nanopatterns. PET-SERS substrate showed enhancement in the Raman signal of the protein peaks, whereas zein-SERS showed the highest signal. This does enhancement observed with the zein-SERS surface might have been caused by a cumulative effect of the background plus Ara h1 protein.

In order to discriminate between the background, antibody functionalization and captured Ara h1, PCA analysis was conducted for Raman spectra collected on zein-SERS platform as well as smooth-gold and PET-gold-pyramid surface.

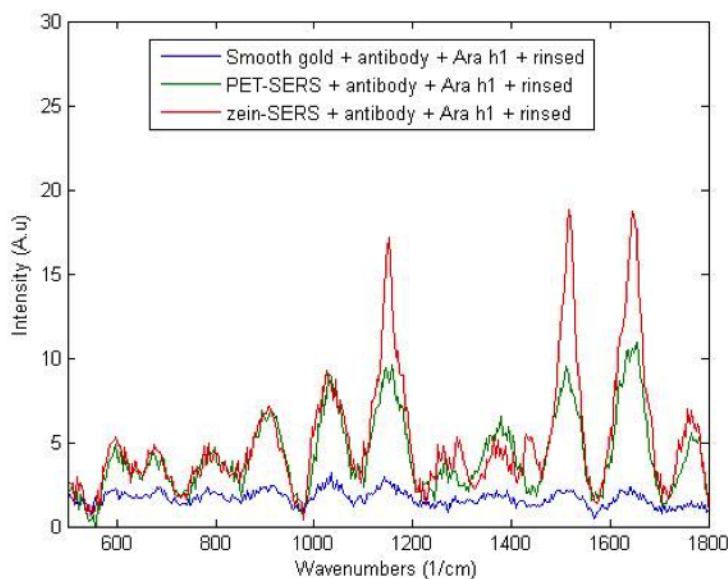


Figure 6.10: Raman spectra generated by Ara h1 protein captured with 2F7 antibody on different platforms. Red: zein-SERS, green: PET-SERS, blue: smooth gold

Plots of PC1 vs PC2 and PC1 and PC3 are shown in Figure 6.11. The color representations are as follows: black: baseline-corrected Raman spectra for background zein-SERS sensor, pink: antibody-functionalized zein-SERS sensor, red: Ara h1 protein captured by antibody-functionalized zein-SERS sensor, cyan: Ara h1 protein on functionalized zein-SERS sensor-not rinsed, blue: Ara h1 protein captured by antibody-functionalized smooth gold surface, and green: Ara h1 protein captured by antibody-functionalized PET-SERS substrate. It was observed that principal component 1 was successful differentiating different platforms from each other, namely smooth-gold (blue), PET-SERS (green) and zein-SERS (all the other colors), however it was not successful in differentiating the presence/absence of Ara h1 on zein-SERS. It was concluded that the first principal component was representative of different substrates in this case and was not reliable in discriminating Ara h1 protein captured by the antibody.

Plots of normalize Raman intensity scores vs PC2 and PC3 gave successful results in clustering these three cases in separate groups (Figure 6.12. Antibody

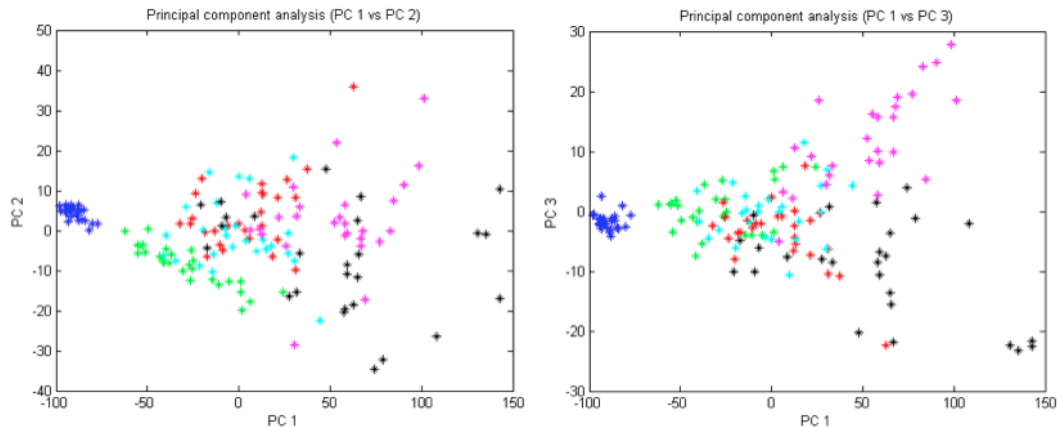


Figure 6.11: Principal component analysis PC1 vs PC2 (Left) and PC1 vs PC3 (Right) of baseline-corrected Raman spectra for background zein-SERS sensor (black), antibody-functionalized zein-SERS sensor (pink), Ara h1 protein captured by antibody-functionalized zein-SERS sensor (red), Ara h1 protein on functionalized zein-SERS sensor-not rinsed(cyan), Ara h1 protein captured by antibody-functionalized smooth gold surface (blue), and Ara h1 protein captured by antibody-functionalized PET-SERS substrate (green).

functionalized zein-SERS sensor formed a separate cluster (blue circle) compared to the background (green circle), which indicated the ability of PCA to discriminate successfully the functionalization of the antibody on the surface. In addition, Ara h1 captured with these antibodies also ended up in a different cluster (red). This shows that it is possible to differentiate the presence of Ara h1 protein that is captured by 2F7 monoclonal antibody which was immobilized onto the surface of zein-SERS substrate. To further validate the correlation of the Ara h1 cluster (red) with the presence of protein, a comparison made by adding the Raman spectra of the non-zein substrates into the PCA analysis.

Figure 6.13 shows the plot for PC 2 vs PC 3 for 5 different cases: Ara h1 on smooth gold surface (cyan), Ara h1 on PET-SERS substrate (green), Ara h1 on zein-SERS substrate (red), antibody-functionalized zein-SERS substrate (blue) and background of zein-SERS sensor (black). Whenever Ara h1 protein was present on a given substrate, it fell in the red cluster. This indicates that analysis of the Raman spectra by plotting normalized scores vs. PC 2 and PC 3 is a successful method to detect the presence of Ara h1 for our given system.

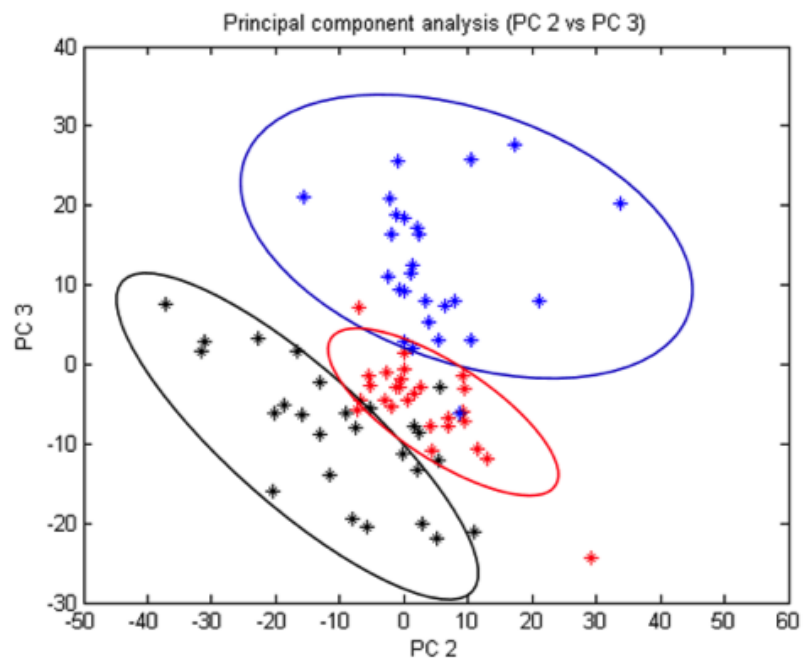


Figure 6.12: Principal component analysis (PC2 vs PC3) of baseline-corrected Raman spectra for background zein-SERS sensor (black), antibody-functionalized zein-SERS sensor (blue) and Ara h1 protein captured by antibody-functionalized zein-SERS sensor (red).

Rinsing process is applied to get rid of the excess Ara h1 that was not bound to the monoclonal antibody on the surface, which provides specificity. An experiment was carried out to compare the before and after rinsing of Ara h1 on the functionalized surface. PCA analysis (Figure 6.14) showed that before (cyan color) and after (red color) rinsing fell inside the same cluster, with a slight shift within the cluster after the rinsing process. This result proved that the red cluster is consistently correlated with Ara h1 protein. In addition, 2F7 monoclonal antibody was successful in bonding to the protein as evident by the signal after the rinsing process.

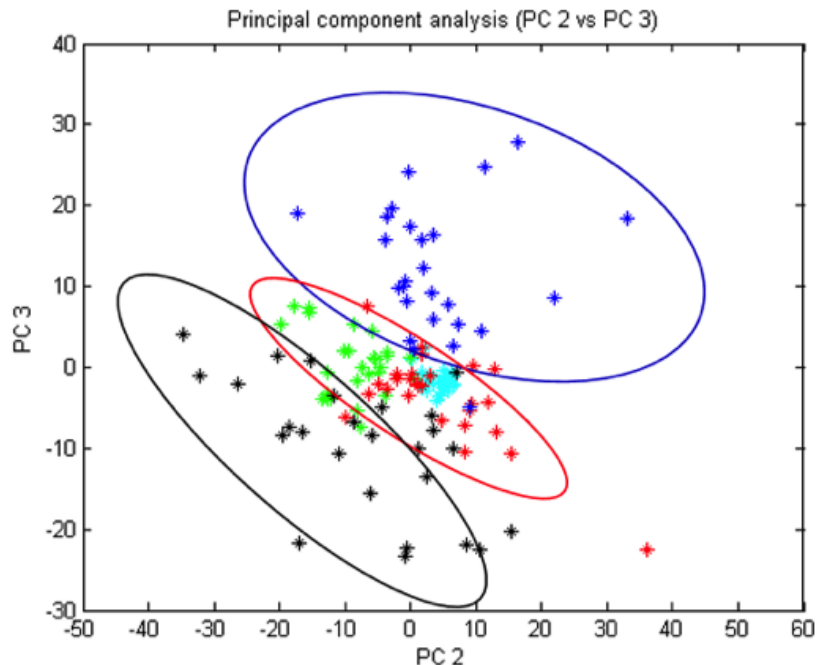


Figure 6.13: Principal component analysis (PC2 vs PC3) of baseline-corrected Raman spectra for background zein-SERS sensor (black), antibody-functionalized zein-SERS sensor (blue) and Ara h1 protein captured by antibody-functionalized zein-SERS sensor (red), Ara h1 protein captured by antibody-functionalized smooth gold surface (cyan), Ara h1 protein captured by antibody-functionalized PET-SERS substrate (green).

6.5 Conclusion

In this research, detecting peanut allergen protein, Ara h1 on a biodegradable SERS platform was developed for the first time. It was possible to detect and quantify Ara h1 protein by using a clustering technique called principal component analysis (PCA). Even though, background of the sensor overlapped with the peaks obtained from Ara h1, PCA method was found successful to differentiate Ara h1 with varying concentrations to separate clusters. This was only achieved when the baseline corrected Raman spectra was used, raw spectra did not give enough differentiation through PCA analysis. Furthermore, specificity of the sensor was provided through functionalization of the gold surface with monoclonal antibody of Ara h1. PCA analysis enabled distinction of Ara h1 protein

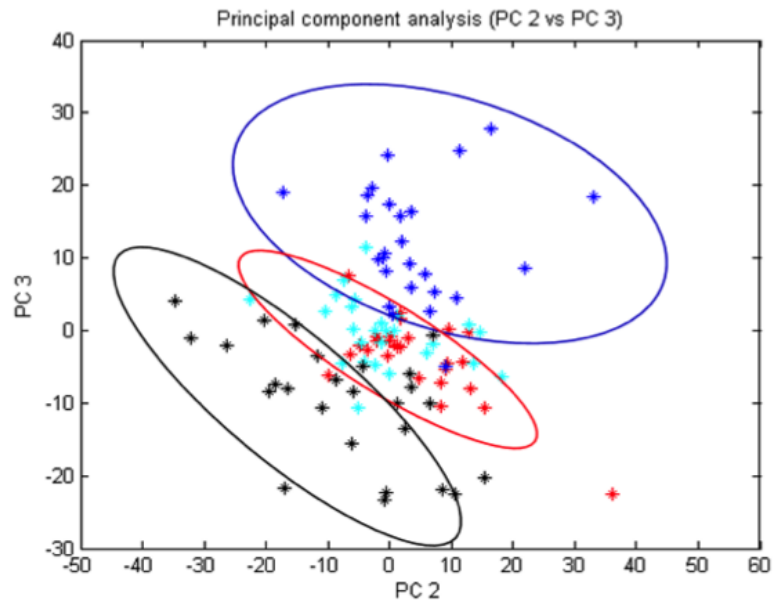


Figure 6.14: Principal component analysis (PC2 vs PC3) of baseline-corrected Raman spectra for background zein-SERS sensor (black), antibody-functionalized zein-SERS sensor (blue) and Ara h1 protein captured by antibody-functionalized zein-SERS sensor (red), Ara h1 protein on functionalized zein-SERS sensor- not rinsed(cyan).

captured by antibodies from background of the sensor, as well as only antibody-functionalized surface. This was a proof-of-concept that zein-SERS sensors can be used in detecting allergen protein, Ara h1 by capturing it with monoclonal antibodies. Further studies are needed to improve sensitivity, as well as application to real food systems.

CHAPTER 7

CONCLUSION

Throughout the research that led to this dissertation, the potential of utilizing zein, a corn protein, as a biodegradable sensor platform was investigated. First, zein film formation and effect of different processing on zein's surface properties was studied. It was found that a non-destructive soft lithography method is capable of engineering zein's surface properties without changing the bulk film properties. This is an important property in sensor platform development. Specifically, casting zein on a hydrophilic surface, oxygen plasma exposed PDMS, as opposed to a hydrophilic surface, regular PDMS resulted in hydrophilic zein film surface. This kind of surface property makes many practical applications possible, such as cell and tissue adhesion, microfluidic platforms, metal adhesion onto zein films to name a few. The role of a plasticizer, oleic acid along with the amphiphilic protein zein was examined in the process of self-assembly during film formation. Second, simultaneous transfer of three dimensional metallic sub-micron and nanostructures was achieved. The resultant nanophotonic zein films formed the base of a platform for an optical sensing technique, called Surface Enhanced Raman Spectroscopy (SERS). SERS is sensitive molecular fingerprinting technique, which has a potential to be an on field method with hand-held portable versions of Raman spectrometers.

The zein nanophotonic sensor platform was tested for two different analytes. First, ability of the sensor to detect a smaller food contaminant, acrylamide, was investigated. Acrylamide is a by-product of Maillard reaction that occurs in certain high temperature processing of food products, such as potato chips, french fries and toasted bread. Quantitative measurement for acrylamide with

the help of a characteristic peak and calibration curve for acrylamide. Sensitivity level was 10 $\mu\text{g}/\text{mg}$ in a model system. Second, the ability of the sensor to detect a larger peanut allergen protein was examined. Peanut allergy is one of the most common food allergies, and in certain individuals it might result in life-threatening reactions. Ara h1, which was the target protein for this research, comprises the highest percentage of all identified allergenic peanut proteins. In addition, it causes almost in 100% of the allergic people. For this reason, it is very important to develop tools that can detect Ara h1 protein. Feasibility of using the zein-SERS platform in detecting this allergen was studied. With the help of a statistical clustering technique called principal component analysis, it was possible to detect and quantify Ara h1 protein. In addition, sensitivity of the sensor was achieved by functionalizing the surface with monoclonal antibodies that attaches to Ara h1. The limit of detection of this sensor was found to be 0.14 mg/ml.

With this dissertation, gold coated zein films with nanophotonic patterns were shown to be able to detect both acrylamide and Ara h1 by using SERS for the first time as a proof-of-concept. In the future, more work is needed to improve the sensitivity level of these sensors. This could be achieved by either designing different nanophotonic patterns to transfer onto zein, working with different analytes or further optimizing detection parameters. We hope that, this research will help advance the investigation and use of biodegradable platforms in sensing technology in the future.

CHAPTER 8

REFERENCES

- Aguiar, H., Serra, J., González, P., and León, B. (2009). Structural study of sol-gel silicate glasses by ir and raman spectroscopies. *Journal of Non-Crystalline Solids*, 355(8):475–480.
- Al-Muhsen, S., Clarke, A. E., and Kagan, R. S. (2003). Peanut allergy: an overview. *Canadian Medical Association Journal*, 168(10):1279–1285.
- Albrecht, M. G. and Creighton, J. A. (1977). Anomalously intense raman spectra of pyridine at a silver electrode. *Journal of the American Chemical Society*, 99(15):5215–5217.
- Altunakar, B., Luceha, J., and Kokini, J. L. (2010). Fabrication of biodegradable zein films by using soft lithography. In *Proceedings of Nanotechnology Conference, Anaheim*, volume 2, pages 253–256.
- Anderson, T. J. and Lamsal, B. P. (2011). Review: Zein extraction from corn, corn products, and coproducts and modifications for various applications: A review. *Cereal Chemistry*, 88(2):159–173.
- Anese, M., Manzocco, L., Calligaris, S., and Nicoli, M. C. (2013). Industrially applicable strategies for mitigating acrylamide, furan, and 5-hydroxymethylfurfural in food. *Journal of agricultural and food chemistry*, 61(43):10209–10214.
- Argos, P., Pedersen, K., Marks, M., and Larkins, B. (1982). A structural model for maize zein proteins. *Journal of Biological Chemistry*, 257(17):9984–9990.
- Arkles, B. (2006). Hydrophobicity, hydrophilicity and silane surface modification. Available at <http://www.gelest.com/goods/pdf/Hydrophobicity.pdf>.
- Arvanitoyannis, I. S. and Dionisopoulou, N. (2014). Acrylamide: formation, occurrence in food products, detection methods, and legislation. *Critical reviews in food science and nutrition*, 54(6):708–733.
- Barbosa, S., Agrawal, A., Rodríguez-Lorenzo, L., Pastoriza-Santos, I., Alvarez-Puebla, R. A., Kornowski, A., Weller, H., and Liz-Marzán, L. M. (2010). Tuning size and sensing properties in colloidal gold nanostars. *Langmuir*, 26(18):14943–14950.

- Barron, A. (2013). Physical methods in chemistry and nano science. OpenStax CNX, <http://cnx.org/contents/ba27839d-5042-4a40-afcf-c0e6e39fb454@17.2@17.2>.
- Başkan, S. and Erim, F. B. (2007). Nace for the analysis of acrylamide in food. *Electrophoresis*, 28(22):4108–4113.
- Bermudo, E., Nunez, O., Puignou, L., and Galceran, M. (2006). Analysis of acrylamide in food samples by capillary zone electrophoresis. *Journal of Chromatography A*, 1120(1):199–204.
- Bethke, P. C. and Bussan, A. J. (2013). Acrylamide in processed potato products. *American journal of potato research*, 90(5):403–424.
- Biswas, A., Selling, G. W., Woods, K. K., and Evans, K. (2009). Surface modification of zein films. *Industrial crops and products*, 30(1):168–171.
- Blank, I. (2005). Current status of acrylamide research in food: Measurement, safety assessment, and formation. *Annals of the New York Academy of Sciences*, 1043(1):30–40.
- Bodas, D. and Khan-Malek, C. (2007). Hydrophilization and hydrophobic recovery of pdms by oxygen plasma and chemical treatment—an sem investigation. *Sensors and Actuators B: Chemical*, 123(1):368–373.
- Bowden, N., Brittain, S., Evans, A. G., Hutchinson, J. W., and Whitesides, G. M. (1998). Spontaneous formation of ordered structures in thin films of metals supported on an elastomeric polymer. *Nature*, 393(6681):146–149.
- Bugs, M. R., Forato, L. A., Bortoleto-Bugs, R. K., Fischer, H., Mascarenhas, Y. P., Ward, R. J., and Colnago, L. A. (2004). Spectroscopic characterization and structural modeling of prolamin from maize and pearl millet. *European Biophysics Journal*, 33(4):335–343.
- Burda, C., Chen, X., Narayanan, R., and El-Sayed, M. A. (2005). Chemistry and properties of nanocrystals of different shapes. *Chemical reviews*, 105(4):1025–1102.
- Burks, A. W., Williams, L. W., Connaughton, C., Cockrell, G., O’Brien, T. J., and Helm, R. M. (1992). Identification and characterization of a second major peanut allergen, ara h ii, with use of the sera of patients with atopic dermatitis and positive peanut challenge. *Journal of Allergy and Clinical Immunology*, 90(6):962–969.
- Cheng, Y. and Dong, Y. (2011). Screening melamine contaminant in eggs with portable surface-enhanced raman spectroscopy based on gold nanosubstrate. *Food Control*, 22(5):685–689.

- Chruszcz, M., Maleki, S. J., Majorek, K. A., Demas, M., Bublin, M., Solberg, R., Hurlburt, B. K., Ruan, S., Mattisohn, C. P., Breiteneder, H., et al. (2011). Structural and immunologic characterization of ara h 1, a major peanut allergen. *Journal of Biological Chemistry*, 286(45):39318–39327.
- Cooper, M. A. (2002). Optical biosensors in drug discovery. *Nature Reviews Drug Discovery*, 1(7):515–528.
- Corradini, E., Curti, P. S., Meniqueti, A. B., Martins, A. F., Rubira, A. F., and Muniz, E. C. (2014). Recent advances in food-packing, pharmaceutical and biomedical applications of zein and zein-based materials. *International journal of molecular sciences*, 15(12):22438–22470.
- Corredor, C., Teslova, T., Cañamares, M. V., Chen, Z., Zhang, J., Lombardi, J. R., and Leona, M. (2009). Raman and surface-enhanced raman spectra of chrysin, apigenin and luteolin. *Vibrational spectroscopy*, 49(2):190–195.
- Craig, A. P., Franca, A. S., and Irudayaraj, J. (2013). Surface-enhanced raman spectroscopy applied to food safety. *Annual review of food science and technology*, 4:369–380.
- Croft*, M., Tong, P., Fuentes, D., and Hambridge, T. (2004). Australian survey of acrylamide in carbohydrate-based foods. *Food additives and contaminants*, 21(8):721–736.
- Dann, J. (1970). Forces involved in the adhesive process: I. critical surface tensions of polymeric solids as determined with polar liquids. *Journal of Colloid and Interface Science*, 32(2):302–320.
- Deegan, R. D., Bakajin, O., Dupont, T. F., Huber, G., Nagel, S. R., and Witten, T. A. (1997). Capillary flow as the cause of ring stains from dried liquid drops. *Nature*, 389(6653):827–829.
- Di Anibal, C. V., Marsal, L. F., Callao, M. P., and Ruisánchez, I. (2012). Surface enhanced raman spectroscopy (sers) and multivariate analysis as a screening tool for detecting sudan i dye in culinary spices. *Spectrochimica Acta Part A: Molecular and Biomolecular Spectroscopy*, 87:135–141.
- Domachuk, P., Tsioris, K., Omenetto, F. G., and Kaplan, D. L. (2010). Bio-microfluidics: Biomaterials and biomimetic designs. *Advanced materials*, 22(2):249–260.
- Dong, F., Padua, G. W., and Wang, Y. (2013). Controlled formation of hydrophobic surfaces by self-assembly of an amphiphilic natural protein from aqueous solutions. *Soft Matter*, 9(25):5933–5941.
- Dong, J., Sun, Q., and Wang, J.-Y. (2004). Basic study of corn protein, zein, as a biomaterial in tissue engineering, surface morphology and biocompatibility. *Biomaterials*, 25(19):4691–4697.

- Dunteman, G. H. (1989). *Principal components analysis*. Sage.
- Eddington, D. T., Puccinelli, J. P., and Beebe, D. J. (2006). Thermal aging and reduced hydrophobic recovery of polydimethylsiloxane. *Sensors and Actuators B: Chemical*, 114(1):170–172.
- Evans, C. D. (1944). Process for extracting prolamines. US Patent 2,354,393.
- Evans, C. D. and Manley, R. H. (1941). Solvents for zein. primary solvents. *Industrial & Engineering Chemistry*, 33(11):1416–1417.
- Evans, C. D. and Manley, R. H. (1944). Ternary solvents for zein. *Industrial & Engineering Chemistry*, 36(5):408–410.
- Fernandes, J. O. and Soares, C. (2007). Application of matrix solid-phase dispersion in the determination of acrylamide in potato chips. *Journal of Chromatography A*, 1175(1):1–6.
- Fleischmann, M., Hendra, P. J., and McQuillan, A. (1974). Raman spectra of pyridine adsorbed at a silver electrode. *Chemical Physics Letters*, 26(2):163–166.
- Flinterman, A. E., Pasmans, S. G., Hoekstra, M. O., Meijer, Y., van Hoffen, E., Knol, E. F., Hefle, S. L., Bruijnzeel-Koomen, C. A., and Knulst, A. C. (2006). Determination of no-observed-adverse-effect levels and eliciting doses in a representative group of peanut-sensitized children. *Journal of Allergy and Clinical Immunology*, 117(2):448–454.
- Forato, L., Yushmanov, V., and Colnago, L. (2004a). Interaction of two prolamins with 1-13c oleic acid by 13c nmr. *Biochemistry*, 43(22):7121–7126.
- Forato, L. A., Doriguetto, A. C., Fischer, H., Mascarenhas, Y. P., Craievich, A. F., and Colnago, L. A. (2004b). Conformation of the z19 prolamin by ftir, nmr, and saxs. *Journal of agricultural and food chemistry*, 52(8):2382–2385.
- Friedman, M. (2003). Chemistry, biochemistry, and safety of acrylamide. a review. *Journal of agricultural and food chemistry*, 51(16):4504–4526.
- Fu, D. and Weller, C. L. (1999). Rheology of zein solutions in aqueous ethanol. *Journal of agricultural and food chemistry*, 47(5):2103–2108.
- Galarreta, B. C., Tabatabaei, M., Guieu, V., Peyrin, E., and Lagugn e-Labarthet, F. (2013). Microfluidic channel with embedded sers 2d platform for the aptamer detection of ochratoxin a. *Analytical and bioanalytical chemistry*, 405(5):1613–1621.

- Gao, J., Hu, Y., Li, S., Zhang, Y., and Chen, X. (2013). Adsorption of benzoic acid, phthalic acid on gold substrates studied by surface-enhanced raman scattering spectroscopy and density functional theory calculations. *Spectrochimica Acta Part A: Molecular and Biomolecular Spectroscopy*, 104:41–47.
- Gartia, M. R., Xu, Z., Behymer, E., Nguyen, H., Britten, J. A., Larson, C., Miles, R., Bora, M., Chang, A. S., Bond, T. C., et al. (2010). Rigorous surface enhanced raman spectral characterization of large-area high-uniformity silver-coated tapered silica nanopillar arrays. *Nanotechnology*, 21(39):395701.
- Gianazza, E., Viglienghi, V., Righetti, P. G., Salamini, F., and Soave, C. (1977). Amino acid composition of zein molecular components. *Phytochemistry*, 16(3):315–317.
- Gorham, J. (1821). Analysis of indian corn. *QJ Sci. Lit. Arts*, 2:206–208.
- Grzelczak, M., Pérez-Juste, J., Mulvaney, P., and Liz-Marzán, L. M. (2008). Shape control in gold nanoparticle synthesis. *Chemical Society Reviews*, 37(9):1783–1791.
- Guicheteau, J., Argue, L., Emge, D., Hyre, A., Jacobson, M., and Christesen, S. (2008). Bacillus spore classification via surface-enhanced raman spectroscopy and principal component analysis. *Applied spectroscopy*, 62(3):267–272.
- Häkkinen, H. (2012). The gold-sulfur interface at the nanoscale. *Nature Chemistry*, 4(6):443–455.
- Hansen, D. W. (1938). Plasticized prolamine base composition. US Patent 2,115,716.
- He, L., Chen, T., and Labuza, T. P. (2014). Recovery and quantitative detection of thiabendazole on apples using a surface swab capture method followed by surface-enhanced raman spectroscopy. *Food chemistry*, 148:42–46.
- He, L., Deen, B., Rodda, T., Ronningen, I., Blasius, T., Haynes, C., Diez-Gonzalez, F., and Labuza, T. P. (2011a). Rapid detection of ricin in milk using immunomagnetic separation combined with surface-enhanced raman spectroscopy. *Journal of food science*, 76(5):N49–N53.
- He, L., Haynes, C. L., Diez-Gonzalez, F., and Labuza, T. P. (2011b). Rapid detection of a foreign protein in milk using ims-sers. *Journal of Raman Spectroscopy*, 42(6):1428–1434.
- He, L., Kim, N.-J., Li, H., Hu, Z., and Lin, M. (2008a). Use of a fractal-like gold nanostructure in surface-enhanced raman spectroscopy for detection of selected food contaminants. *Journal of agricultural and food chemistry*, 56(21):9843–9847.

- He, L., Lin, M., Li, H., and Kim, N.-J. (2010). Surface-enhanced raman spectroscopy coupled with dendritic silver nanosubstrate for detection of restricted antibiotics. *Journal of Raman Spectroscopy*, 41(7):739–744.
- He, L., Liu, Y., Lin, M., Awika, J., Ledoux, D. R., Li, H., and Mustapha, A. (2008b). A new approach to measure melamine, cyanuric acid, and melamine cyanurate using surface enhanced raman spectroscopy coupled with gold nanosubstrates. *Sensing and Instrumentation for Food Quality and Safety*, 2(1):66–71.
- Hildebrandt, P. and Stockburger, M. (1984). Surface-enhanced resonance raman spectroscopy of rhodamine 6g adsorbed on colloidal silver. *The Journal of Physical Chemistry*, 88(24):5935–5944.
- Hillborg, H. and Gedde, U. (1999). Hydrophobicity changes in silicone rubbers. *IEEE Transactions on Dielectrics and Electrical Insulation*, 6(5):703–717.
- Holding, D. R. and Larkins, B. A. (2009). Zein storage proteins. In *Molecular Genetic Approaches to Maize Improvement*, pages 269–286. Springer.
- Hu, H., Wang, Z., Wang, S., Zhang, F., Zhao, S., and Zhu, S. (2011). ZnO/ag heterogeneous structure nanoarrays: Photocatalytic synthesis and used as substrate for surface-enhanced raman scattering detection. *Journal of Alloys and Compounds*, 509(5):2016–2020.
- Huang, T. C., Bruechert, L. J., Hartman, T. G., Rosen, R. T., and Ho, C. T. (1987). Effect of lipids and carbohydrates on thermal generation of volatiles from commercial zein. *Journal of Agricultural and Food Chemistry*, 35(6):985–990.
- Huang, Y., Bell, M. C., and Suni, I. I. (2008). Impedance biosensor for peanut protein ara h 1. *Analytical chemistry*, 80(23):9157–9161.
- Hutter, E. and Fendler, J. H. (2004). Exploitation of localized surface plasmon resonance. *Advanced Materials*, 16(19):1685–1706.
- Jeanmaire, D. L. and Van Duyne, R. P. (1977). Surface raman spectroelectrochemistry: Part i. heterocyclic, aromatic, and aliphatic amines adsorbed on the anodized silver electrode. *Journal of Electroanalytical Chemistry and Interfacial Electrochemistry*, 84(1):1–20.
- Ji, K.-M., Chen, J.-J., Gao, C., Liu, X.-y., Xia, L.-x., Liu, Z.-G., Li, L., and Yang, S. (2011). A two-site monoclonal antibody immunochromatography assay for rapid detection of peanut allergen ara h1 in chinese imported and exported foods. *Food Chemistry*, 129(2):541–545.

- Jiao, J., Zhang, Y., Ren, Y., Wu, X., and Zhang, Y. (2005). Development of a quantitative method for determination of acrylamide in infant powdered milk and baby foods in jars using isotope dilution liquid chromatography/electrospray ionization tandem mass spectrometry. *Journal of Chromatography A*, 1099(1):198–202.
- Johnson, T. J., Su, Y.-F., Jarman, K. H., Kunkel, B. M., Birnbaum, J. C., Joly, A. G., Stephan, E. G., Tonkyn, R. G., Ewing, R. G., and Dunham, G. C. (2012). Demonstrated wavelength portability of raman reference data for explosives and chemical detection. *International Journal of Spectroscopy*, 2012.
- Jonathan, N. (1961). The infrared and raman spectra and structure of acrylamide. *Journal of Molecular Spectroscopy*, 6:205–214.
- Jou, S. and Hsu, C. K. (2004). Preparation of carbon nanotubes from vacuum pyrolysis of polycarbosilane. *Materials Science and Engineering: B*, 106(3):275–281.
- Kanig, J. L. and Goodman, H. (1962). Evaluative procedures for film-forming materials used in pharmaceutical applications. *Journal of pharmaceutical sciences*, 51(1):77–83.
- Kendall, K. (1971). The adhesion and surface energy of elastic solids. *Journal of Physics D: Applied Physics*, 4(8):1186.
- Keramat, J., LeBail, A., Prost, C., and Soltanizadeh, N. (2011). Acrylamide in foods: chemistry and analysis. a review. *Food and bioprocess technology*, 4(3):340–363.
- Koppelman, S., Vlooswijk, R., Knippels, L., Hessing, M., Knol, E., Van Reijssen, F., and Bruijnzeel-Koomen, C. (2001). Quantification of major peanut allergens ara h 1 and ara h 2 in the peanut varieties runner, spanish, virginia, and valencia, bred in different parts of the world. *Allergy*, 56(2):132–137.
- Krishnakumar, T., Visvanathan, R., et al. (2014). Acrylamide in food products: a review. *Journal of Food Processing and Technology*, 5(7).
- Lai, H.-M., Geil, P., and Padua, G. (1999). X-ray diffraction characterization of the structure of zein–oleic acid films. *Journal of applied polymer science*, 71(8):1267–1281.
- Lai, H.-M. and Padua, G. W. (1997). Properties and microstructure of plasticized zein films. *Cereal Chemistry*, 74(6):771–775.
- Lai, H.-M. and Padua, G. W. (1998). Water vapor barrier properties of zein films plasticized with oleic acid. *Cereal Chemistry*, 75(2):194–199.

- Lai, H.-M., Padua, G. W., and Wei, L. S. (1997). Properties and microstructure of zein sheets plasticized with palmitic and stearic acids. *Cereal Chemistry*, 74(1):83–90.
- Lai, K., Zhang, Y., Du, R., Zhai, F., Rasco, B. A., and Huang, Y. (2011). Determination of chloramphenicol and crystal violet with surface enhanced raman spectroscopy. *Sensing and Instrumentation for Food Quality and Safety*, 5(1):19–24.
- Lawton, J. (2004). Plasticizers for zein: their effect on tensile properties and water absorption of zein films. *Cereal chemistry*, 81(1):1–5.
- Lawton, J. W. (2002). Zein: A history of processing and use. *Cereal Chemistry*, 79(1):1–18.
- Lee, H. J. and Owens, J. (2011). *Superhydrophobic Superoleophobic Woven Fabrics*. INTECH Open Access Publisher.
- Lee, M.-R., Chang, L.-Y., and Dou, J. (2007). Determination of acrylamide in food by solid-phase microextraction coupled to gas chromatography–positive chemical ionization tandem mass spectrometry. *Analytica chimica acta*, 582(1):19–23.
- Li, C., Adamcik, J., and Mezzenga, R. (2012). Biodegradable nanocomposites of amyloid fibrils and graphene with shape-memory and enzyme-sensing properties. *Nature nanotechnology*, 7(7):421–427.
- Li, J. F., Huang, Y. F., Ding, Y., Yang, Z. L., Li, S. B., Zhou, X. S., Fan, F. R., Zhang, W., Zhou, Z. Y., Ren, B., et al. (2010). Shell-isolated nanoparticle-enhanced raman spectroscopy. *nature*, 464(7287):392–395.
- Li, R., Zhang, H., Chen, Q.-W., Yan, N., and Wang, H. (2011). Improved surface-enhanced raman scattering on micro-scale au hollow spheres: Synthesis and application in detecting tetracycline. *Analyst*, 136(12):2527–2532.
- Li, Y., White, T., and Lim, S. H. (2003). Structure control and its influence on photoactivity and phase transformation of tio. *Rev. Adv. Mater. Sci*, 5:211–215.
- Lin, C.-C., Yang, Y.-M., Chen, Y.-F., Yang, T.-S., and Chang, H.-C. (2008a). A new protein a assay based on raman reporter labeled immunogold nanoparticles. *Biosensors and Bioelectronics*, 24(2):178–183.
- Lin, M., He, L., Awika, J., Yang, L., Ledoux, D., Li, H. a., and Mustapha, A. (2008b). Detection of melamine in gluten, chicken feed, and processed foods using surface enhanced raman spectroscopy and hplc. *Journal of food science*, 73(8):T129–T134.
- Lineback, D. R., Coughlin, J. R., and Stadler, R. H. (2012). Acrylamide in foods: a review of the science and future considerations. *Annual review of food science and technology*, 3:15–35.

- Liu, B., Han, G., Zhang, Z., Liu, R., Jiang, C., Wang, S., and Han, M.-Y. (2011). Shell thickness-dependent raman enhancement for rapid identification and detection of pesticide residues at fruit peels. *Analytical chemistry*, 84(1):255–261.
- Liu, B., Zhou, P., Liu, X., Sun, X., Li, H., and Lin, M. (2013a). Detection of pesticides in fruits by surface-enhanced raman spectroscopy coupled with gold nanostructures. *Food and Bioprocess Technology*, 6(3):710–718.
- Liu, G. L., Zheng, W., Zhang, P., and Chen, F. F. (2013b). Biosensing based on surface-enhanced raman spectroscopy. *Biosensors Based on Nanomaterials and Nanodevices*, page 111.
- Liu, L. (2010). *Introduction to Nanophotonics, Nanobiophotonics*. McGraw Hill Professional.
- Luecha, J., Hsiao, A., Brodsky, S., Liu, G. L., and Kokini, J. L. (2011). Green microfluidic devices made of corn proteins. *Lab on a Chip*, 11(20):3419–3425.
- Manley, R. H. and Evans, C. D. (1943). Binary solvents for zein. *Industrial & Engineering Chemistry*, 35(6):661–665.
- Martinez, A. W., Phillips, S. T., Whitesides, G. M., and Carrilho, E. (2009). Diagnostics for the developing world: microfluidic paper-based analytical devices. *Analytical chemistry*, 82(1):3–10.
- Matsushima, N., Danno, G.-i., Takezawa, H., and Izumi, Y. (1997). Three-dimensional structure of maize α -zein proteins studied by small-angle x-ray scattering. *Biochimica et Biophysica Acta (BBA)-Protein Structure and Molecular Enzymology*, 1339(1):14–22.
- Maya, L., Paranthaman, M., Thundat, T., and Bauer, M. (1996). Gold oxide as precursor to gold/silica nanocomposites. *Journal of Vacuum Science & Technology B*, 14(1):15–21.
- McGrath, T., Elliott, C., and Fodey, T. (2012). Biosensors for the analysis of microbiological and chemical contaminants in food. *Analytical and bioanalytical chemistry*, 403(1):75–92.
- McKeown, D. A. (2005). Raman spectroscopy and vibrational analyses of albite: From 25 °C through the melting temperature. *American Mineralogist*, 90(10):1506–1517.
- Mecker, L. C., Tyner, K. M., Kauffman, J. F., Arzhantsev, S., Mans, D. J., and Gryniewicz-Ruzicka, C. M. (2012). Selective melamine detection in multiple sample matrices with a portable raman instrument using surface enhanced raman spectroscopy-active gold nanoparticles. *Analytica chimica acta*, 733:48–55.

- Michaels, A. M., Jiang, J., and Brus, L. (2000). Ag nanocrystal junctions as the site for surface-enhanced raman scattering of single rhodamine 6g molecules. *The Journal of Physical Chemistry B*, 104(50):11965–11971.
- Mohammed, I., Mullett, W. M., Lai, E. P., and Yeung, J. M. (2001). Is biosensor a viable method for food allergen detection? *Analytica Chimica Acta*, 444(1):97–102.
- Momany, F. A., Sessa, D. J., Lawton, J. W., Selling, G. W., Hamaker, S. A., and Willett, J. L. (2006). Structural characterization of α -zein. *Journal of agricultural and food chemistry*, 54(2):543–547.
- Mondelaers, D., Vanhoyland, G., Van den Rul, H., D’Haen, J., Van Bael, M., Mullens, J., and Van Poucke, L. (2002). Synthesis of zno nanopowder via an aqueous acetate–citrate gelation method. *Materials research bulletin*, 37(5):901–914.
- Moskovits, M. (1985). Surface-enhanced spectroscopy. *Reviews of modern physics*, 57(3):783.
- Mottram, D. S., Wedzicha, B. L., and Dodson, A. T. (2002). Food chemistry: acrylamide is formed in the maillard reaction. *Nature*, 419(6906):448–449.
- Nawrocka, A. and Lamorska, J. (2013). Determination of food quality by using spectroscopic methods. *Advances in Agrophysical Research*, pages 347–367.
- Oh, E., Gupta, R., and Whang, C. (2003). Effects of ph and dye concentration on the optical and structural properties of coumarin-4 dye-doped sio₂-pdms xerogels. *Journal of sol-gel science and technology*, 28(3):279–288.
- Oliver, N., Toumazou, C., Cass, A., and Johnston, D. (2009). Glucose sensors: a review of current and emerging technology. *Diabetic Medicine*, 26(3):197–210.
- Osterballe, M., Hansen, T. K., Mortz, C., Høst, A., and Bindslev-Jensen, C. (2005). The prevalence of food hypersensitivity in an unselected population of children and adults. *Pediatric Allergy and Immunology*, 16(7):567–573.
- Owen, M. J. and Smith, P. J. (1994). Plasma treatment of polydimethylsiloxane. *Journal of adhesion science and technology*, 8(10):1063–1075.
- Pedreschi, F., Moyano, P., Kaack, K., and Granby, K. (2005). Color changes and acrylamide formation in fried potato slices. *Food Research International*, 38(1):1–9.
- Peica, N. (2009). Identification and characterisation of the e951 artificial food sweetener by vibrational spectroscopy and theoretical modelling. *Journal of Raman Spectroscopy*, 40(12):2144–2154.

- Peica, N., Lehene, C., Leopold, N., Schlücker, S., and Kiefer, W. (2007). Monosodium glutamate in its anhydrous and monohydrate form: Differentiation by raman spectroscopies and density functional calculations. *Spectrochimica Acta Part A: Molecular and Biomolecular Spectroscopy*, 66(3):604–615.
- Peng, B., Li, G., Li, D., Dodson, S., Zhang, Q., Zhang, J., Lee, Y. H., Demir, H. V., Yi Ling, X., and Xiong, Q. (2013). Vertically aligned gold nanorod monolayer on arbitrary substrates: self-assembly and femtomolar detection of food contaminants. *ACS nano*, 7(7):5993–6000.
- Petryayeva, E. and Krull, U. J. (2011). Localized surface plasmon resonance: Nanostructures, bioassays and biosensing—a review. *Analytica chimica acta*, 706(1):8–24.
- Picó, Y. (2012). *Chemical analysis of food: Techniques and applications*. Academic Press.
- Pilolli, R., Monaci, L., and Visconti, A. (2013). Advances in biosensor development based on integrating nanotechnology and applied to food-allergen management. *TrAC Trends in Analytical Chemistry*, 47:12–26.
- Plečis, A. and Chen, Y. (2007). Fabrication of microfluidic devices based on glass–pdms–glass technology. *Microelectronic Engineering*, 84(5):1265–1269.
- Pollet, J., Delport, F., Janssen, K., Tran, D., Wouters, J., Verbiest, T., and Lamertyn, J. (2011). Fast and accurate peanut allergen detection with nanobead enhanced optical fiber spr biosensor. *Talanta*, 83(5):1436–1441.
- Pomés, A., Helm, R. M., Bannon, G. A., Burks, A. W., Tsay, A., and Chapman, M. D. (2003). Monitoring peanut allergen in food products by measuring ara h 1. *Journal of Allergy and Clinical Immunology*, 111(3):640–645.
- Raman, C. V. and Krishnan, K. S. (1928). A new type of secondary radiation. *Nature*, 121(3048):501–502.
- Rosén, J. and Hellenäs, K.-E. (2002). Analysis of acrylamide in cooked foods by liquid chromatography tandem mass spectrometry. *Analyst*, 127(7):880–882.
- Santosa, F. B. and Padua, G. W. (1999). Tensile properties and water absorption of zein sheets plasticized with oleic and linoleic acids. *Journal of agricultural and food chemistry*, 47(5):2070–2074.
- Santosa, F. B. and Padua, G. W. (2000). Thermal behavior of zein sheets plasticized with oleic acid. *Cereal chemistry*, 77(4):459–462.
- Schubert-Ullrich, P., Rudolf, J., Ansari, P., Galler, B., Führer, M., Molinelli, A., and Baumgartner, S. (2009). Commercialized rapid immunoanalytical tests for determination of allergenic food proteins: an overview. *Analytical and bioanalytical chemistry*, 395(1):69–81.

- Segtnan, V. H., Kita, A., Mielnik, M., Jørgensen, K., and Knutsen, S. H. (2006). Screening of acrylamide contents in potato crisps using process variable settings and near-infrared spectroscopy. *Molecular nutrition & food research*, 50(9):811–817.
- Sepúlveda, B., Angelomé, P. C., Lechuga, L. M., and Liz-Marzán, L. M. (2009). Lspr-based nanobiosensors. *Nano Today*, 4(3):244–251.
- Shewry, P. R. and Tatham, A. S. (1990). The prolamin storage proteins of cereal seeds: structure and evolution. *Biochemical Journal*, 267(1):1.
- Shi, K., Huang, Y., Yu, H., Lee, T.-C., and Huang, Q. (2010). Reducing the brittleness of zein films through chemical modification. *Journal of agricultural and food chemistry*, 59(1):56–61.
- Shi, K., Kokini, J. L., and Huang, Q. (2009). Engineering zein films with controlled surface morphology and hydrophilicity. *Journal of agricultural and food chemistry*, 57(6):2186–2192.
- Shukla, R. and Cheryan, M. (2001). Zein: the industrial protein from corn. *Industrial Crops and Products*, 13(3):171–192.
- Soares, C., Cunha, S., and Fernandes, J. (2006). Determination of acrylamide in coffee and coffee products by gc-ms using an improved spe clean-up. *Food additives and contaminants*, 23(12):1276–1282.
- Song, C., Wang, Z., Zhang, R., Yang, J., Tan, X., and Cui, Y. (2009). Highly sensitive immunoassay based on raman reporter-labeled immuno-au aggregates and sers-active immune substrate. *Biosensors and Bioelectronics*, 25(4):826–831.
- Sowell, R., DeLollis, N., Gregory, H., and Montoya, O. (1972). Effect of activated gas plasma on surface characteristics and bondability of rtv silicone and polyethylene. *The Journal of Adhesion*, 4(1):15–24.
- Stropp, J., Trachta, G., Brehm, G., and Schneider, S. (2003). A new version of agfon substrates for high-throughput analytical sers applications. *Journal of Raman Spectroscopy*, 34(1):26–32.
- Subramanian, S. and Sampath, S. (2007a). Adsorption of zein on surfaces with controlled wettability and thermal stability of adsorbed zein films. *Biomacromolecules*, 8(7):2120–2128.
- Subramanian, S. and Sampath, S. (2007b). Dewetting phenomenon: Interfacial water structure at well-organized alkanethiol-modified gold–aqueous interface. *Journal of colloid and interface science*, 313(1):64–71.

- Sun, Q.-S., Dong, J., Lin, Z.-X., Yang, B., and Wang, J.-Y. (2005). Comparison of cytocompatibility of zein film with other biomaterials and its degradability in vitro. *Biopolymers*, 78(5):268–274.
- Sun, Y., Mayers, B., and Xia, Y. (2003). Metal nanostructures with hollow interiors. *Advanced Materials*, 15(78):641–646.
- Sun, Y. and Wiederrecht, G. P. (2007). Surfactantless synthesis of silver nanoplates and their application in sers. *Small*, 3(11):1964–1975.
- Tao, H., Brenckle, M. A., Yang, M., Zhang, J., Liu, M., Siebert, S. M., Averitt, R. D., Mannoor, M. S., McAlpine, M. C., Rogers, J. A., et al. (2012). Silk-based conformal, adhesive, edible food sensors. *Advanced Materials*, 24(8):1067–1072.
- Tareke, E., Rydberg, P., Karlsson, P., Eriksson, S., and Törnqvist, M. (2002). Analysis of acrylamide, a carcinogen formed in heated foodstuffs. *Journal of agricultural and food chemistry*, 50(17):4998–5006.
- Tatham, A., Field, J., Morris, V., I'Anson, K., Cardle, L., Dufton, M., and Shewry, P. (1993). Solution conformational analysis of the alpha-zein proteins of maize. *Journal of Biological Chemistry*, 268(35):26253–26259.
- Tekkeli, S. E. K., Önal, C., and Önal, A. (2012). A review of current methods for the determination of acrylamide in food products. *Food Analytical Methods*, 5(1):29–39.
- Teslova, T., Corredor, C., Livingstone, R., Spataru, T., Birke, R. L., Lombardi, J. R., Canameres, M., and Leona, M. (2007). Raman and surface-enhanced raman spectra of flavone and several hydroxy derivatives. *Journal of Raman Spectroscopy*, 38(7):802–818.
- Turner, A. P. (2013). Biosensors: sense and sensibility. *Chemical Society Reviews*, 42(8):3184–3196.
- Van der Schueren, L., De Meyer, T., Steyaert, I., Ceylan, Ö., Hemelsoet, K., Van Speybroeck, V., and De Clerck, K. (2013). Polycaprolactone and polycaprolactone/chitosan nanofibres functionalised with the ph-sensitive dye nitrazine yellow. *Carbohydrate polymers*, 91(1):284–293.
- Van Dorst, B., Mehta, J., Bekaert, K., Rouah-Martin, E., De Coen, W., Dubruel, P., Blust, R., and Robbens, J. (2010). Recent advances in recognition elements of food and environmental biosensors: a review. *Biosensors and Bioelectronics*, 26(4):1178–1194.
- van Hengel, A. J. (2007). Food allergen detection methods and the challenge to protect food-allergic consumers. *Analytical and bioanalytical chemistry*, 389(1):111–118.

- Vandenabeele, P. (2013). *Practical Raman spectroscopy: an introduction*. John Wiley & Sons.
- Vesela, H., SUCMAN, E., et al. (2013). Determination of acrylamide in food using adsorption stripping voltammetry. *Czech J. Food Sci. Vol*, 31(4):401–406.
- Viano, A., Mishra, S., Lloyd, R., Losby, J., and Gheyi, T. (2003). Thermal effects on esr signal evolution in nano and bulk cuo powder. *Journal of non-crystalline solids*, 325(1):16–21.
- Viereck, N., Salomonsen, T., van den Berg, F., and Engelsen, S. B. (2009). Raman applications in food analysis. *Raman Spectroscopy for Soft Matter Applications*, ed. MS Amer, Wiley Interscience, MA, USA, pages 199–223.
- Vitos, L., Ruban, A., Skriver, H. L., and Kollar, J. (1998). The surface energy of metals. *Surface Science*, 411(1):186–202.
- Vroman, I. and Tighzert, L. (2009). Biodegradable polymers. *Materials*, 2(2):307–344.
- Wang, Q., Crofts, A. R., and Padua, G. W. (2003a). Protein-lipid interactions in zein films investigated by surface plasmon resonance. *Journal of agricultural and food chemistry*, 51(25):7439–7444.
- Wang, Q., Geil, P., and Padua, G. (2004a). Role of hydrophilic and hydrophobic interactions in structure development of zein films. *Journal of Polymers and the Environment*, 12(3):197–202.
- Wang, Q., Wang, J.-F., Geil, P. H., and Padua, G. W. (2004b). Zein adsorption to hydrophilic and hydrophobic surfaces investigated by surface plasmon resonance. *Biomacromolecules*, 5(4):1356–1361.
- Wang, Q., Xian, W., Li, S., Liu, C., and Padua, G. W. (2008). Topography and biocompatibility of patterned hydrophobic/hydrophilic zein layers. *Acta biomaterialia*, 4(4):844–851.
- Wang, Y., Geil, P., Padua, G. W., et al. (2005). Effects of processing on the structure of zein/oleic acid films investigated by x-ray diffraction. *Macromolecular bioscience*, 5(12):1200–1208.
- Wang, Y., Rakotonirainy, A. M., and Padua, G. W. (2003b). Thermal behavior of zein-based biodegradable films. *Starch - Stärke*, 55(1):25–29.
- Weiping, C. and Lide, Z. (1997). Synthesis and structural and optical properties of mesoporous silica containing silver nanoparticles. *Journal of Physics: Condensed Matter*, 9(34):7257.

- Wen, H.-W., Borejsza-Wysocki, W., DeCory, T. R., and Durst, R. A. (2007). Peanut allergy, peanut allergens, and methods for the detection of peanut contamination in food products. *Comprehensive reviews in food science and food safety*, 6(2):47–58.
- West, P. E. (2007). *Introduction to atomic force microscopy: Theory, practice, applications*. Pacific Nanotechnology.
- Willets, K. A. and Van Duyne, R. P. (2007). Localized surface plasmon resonance spectroscopy and sensing. *Annu. Rev. Phys. Chem.*, 58:267–297.
- Wilson, C. M. (1991). Multiple zeins from maize endosperms characterized by reversed-phase high performance liquid chromatography. *Plant physiology*, 95(3):777–786.
- Wu, X., Gao, S., Wang, J.-S., Wang, H., Huang, Y.-W., and Zhao, Y. (2012). The surface-enhanced raman spectra of aflatoxins: spectral analysis, density functional theory calculation, detection and differentiation. *Analyst*, 137(18):4226–4234.
- Xiaoyan, Z., Ruiyi, L., Zaijun, L., Junkang, L., Zhiguo, G., and Guangli, W. (2014). A surface-enhanced raman scattering strategy for detection of peanut allergen ara h 1 using a bipyramid-shaped gold nanocrystal substrate with an improved synthesis. *RSC Advances*, 4(30):15363–15370.
- Xie, Y., Zhu, X., Sun, Y., Wang, H., Qian, H., and Yao, W. (2012). Rapid detection method for nitrofurantoin antibiotic residues by surface-enhanced raman spectroscopy. *European Food Research and Technology*, 235(3):555–561.
- Xu, H., Chai, Y., and Zhang, G. (2012). Synergistic effect of oleic acid and glycerol on zein film plasticization. *Journal of agricultural and food chemistry*, 60(40):10075–10081.
- Xu, N. and Huq, S. E. (2005). Novel cold cathode materials and applications. *Materials Science and Engineering: R: Reports*, 48(2):47–189.
- Xu, Z., Wu, H.-Y., Ali, S. U., Jiang, J., Cunningham, B. T., and Liu, G. L. (2011). Nanoreplicated positive and inverted submicrometer polymer pyramid array for surface-enhanced raman spectroscopy. *Journal of Nanophotonics*, 5(1):053526–053526.
- Yman, I. M., Eriksson, A., Johansson, M. A., and Hellens, K.-E. (2006). Food allergen detection with biosensor immunoassays. *Journal of AOAC International*, 89(3):856–861.
- Yoshimoto, N. and Sato, K. (1994). Preheating effects of melt on nucleation and growth of oleic acid polymorphs. *Japanese journal of applied physics*, 33(5R):2746.

- Yoshino, T., Isobe, S., and Maekawa, T. (2000). Physical evaluation of pure zein films by atomic force microscopy and thermal mechanical analysis. *Journal of the American Oil Chemists' Society*, 77(7):699–704.
- Yoshino, T., Isobe, S., and Maekawa, T. (2002). Influence of preparation conditions on the physical properties of zein films. *Journal of the American Oil Chemists' Society*, 79(4):345–349.
- Zhang, H. and Mittal, G. (2010). Biodegradable protein-based films from plant resources: A review. *Environmental progress & sustainable energy*, 29(2):203–220.
- Zhang, X.-F., Zou, M.-Q., Qi, X.-H., Liu, F., Zhu, X.-H., and Zhao, B.-H. (2010). Detection of melamine in liquid milk using surface-enhanced raman scattering spectroscopy. *Journal of Raman Spectroscopy*, 41(12):1655–1660.
- Zhang, Y., Huang, Y., Zhai, F., Du, R., Liu, Y., and Lai, K. (2012). Analyses of enrofloxacin, furazolidone and malachite green in fish products with surface-enhanced raman spectroscopy. *Food chemistry*, 135(2):845–850.
- Zhao, Y., Luo, W., Kanda, P., Cheng, H., Chen, Y., Wang, S., and Huan, S. (2013). Silver deposited polystyrene (ps) microspheres for surface-enhanced raman spectroscopic-encoding and rapid label-free detection of melamine in milk powder. *Talanta*, 113:7–13.
- Zheng, J. and He, L. (2014). Surface-enhanced raman spectroscopy for the chemical analysis of food. *Comprehensive Reviews in Food Science and Food Safety*, 13(3):317–328.
- Zheng, J., Pang, S., Labuza, T. P., and He, L. (2013). Semi-quantification of surface-enhanced raman scattering using a handheld raman spectrometer: a feasibility study. *Analyst*, 138(23):7075–7078.

APPENDIX A

A.1 Example code for Principal component analysis

Below is given example code for PCA analysis done by using Matlab R2013a software

```
\% Load baseline corrected data
\%A1
Imp=importdata('@A1.1.txt');
a11=Imp(:,2);
Imp=importdata('@A1.2.txt');
a12=Imp(:,2);
Imp=importdata('@A1.3.txt');
a13=Imp(:,2);
Imp=importdata('@A1.4.txt');
a14=Imp(:,2);
Imp=importdata('@A1.5.txt');
a15=Imp(:,2);
Imp=importdata('@A1.6.txt');
a16=Imp(:,2);
Imp=importdata('@A1.7.txt');
a17=Imp(:,2);
Imp=importdata('@A1.8.txt');
a18=Imp(:,2);
Imp=importdata('@A1.9.txt');
a19=Imp(:,2);
\%A2
```

```

Imp=importdata('@A2.1.txt');
a21=Imp(:,2);
Imp=importdata('@A2.2.txt');
a22=Imp(:,2);
Imp=importdata('@A2.3.txt');
a23=Imp(:,2);
Imp=importdata('@A2.4.txt');
a24=Imp(:,2);
Imp=importdata('@A2.5.txt');
a25=Imp(:,2);
Imp=importdata('@A2.6.txt');
a26=Imp(:,2);
Imp=importdata('@A2.7.txt');
a27=Imp(:,2);
Imp=importdata('@A2.8.txt');
a28=Imp(:,2);
Imp=importdata('@A2.9.txt');
a29=Imp(:,2);
\%\% A3
Imp=importdata('@A3.1.txt');
a31=Imp(:,2);
Imp=importdata('@A3.2.txt');
a32=Imp(:,2);
Imp=importdata('@A3.3.txt');
a33=Imp(:,2);
Imp=importdata('@A3.4.txt');
a34=Imp(:,2);
Imp=importdata('@A3.5.txt');
a35=Imp(:,2);
Imp=importdata('@A3.6.txt');
a36=Imp(:,2);
Imp=importdata('@A3.7.txt');
a37=Imp(:,2);
Imp=importdata('@A3.8.txt');
a38=Imp(:,2);
Imp=importdata('@A3.9.txt');

```



```

a39=Imp(:,2);
\% \% B1
Imp=importdata('@B1.1.txt');
b11=Imp(:,2);
Imp=importdata('@B1.2.txt');
b12=Imp(:,2);
Imp=importdata('@B1.3.txt');
b13=Imp(:,2);
Imp=importdata('@B1.4.txt');
b14=Imp(:,2);
Imp=importdata('@B1.5.txt');
b15=Imp(:,2);
Imp=importdata('@B1.6.txt');
b16=Imp(:,2);
Imp=importdata('@B1.7.txt');
b17=Imp(:,2);
Imp=importdata('@B1.8.txt');
b18=Imp(:,2);
Imp=importdata('@B1.9.txt');
b19=Imp(:,2);
\% \% B2
Imp=importdata('@B2.1.txt');
b21=Imp(:,2);
Imp=importdata('@B2.2.txt');
b22=Imp(:,2);
Imp=importdata('@B2.3.txt');
b23=Imp(:,2);
Imp=importdata('@B2.4.txt');
b24=Imp(:,2);
Imp=importdata('@B2.5.txt');
b25=Imp(:,2);
Imp=importdata('@B2.6.txt');
b26=Imp(:,2);
Imp=importdata('@B2.7.txt');
b27=Imp(:,2);
Imp=importdata('@B2.8.txt');

```

```

b28=Imp(:,2);
Imp=importdata('@B2_9.txt');
b29=Imp(:,2);
\%\% B3
Imp=importdata('@B3_1.txt');
b31=Imp(:,2);
Imp=importdata('@B3_2.txt');
b32=Imp(:,2);
Imp=importdata('@B3_3.txt');
b33=Imp(:,2);
Imp=importdata('@B3_4.txt');
b34=Imp(:,2);
Imp=importdata('@B3_5.txt');
b35=Imp(:,2);
Imp=importdata('@B3_6.txt');
b36=Imp(:,2);
Imp=importdata('@B3_7.txt');
b37=Imp(:,2);
Imp=importdata('@B3_8.txt');
b38=Imp(:,2);
Imp=importdata('@B3_9.txt');
b39=Imp(:,2);
\%\% C1
Imp=importdata('@C1_1.txt');
c11=Imp(:,2);
Imp=importdata('@C1_2.txt');
c12=Imp(:,2);
Imp=importdata('@C1_3.txt');
c13=Imp(:,2);
Imp=importdata('@C1_4.txt');
c14=Imp(:,2);
Imp=importdata('@C1_5.txt');
c15=Imp(:,2);
Imp=importdata('@C1_6.txt');
c16=Imp(:,2);
Imp=importdata('@C1_7.txt');

```

```

c17=Imp(:,2);
Imp=importdata('@C1.8.txt');
c18=Imp(:,2);
Imp=importdata('@C1.9.txt');
c19=Imp(:,2);
\% \% C2
Imp=importdata('@C2.1.txt');
c21=Imp(:,2);
Imp=importdata('@C2.2.txt');
c22=Imp(:,2);
Imp=importdata('@C2.3.txt');
c23=Imp(:,2);
Imp=importdata('@C2.4.txt');
c24=Imp(:,2);
Imp=importdata('@C2.5.txt');
c25=Imp(:,2);
Imp=importdata('@C2.6.txt');
c26=Imp(:,2);
Imp=importdata('@C2.7.txt');
c27=Imp(:,2);
Imp=importdata('@C2.8.txt');
c28=Imp(:,2);
Imp=importdata('@C2.9.txt');
c29=Imp(:,2);
\% \% C3
Imp=importdata('@C3.1.txt');
c31=Imp(:,2);
Imp=importdata('@C3.2.txt');
c32=Imp(:,2);
Imp=importdata('@C3.3.txt');
c33=Imp(:,2);
Imp=importdata('@C3.4.txt');
c34=Imp(:,2);
Imp=importdata('@C3.5.txt');
c35=Imp(:,2);
Imp=importdata('@C3.6.txt');

```

```

c36=Imp(:,2);
Imp=importdata('@C3_7.txt');
c37=Imp(:,2);
Imp=importdata('@C3_8.txt');
c38=Imp(:,2);
Imp=importdata('@C3_9.txt');
c39=Imp(:,2);
\%\% D1
Imp=importdata('@D1_1.txt');
d11=Imp(:,2);
Imp=importdata('@D1_2.txt');
d12=Imp(:,2);
Imp=importdata('@D1_3.txt');
d13=Imp(:,2);
Imp=importdata('@D1_4.txt');
d14=Imp(:,2);
Imp=importdata('@D1_5.txt');
d15=Imp(:,2);
Imp=importdata('@D1_6.txt');
d16=Imp(:,2);
Imp=importdata('@D1_7.txt');
d17=Imp(:,2);
Imp=importdata('@D1_8.txt');
d18=Imp(:,2);
Imp=importdata('@D1_9.txt');
d19=Imp(:,2);
\%\% D2
Imp=importdata('@D2_1.txt');
d21=Imp(:,2);
Imp=importdata('@D2_2.txt');
d22=Imp(:,2);
Imp=importdata('@D2_3.txt');
d23=Imp(:,2);
Imp=importdata('@D2_4.txt');
d24=Imp(:,2);
Imp=importdata('@D2_5.txt');

```

```

d25=Imp(:,2);
Imp=importdata('@D2_6.txt');
d26=Imp(:,2);
Imp=importdata('@D2_7.txt');
d27=Imp(:,2);
Imp=importdata('@D2_8.txt');
d28=Imp(:,2);
Imp=importdata('@D2_9.txt');
d29=Imp(:,2);
\% \% D3
Imp=importdata('@D3_1.txt');
d31=Imp(:,2);
Imp=importdata('@D3_2.txt');
d32=Imp(:,2);
Imp=importdata('@D3_3.txt');
d33=Imp(:,2);
Imp=importdata('@D3_4.txt');
d34=Imp(:,2);
Imp=importdata('@D3_5.txt');
d35=Imp(:,2);
Imp=importdata('@D3_6.txt');
d36=Imp(:,2);
Imp=importdata('@D3_7.txt');
d37=Imp(:,2);
Imp=importdata('@D3_8.txt');
d38=Imp(:,2);
Imp=importdata('@D3_9.txt');
d39=Imp(:,2);
\% \% E1
Imp=importdata('@E1_1.txt');
e11=Imp(:,2);
Imp=importdata('@E1_2.txt');
e12=Imp(:,2);
Imp=importdata('@E1_3.txt');
e13=Imp(:,2);
Imp=importdata('@E1_4.txt');

```

```

e14=Imp(:,2);
Imp=importdata('@E1.5.txt');
e15=Imp(:,2);
Imp=importdata('@E1.6.txt');
e16=Imp(:,2);
Imp=importdata('@E1.7.txt');
e17=Imp(:,2);
Imp=importdata('@E1.8.txt');
e18=Imp(:,2);
Imp=importdata('@E1.9.txt');
e19=Imp(:,2);
\%\% E2
Imp=importdata('@E2.1.txt');
e21=Imp(:,2);
Imp=importdata('@E2.2.txt');
e22=Imp(:,2);
Imp=importdata('@E2.3.txt');
e23=Imp(:,2);
Imp=importdata('@E2.4.txt');
e24=Imp(:,2);
Imp=importdata('@E2.5.txt');
e25=Imp(:,2);
Imp=importdata('@E2.6.txt');
e26=Imp(:,2);
Imp=importdata('@E2.7.txt');
e27=Imp(:,2);
Imp=importdata('@E2.8.txt');
e28=Imp(:,2);
Imp=importdata('@E2.9.txt');
e29=Imp(:,2);
\%\% E3
Imp=importdata('@E3.1.txt');
e31=Imp(:,2);
Imp=importdata('@E3.2.txt');
e32=Imp(:,2);
Imp=importdata('@E3.3.txt');

```

```

e33=Imp(:,2);
Imp=importdata('@E3.4.txt');
e34=Imp(:,2);
Imp=importdata('@E3.5.txt');
e35=Imp(:,2);
Imp=importdata('@E3.6.txt');
e36=Imp(:,2);
Imp=importdata('@E3.7.txt');
e37=Imp(:,2);
Imp=importdata('@E3.8.txt');
e38=Imp(:,2);
Imp=importdata('@E3.9.txt');
e39=Imp(:,2);
\%\% F1
Imp=importdata('@F1.1.txt');
f11=Imp(:,2);
Imp=importdata('@F1.2.txt');
f12=Imp(:,2);
Imp=importdata('@F1.3.txt');
f13=Imp(:,2);
Imp=importdata('@F1.4.txt');
f14=Imp(:,2);
Imp=importdata('@F1.5.txt');
f15=Imp(:,2);
Imp=importdata('@F1.6.txt');
f16=Imp(:,2);
Imp=importdata('@F1.7.txt');
f17=Imp(:,2);
Imp=importdata('@F1.8.txt');
f18=Imp(:,2);
Imp=importdata('@F1.9.txt');
f19=Imp(:,2);
\%\% F2
Imp=importdata('@F2.1.txt');
f21=Imp(:,2);
Imp=importdata('@F2.2.txt');

```

```

f22=Imp(:,2);
Imp=importdata('@F2.3.txt');
f23=Imp(:,2);
Imp=importdata('@F2.4.txt');
f24=Imp(:,2);
Imp=importdata('@F2.5.txt');
f25=Imp(:,2);
Imp=importdata('@F2.6.txt');
f26=Imp(:,2);
Imp=importdata('@F2.7.txt');
f27=Imp(:,2);
Imp=importdata('@F2.8.txt');
f28=Imp(:,2);
Imp=importdata('@F2.9.txt');
f29=Imp(:,2);
\%\% F3
Imp=importdata('@F3.1.txt');
f31=Imp(:,2);
Imp=importdata('@F3.2.txt');
f32=Imp(:,2);
Imp=importdata('@F3.3.txt');
f33=Imp(:,2);
Imp=importdata('@F3.4.txt');
f34=Imp(:,2);
Imp=importdata('@F3.5.txt');
f35=Imp(:,2);
Imp=importdata('@F3.6.txt');
f36=Imp(:,2);
Imp=importdata('@F3.7.txt');
f37=Imp(:,2);
Imp=importdata('@F3.8.txt');
f38=Imp(:,2);
Imp=importdata('@F3.9.txt');
f39=Imp(:,2);
\%\% Combine all the data
a1=[a11 a12 a13 a14 a15 a16 a17 a18 a19];

```



```

a2=[a21 a22 a23 a24 a25 a26 a27 a28 a29];
a3=[a31 a32 a33 a34 a35 a36 a37 a38 a39];
b1=[b11 b12 b13 b14 b15 b16 b17 b18 b19];
b2=[b21 b22 b23 b24 b25 b26 b27 b28 b29];
b3=[b31 b32 b33 b34 b35 b36 b37 b38 b39];
c1=[c11 c12 c13 c14 c15 c16 c17 c18 c19];
c2=[c21 c22 c23 c24 c25 c26 c27 c28 c29];
c3=[c31 c32 c33 c34 c35 c36 c37 c38 c39];
d1=[d11 d12 d13 d14 d15 d16 d17 d18 d19];
d2=[d21 d22 d23 d24 d25 d26 d27 d28 d29];
d3=[d31 d32 d33 d34 d35 d36 d37 d38 d39];
e1=[e11 e12 e13 e14 e15 e16 e17 e18 e19];
e2=[e21 e22 e23 e24 e25 e26 e27 e28 e29];
e3=[e31 e32 e33 e34 e35 e36 e37 e38 e39];
f1=[f11 f12 f13 f14 f15 f16 f17 f18 f19];
f2=[f21 f22 f23 f24 f25 f26 f27 f28 f29];
f3=[f31 f32 f33 f34 f35 f36 f37 f38 f39];

\%\%
a=[a1 a2 a3];
b=[b1 b2 b3];
c=[c1 c2 c3];
d=[d1 d2 d3];
e=[e1 e2 e3];
f=[f1 f2 f3];

\%\%
\% Combine all of the data
all=[a b c d e f];

\%\%
\% Visualize pca analysis for reference
mapcaplot(all');

\%\%
\% Extract pca scores for each measurement
[coeff,scores]=pca(all');
as11=scores(1:9,1);
as12=scores(1:9,2);
as13=scores(1:9,3);

```

```
as14=scores (1:9,4);
as15=scores (1:9,5);
as21=scores (10:18,1);
as22=scores (10:18,2);
as23=scores (10:18,3);
as24=scores (10:18,4);
as25=scores (10:18,5);
as31=scores (19:27,1);
as32=scores (19:27,2);
as33=scores (19:27,3);
as34=scores (19:27,4);
as35=scores (19:27,5);
bs11=scores (28:36,1);
bs12=scores (28:36,2);
bs13=scores (28:36,3);
bs14=scores (28:36,4);
bs15=scores (28:36,5);
bs21=scores (37:45,1);
bs22=scores (37:45,2);
bs23=scores (37:45,3);
bs24=scores (37:45,4);
bs25=scores (37:45,5);
bs31=scores (46:54,1);
bs32=scores (46:54,2);
bs33=scores (46:54,3);
bs34=scores (46:54,4);
bs35=scores (46:54,5);
cs11=scores (55:63,1);
cs12=scores (55:63,2);
cs13=scores (55:63,3);
cs14=scores (55:63,4);
cs15=scores (55:63,5);
cs21=scores (64:72,1);
cs22=scores (64:72,2);
cs23=scores (64:72,3);
cs24=scores (64:72,4);
```

```
cs25=scores (64:72,5);
cs31=scores (73:81,1);
cs32=scores (73:81,2);
cs33=scores (73:81,3);
cs34=scores (73:81,4);
cs35=scores (73:81,5);
ds11=scores (82:90,1);
ds12=scores (82:90,2);
ds13=scores (82:90,3);
ds14=scores (82:90,4);
ds15=scores (82:90,5);
ds21=scores (91:99,1);
ds22=scores (91:99,2);
ds23=scores (91:99,3);
ds24=scores (91:99,4);
ds25=scores (91:99,5);
ds31=scores (100:108,1);
ds32=scores (100:108,2);
ds33=scores (100:108,3);
ds34=scores (100:108,4);
ds35=scores (100:108,5);
es11=scores (109:117,1);
es12=scores (109:117,2);
es13=scores (109:117,3);
es14=scores (109:117,4);
es15=scores (109:117,5);
es21=scores (118:126,1);
es22=scores (118:126,2);
es23=scores (118:126,3);
es24=scores (118:126,4);
es25=scores (118:126,5);
es31=scores (127:135,1);
es32=scores (127:135,2);
es33=scores (127:135,3);
es34=scores (127:135,4);
es35=scores (127:135,5);
```

```

fs11=scores(136:144,1);
fs12=scores(136:144,2);
fs13=scores(136:144,3);
fs14=scores(136:144,4);
fs15=scores(136:144,5);
fs21=scores(145:153,1);
fs22=scores(145:153,2);
fs23=scores(145:153,3);
fs24=scores(145:153,4);
fs25=scores(145:153,5);
fs31=scores(154:162,1);
fs32=scores(154:162,2);
fs33=scores(154:162,3);
fs34=scores(154:162,4);
fs35=scores(154:162,5);

\% \% PLOT different principal component combinations,
each sample with a different color

plot(as11,as12,'b*',as21,as22,'b*',as31,as32,'b*',
bs11,bs12,'g*',bs21,bs22,'g*',bs31,bs32,'g*',
cs11,cs12,'r*',cs21,cs22,'r*',cs31,cs32,'r*',ds11,ds12,'c*',
ds21,ds22,'c*',ds31,ds32,'c*',es11,es12,'m*',
es21,es22,'m*',es31,es32,'m*',fs11,fs12,'k*',
fs21,fs22,'k*',fs31,fs32,'k*');
xlim([-100 150]);
ylim([-40 50]);
xlabel('PC 1')
ylabel('PC 2')
\% \% legend('Smooth gold + antibody + Ara h1 + rinsed','
Gold-pyr-PET + antibody + Ara h1 + rinsed ',
'Gold-pyr-zein + antibody + Ara h1 + rinsed','r',
'Gold-pyr-zein + antibody + Ara h1','c',
'Gold-pyr-zein + antibody','m','Gold-pyr-zein','k');
title ('Principal component analysis (PC 1 vs PC 2)');
\% \%

```

```

plot(as11,as13,'b*',as21,as23,'b*',as31,as33,'b*',
bs11,bs13,'g*',bs21,bs23,'g*',bs31,bs33,'g*',
cs11,cs13,'r*',cs21,cs23,'r*',cs31,cs33,'r*',
ds11,ds13,'c*',ds21,ds23,'c*',ds31,ds33,'c*',
es11,es13,'m*',es21,es23,'m*',es31,es33,'m*',
fs11,fs13,'k*',fs21,fs23,'k*',fs31,fs33,'k*');
xlim([-100 150]);
ylim([-30 30]);
xlabel('PC 1')
ylabel('PC 3')
\%legend('Smooth gold + antibody + Ara h1 + rinsed',
'Gold-pyr-PET + antibody + Ara h1 + rinsed ',
'Gold-pyr-zein + antibody + Ara h1 + rinsed','r',
'Gold-pyr-zein + antibody + Ara h1','c',
'Gold-pyr-zein + antibody','m','Gold-pyr-zein','k');
title ('Principal component analysis (PC 1 vs PC 3)');

```

```

\%\%
plot(as12,as13,'b*',as22,as23,'b*',as32,as33,'b*',
bs12,bs13,'g*',bs22,bs23,'g*',bs32,bs33,'g*',
cs12,cs13,'r*',cs22,cs23,'r*',cs32,cs33,'r*',
ds12,ds13,'c*',ds22,ds23,'c*',ds32,ds33,'c*',
es12,es13,'m*',es22,es23,'m*',es32,es33,'m*',
fs12,fs13,'k*',fs22,fs23,'k*',fs32,fs33,'k*');
xlim([-50 60]);
ylim([-30 40]);
xlabel('PC 2')
ylabel('PC 3')
\%legend('Smooth gold + antibody + Ara h1 + rinsed',
'Gold-pyr-PET + antibody + Ara h1 + rinsed ',
'Gold-pyr-zein + antibody + Ara h1 + rinsed','r',
'Gold-pyr-zein + antibody + Ara h1','c',
'Gold-pyr-zein + antibody','m','Gold-pyr-zein','k');
title ('Principal component analysis (PC 2 vs PC 3)');
\%\% Without non-rinsed option
plot(as12,as13,'c*',as22,as23,'c*',as32,as33,'c*',

```

```

bs12,bs13,'g*',bs22,bs23,'g*',bs32,bs33,'g*',
cs12,cs13,'r*',cs22,cs23,'r*',cs32,cs33,'r*',
es12,es13,'b*',es22,es23,'b*',es32,es33,'b*',
fs12,fs13,'k*',fs22,fs23,'k*',fs32,fs33,'k*');
xlim([-50 60]);
ylim([-30 40]);
xlabel('PC 2')
ylabel('PC 3')
\%legend('Smooth gold + antibody + Ara h1 + rinsed',
'Gold-pyr-PET + antibody + Ara h1 + rinsed ',
'Gold-pyr-zein + antibody + Ara h1 + rinsed','r',
'Gold-pyr-zein + antibody + Ara h1','c',
'Gold-pyr-zein + antibody','m','Gold-pyr-zein','k');
title ('Principal component analysis (PC 2 vs PC 3)');
\%\% Without non-rinsed option
plot(cs12,cs13,'r*',cs22,cs23,'r*',cs32,cs33,'r*',
ds12,ds13,'c*',ds22,ds23,'c*',ds32,ds33,'c*',
es12,es13,'b*',es22,es23,'b*',es32,es33,'b*',
fs12,fs13,'k*',fs22,fs23,'k*',fs32,fs33,'k*');
xlim([-50 60]);
ylim([-30 40]);
xlabel('PC 2')
ylabel('PC 3')
\%legend('Smooth gold + antibody + Ara h1 + rinsed',
'Gold-pyr-PET + antibody + Ara h1 + rinsed ',
'Gold-pyr-zein + antibody + Ara h1 + rinsed','r',
'Gold-pyr-zein + antibody + Ara h1','c',
'Gold-pyr-zein + antibody','m','Gold-pyr-zein','k');
title ('Principal component analysis (PC 2 vs PC 3)');
\%\%
plot(as11,as15,'b*',as21,as25,'b*',as31,as35,'b*',
bs11,bs15,'g*',bs21,bs25,'g*',bs31,bs35,'g*',
cs11,cs15,'r*',cs21,cs25,'r*',cs31,cs35,'r*',
ds11,ds15,'c*',ds21,ds25,'c*',ds31,ds35,'c*',
es11,es15,'m*',es21,es25,'m*',es31,es35,'m*',
fs11,fs15,'k*',fs21,fs25,'k*',fs31,fs35,'k*');

```

```

xlim([-100 150]);
ylim([-50 50]);
xlabel('PC 1')
ylabel('PC 5')
\%legend('Smooth gold + antibody + Ara h1 + rinsed',
'Gold-pyr-PET + antibody + Ara h1 + rinsed ',
'Gold-pyr-zein + antibody + Ara h1 + rinsed','r',
'Gold-pyr-zein + antibody + Ara h1','c',
'Gold-pyr-zein + antibody','m','Gold-pyr-zein','k');
title ('Principal component analysis (PC 1 vs PC 5)');
\%
plot(as12,as15,'b*',as22,as25,'b*',as32,as35,'b*',
bs12,bs15,'g*',bs22,bs25,'g*',bs32,bs35,'g*',
cs12,cs15,'r*',cs22,cs25,'r*',cs32,cs35,'r*',
ds12,ds15,'c*',ds22,ds25,'c*',ds32,ds35,'c*',
es12,es15,'m*',es22,es25,'m*',es32,es35,'m*',
fs12,fs15,'k*',fs22,fs25,'k*',fs32,fs35,'k*');
xlim([-40 40]);
ylim([-30 30]);
xlabel('PC 2')
ylabel('PC 5')
\%legend('Smooth gold + antibody + Ara h1 + rinsed',
'Gold-pyr-PET + antibody + Ara h1 + rinsed ',
'Gold-pyr-zein + antibody + Ara h1 + rinsed','r',
'Gold-pyr-zein + antibody + Ara h1','c',
'Gold-pyr-zein + antibody','m','Gold-pyr-zein','k');
title ('Principal component analysis (PC 2 vs PC 5)');

```

A.2 Specifications of Atomic Force Microscopy

Figure A.1: Specifications of Atomic Force Microscopy used in this study

Specifications

Operating Modes

Contact Mode: Imaging using feedback on deflection. Height, deflection, and lateral force signals available.

AC: Q-controlled imaging using feedback on amplitude. Signals available include height, amplitude/phase, I/Q, deflection; both air and fluid.

Force Mode: Force curve acquisition in contact or AC mode. All signals available.

Lateral Force: Frictional force imaging.

MicroAngelo: Built-in nanolithography/nanomanipulation.

EFM/Surface Potential/Conductive AFM with ORCA™ (optional)/Magnetic Force Microscopy (MFM)

Data Acquisition

Data size is limited only by the memory on the PC (i.e., 10 million point force curves and >5k x 5k point images are possible). It is possible to capture data at 5MHz for up to two million points continuously.

Scan Axes

X&Y: 90µm travel in closed loop. Closed loop position control with sensor noise <0.6nm average deviation (Adev) in a 0.1Hz-1kHz bandwidth (BW) and sensor nonlinearity <0.5% (Adev/full travel) at full scan.

Z: >15µm sensed travel in closed loop. Sensor noise <0.3nm Adev in a 0.1Hz-1kHz BW and sensor non-linearity less than 0.2% (Adev/full travel) at full scan.

Z height: noise <0.06nm Adev, 0.1Hz-1kHz BW.

Optical Lever

Noise <0.03nm Adev in a 0.1Hz to 1kHz BW.

Controller Electronics

A/Ds: One 16-bit input operating at 5MHz with seven gains and a 16-bit offset. Used primarily for cantilever deflection, but also user accessible; Five 16-bit inputs operating at 100kHz (sampling rate can be increased for user experiments). Typically three are used for the reading of the X, Y, and Z sensors and two are available for user inputs.

Frequency Synthesizer: Output from a Direct Digital Synthesizer (DDS) is available on a 16-bit, 10MHz D/A.

Frequency: DC to 2.0MHz in 2mHz increments.

Amplitude: 0 to 20V(p-p) in 0.6mV increments. Amplitude, phase, and frequency of the oscillator can be controlled from software at 100kHz update rates.

D/As: Six high resolution, 24-bit channels operating at 100kHz (sampling rate can be increased for user experiments)—three for scanning, and three for user outputs.

Digital Lock-in: Fully digital lock-in operating at 5MHz provides quadrature outputs. Both R/θ (amplitude/phase) and I/Q (Rcosθ/Rsinθ) are available in output bandwidths up to 35kHz.

DSP: Floating point processor running at 80MHz.

Digital Q-Control: for cantilevers from 2kHz to 2MHz; typically enhances or suppresses Q by 5X.

Computer-to-Controller Communication:

Universal Serial Bus (USB).

X, Y, & Z High Voltage Outputs: -10 to +150V.

Computer: Minimum: Dell® Precision 370, 2.8GHz, 2GB RAM, 80GB hard drive, DVD writer, two 19" LCD Panels, Windows® XP Professional. Custom configurations available.

Light Source

Superluminescent diode (SLD) is classified as Class 1M. Viewing with an optical instrument within a distance of 100mm may pose an eye hazard.

Stage

Micrometer driven stage for mechanical alignment of the cantilever tip and sample.

Motorized X-Y (optional)

MFP Head

Standard Head: Flexure-mounted optical lever system with low-coherence SLD, liquid-compatible and AC-capable cantilever holder, dichroic mirror and window for optical access to cantilever, 80-pitch engage screws, and Invar shell.

Extended Head (optional): 28µm Z scan range.

Top View Head (optional): Adds 10x, 0.28 NA long-working distance objective with focus and beamsteering adjustments, allows high resolution optical imaging of tip and sample.

Narrowband Source (optional): Eliminates interference with sensitive optical experiments.

Base Models

Stand Alone (SA): Three models are available. All feature bright field microscopy with Kohler illumination, adjustable aperture and field diaphragm, remote 150W light source coupled via fiber bundle, dual 1/4" CCD's with 720µm and 240µm fields of view; integrated scanning and interconnect board, and rigid low-vibration construction.

• **Top View:** Uses infinity-corrected Mitutoyo objective in Top View head for imaging of opaque samples at 3µm resolution.

• **Bottom View:** For transparent samples only. Default configuration is 10x/0.25 NA infinity-corrected objective. Others available upon request.

• **Dual View Base:** Combines features of Top and Bottom View, with switchable shutters. Allows for transmitted light in either direction.

Sample Holders

For samples up to 3"x1", including glass slides and coverslips. Specialized sample holders including flow-through and heating available (see Options Data Sheet).

Software

Based in IGOR Pro by WaveMetrics, a powerful scientific data acquisition and analysis environment. The software is user-programmable.

Features include but not limited to:

- Nonlinear curve fitting to arbitrary user-defined functions.
- Extensive image analysis including 2D FFT's, wavelet transformations, convolutions, line profiles, particle analysis, edge detection (eight methods, including Sobel), and thresholding (five methods, including fuzzy entropy).
- Automatic spectral fitting and calibration of cantilever spring constants using thermal noise and Sader method.
- DSPDirector: Optional software for controlling the DSP in the controller.
- Easy generation of scientific publication quality graphs and page layouts.

ARgyle: OpenGL® 3D rendering technology for advanced image display.

• Generate, display, and visualize 3D images in real-time while you scan as well as off-line processing.

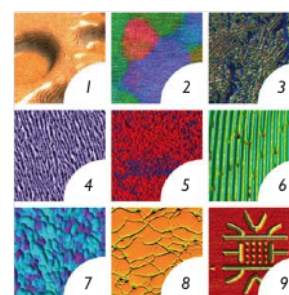
- Overlay alternate channel data with primary to view feature correlation.
- Independent scaling of axes for true 1:1 aspect ratio.
- Mouse-driven rotating, panning, scaling, and specular lighting control of images.
- Export 3D images to clipboard, JPEG, TIFF, BMP, PNG.
- Stereo anaglyph creation from 3D images.

Vibration Isolation

Vibration isolation is recommended for all systems. See Options Data Sheet.

Additional Options

See Options Data Sheet.



Cover Images

1. SEBS spuncoat on a silicon wafer. Phase channel overlaid on rendered topography, 2µm scan. Sample courtesy R. Segalman and A. Hexemer, Kramer Group, UCSB.
2. Block copolymer self-organized into a close-packed lattice of spherical microdomains. Lattice orientation (color) overlaid on height data (light/dark) illustrates grain boundaries and defects, 16µm scan. Sample courtesy M. Trawick, Univ. of Richmond.
3. Phase channel overlaid on rendered topography of polypropylene sample, 1.6µm scan. Sample courtesy L. Chen, Ohio University.
4. Corkscrew pattern on MBE grown GaAs, 12µm scan. Sample courtesy Y. Daniels-Race, LSU.
5. Conductive AFM on AlOx shows electric current. Purple color represents areas of high conductivity overlaid on rendered topography, 2µm scan.
6. Heating of polymer grating to 135°C, 10µm scan. Sample courtesy Y. Kong, UC Irvine.
7. Piezo response image of PZT, 1µm scan. Sample courtesy J. Spanier, Drexel University.
8. Network of nanostructured calcium phosphate particles (green areas) interconnected by DNA (dark interconnecting lines), 4µm scan. Sample courtesy Prashant N. Kumta, Carnegie Mellon University.
9. Quantum dot structure created on a GaAs wafer using oxidation lithography, 2.5µm scan. Image courtesy D. Graf and R. Shleser, Ensslin Group, ETH Zurich.

ARgyle, DSPDirector, MFP-3D, MicroAngelo, ModeMaster, NPS, ORCA, Savant, and SmartStart are trademarks of Asylum Research. Quicktime is a registered trademark of Apple Computer. OpenGL is a registered trademark of SGI. Windows is a registered trademark of Microsoft, Inc. Dell is a registered trademark of Dell Computer Corp.

Represented by:



6310 Hollister Avenue
Santa Barbara, CA 93117

voice: 805-696-6466
fax: 805-696-6444
Toll free: 888-472-2795

www.AsylumResearch.com
info@AsylumResearch.com

Specifications subject to
change without notice